DNA MECHANOTECHNOLOGY FOR SENSING AND GENERATING PICONEWTON SCALE MECHANICAL FORCES

A Dissertation
Presented to
The Academic Faculty

by

Aaron Thomas Blanchard

In Partial Fulfillment
of the Requirements for the Degree
Doctor of Philosophy in
Biomedical Engineering

Emory University
and
Georgia Institute of Technology
August 2020

DNA MECHANOTECHNOLOGY FOR SENSING AND GENERATING PICONEWTON SCALE MECHANICAL FORCES

Approved by:

Dr. Khalid Salaita, Advisor
Department of Chemistry
Emory University

Dr. Eric Weeks
Department of Physics
Emory University

Dr. Yonggang Ke
Department of Biomedical Engineering
Emory University

Dr. Todd Sulchek
Department of Mechanical Engineering
Georgia Institute of Technology

Dr. Keir Neuman
National Heart, Lung, and Blood Institute
National Institutes of Health

Date Approved: July 23rd, 2020

I dedicate this thesis to my hometown, El Paso, TX, USA.

With a combined population of 2.5 million people, El Paso and Juarez, Mexico together make up the largest international community in the world. El Paso's culture is a special hybrid that produces unique art, music, and cuisine. It is surrounded by beautiful landscapes and filled with amazing people. Growing up in El Paso's fusion culture taught me that there is vast richness in the space between things. This perspective has heavily shaped the ways in which I approach scientific research. As a collaborative effort between cultures, the city also taught me the importance of collaboration, which has been central to my thesis work.

ACKNOWLEDGEMENTS

I would like to acknowledge my mentors who helped me become a scientists in various ways. My advisor Dr. Khalid Salaita, has always supported me and helped me bring my ideas into fruition. He has also created a collaborative, stimulating, and interdisciplinary research environment that I have thrived in. I thank my collaborator Dr. Alexa Mattheyses for acting at times as a second mentor for me and for helping me expand my realm of expertise to new areas. I thank my department's former director of graduate studies Dr. Kyla Ross, who invested so much time in helping me develop the professional skills that have immensely boost my productivity and happiness throughout graduate school. I thank Emory Counseling and Psychiatric Services (CAPS), who provide high-quality free counseling services to Emory students. In particular I thank the CAPS director Dr. Wanda Collins, who facilitated three semesters of group counseling sessions that had tremendous, lasting benefits to my mental health. I would like to thank all of the students who have contributed to my projects and who welcomed me on to their projects. In particular, I want to thank Yun "Yvonne" Zhang and Josh Brockman for welcoming me to collaborate on their projects when I was an early-stage graduate student. I want to thank my fiancé, Aurelia Allen, for supporting me throughout my graduate studies and helping me find the happiness that has been so important to my work. In particular, I would like to thank her for always talking to me about my research, and for spending her gap year and summer and winter breaks with me while we studied in separate cities. I would like to thank my friends and family – particularly my mom Rachel, my dad Mike, my stepdad Larry, and sister Alison – for providing me with the lifelong emotional, professional, and financial

support necessary to grow into a scientist. I would like to thank the people at the Atlanta Wild Animal Rescue Effort (AWARE) for committing so much of their time and energy to the treatment and release of injured wildlife. My ~1.5 years volunteering with AWARE was one of the highlights of my time in Atlanta. I thank my colleagues in the Salaita lab for maintaining research lab equipment and for contributing to a positive social environment. I thank the administrative staff of the biomedical engineering department for making the department run. Finally, I would like to thank the maintenance and custodial staff of the Atwood chemistry building for keeping the building clean, safe, and properly functioning so that I could always focus on my scientific research.

TABLE OF CONTENTS

ACKNOWLEDGEMENTS iv

LIST OF TABLES ix

LIST OF FIGURES x

SUMMARY xii

CHAPTER 1. Introduction to DNA mechanotechnology 1
1.1 Historical description of the emergence of DNA mechanotechnology 1
1.2 Force transmitting DNA mechanotechnology 6
1.3 Structural DNA mechanotechnology 7
1.4 Force Sensing 8
1.5 Force generating DNA mechanotechnology 10
1.6 Outlook 12

CHAPTER 2.Highly polyvalent DNA motors generate 100+ piconewtons of force via autochemophoresis 14
2.1 Summary 14
2.2 Introduction to highly polyvalent DNA motors 16
2.3 Particle tracking reveals that HPDMs generate forces exceeding 35 pN 27
2.4 Quantitative estimate of F_{HPDM} 37
Figure 11: High throughput HPDM tracking results, part 2. 44
2.5 Direct visualization of HPDM-induced TGT rupture with single molecule imaging 51
2.6 Demonstration that HPDMs can rupture biotin-streptavidin bonds 59
2.7 Nanopatterning with HPDMs and unzip-mode TGTs 67
2.8 Methods for chapter 2 89
2.8.1 Materials**:** 89
2.8.2 Preparation of custom-designed surface reaction chambers and imaging chambers**:** 90
2.8.3 HPDM preparation for ensemble experiment 93
2.8.4 Substrate preparation for ensemble experiment**:** 94
2.8.5 Microscopy: 94
2.8.6 Ensemble HPDM tracking experiment for 15 bp TGTs: 95
2.8.7 Ensemble HPDM tracking experiment for biotin-streptavidin and 13 bp, 11 bp, 9 bp, and 25 bp TGTs: 96
2.8.8 Automated HPDM detection and tracking for ensemble experiment**:** 97
2.8.9 Prediction of average displacement vs. time curves using mass action model**:** 98
2.8.10 Parameter fitting to estimate F_{HPDM} and calculation of T_{tol}**:** 99
2.8.11 Substrate preparation for single molecule imaging experiments 100
2.8.12 Preparation of fluorescent streptavidin**:** 102
2.8.13 HPDM preparation for single molecule imaging of TGT rupture**:** 102

2.8.14 HPDM preparation for single molecule imaging of biotin-streptavidin bond rupture**:** 103
2.8.15 Single molecule imaging experiment**:** 103
2.8.16 Automated detection of single streptavidin molecules and measurement of colocalization with depletion tracks**:** 103
2.8.17 Calculation of biotin-streptavidin rupture force**:** 104
2.8.18 Estimation of χ' for TGT-coated HPDMs: 104
2.9 Supplemental Note 1 – Calculation of RNA fuel exchange rate 109
2.10 Supplemental Note 2 – Justification of the approximation $F_{HPDM} = T_{tol}N$ 110
2.11 Supplemental Note 3 – multiple TGTs must form within a short time span to contribute cooperatively towards HPDM stalling 116
2.12 Supplemental Note 4 – Calculation of power conversion efficiency 118
2.13 Supplemental Note 5 – Effect of polyvalency on HPDM mobility 120

CHAPTER 3. Properties of highly polyvalent DNA motors revealed with Adhesive dynamics simulations 126
3.1 Introduction to adhesive dynamics 126
3.2 Description of RoloSim 130
3.2.1 Overview 130
3.2.2 Energy minimization 130
3.2.3 Stochastic application of changes to tether set 135
3.3 Goals 139
3.4 Optimization of RoloSim 142
3.4.1 Metrics 142
3.4.2 Optimization of mechanical parameters 151
3.4.3 Assumptions 159
3.5 Results 160
3.5.1 Mean squared displacement analysis 160
3.5.2 Use of RoloSim to parameterize RNase H kinetics 162
3.5.3 Relationship between $[RNase\ H]$ and F_{HPDM}. 163
3.5.4 The effect of HPDM diameter on F_{HPDM} and v_{avg} 167
3.5.5 The effect of RNA fuel and DNA guide density on F_{HPDM} and v_{avg} 170
3.5.6 Simulations of rod-shaped HPDMS (rHPDMs) 174
3.5.7 HPDM motion with a biasing force 178

CHAPTER 4. Fluorescence polarization-based traction force orientation mapping with DNA mechanotechnology and structured illumination molecular force microscopy 183
4.1 Summary 183
4.2 Introduction to molecular force microscopy 184
4.3 Methods 229
4.3.1 Preparation of supported lipid bilayer (SLB) functionalized microparticles. 229
4.3.2 Isolation and handling of platelets 230
4.3.3 Culture and handling of 3T3 fibroblast cells 230
4.3.4 Surface preparation 231
4.3.5 DNA strand hybridization 232
4.3.6 Structured illumination microscopy 232

4.3.7 Standard resolution image processing 233
4.3.8 Preparation of illumination profile correction images 233
4.3.9 Super resolution image processing 234
4.4 Supplemental Note I – derivation of equations for analytical orientation measurement 236

CHAPTER 5. Variable incidence angle linear dichroism (VALiD): a technique for unique 3D orientation measurement of fluorescent ensembles 240
5.1 Introduction 240
5.1.1 Summary 240
5.1.2 Introduction to fluorescence polarization microscopy 241
5.2 Mathematical modeling and computational methods 247
5.2.1 Fluorescence intensity of a conical ensemble 248
5.2.2 Fluorescence Intensity of a Watson ensemble 253
5.2.3 Microscope configurations 256
5.2.4 Monte Carlo simulation method 257
5.2.5 Monte Carlo simulation assessment metrics 261
5.3 Results 266
5.3.1 Initial configuration assessment 266
5.3.2 Optimization of VALiD parameters 271
5.3.3 VALiD accuracy as a function of total photon count 275
5.3.4 Accounting for non-conical distributions and orientation-dependence of emission 278
5.4 Discussion and conclusions 284

CHAPTER 6. Nondegenerate nanoscale traction force orientation mapping with Variable incidence angle molecular force microscopy 288

References 297

LIST OF TABLES

Table 1: Oligonucleotide Sequences 107
Table 2: Timelapse fit parameters for platelet spreading and tension alignment: Median (Inter-quartile range) with Wilcoxen rank-sum test p-values 215
Table 3: Optimal experimental parameters and assessment metrics under optimal conditions 273

LIST OF FIGURES

Figure 1: Emergence of DNA mechanotechnology 4
Figure 2: Highly polyvalent DNA motors with DNA TGT strands 19
Figure 3: Illustrations of surface functionalization processes. 21
Figure 4: HPDMs exhibit persistent motion. 25
Figure 5: Automated HPDM detection algorithm used for ensemble experiments. 30
Figure 6: Automated HPDM tracking algorithm used for ensemble experiments. 32
Figure 7: Automated drift correction process. 33
Figure 8: High throughput HPDM tracking results, part 1. 35
Figure 9: Quantitative estimate of F_{HPDM} 38
Figure 10: 1-TGT, 2-TGT, and 3-TGT models used to simulate R(t) curves. 40
Figure 11: High throughput HPDM tracking results, part 2. 44
Figure 12: Generalized N-TGT model scheme and results. 46
Figure 13: Ensemble HPDM tracking results for TGTs of different lengths. 49
Figure 14: Estimation of TGT strand dissociation constant. 52
Figure 15: Automated image processing for single molecule localization experiments. . 55
Figure 16: Single molecule TGT-rupture experiment results. 57
Figure 17: Single molecule imaging of bond rupture driven by HPDM force generation. 61
Figure 18: Population data for single molecule localization experiment 63
Figure 19: Single molecule biotin-streptavidin (SA) bond-rupture experiment results. .. 65
Figure 20: HPDM-mediated nanopatterning enabled by unzip-mode TGT rupture 69
Figure 21: Ensemble HPDM tracking experiments for 25 bp shear- and unzip-mode TGT and biotin-SA bond rupture experiments 71
Figure 22: Nano-patterning via unzip-mode TGT rupture. 73
Figure 23: Depletion track streptavidin coverage fraction. 75
Figure 24: Streptavidin intensity in TGT-coated HPDM depletion tracks. 77
Figure 25: HPDMs generate force through autochemophoresis. 82
Figure 26: HPDM mobility decreases with increasing polyvalency 85
Figure 27: Delrin reaction chambers and imaging chambers. 92
Figure 28: Oligonucleotide modifications 108
Figure 29: Time dependence of duplex rupture 114
Figure 30: Schematic depiction of the iterative RoloSim simulation method. 129
Figure 31: Tether WLC calculation and approximation 133
Figure 32: E_{teth} measured using WLC Monte Carlo simulations 134
Figure 33: Depiction and calculation of association 137
Figure 34: Depiction of the size difference between rod-shaped and spherical HPDMS 141
Figure 35: Automated analysis of depletion tracks 144
Figure 36: Experimental measurement of path persistence (L_{traj}). 146
Figure 37: RoloSim-based estimation of F_{HPDM} 148
Figure 38: Experimental measurement of average velocity, v_{avg} 150

Figure 39: Depletion tracks from simulations run with varying κ_t^* and $k_{on,0}/k_{clvg}$ values 154
Figure 40: Metrics for first round of optimization 155
Figure 41: RoloSim optimization results, round 2 158
Figure 42: MSD analysis of optimized RoloSim results 161
Figure 43: [RNase H]-dependence of F_{HPDM} and v_{avg} 165
Figure 44: Dependence of F_{HPDM} and v_{avg} on HPDM diameter 169
Figure 45: Dependence of F_{HPDM} and v_{avg} on RNA fuel and DNA guide density 172
Figure 46: Results of simulations of rod-shaped HPDMs (rHPDMs) 176
Figure 47: Simulation results of HPDM translocation in the presence of a biasing force 180
Figure 48: Images of depletion tracks following HPDM translocation with flow-based bias force 182
Figure 49: SIM-MFM concept 189
Figure 50: Analysis of DiI-doped SLB-coated microspheres imaged using SIM microscope. 193
Figure 51: Representative SIM-MFM data 198
Figure 52: Azimuthal angle maps of 15 representative platelets. 202
Figure 53: Reproduction of previous finding that platelets exhibit two distinct zones of force orientation. 203
Figure 54: Results of Monte Carlo simulations of force orientation measurement. 206
Figure 55: Extended analysis of Monte Carlo simulation results. 208
Figure 56: Analysis of measurement errors 209
Figure 57: Dependence of measured $\langle\theta\rangle$ on measured ϕ values. 211
Figure 58: Dynamic properties of human platelets revealed using SIM-MFM. 217
Figure 59: Analysis of T-cell receptor tension does not reveal a polarization-dependent response 220
Figure 60: Analysis of T-cell receptor tension reveals no polarization-dependence 222
Figure 61: fPAINT reveals the orientation of forces applied by individual integrins. 226
Figure 62: VALiD concept 245
Figure 63: Coordinate system used in this work 252
Figure 64: Monte Carlo error simulation results 264
Figure 65: Optimization results 269
Figure 66: Comparison of different configurations 277
Figure 67: Comparison of different ensemble types 282
Figure 68: VALiD-MFM concept 289
Figure 69: Depiction of VALiD-MFM-based measurement 290
Figure 70: Experimental calibration of microscope 292
Figure 71: VALiD-MFM proof of principle experimental results 294

SUMMARY

Mechanical systems are composed of force-generating motors, force sensors, and load-bearing structures. Macro- and micro-scale mechanical systems have revolutionized human civilization, and nanoscale mechanical systems have similar potential. DNA nanotechnology, a unique platform for the self-assembly of complex nanostructures, offers unprecedented capacity to design the components of nanoscale mechanical systems. Today, mechanical DNA devices are playing increasingly critical roles in molecular biophysics, immunology, regenerative medicine, materials science, and nanorobotics.

As a student in Dr. Khalid Salaita's lab, I have spent my PhD developing and studying DNA-based devices that generate and/or sense piconewton (pN)-scale molecular forces. This research area, which I call DNA mechanotechnology, has recently emerged at the intersection of DNA nanotechnology and mechanobiology. As such, much of my work centers around quantitative biophysical modeling of biomolecules under mechanical force. Using this approach, I helped develop the world's most powerful DNA-based motor, which can generate ~100-150 pN of force as it translocates (compared to ~0.02 pN of previous motors) and developed rigorous computational models for studying this novel mechanism of force-generation [1]. I have also helped develop cutting-edge DNA-based tension probes that change shape and subsequently emit fluorescence when pulled on by individual cell-surface receptors.

CHAPTER 1. INTRODUCTION TO DNA MECHANOTECHNOLOGY

Mechanical systems, which are composed of force-generating motors, force sensors, and load-bearing structures, drove the industrial revolution of the 18th and 19th centuries and are, in many ways, the backbone of modern human civilization. Miniaturization of mechanical systems to the mm scale has led to portable electronics, microfluidics, and countless other technological advances. Further miniaturization to the nanometer scale is highly desirable but challenging due to fundamental limitations in top-down manipulation of molecules. DNA nanotechnology[2], a unique platform for bottom-up assembly of complex nanostructures, has recently opened the door to the rational design of nanoscale mechanical systems. As the introduction to my thesis, I highlight this new technological area, which I call *DNA mechanotechnology*. The rest of my thesis will detail specific projects that I have worked within the field.

1.1 Historical description of the emergence of DNA mechanotechnology

Over the past decade, DNA mechanotechnology emerged at the intersection of the fields of molecular mechanobiology[3] and DNA nanotechnology[2] (**Figure 1**). Molecular mechanobiology is the study of the coupling between forces and biochemistry. For example, motor proteins generate mechanical forces [4] (e.g. myosin, kinesin, and dynein), cytoskeletal filaments transmit and store those forces (e.g. actin filaments and microtubules), and mechanosensor proteins detect and respond to these physical inputs[5] (e.g. integrin, notch, and cadherin receptors). Biological filaments, which were first

theorized in the 1950s[6,7], and motor proteins and mechanosensors, which were first observed in the 1980s [8-12], could be directly mechanically interrogated following the invention of single-molecule force spectroscopy (SMFS) in the early 1990s [13,14]. The emergence of DNA nanotechnology, which is the use of DNA to design nanostructures and nanomachines, followed a similar trajectory: the 1953 discovery of the structure of the DNA double helix sparked fervent biological research that drove low-cost methods for DNA synthesis (e.g. the polymerase chain reaction[15] and solid phase oligonucleotide synthesis [16]), conjugation, and structure prediction, ultimately leading to the first synthetic DNA nanostructures and DNA-based nanomachines in the late 80s and early 90s [17,18]. Notably, the DNA origami technique, in which sophisticated nanostructures are assembled in one-pot reactions by "stapling" a long scaffold together at prescribed locations, has revolutionized the DNA nanotechnology field since its invention in 2006 [19].

Since their inceptions, these two research areas have been highly intertwined. Early SMFS research on DNA biomechanics yielded techniques and models that are now crucial to cutting edge DNA nanotechnology structure prediction. DNA has found numerous uses in SMFS research, particularly as handles for connecting SMFS devices to target molecules [20]. In fact, the first recorded use of SMFS involved the stretching of DNA [13]. The study of mechano-biomolecules has produced conceptual models, tools, and design principles that have been inspirational to and useful for the creation of DNA-based nanomechanical devices. The primary use of such devices lies in molecular mechanobiology research, and SMFS, in turn, is one of the primary techniques for their characterization.

Here I define four categories of DNA mechanotechnology – force-generating, force-sensing, force transmitting, and structural – which correspond to biological counterparts of

motors, mechanosensors, and cytoskeleton filaments. Collectively DNA mechanotechnology tools are rapidly growing in number and are becoming central to advances in cell biology, immunology, material science, and single molecule mechanics. I focus my discussion on experimentally-realized mechanotechnology that is explicitly designed to generate, transmit, or sense piconewton (pN)-scale forces. Dynamic shape-shifting DNA nanotechnology, computational tools for prediction of DNA structure/mechanics, and the general mechanical properties of DNA have been extensively reviewed elsewhere [21,22].

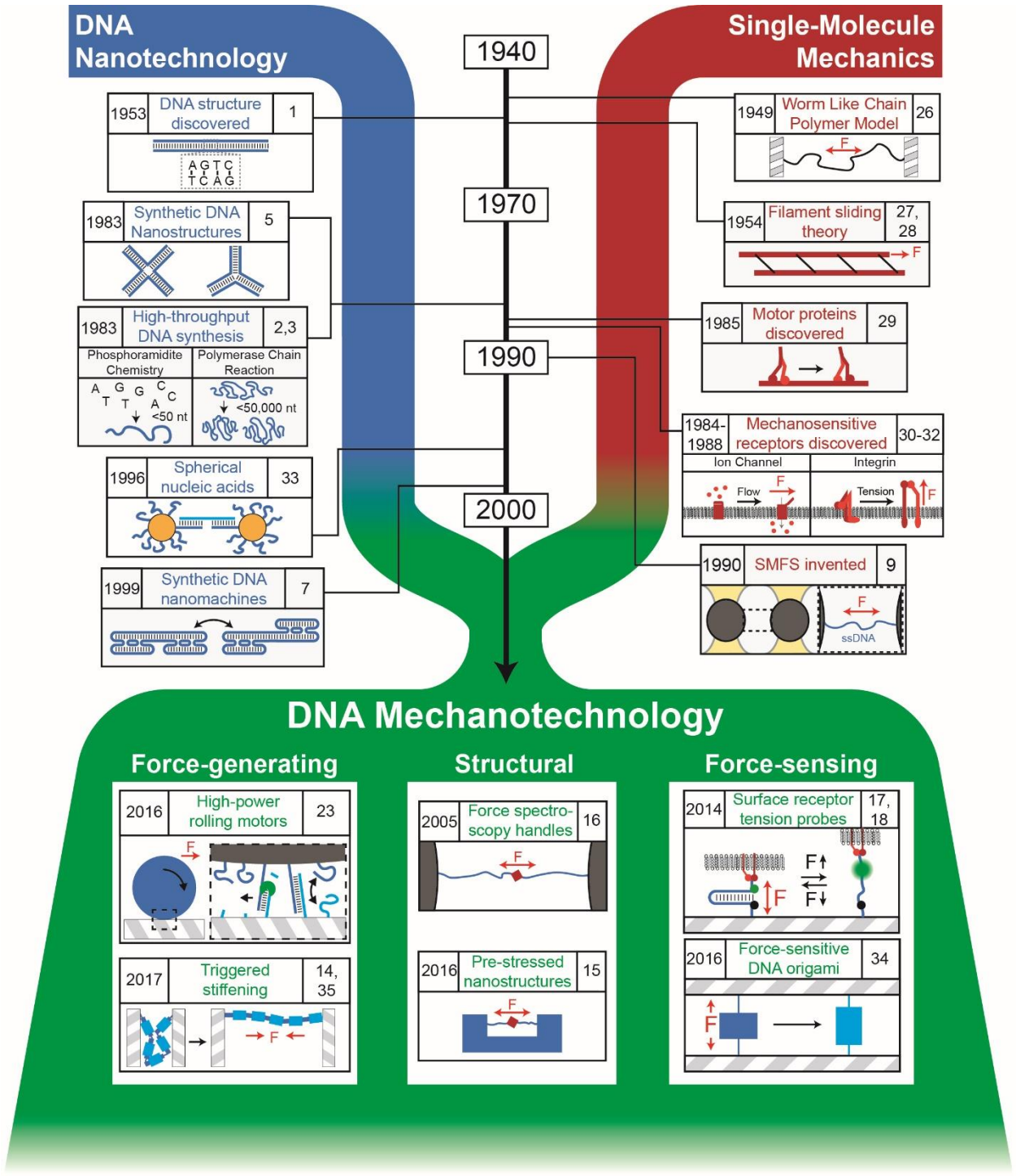

Figure 1: Emergence of DNA mechanotechnology

A diagrammed timeline depicting some of the seminal discoveries and inventions leading up to and within the emerging DNA mechanotechnology research field. Each highlighted

discovery and invention has one (or more) associated reference(s) [6,7,9,11,15-18,23-31] (top right) and date (top left).

1.2 Force transmitting DNA mechanotechnology

Like other flexible polymers, single-stranded DNA (ssDNA) behaves like an entropic spring; if a ssDNA strand is pulled from both ends, the force required to extend it increases in an exponential fashion. The force-extension relationship of ssDNA has been exceptionally well-characterized (e.g. using the freely jointed chain and worm like chain models[23,32,33]), and ssDNA can be synthesized with very precise lengths using conventional DNA replication methods such as polymerase chain reachion (PCR). As such, ssDNA "handles" have long served as useful tools for connecting target molecules to SMFS devices because a DNA strand's mechanical response can be largely decoupled from the mechanical response of the target molecule it is linked to [20]. A limitation of ssDNA handles is that they are very flexible and, as such, undergo substantial thermal fluctuations that add noise to SMFS data. Double stranded DNA (dsDNA) is stiffer than ssDNA and therefore subject to fewer noise-inducing thermal fluctuations. Recently Dietz *et. al.* extended this principle further by using ultra-stiff bundles of several dsDNA helices linked in parallel via the DNA origami technique [34,35]. The minimal measurement noise exhibited by these multi-helix bundles enable the mechanical studies of very weak bonds that would otherwise be impossible to study such as intermolecular base-stacking interactions [35].

A challenge with SMFS studies of generic intermolecular interactions is the need to conjugate molecules directly to SMFS handles. Recent work by Kostrz *et al.* adapted DNA conjugation techniques to a novel SMFS design that uses a DNA "leash" (similar to handles) consisting of three DNA strands[36]. One strand is bound to a magnetic bead and a

molecule of interest, while a second strand is bound to a planar surface and a second molecule of interest. The third strand then covalently links the other two strands. The two molecules of interest interact with each other, and a magnet is used to create a tensile force applied through the leash. The distance between the bead and the surface is monitored using microscopy, allowing quantification of rupture forces and the characterization of the receptor ligand interaction. As with the ultra-stiff bundles described above, this approach enables the study of interactions under very low forces (down to 0.3 pN). The technique was used to investigate receptor-drug interactions, and is expected to expand the breadth of SMFS techniques to have a larger impact on translational research.

Despite these advances in force-transmitting DNA mechanotechnology, the need to tether target molecules to SMFS devices represents a fundamental limitation of SMFS. The DNA nanospring recently reported by Shih et. al. is an innovative force-transmitting nanodevice that also enables SMFS without connection to a SMFS device [37]. This DNA nanospring consists of two parallel dsDNA helices that have been stapled together with the DNA origami technique. Selective mismatches at the staple sites induce curvature, creating a spring structure that is optimal for measuring forces in the <10 pN range. The research team connected cytoskeletal motors to one or both ends of the spring and characterized the relative strength of the motors and their stall forces by tracking the motor force-induced extension of the spring with single molecule fluoresce microscopy.

1.3 Structural DNA mechanotechnology

While the previous section focused on tools for transmitting externally-generated forces, recently-reported multiple DNA origami structures with pre-stressed internal components

[38] have, for the first time, enabled the study of mechanosensitive biomolecules under force without tethers or conventional SMFS devices. An early example presented by Endo *et al.* utilized a "DNA frame" to apply intrinsic stress to dsDNA. Under different levels of tension, the activity of the DNA methylation enzyme *Eco*RI methyltransferase was recorded. The team found that higher tension inhibited activity, providing early evidence for the effect of mechanical tension on enzymatic activity.

More recently Liedl *et. al.* reported a DNA origami force clamp [39] that contains an ssDNA segment that is intrinsically pre-stressed with a tensile force up to 20 pN in magnitude. A mechanosensitive target molecule that alternates between folding states in a force-dependent manner can then be inserted into this ssDNA region. The molecule's force-dependent functions can be then monitored using single molecule fluorescence imaging, yielding unprecedented insight into the target molecule's force-dependent folding properties. Since its initial presentation, the force clamp has found use in multiple studies[40,41].

1.4 Force Sensing

DNA nanostructures that exhibit well-understood mechanical responses to externally-applied forces can also be engineered for force *sensing* applications. The largest class of DNA-based force sensors centers around the force-induced separation of dsDNA strands: The force threshold at which two hybridized strands mechanically separate depends on duplex length, GC content and pulling geometry. If tension is applied at one end of the duplex, the two strands will "unzip" one base pair-at-a-time, resulting in a relatively low force threshold. In contrast, if tension is applied at opposite ends of the duplex then all base

pairs must simultaneously “shear”, resulting in a relatively high separation force. In 2003, Gaub et. al. leveraged these properties and used dsDNA as a force sensor [42]. The team linked dsDNA duplexes in series with a receptor-ligand pair of interest and applied tension until one of the complexes – either the dsDNA duplex or the receptor-ligand pair – mechanically separated. They then then used fluorescence to determine which of the two complexes separated, allowing them to comparatively measure the rupture strength of the receptor-ligand complex.

Wang and Ha recently adapted the mechanical melting of DNA duplexes to control the forces experienced by cell-surface adhesion receptors in receptor mechanobiology studies [43]. In this approach, one oligonucleotide in a duplex is anchored to a glass microscope slide and its complement presents an adhesion ligand. A cell surface receptor binds the ligand and, if the receptor applies high force, separates the two strands. In this way, the DNA duplex tunes the magnitude of forces transmitted to its receptor.

To visualize the piconewton forces applied by cell surface receptors without substantially altering them, we developed molecular fluorescence-based tension microscopy (MTFM), which uses a DNA hairpin flanked by a fluorophore-quencher pair [44-46]. Tension exceeding the hairpin’s characteristic tension threshold unfolds the hairpin, leading to dequenching of the fluorophore that can be visualized on a conventional fluorescence microscope. Mechanical unfolding is fully reversible and the hairpin refolds upon termination of force, thus allowing for real-time visualization of cellular forces with pN resolution without altering biological function. This technology continues to develop. For example, we recently imaged these hairpin probes using a polarized fluorescence-based approach to measure force orientation as well as magnitude [45].

DNA-based MTFM probes are rapidly transforming the field of mechanobiology. For example, these probes helped reveal that platelet integrins are anisotropic mechanosensors[44]. In the area of immunology, DNA-based MTFM probes showed that the B cell receptor [47] and the T cell receptor [46] are both mechanosensors. These studies show that cells harness mechanical forces to enhance the specificity of antigen recognition. This mechanism has recently been described as mechanical proof-reading [48].

A separate class of DNA-based force sensor utilizes the specific chemical properties of DNA under tension. For example, some intercalating dyes (which are fluorescent molecules that wedge themselves into the inter-helix space of DNA duplexes), display increased affinity for duplexes that are under tension. This property has recently been used to create DNA duplex-based force sensors that, when observed under a fluorescence microscope, brighten when subjected to shear forces [49].

DNA origami nanostructures themselves can also exhibit engineered responses to pN-scale forces. For example, the Holliday junction is a four-branched DNA secondary structure that is used extensively in DNA origami design. The Holliday function has two isomer forms, and neighboring Holliday junctions will tend to take on the same isomer. The application of force, however, can trigger cooperative isomerization of the Holliday junctions until the whole structure has isomerized[50]. As an example, this principle has been used to mechanically trigger shape-change of DNA origami nanotubes between long/thin and short/wide equilibrium states[30]. Future extension of this work and principle will likely lead to mechanically responsive functional devices.

1.5 Force generating DNA mechanotechnology

One of the most challenging goals in this research area is the development of devices that generate piconewton-scale forces. Molecular walkers such as kinesin, myosin, and dynein enable efficient and rapid conversion of chemical energy (stored in ATP) to generate 1-10 pN of mechanical force to perform a wide variety of biological tasks. Engineering similar functionality from the bottom-up is challenging but is critical to the development of next-generation nanomachines. The recent development of DNA walkers, which walk upon molecular tracks via hybridization interactions, has been an important step toward the creation of synthetic molecular motors. DNA walkers have been engineered to perform diverse tasks at the nanoscale, such as sorting randomly patterned molecular cargo into defined collection bins [51]. However, DNA walkers are highly reliant on thermal (Brownian) fluctuations and, as such, are currently incapable of generating and sustaining pN-scale forces. pN-scale force generation is a fundamental property of molecular motors that must achieved for the development of next-generation nanomachines to occur.

We recently demonstrated progress toward this goal by showing that highly polyvalent DNA motors, which are large versions of DNA walkers that form hundreds of contacts with the track simultaneously, can generate force in the excess of 100 pN [29]. These motors, which are the first example of pN-scale force generation by a DNA-based motors, are micron-scale and will therefore need to be substantially reduced in size before any nanoscale force-generation applications are possible.

Most existing force-generating DNA devices convert the energy released by DNA hybridization into mechanical work [21]. However, DNA hybridization offers a low energy output relative to chemical fuel sources such as ATP. DNA mechanotechnology powered

by alternative energy sources, such as externally applied electric field [52], offer solutions to this fundamental limitation.

1.6 Outlook

While the DNA nanodevices presented here are relatively simple, next-generation DNA mechanotechnology will combine multiple types of DNA nanostructures together. For example, we recently developed a DNA origami multi-helix bundle to detect forces associated with human platelet activation, allowing us to access increased force response thresholds and paving the way for future study of mechanics of multivalent, cooperative mechanosensing interactions in vivo [53]. A key limitation of future DNA mechanotechnology lies in the maximal magnitude of force that can be experienced by a DNA duplex. All DNA duplexes, regardless of length, denature when subject to force around 60 pN. Existing DNA structures will be unable to access force regimes surpassing this limit without future innovations that will likely involve incorporation of stabilizing agents, structural integrity-increasing modifications to the DNA (e.g. by incorporating locked nucleic acids, LNA[54]), or introduction of covalent linkages at key locations within nanostructures[55].

Biological machines that generate, sense, and transmit mechanical forces are essential for all living systems. Accordingly, the rational design of synthetic analogs of these biological machines has been a dream of nanotechnologists dating back to Feynman[56] and earlier. DNA mechanotechnology is currently the leading platform for creating synthetic molecular machines and is rapidly producing tools with utility and versatility approaching that of biological machines. We anticipate advances in theoretical modeling and synthesis that

will improve the efficiency, yield, and endurance of these tools. The next generation of DNA mechanotechnology will likely demonstrate new emergent behaviors that mirror those of bacteria and social insects by connecting multiple DNA mechanotechnology components. Future efforts to characterize and engineer the mechanical properties of more complex DNA structures will inevitably lead to more sophisticated and useful nanomachines and mechanosensors. Furthermore, this research area is opening a new paradigm for nanoscale mechanical systems that will extend into other alternative platforms, including self-assembled RNA- and peptide-based nanotechnology.

CHAPTER 2. HIGHLY POLYVALENT DNA MOTORS GENERATE 100+ PICONEWTONS OF FORCE VIA AUTOCHEMOPHORESIS

This chapter is an adaptation of Blanchard *et al.*, *Nano Letters* 2019, 19 (10), 6977–6986 (ref. [1]).

2.1 Summary

Motor proteins such as myosin, kinesin, and dynein are essential to eukaryotic life and power countless processes including muscle contraction, wound closure, cargo transport, and cell division. The design of synthetic nanomachines that can reproduce the functions of these motors is a longstanding goal in the field of nanotechnology. DNA walkers, which are programmed to "walk" along defined tracks via the burnt bridge Brownian ratchet mechanism, are among the most promising synthetic mimics of these motor proteins. While these DNA-based motors can perform useful tasks such as cargo transport, they have not been shown to be capable of cooperating to generate large collective forces for tasks akin to muscle contraction. In this work, we demonstrate that highly polyvalent DNA motors (HPDMs), which can be viewed as cooperative teams of thousands of DNA walkers attached to a microsphere, can generate and sustain substantial forces in the 100+ pN regime. Specifically, we show that HPDMs can generate forces that can unzip and shear DNA duplexes (~12 and ~50 pN, respectively) and rupture biotin-streptavidin bonds (~100-150 pN). To help explain these results we present a variant of the burnt-bridge

Brownian ratchet mechanism that we term autochemophoresis, wherein many individual force generating units generate a self-propagating chemomechanical gradient that produces large collective forces. In addition, we demonstrate the potential of this work to impact future engineering applications by harnessing HPDM autochemophoresis to deposit "molecular ink" via mechanical bond rupture. This work expands the capabilities of synthetic DNA motors to mimic the force-generating functions of biological motors. Our work also builds upon previous observations of autochemophoresis in bacterial transport processes, indicating that autochemophoresis may be a fundamental mechanism of pN-scale force generation in living systems.

2.2 Introduction to highly polyvalent DNA motors

Walker-type DNA motors[29,51,57-75], which use two or more DNA "feet" to translocate across nanoscale tracks, are among the most promising synthetic analogs of biological motor proteins such as myosin, kinesin, and dynein[76]. These DNA motors can be used to transport[64,68,69] and assemble[62,63] nanoscale cargo, but have not been shown to be generate sustained piconewton (pN)-scale forces. Force generation is a fundamental property of biological motors, and processes such as muscle contraction, wound closure, mechanosensation, and cell motility all require collective action of many motors, each exerting 1-10 pN via ATP-fueled powerstrokes. The development of DNA-based motors that can generate pN-scale forces may enable next-generation motors and actuators that can power similar tasks.

DNA walker translocation can be described using the burnt bridge Brownian ratchet (BBBR) mechanism. This mechanism involves binding between DNA feet and their

corresponding footholds, which is followed by irreversible destruction of the footholds, release of the feet, and translocation of the motor to bind fresh foothold sites[57-59]. The BBBR mechanism is generally known to exhibit low chemomechanical coupling and thus produce less force per motor (~10-100 fN as estimated via experimentally-informed simulations and modeling[77-80]) than the pN-scale forces generated via the ATP-fueled powerstroke mechanism of motor proteins. Nonetheless there is, to our knowledge, no fundamental limitation on the ability of BBBR motors to cooperate and generate larger collective forces. Indeed, simulations by Samii et. al. predict that increasing the polyvalency (i.e. the number of DNA feet) from two to four increases the collective force generated in a linear fashion[77]. However, it is still an open question as to whether (and, if so, to what extent) cooperative force generation by multiple DNA-based motors can be implemented in practice. Herein, we demonstrate progress towards addressing this question by showing that highly polyvalent DNA motors (HPDMs), which have thousands of DNA feet, can generate and sustain 100+ pN forces. This work suggests that BBBR motors can be scaled to generate cooperative pN-scale forces.

HPDMs are a class of DNA motors that autonomously move across planar RNA-functionalized substrates[29]. Translocating at velocities up to 5 μm/min across distances approaching the millimeter length scale, HPDMs are the fastest and most processive DNA-based motors reported thus far. The HPDM is composed of a 5 μm silica bead coated with a dense monolayer of DNA oligonucleotide feet at a surface density of ~91,000 molecules/μm^2 (**Figure 2**a – see **Figure 3**a for surface functionalization scheme). The DNA feet are complementary to the RNA "fuel", which is anchored to the substrate at a density of ~50,000 molecules/μm^2 (**Figure 2**b – see **Figure 3**b for surface functionalized

scheme). When the HPDM particles are introduced to the substrate, they sediment and bind via 15 base pair (bp) hybridization interactions between their DNA feet and the substrate's RNA fuel (which together form "tethers", **Figure 2**c). The HPDMs remain stationary until the addition of ribonuclease H (RNase H), which is an enzyme that selectively hydrolyzes the phosphodiester backbone of RNA in DNA-RNA hybrid duplexes (**Figure 2**c). RNase H is highly specific and does not covalently modify DNA or single stranded RNA. At standard conditions the RNA strands in DNA-RNA tethers are cleaved at a maximal rate of $k_{cat} = 25\ min^{-1}$ (ref. [29]). Because there are hundreds of tethers at any given time, complete detachment from the substrate is prevented by the HPDM's high polyvalency. This combination of rapid fuel consumption and continuous substrate attachment allows HPDMs to rapidly translocate for hours or longer, consuming ~10^4 RNA fuel strands per minute (calculation in **Supplemental Note 1 – Calculation of RNA fuel exchange rate**). Due to the large size of an individual microparticle (5 μm), HPDM motion can be monitored using brightfield microscopy (BF, **Figure 2**d). Because RNA cleavage is irreversible, fluorescence imaging of the Cyanine-3 (Cy3)-tagged RNA fuel (**Figure 2**d) reveals a ~400 nm-wide region of ~50% reduced intensity in the HPDM's wake that we call a depletion track. HPDMs generally exhibit superdiffusive motion due to depletion track-avoidance, but sometimes become "self-entrapped" within their own depletion tracks and, as a result, substantially slow or stall for minutes or longer[29]. Notably, HPDMs roll as they translocate, as is most clearly illustrated by the ballistic (linear) motion of dimerized or rod-shaped HPDMs[29].

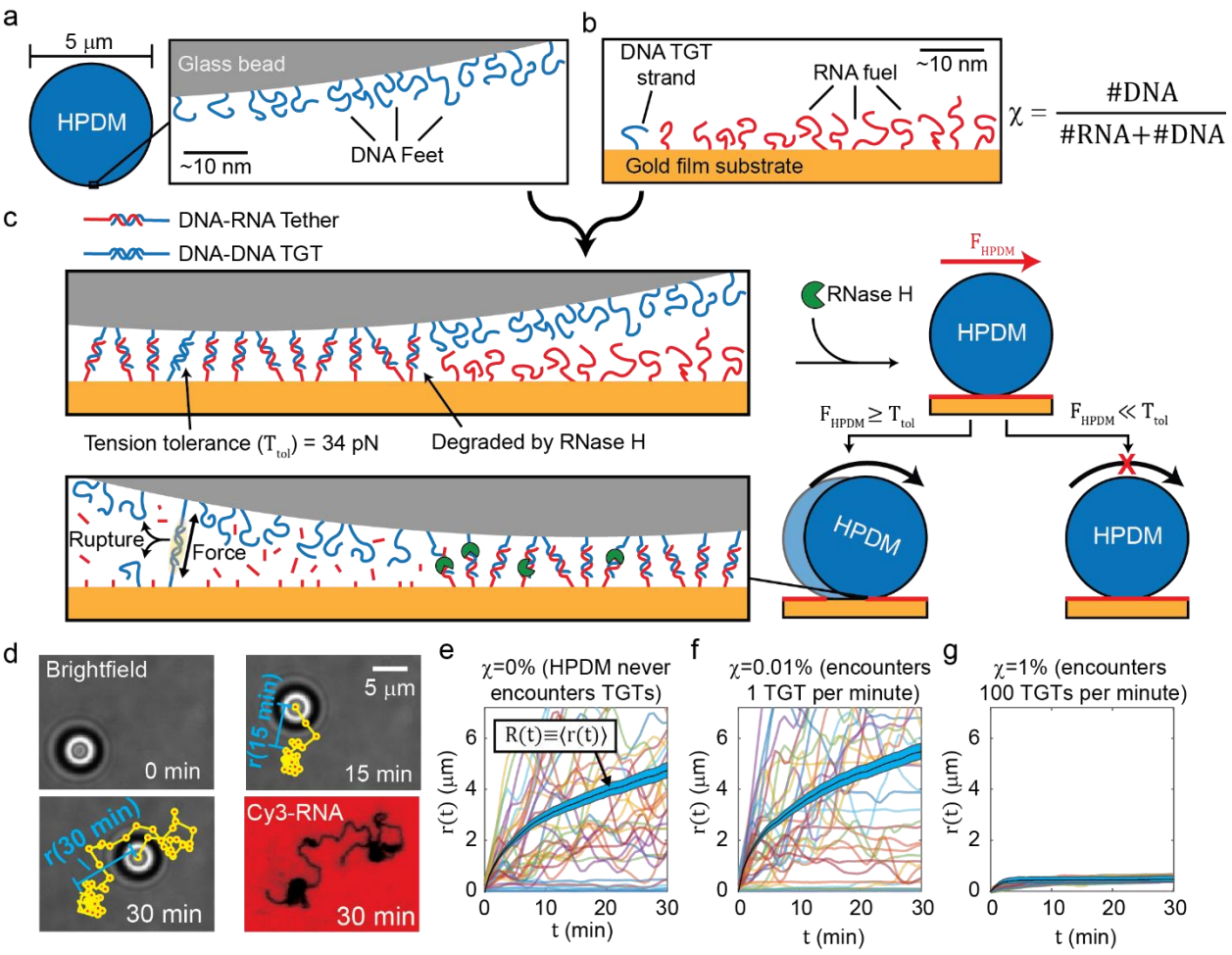

Figure 2: Highly polyvalent DNA motors with DNA TGT strands

HPDMs mechanically rupture tension gauge tethers (TGTs). **a)** HPDMs are silica (gray) microspheres coated with DNA (blue) "feet". **b)** These feet bind with RNA (red) "fuel" strands that are attached to an underlying gold substrate (yellow) to form **c)** "tethers" that are cleaved by the enzyme RNase H (green). We doped a small fraction (denoted by χ) of DNA strands into the RNA monolayer that also bind to DNA feet to form DNA-DNA duplexes that we refer to as TGTs. These TGTs are impervious to RNase H, so when an HPDM encounters a TGT it must generate force (denoted F_{HPDM}) surpassing the TGT's tension tolerance (T_{tol}) in order to rupture the TGT and continue moving. **d)** Brightfield

microscopy (BF) snapshots of an HPDM rolling on a TGT-free substrate and a final fluorescence image of the Cy3-tagged RNA. Yellow denotes the HPDM's measured trajectory. **e-g)** Displacement vs. time curves of 30 representative HPDMs with **e)** $\chi = 0\%$, **f)** $\chi = 0.01\%$ (which should stall HPDM motion if $F_{HPDM} \ll T_{tol}$), and **g)** $\chi = 1\%$. Black curves show the average of 700+ HPDMs per condition, denoted $R(t)$, and blue shading denotes 95% confidence interval of our estimate of $R(t)$. The $\chi = 0\%$ condition is a negative control showing that we could demonstrate RNase H-mediated HPDM translocation in our experiment and the $\chi = 1\%$ condition is a positive control showing that TGTs can stall HPDM motion at high χ values. The $\chi = 0.01\%$ condition demonstrates largely unperturbed HPDM translocation, which is consistent with the hypothesis that $F_{HPDM} \geq T_{tol}$.

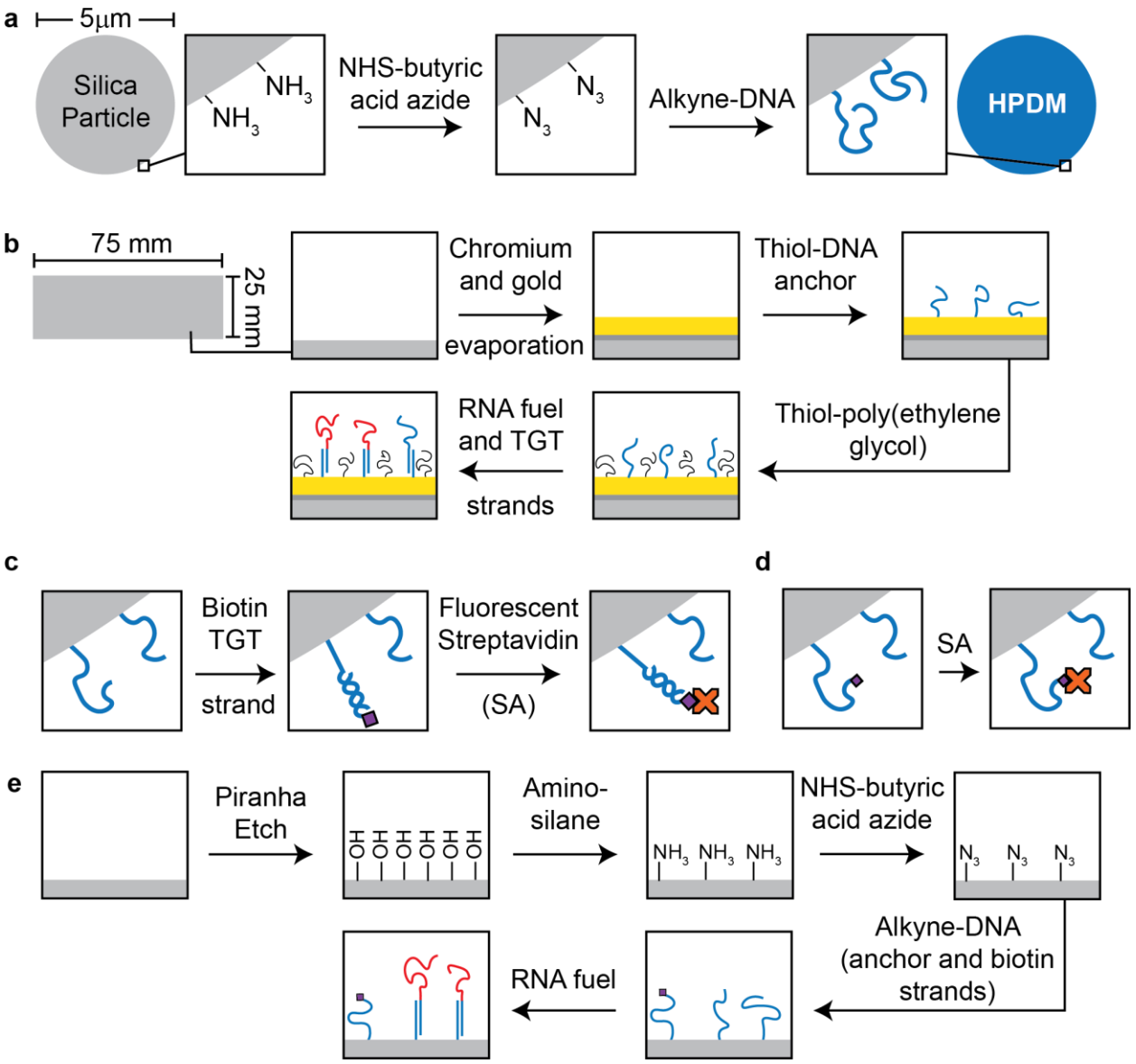

Figure 3: Illustrations of surface functionalization processes.

Glass is light gray, DNA is blue, chromium is dark gray, gold is yellow, black denotes a general linker or poly(ethylene glycol), RNA is red, purple square is biotin, and orange is streptavidin. Please see the methods section for more details about specific reaction conditions. **a)** Process for conjugating DNA to HPDMs as described in methods section "*HPDM preparation for ensemble experiment*". **b)** Process for conjugating RNA fuel and TGTs to the substrate as described in methods section "*Substrate preparation for ensemble*

*experiment***:**". **c)** Process for pre-assembling streptavidin-capped TGTs on HPDMs as described in methods section "*HPDM preparation for single molecule imaging of TGT rupture***:**". **d)** Process for pre-assembling biotin-streptavidin bonds on HPDMs as described in methods section "*HPDM preparation for single molecule imaging of biotin-streptavidin bond rupture***:**". **e)** Process for conjugating RNA fuel and biotin strands to surface as described in methods section "*Substrate preparation for single molecule imaging experiments*".

As with conventional DNA walkers, HPDM translocation can be described using a BBBR mechanism. According to this framework, the particle initially adopts a position that maximizes the number of tethers formed. When the bound RNA is degraded by RNase H, the HPDM displays increased Brownian motion that leads to forward translocation and enables subsequent binding to new RNA fuel strands. Repetition of this cycle with thousands of tethers per minute results in forward translocation of the HPDM at μm/min-scale speeds.

Because the RNA-coated substrates lack inherent directionality (i.e., the HPDM is surrounded by fuel on all sides, save for directly behind it) we initially assumed that tethers would not act in a cooperative manner and thus assumed that HPDMs could not produce persistent forces beyond the fN range. However, we made multiple observations that were not consistent with this assumption. For example, we found that HPDMs move in a ballistic manner at sub-minute timescales (i.e., HPDMs travel persistently for seconds or longer, **Figure 4**). Because the momentum of microscale objects undergoing Brownian diffusion generally dissipates within microseconds[81], this observation instead suggested that tethers act in a more cooperative manner than originally thought. Ballistic HPDM motion also resembles the persistent motion of microparticles observed by Vecchiarelli et. al.[82] in studies of the bacterial partition system, wherein a BBBR mechanism generates a persistent *chemophoretic* force that can ballistically transport cargo such as plasmids across micron-scale distances. We were also unable to stall HPDM motion by doping non-cleavable DNA into the RNA fuel monolayer. This second observation suggested that HPDMs were generating the 10s of pN of force required to rupture DNA duplexes[83]. Together, these

results led us to hypothesize that HPDM motion is coupled to a chemophoretic driving force (F_{HPDM}) that is substantially greater than the fN-scale forces originally expected for uncoordinated DNA walkers.

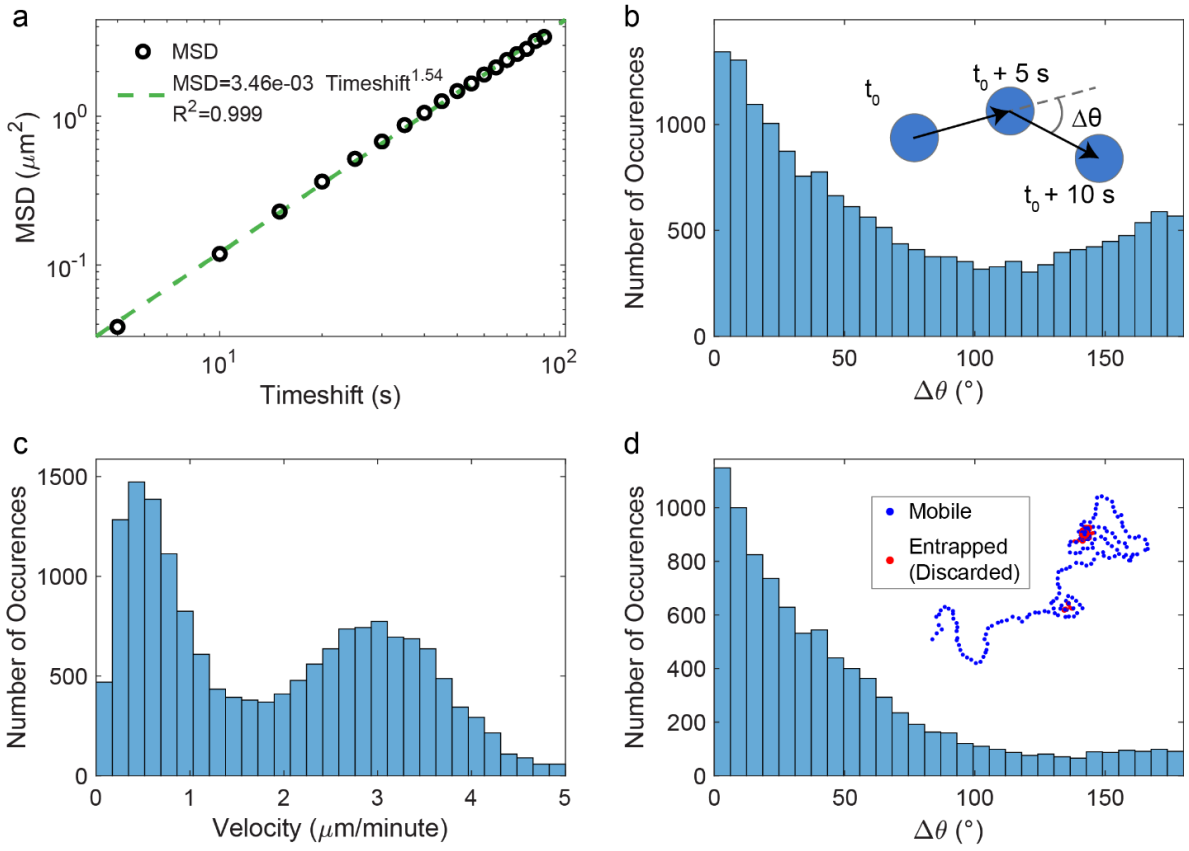

Figure 4: HPDMs exhibit persistent motion.

We performed particle tracking on a previously published HPDM translocation video[29] using a custom-written MATLAB code. **a)** MATLAB-based particle tracking of data published in ref. [29] yields a mean-squared displacement (MSD) power law fit exponent of ~1.5. A similar value was obtained in ref. [29]. This result validates the HPDM tracking algorithm that we used. **b)** for each successive pair of frames (acquisition interval of 5 seconds) we measured the movement direction θ. We then measured Δθ (as shown in inset) for each successive pair of steps and repeated this measurement for each HPDM such that with 181 images and 31 particles we obtained 179*31=5,549 independent Δθ measurements. A histogram of these Δθ measurements shows an enhancement around $\Delta\theta = 0°$ and another at $\Delta\theta = 180°$. If particle motion was non-persistent, then this

histogram would be flat (or perhaps be primarily flat with a decrease around $\Delta\theta = 180°$ to reflect depletion track avoidance) because successive steps would not be directionally correlated. **c)** The histogram of 180*31=5,580 velocity measurements shows two peaks: one high-velocity peak representing mobile HPDMs and one low-velocity peak representing entrapped HPDMs. We hypothesized that entrapped HPDMs could account for the enhanced population of high $\Delta\theta$ measurements because localization error will cause successive localizations of an immobile HPDM to bounce around the true location. *d)* Applying a filtering algorithm to exclude $\Delta\theta$ measurements corresponding to the stalled population (see inset), we found that the new $\Delta\theta$ histogram shows a substantial enhancement around $\Delta\theta = 0°$ and an exponentially decaying behavior, strongly supporting the conclusion that HPDM motion is persistent at short (sub-minute) timescales and self-avoiding at longer timescales.

2.3 Particle tracking reveals that HPDMs generate forces exceeding 35 pN

To test our hypothesis that HPDMs generate pN-scale forces, we started by rigorously testing HPDMs' ability to mechanically rupture short DNA duplexes, which have well-characterized force-induced dehybridization properties, using an ensemble-level particle tracking experiment. We then compared the results of this experiment to mass-action simulation models, allowing us to estimate that HPDMs generate ~150 pN of force. To validate these findings, we next implemented single molecule localization measurements to directly visualize DNA duplexes that have been mechanically ruptured by HPDMs. We then employed single molecule imaging to show that HPDMs can also mechanically rupture the biotin-streptavidin bond, which is often described as the strongest noncovalent bond found in nature. We next demonstrated that HPDMs can easily rupture DNA duplexes arranged in the unzipping geometry, revealing that HPDMs can act as autonomous lithographic probes to mechanically pattern dense arrays of DNA duplexes (or "molecular ink") within the wake of their depletion tracks. Finally, we extend upon existing conceptual frameworks to help describe the mechanism of HPDM force generation, which we term autochemophoresis.

We first replaced a fraction of the RNA fuel with a DNA analog with the same sequence. We quantitatively denote this fraction as χ (**Figure 2**b). We anticipated that the DNA on the planar substrate would hybridize to the DNA feet on the surface of the HPDM, thus creating a non-hydrolysable duplex that is akin to the tension gauge tether (TGT)[43]. TGTs are stable DNA duplexes that are engineered to mechanically rupture at specific magnitudes of tension, described as the tension tolerance (T_{tol}, roughly 34 pN for a 15 bp duplex). Because TGTs irreversibly denature at specific values of T_{tol}, one application of

TGTs is to quantify the minimum pN-scale forces[42,46,83-94] exerted by individual cell surface receptors. In our experiments, substrate-bound TGT strands were designed to display identical sequences to (and thus behave similarly to) RNA fuel strands but are immune to RNase H-mediated degradation because they form DNA-DNA duplexes (sequences listed in **Table 1**). As such, feet will occasionally pair with TGT strands to form RNase H-impervious tethers, resulting in either 1) HPDM stalling if $F_{HPDM} \ll T_{tol}$, or 2) TGT rupture and continued HPDM motion if $F_{HPDM} \geq T_{tol}$ (**Figure 2**c). Note that the zero-force lifetime of a 15 bp duplex at room temperature is ~10^7 s (the zero-force activation energy barrier is ~35 k_BT, as calculated using the mathematical framework presented in ref. [83]). Thus, force-induced bond rupture is a requirement for continued HPDM motion after the engagement of a TGT.

We tested for force-induced rupture of TGTs at the ensemble level using a high-throughput particle tracking experiment and a custom MATLAB-based particle tracking code (**Figure 5**, **Figure 6**, **Figure 7**). As a negative control, we simultaneously tracked 721 HPDMs rolling in the absence of TGT strands ($\chi = 0\%$) for 30 min. For each HPDM, we calculated $r(t)$, which is the displacement from the initial position as a function of time (**Figure 2**d), and then we averaged all $r(t)$ curves to obtain $R(t)$, the ensemble average displacement as a function of time (**Figure 2**e, **Figure 8**). We next replaced a small fraction of RNA strands with TGT strands. Based on our estimate that $k_1 = 10^4\ s^{-1}$ (where k_1 is the steady-state rate of tether formation, see **Supplemental Note 1 – Calculation of RNA fuel exchange rate** for calculation), we predict that when $\chi = 0.01\%$ (that is, 1 in every 10,000 RNA strands is replaced with a DNA TGT strand) HPDMs will encounter TGTs at a rate of $1\ min^{-1}$. In this scenario, if $F_{HPDM} \ll 34$ pN, HPDMs will become immobilized upon

encountering TGT strands, so all HPDMs will be immobilized within a few minutes. In contrast, if $F_{HPDM} \geq 34$ pN HPDMs should continue rolling processively when $\chi = 0.01\%$. We tested this by tracking 982 HPDMs on a substrate with $\chi = 0.01\%$ and found that $R(t)$ was unperturbed when compared to the $\chi = 0\%$ control (**Figure 2**f, **Figure 8**)., which supports the hypothesis that HPDMs can rupture TGTs. A statistical comparison of the $r(30\ \mathrm{min})$ populations (**Figure 8**) showed no difference in the median values between the $\chi = 0\%$ and $\chi = 0.01\%$ conditions (4.0 μm and 4.2 μm, respectively, p = 0.09, Wilcoxon rank sum test). As such, these results suggest that $F_{HPDM} \geq 34$ pN. As a positive control, we found that when $\chi = 1\%$ (HPDMs encounter 100 TGT strands per second), virtually no HPDM motion was observed (**Figure 2**g, p<0.001 when compared to the $r(30\ \mathrm{min})$ populations with $\chi = 0.01\%$ or $\chi = 0\%$, Wilcoxon rank sum test).

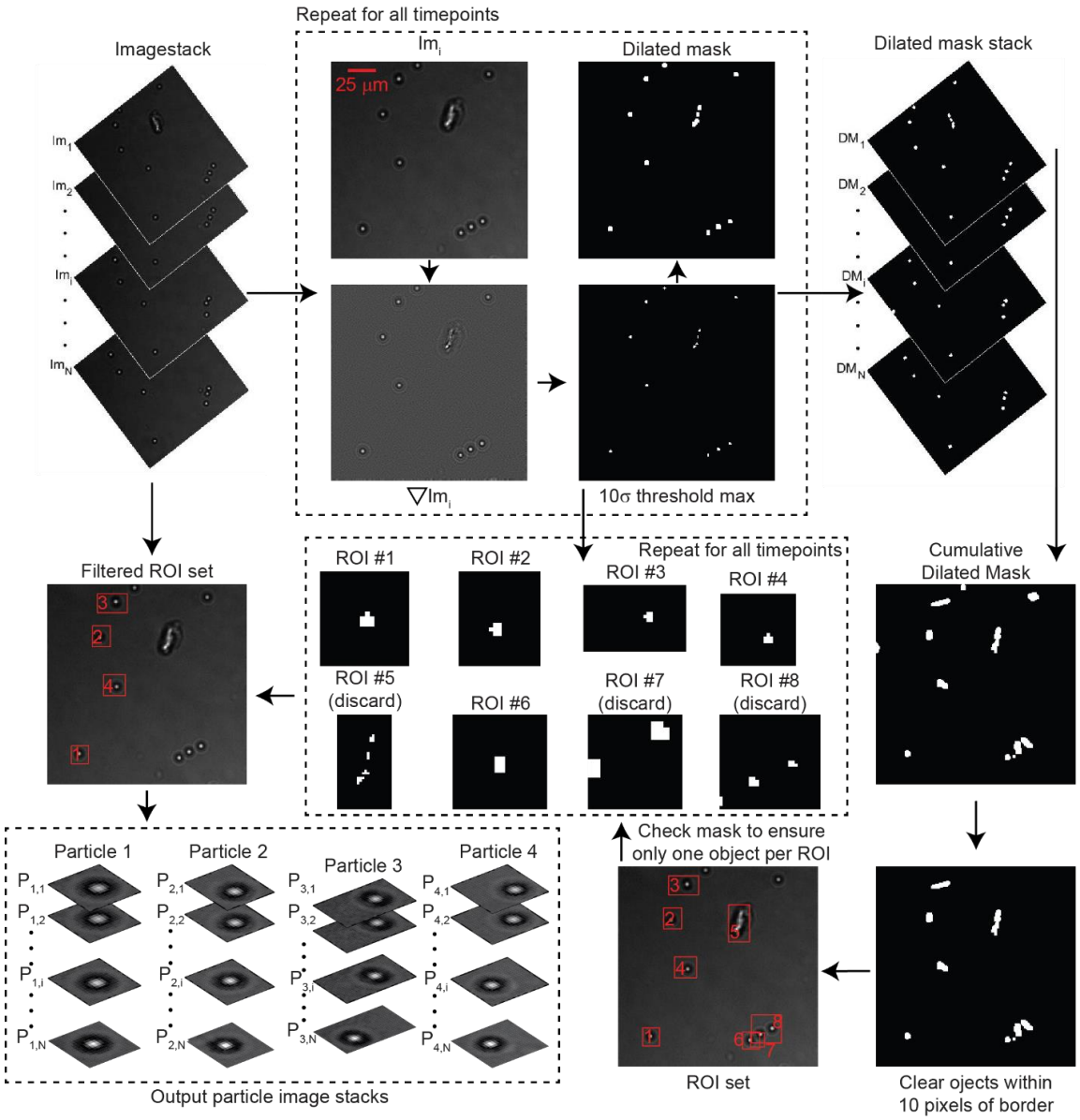

Figure 5: Automated HPDM detection algorithm used for ensemble experiments.

The top half of the figure depicts the process used to detect objects in an imagestack. A dilated mask (DM) is generated for each image (Im) in the imagestack by 1) taking the Laplacian of Im using MATLAB's del2() function, 2) generating a 10σ mask by applying a cutoff calculated as 10x the standard deviation of the entire Laplacian image, and 3) dilating the mask using a 3x3 pixel square. The masks from each timepoint were then

combined to create a cumulative dilated mask. The bottom half of the figure depicts the process used to determine which objects are single isolated HPDMs. Objects within 10 pixels of a b and border-touching objects in the cumulative dilated mask were removed, and a rectangular ROI was drawn around each object. Each ROI was then cross-checked at each timepoint using the 10σ mask. Any ROI without exactly one object in the 10σ mask at each timepoint was discarded. The raw image-stacks were extracted and stored for each remaining ROI.

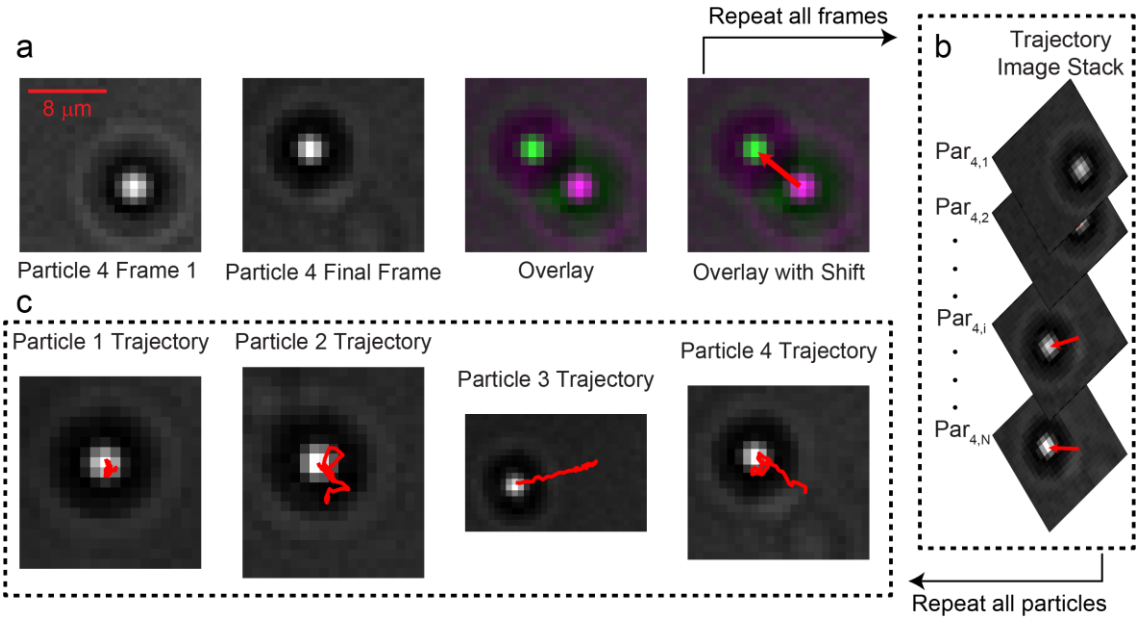

Figure 6: Automated HPDM tracking algorithm used for ensemble experiments.

a) Each ROI's imagestack (see **Figure 5** for extraction process) was processed to generate an HPDM trajectory by comparing each timepoint to the first timepoint using a cross-correlation image registration algorithm[95]. **b)** The relative shifts for each timepoint were then strung together to create a trajectory for the HPDM. **c)** Four trajectories are shown overlain on each ROI's image from the final timepoint.

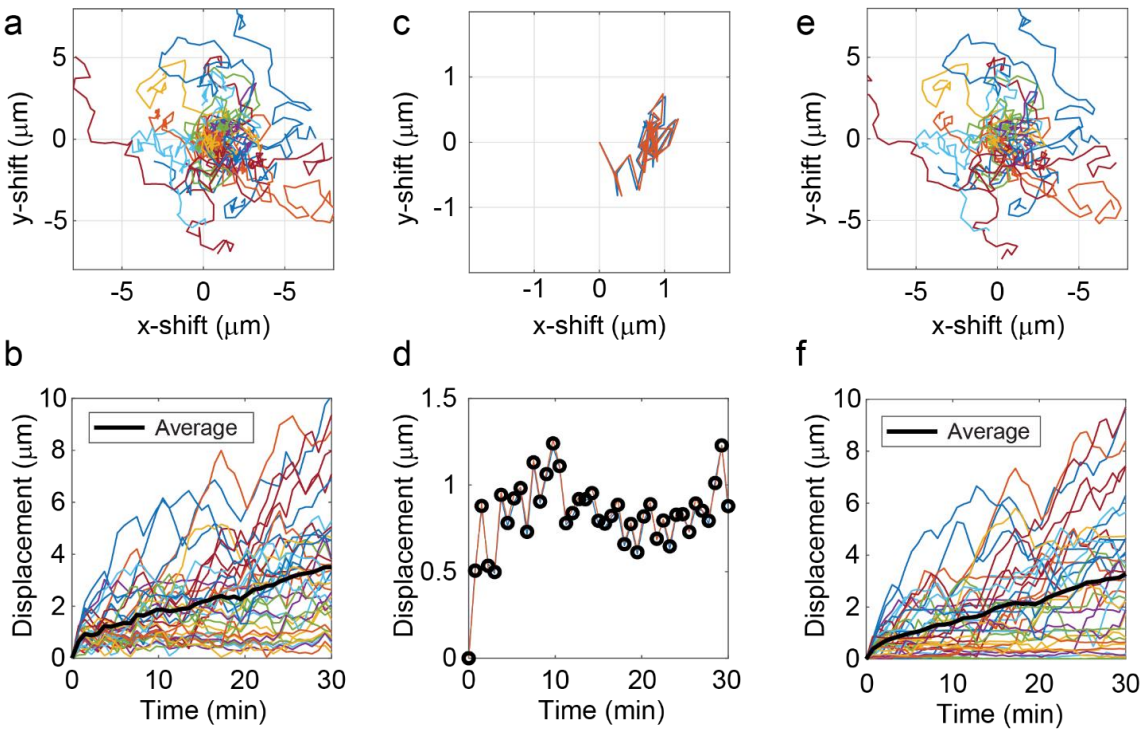

Figure 7: Automated drift correction process.

Imaging was performed on several locations simultaneously by using an automatic scanning microscope stage to cycle between locations. Each location has unique x- and y-drift profiles that cannot reliably be determined using conventional drift correction techniques. As such, we developed a drift correction method that utilizes specific aspects of HPDM motion. Namely, almost all locations have multiple HPDMs that do not move due to nonspecific adhesion to the underlying substrate. We use these immobile HPDMs to calculate the x- and y-drift profiles. To determine which particles are stuck, we first **a,b)** calculate the set of all trajectories from a location and **c,d)** find trajectories that are highly similar to one another. To do this, we calculate the differences between all pairs of trajectories and screen for trajectories that have a maximum difference of less than 0.1 μm. If no pair (or set) of trajectories satisfies this condition, then the threshold is increased in

0.1 μm increments until a pair or set satisfies this condition. This pair or set of trajectories is then averaged (black circles in **d)** and subtracted from all of the other trajectories in the location. **e)** Drift-corrected trajectories appear qualitatively smoother and more clearly exhibit the self-avoiding behavior that is characteristic of HPDM motion. **f)** Furthermore, drift-corrected displacement vs. time curves appear smoother, as is best illustrated by the "flat-lining" of displacement vs. time curves after HPDM stalling.

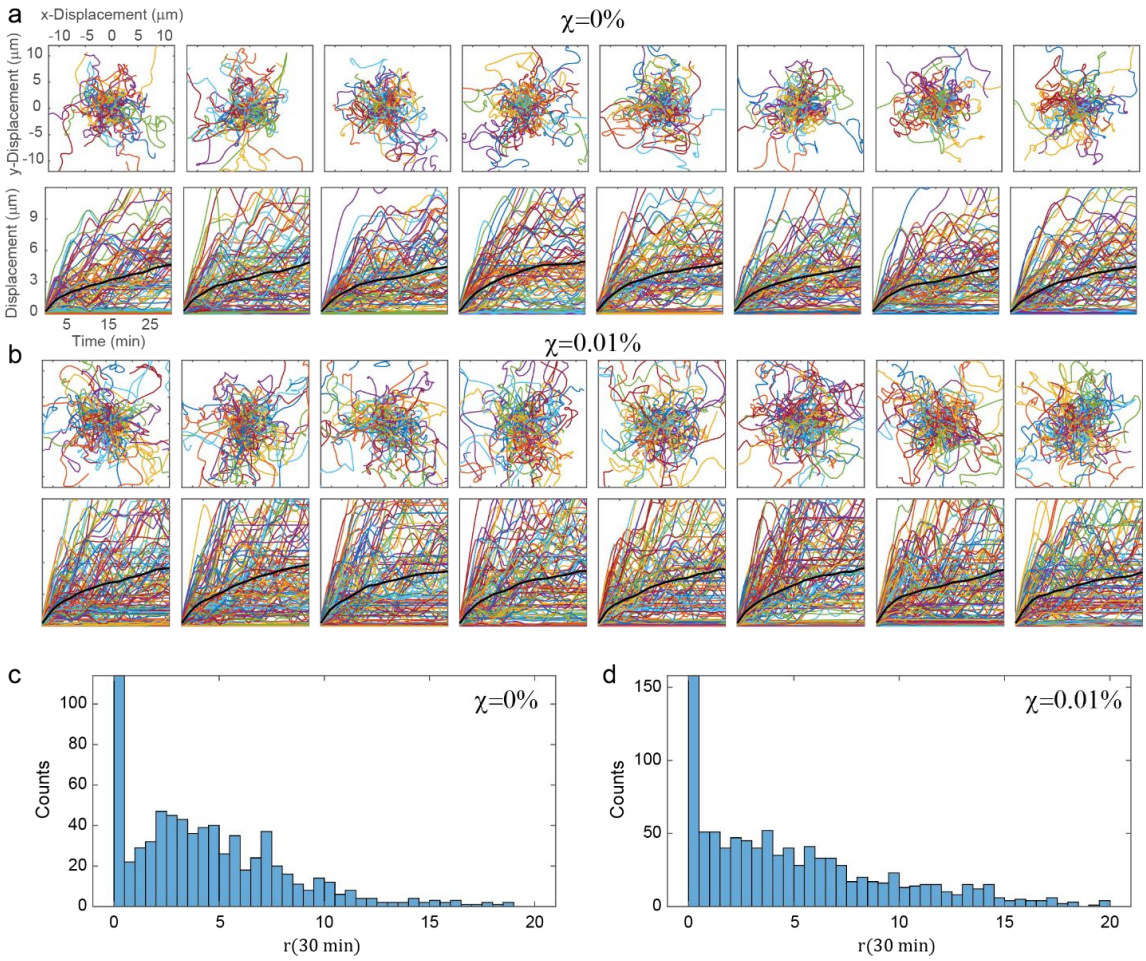

Figure 8: High throughput HPDM tracking results, part 1.

a,b) Trajectories (top) and displacement vs. time curves (bottom) for HPDMs rolling on substrates with **a)** $\chi = 0\%$ and **b)** $\chi = 0.01\%$. Sample sizes are 721 and 942 HPDMs, respectively. For each condition, trajectories and HPDMs are randomly divided into 8 sets, corresponding to the 8 pairs of plots. All plots have the same axes limits, as shown in the leftmost pair of plots in **a**. The average displacement vs. time curve for each set is shown as a thick black curve. All x- and y-trajectories are smoothed using a [.05, .25, .4, .25, .05] smoothing filter for clarity. These sub-figures are intended to provide a visual representation of the throughput of the experiment, as well as the similarity between the

$\chi = 0\%$ and the $\chi = 0.01\%$ conditions. **c,d)** Histograms of final displacement ($r(30\ \mathrm{min})$) populations for **c)** $\chi = 0\%$ and **b)** $\chi = 0.01\%$.

2.4 Quantitative estimate of F_{HPDM}

We next sought to quantitatively estimate F_{HPDM}. To accomplish this task, we first developed a series of mass-action models to predict how $R(t)$ should change as a function of F_{HPDM} and χ (**Figure 9**a, **Figure 10**). These models assume that the number of TGTs required to stall an HPDM should be positively correlated with F_{HPDM}. In the "1-TGT" model, a single TGT is sufficient to irreversibly stall HPDM motion (e.g. $F_{HPDM} \ll T_{tol}$). The 2-TGT model assumes that an HPDM can generate enough force to break a single TGT but cannot generate enough force to mechanically denature two TGTs simultaneously (roughly, $F_{HPDM} > T_{tol} > \frac{1}{2}F_{HPDM}$). This model produces an $R(t)$ curve that much more closely resembles the experimentally observed result (**Figure 9**b). Further still, the 3-TGT model, in which HPDMs are mobile when bound to 0, 1, or 2 TGTs but stall when bound to 3 TGTs, nearly predicts the observed unperturbed behavior because simultaneous encounter of 3 TGTs is rare when $\chi = 0.01\%$ (**Figure 9**b). These results suggest that HPDMs consistently rupture TGTs and may even be strong enough to rupture three or more TGTs simultaneously, indicating that $F_{HPDM} \geq 102$ pN.

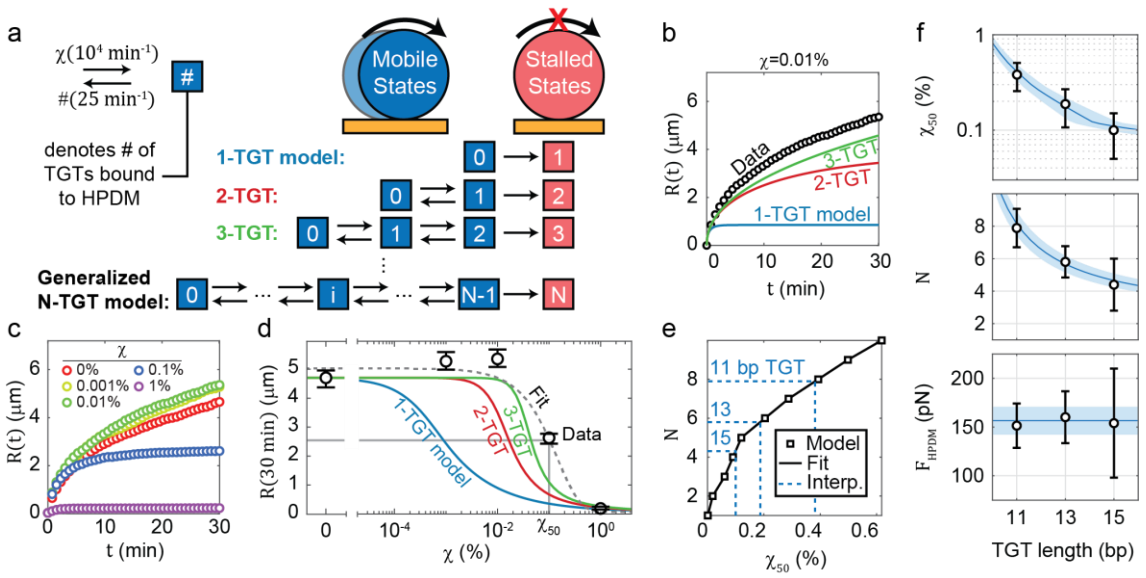

Figure 9: Quantitative estimate of F_{HPDM}

a) Block diagrams for 1-TGT, 2-TGT, and 3-TGT simulation stall models, as well as a generalized N-TGT model. In these models, all HPDMs are bound to zero TGTs at $t = 0$ and encounter TGTs at a rate of $\chi * 10^4$ min^{-1}. HPDMs bound to fewer than N TGTs are mobile and mechanically rupture TGTs at a rate of $\# * 25\ \mathrm{min}^{-1}$, where # denotes the number of TGTs bound to the HPDM. HPDMs immediately and irreversibly stall when bound to N TGTs. **b)** R(t) curve measured experimentally with $\chi = 0.01\%$ (circles, **Figure 2d**) and simulated using the 1-, 2-, and 3-TGT stall models (solid curves) shown in **a**. **c)** R(t) curves measured experimentally with χ ranging from 0% to 1%. **d)** R(30 min) with respect to χ. Exponential decay fit curve (dashed line) and best-fit χ_{50} are shown, as well as simulated curves for 1-, 2-, and 3-TGT stall models (solid curves). Circles show measured datapoints, and error bars are 95% confidence interval of our estimate of R(30 min), as calculated via 3,000 iterations of a bootstrapping algorithm. **e)** N vs. χ_{50} simulated for N-TGT models with N ranging from 1 to 10. Squares denote simulation

outputs, while solid black curve shows a linear interpolation fit. Dashed blue lines show interpolations of χ_{50} values experimentally measured with 11, 13, and 15 bp TGTs. **f)** Best-fit values for χ_{50} (top), N (middle) and $F_{HPDM} \approx T_{tol} * N$ (bottom) as a function of TGT length. Error bars are 95% confidence interval of fit. Blue curves in all three subplots in **f** denote global fit value of $F_{HPDM} = 157$ pN and light blue shading denotes global fit 95% confidence bounds of ± 14 pN.

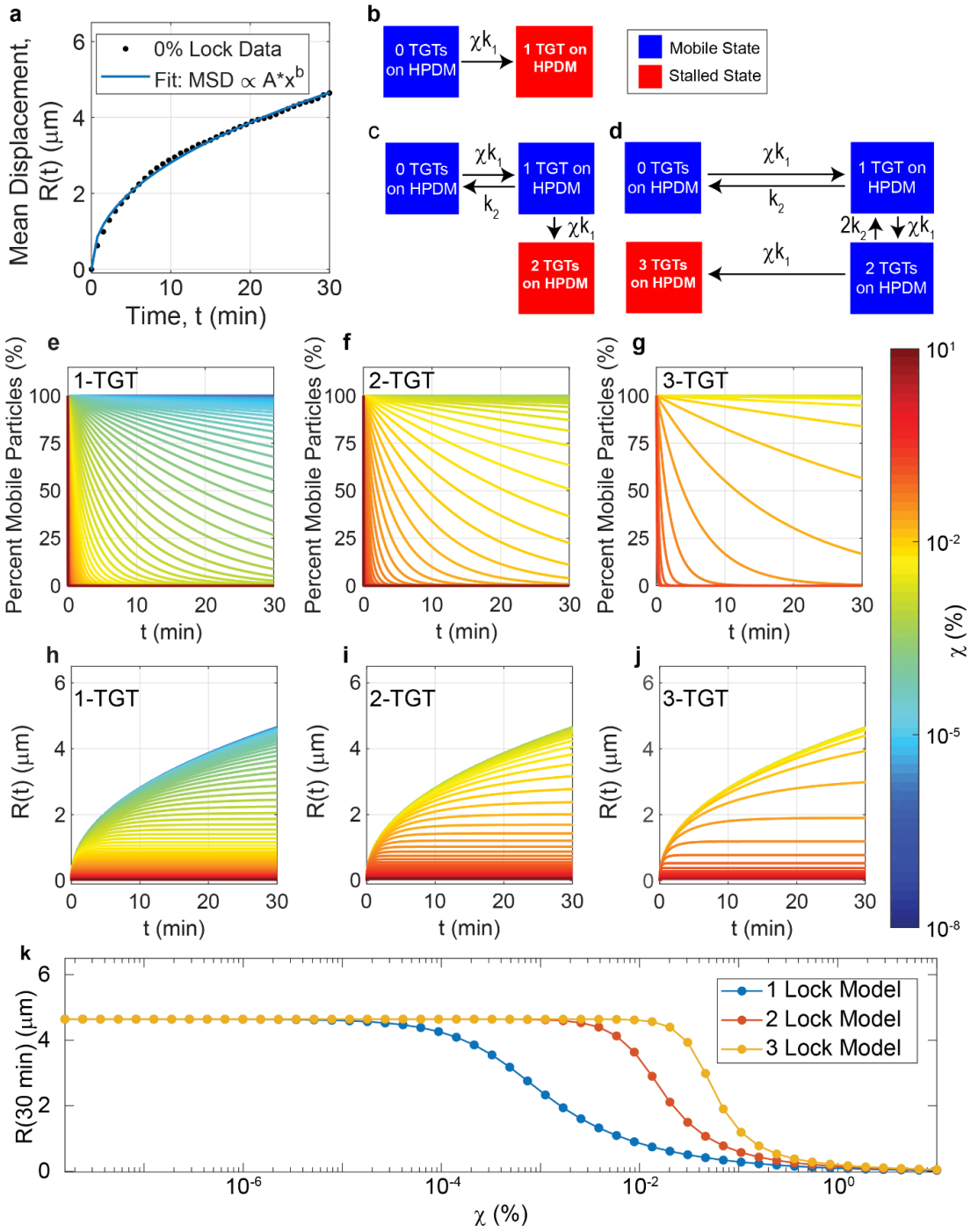

Figure 10: 1-TGT, 2-TGT, and 3-TGT models used to simulate R(t) curves.

a) R(t) measured experimentally with $\chi = 0\%$ (black circles) and power-law curve fit. This curve-fit was used to simulate R(t) curves. **b-d)** flow diagrams showing mass-action

models for the **b)** 1-TGT, **c)** 2-TGT, and **d)** 3-TGT models. Each state corresponds to an integer number of TGTs, and the final state is an irreversibly stalled state while all other states are mobile states. **e-g)** Simulated curves with varying χ showing the percentage of HPDMs in a mobile state as a function of time (for 0-30 min) for the **e)** 1-TGT, **f)** 2-TGT, and **g)** 3-TGT models. The color of each curve denotes the χ value as shown on the colorbar. **h-j)** Simulated R(t) curves for 0-30 min with varying χ for the **h)** 1-TGT, **i)** 2-TGT, and **j)** 3-TGT models. **k)** R(30 min) shown as a function of χ for the 1-TGT model (blue), 2-TGT model (orange-red), and 3-TGT model (yellow).

Note that, although we performed statistical comparison of population medians (which are more appropriate to report than population means for skewed distributions such as ours), we chose to display and analyze population means because the N-TGT models can only predict expected changes in mean displacement vs. time curves. A similar modeling approach that predicts the expected population median as a function of time would not be accurate because, in short, the median is not a linear operator and our models rely on the use of linear mathematical operations.

We next performed particle tracking of HPDMs on surfaces with χ ranging from 0.001% to 1% (**Figure 9**c, **Figure 11**). While no significant differences in the median $r(30\ \mathrm{min})$ values were observed between the $\chi = 0.001\%$ population (median of 4.1 μm) and the $\chi = 0\%$ or $\chi = 0.01\%$ populations (p=0.19 and p=0.65, respectively, Wilcoxon rank sum test), the $\chi = 0.1\%$ and $\chi = 1\%$ populations had median $r(30\ \mathrm{min})$ values (1.6 μm and 0.03 μm, respectively) that were significantly different from all other tested conditions (p<0.001, Wilcoxon rank sum test). We then performed parameter fitting on the combined datasets to estimate χ_{50}, which is the χ that leads to a 50% reduction of $R(30\ \mathrm{min})$ (**Figure 9**d, **Figure 8**, **Figure 11**). The best-fit χ_{50} of $0.10\% \pm 0.05\%$ (bounds denote 95% confidence interval) is ~100-fold greater than the 1-TGT model's prediction of χ_{50} = 0.0011%, whereas the 2-TGT model more accurately predicts $\chi_{50} = 0.018\%$ and the 3-TGT model predicts an even more accurate $\chi_{50} = 0.061\%$. We then used the output of our N-TGT simulations and linear interpolation (**Figure 9**e, **Figure 12**) to back-calculate N as a function of χ_{50} and estimated that $N = 4.4 \pm 1.6$ TGTs are required to stall a single HPDM, allowing us to obtain a crude approximation of $F_{HPDM} \approx N * T_{tol} = 154 \pm 56\mathrm{pN}$ (**Figure 9**f). In "**Supplemental Note 2 – Justification of the approximation $F_{HPDM} =$**

T_{tol}N", we show that this approximation is reasonable because T_{tol} should accurately reflect the average force at which HPDMs rupture duplexes. For our N-TGT simulations, we assume that TGTs form at a rate of $\chi * k_1 = \chi * 10^4\ min^{-1}$ and rupture at a rate of $k_2 = 25\ min^{-1}$. In "**Supplemental Note 3 – multiple TGTs must form within a short time span to contribute cooperatively towards HPDM stalling**" we show that, although HPDMs likely take 20+ seconds to extend and rupture TGTs (which is much longer than $k_2^{-1} = 2.4$ s), the use of k_2 is still reasonable because TGTs must form within a few seconds of each other in order for their resistive forces to contribute collectively to HPDM stalling.

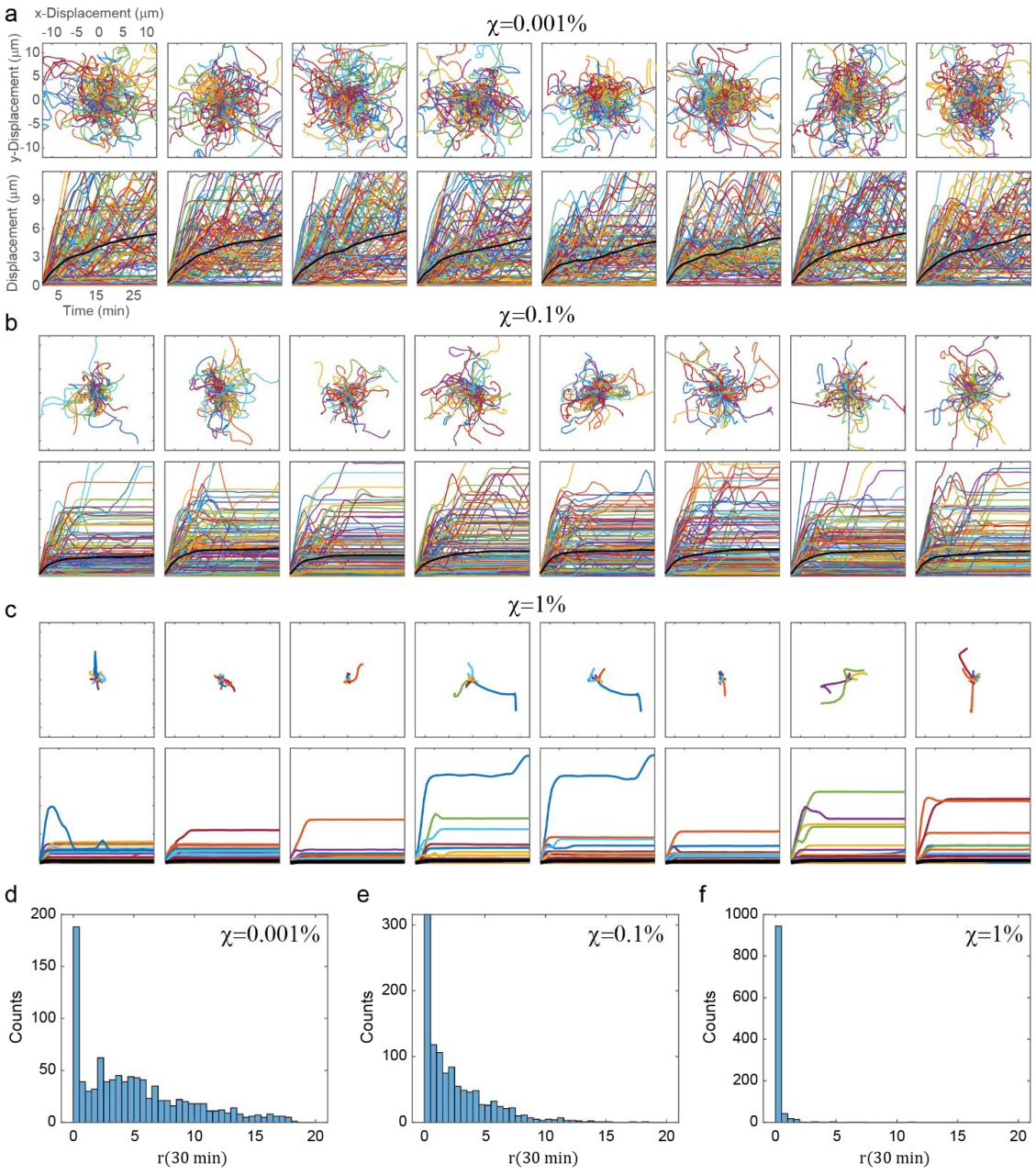

Figure 11: High throughput HPDM tracking results, part 2.

Similar to **Figure 8**, but with **a,d)** $\chi = 0.001\%$, **b,e)** $\chi = 0.1\%$, and **c,f)** $\chi = 1\%$. Sample sizes were 981, 1118, and 1035 individual HPDMs, respectively. Substantial amounts of

HPDM stalling can clearly be seen in the last two cases, as can be seen through the apparent "flatlining" of the displacement vs. time curves.

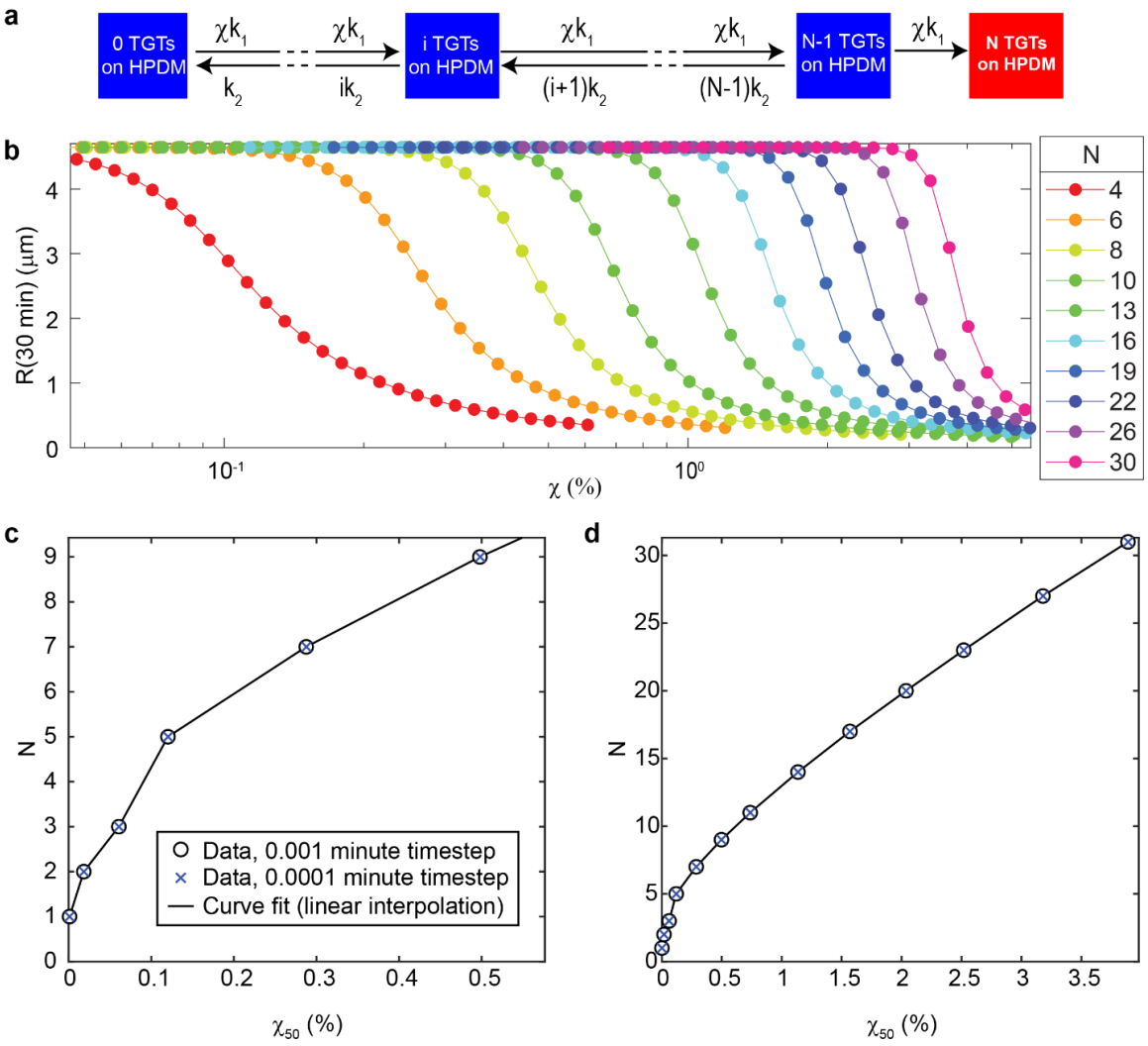

Figure 12: Generalized N-TGT model scheme and results.

This is an expansion of modeling presented in **Figure 10**. **a)** flow diagram showing generalized mass-action model scheme used to calculate R(t) as a function of χ for any positive integer value of N. **b)** Simulated R(30 min) as a function of χ for N-TGT models with N ranging from 4 to 30. **c-d)** Relationship between simulated χ_{50} and N. Plot is shown at **c)** high magnification and **d)** low magnification. Curves were calculated with two distinct timesteps to show that the selected timestep of 0.001 minutes is not too large for faithful

calculation of curves. Black line shows linear interpolant fit curve used for subsequent calculations.

Repeating these experiments and calculations with weaker 13 or 11 bp TGTs (T_{tol} = 28 pN and 19 pN, respectively) increased χ_{50} ($0.19\% \pm 0.08\%$ and $0.38\% \pm 0.12\%$) and thus increased N (5.8 ± 1.0 and 7.9 ± 1.2) in a manner that kept F_{HPDM} fairly constant at 160 ± 26 pN and 152 ± 23 pN, respectively (**Figure 9**e, **Figure 13**). A global fit of these combined datasets yielded $F_{HPDM} = 157 \pm 14$ pN. Our estimate of $F_{HPDM} \approx 157$ pN indicates that HPDMs possess a peak chemical energy to mechanical energy conversion efficiency of ~3.6% ("**Supplemental Note 4 – Calculation of power conversion efficiency**"), which is roughly an order of magnitude lower than that of cytoskeletal motors but several orders of magnitude higher than our previous estimate (and could potentially be increased through optimization). Impressively, this estimate suggests that HPDMs have a force-generating capacity that far surpasses that of individual cytoskeletal walkers (1-10 pN) and even the bacterial pilus machine[96], which is the strongest-reported molecular motor (100 pN).

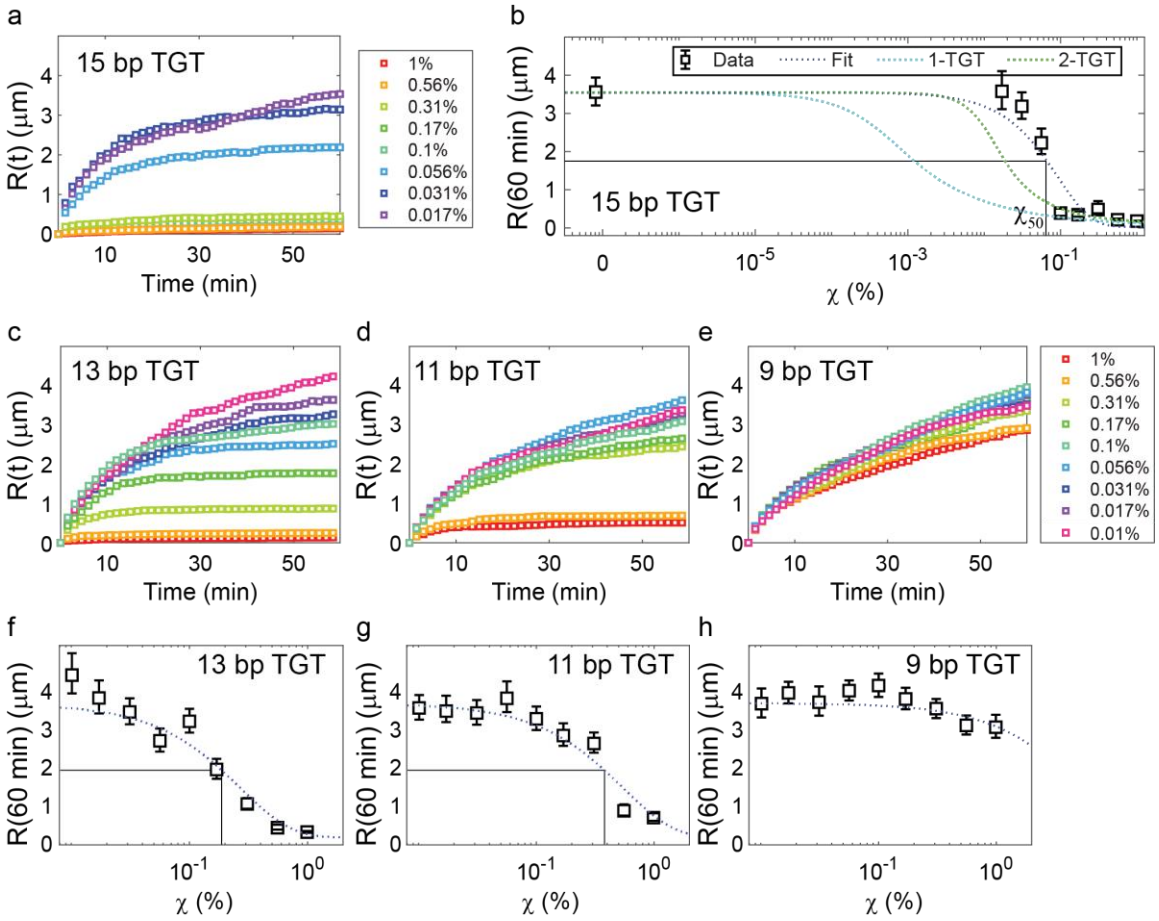

Figure 13: Ensemble HPDM tracking results for TGTs of different lengths.

a) Average displacement vs. time curves, R(t), for ≥ 100 HPDMs rolling on substrates with 15 bp TGTs with χ ranging from 0.017% to 1% (see legend, not all datapoints can be seen due to overlap). **b)** R(60 min) vs. χ data (squares, errorbars are 95% confidence interval of the mean calculation and may, in some cases, be difficult to see due to overlap with square edges) and best fit curve $R(60\text{ min}) = (3.5\ \mu m)\exp\left(-\frac{\ln(2)}{\chi_{50}}t\right)$ where χ_{50} is the only fit parameter. The best-fit curve is denoted by the dotted gray curve, and χ_{50} is denoted by the solid black line. Results of 1-TGT and 2-TGT model are shown. Note that this data was obtained from a different experiment than the data presented in **Figure 8**, **Figure 9**, and **Figure 11** in order to demonstrate that data can be reliably obtained from

the high-throughput experiment described in methods subsection "*Ensemble HPDM tracking experiment for biotin-streptavidin and 13 bp, 11 bp, 9 bp, and 25 bp TGTs*:". **c-e)** R(t) curves for χ values ranging from 0.01% to 1% (see legend) for **c)** 13 bp TGTs ($T_{tol} = 27.6$ pN), **d)** 11 bp TGTs ($T_{tol} = 19.2$ pN), and **e)** 9 bp TGTs ($T_{tol} = 6.6$ pN). **f-h)** R(60 min) vs. χ curves for **f)** 13 bp TGTs, **g)** 11 bp TGTs, and **h)** 9 bp TGTs. As in **b**, best-fit curves are shown. χ_{50} values are also shown, except for the 9 bp case where the best-fit $\chi_{50} \approx 3\%$ value did not lie in the tested range and had a very large 95% confidence interval.

2.5 Direct visualization of HPDM-induced TGT rupture with single molecule imaging

To obtain more direct evidence for force-induced duplex rupture by HPDMs, we pre-assembled biotin-terminated 25 bp TGTs (T_{tol}=49 pN) on HPDMs and linked an Alexa 647 fluorophore (A647)-functionalized streptavidin molecule to the terminus of each TGT through biotin-streptavidin binding (**Figure 17**a,b). We also replaced ~10% of RNA fuel strands on the underlying surface with biotin-presenting DNA strands. Streptavidin is a globular protein that can form high affinity bonds with up to four biotin molecules simultaneously. As such, HPDM motion will occasionally lead to biotin-streptavidin crosslinking between a TGT's terminal streptavidin and a biotin attached to the underlying surface. The resulting linkage contains a rupturable TGT duplex and two biotin-streptavidin bonds. The T_{tol} of a biotin-streptavidin bond is ~147 pN (see Methods for calculation), making it substantially stronger than even the strongest DNA duplexes and one of the strongest non-covalent bonds found in nature. Therefore, as in the experiments described above, formation of one of these linkages will either be followed by 1) HPDM stalling, if $F_{HPDM} \ll 49$ pN, or 2) TGT rupture and continued HPDM motion, if $F_{HPDM} \geq 49$ pN. However, in this case TGT rupture will also result in deposition of the fluorescent streptavidin molecule onto the substrate. Therefore, if $F_{HPDM} \geq 49$ pN then HPDM depletion tracks will be dotted with fluorescent streptavidin molecules that can be directly visualized via single molecule localization microscopy. As in previous studies that utilize TGTs, fluorescent streptavidin images can thus be loosely interpreted as reporting the cumulative history of HPDM force. The frequency of biotin-streptavidin engagement will depend on the percent of DNA feet that have been replaced with streptavidin-capped TGTs,

which we denote as χ'. The quantity χ' is functionally very similar to χ as defined above (see methods and **Figure 14** for a description of how we calculated χ').

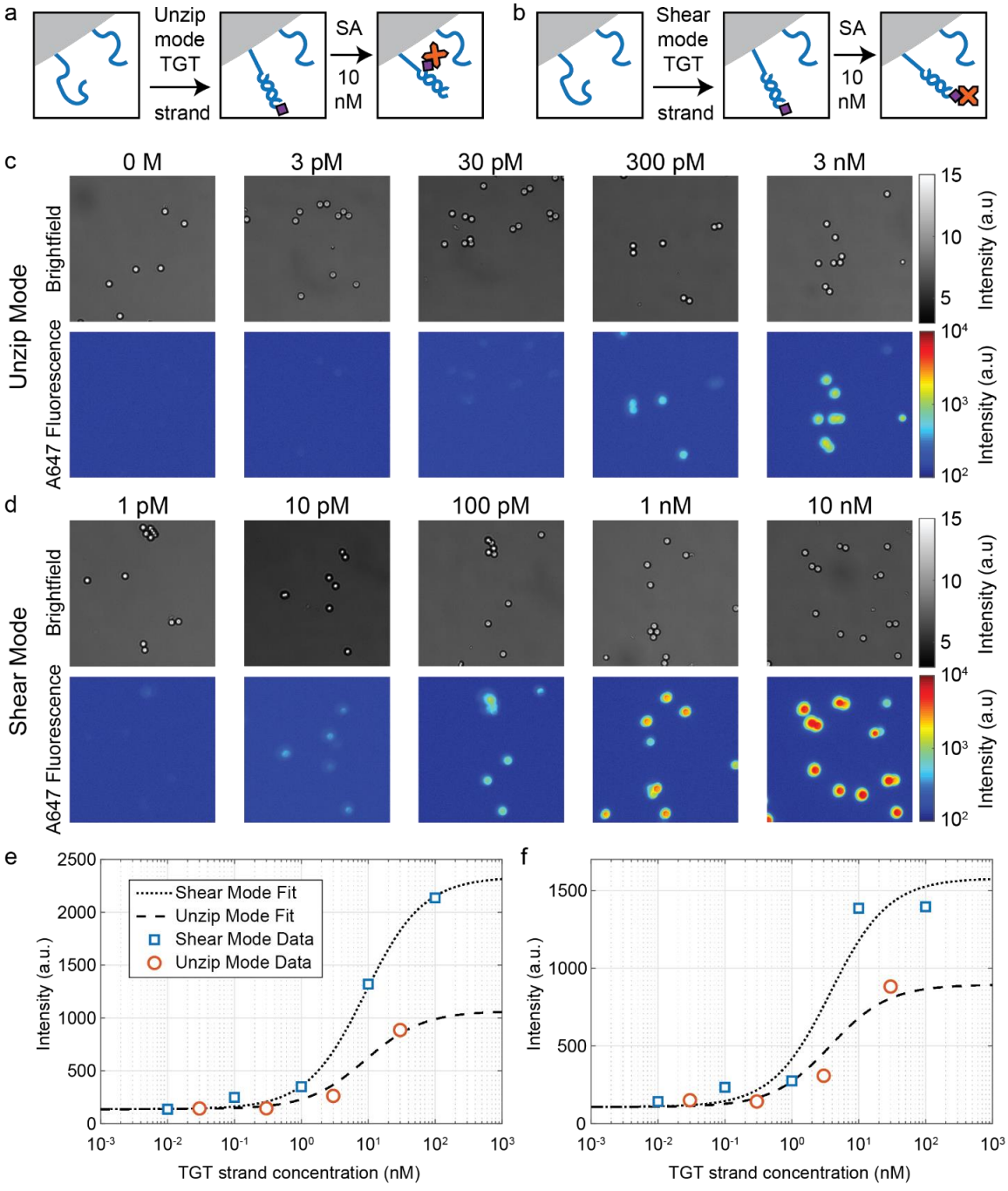

Figure 14: Estimation of TGT strand dissociation constant.

a,b) Cartoon schemes shown on-HPDM TGT assembly process for **a)** shear-mode TGTs and **b)** unzip-mode TGTs. **c,d)** Brightfield and A647 fluorescence microscopy images of HPDMs functionalized with **c)** unzip-mode and **d)** shear-mode TGTs. **e,f)** Results of two independent experiments, as described in the methods section "**Estimation of χ' for TGT-coated HPDMs**".

As expected, we observed highly processive HPDM motion along with the periodic deposition of streptavidin within depletion tracks using single-molecule localization microscopy when $\chi' = 0.5\%$ (**Figure 17**c, **Figure 15**, **Figure 16**). While some localizations did appear outside of depletion tracks, quantitative analysis of ~100 HPDMs' depletion tracks revealed a 40-fold enhancement of localization density within depletion tracks when compared to the background (p<0.001, paired t-test, **Figure 20**e, **Figure 18**). When repeating this experiment in the absence of either HPDM-bound TGT strands or substrate-bound biotin-presenting strands we observed no significant change in localization density within depletion tracks (p>0.05, paired t-test), indicating minimal (if any) contribution of the shedding of nonspecifically-bound streptavidin molecules to the observed result (**Figure 20**e, **Figure 18**).

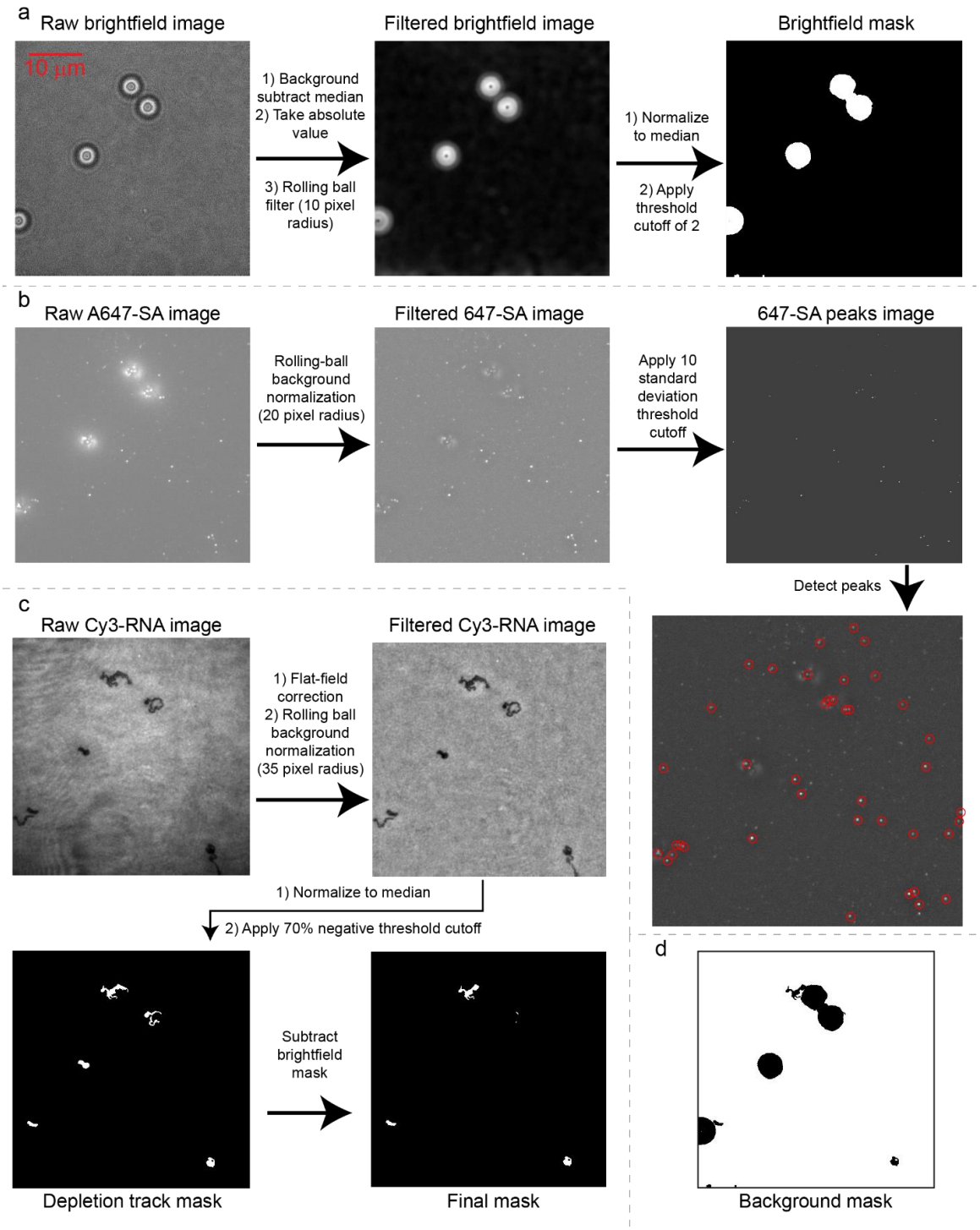

Figure 15: Automated image processing for single molecule localization experiments.

a) HPDMs are first detected using the brightfield image. The image is first filtered in a three-step process and then a threshold is applied to the filtered image to produce a mask

that approximately denotes the locations of HPDMs. This mask is later used to exclude HPDM-overlapping regions from image processing due to the substantial background fluorescence generated by HPDMs. **b)** The A647 TIRF image is used to detect single streptavidin molecules. The raw image is filtered and then a cutoff is used to select for pixels that are substantially brighter than the pixels surrounding them. Peak detection is then used to locate single molecules. **c)** Cy3 TIRF imaging is used to detect depletion tracks. The raw image is first filtered and then a cutoff is used to select for pixels that are less than 70% as bright as the surrounding region, generating a depletion track mask. A final mask is then generated by subtracting the HPDM mask from the depletion track mask, leaving only pixels that are associated with depletion tracks but not HPDMs. This mask is used for calculating the molecular density of single streptavidin molecules within depletion tracks. **d)** Finally, the background mask is calculated by finding all pixels that are neither in the depletion track mask nor in the HPDM mask. This background mask is used when calculating the molecular density of single streptavidin molecules in the image background.

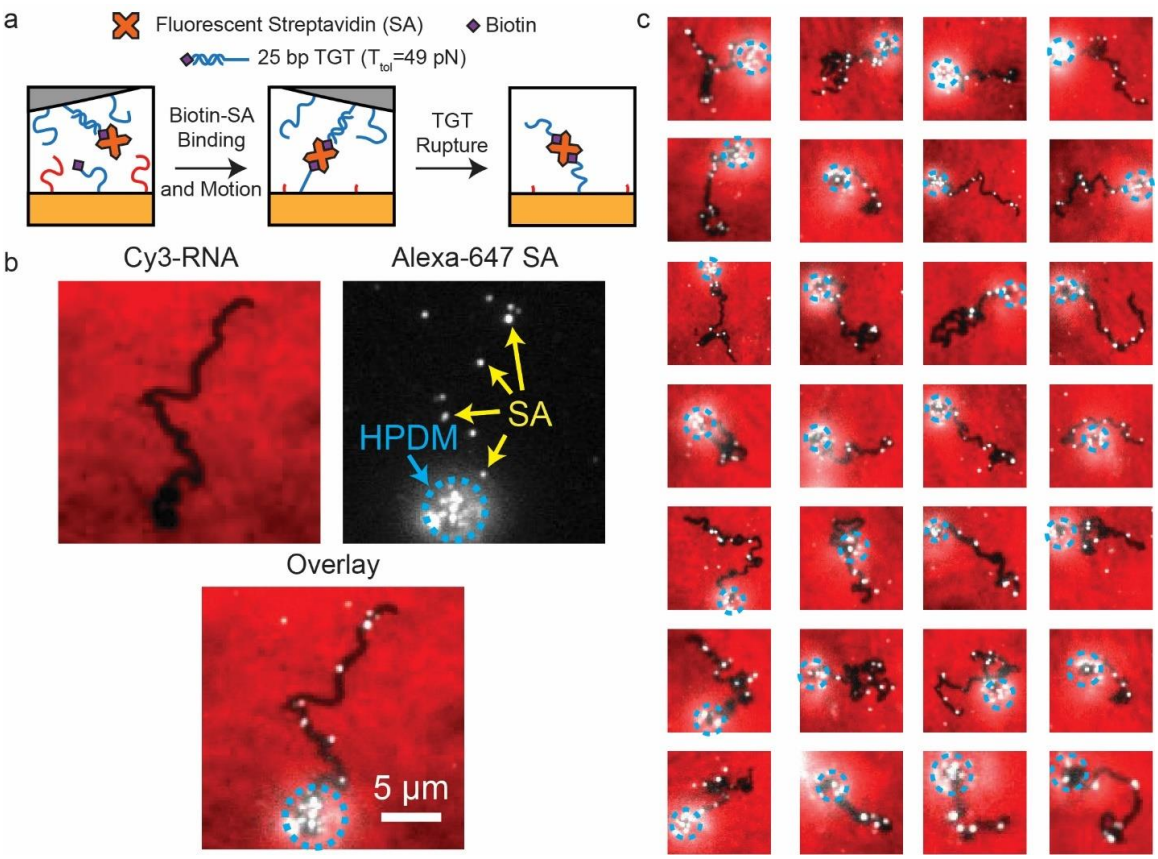

Figure 16: Single molecule TGT-rupture experiment results.

a) Cartoon depiction of the biomolecular process used to detect TGT rupture. A 25-bp TGT ($T_{tol} = 49$ pN) is pre-assembled on an HPDM and capped with a fluorescent streptavidin (SA) molecule. As the HPDM translocates, the streptavidin molecules engage with surface-tethered biotin molecules. The HPDM then translocates, generating force and eventually rupturing the TGTs. **b)** Representative Cy3-RNA TIRF image (top left), A647-SA TIRF image (top right), and overlay (bottom), taken ~1 hr after the addition of RNase H. In the Cy3-RNA image, the former path of the HPDM can be seen as the dark depletion track. In the A647-SA TIRF image, some individual SA molecules are denoted via yellow arrows and the location of the HPDM is denoted using a blue dotted circle. Note that the SA molecules are predominantly co-localized with the depletion track in the overlay,

indicating the HPDMs rupture TGTs during translocation as shown in the cartoon. **c)** 28 representative overlay images, showing that the observation of SA-depletion track co-localization is common. Not all of these images are the same size and, as such, the apparent magnification can vary. However, depletion tracks, which are generally ~400 nm in width, can be used to obtain a rough understanding of image scale. In each image, the HPDM's location is shown with a blue dotted circle.

2.6 Demonstration that HPDMs can rupture biotin-streptavidin bonds

We next tested whether HPDMs are capable of rupturing biotin-streptavidin bonds by replacing the biotin-terminated TGT in the above experiment with a biotin-terminated DNA strand that is covalently linked to the HPDM (**Figure 17**d). Following biotin-streptavidin binding, the HPDM can only continue rolling if it mechanically ruptures one of the two biotin-streptavidin bonds ($T_{tol} = 147$ pN), resulting in deposition of a streptavidin molecule with 50% probability. As with the TGTs, we observed a 10-fold increase in streptavidin localization density within these depletion tracks when $\chi' = 0.03\%$ (p<0.01, paired t-test, **Figure 17**d,e, **Figure 19**). These localizations tended to be surrounded by "depletion patches" that were significantly wider than the 400 nm width of typical depletion tracks, indicating that HPDMs may execute extended searches to generate the force necessary to rupture biotin-streptavidin bonds. Via high-throughput tracking, we found that $\chi'_{50} = 0.08 \pm 0.06\%$. When dividing this quantity by 10 (reflecting that only 10% of substrate RNA was replaced with biotin-presenting strands) and interpolating into our N-TGT simulation models, we found that $N = 1.4 \pm 0.3$ molecules, and $F_{HPDM} = 207 \pm 48$ pN (**Figure 21**). We expect that this estimate of F_{HPDM} is an overestimation because the N-TGT models were constructed assuming that HPDM velocity is unperturbed by bond engagement, which is likely not true in this case because T_{tol} is similar to F_{HPDM}. This hypothesis is supported by the observation of depletion patches and the finding that $1 < N < 2$. As stated above, when repeating these single-molecule experiments in the absence of surface-bound biotin we generally observed no significant enhancement of localizations within depletion tracks (**Figure 17**e, **Figure 16**) or HPDM stalling, thus

confirming that streptavidin localizations represent HPDM-mediated and force-induced deposition.

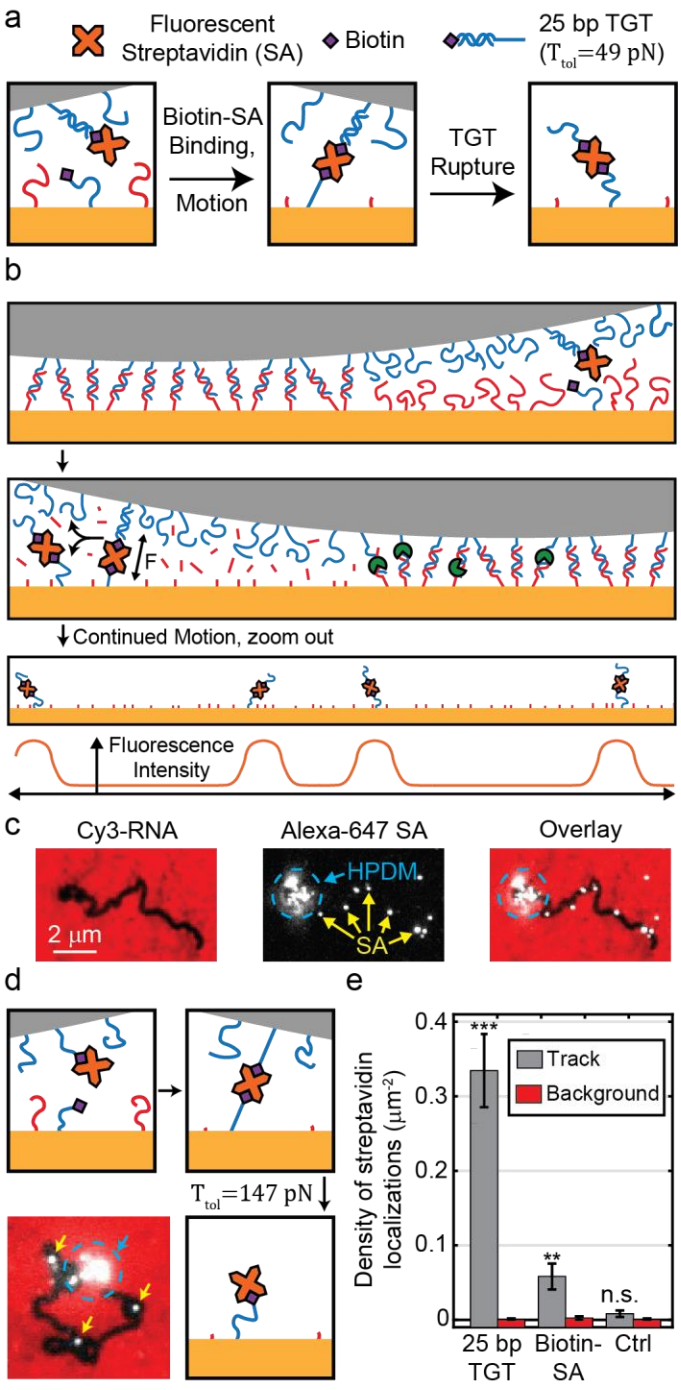

Figure 17: Single molecule imaging of bond rupture driven by HPDM force generation.

a,b) Cartoons depicting force sensor function. Fluorescent streptavidin-capped TGTs are pre-assembled on HPDMs and as the HPDMs translocate the streptavidin molecules bind

to surface-tethered biotin strands. Subsequent movement by the HPDM then generates enough force to rupture the TGT, and the deposited streptavidin molecules can be visualized using single molecule fluorescence microscopy. **a)** Zoom-in on single force sensor, and **b)** expanded view. **c)** Cy3-RNA fluorescence image (left) and A647-streptavidin image with streptavidin molecules denoted using yellow arrows (middle). The HPDM, which has several SA localizations associated with it and therefore produces substantial background signal, is shown using a blue arrow and a dashed blue circle. An overlay (right) shows co-localization between depletion tracks and streptavidin. **d)** Cartoon depiction and representative data for experimental test of biotin-streptavidin bond rupture. **e)** Surface density of single streptavidin molecule localizations in depletion tracks (gray) and the background (red) for 25 bp TGT ($\chi' = 0.5\%$) and biotin-streptavidin ($\chi' = 0.03\%$) rupture experiments, as well as a control experiment conducted with biotin-lacking HPDMs. Result of statistical comparison (paired t-test) between depletion track and background localization densities are shown, where ** denotes $p<0.01$, *** denotes $p<0.001$, and n.s. denotes $p>0.05$. Error bars are standard error of the mean. Fluorescence images in **c** and **d** were filtered with rolling-ball background normalization and contrast enhancement to better highlight depletion tracks and single molecules.

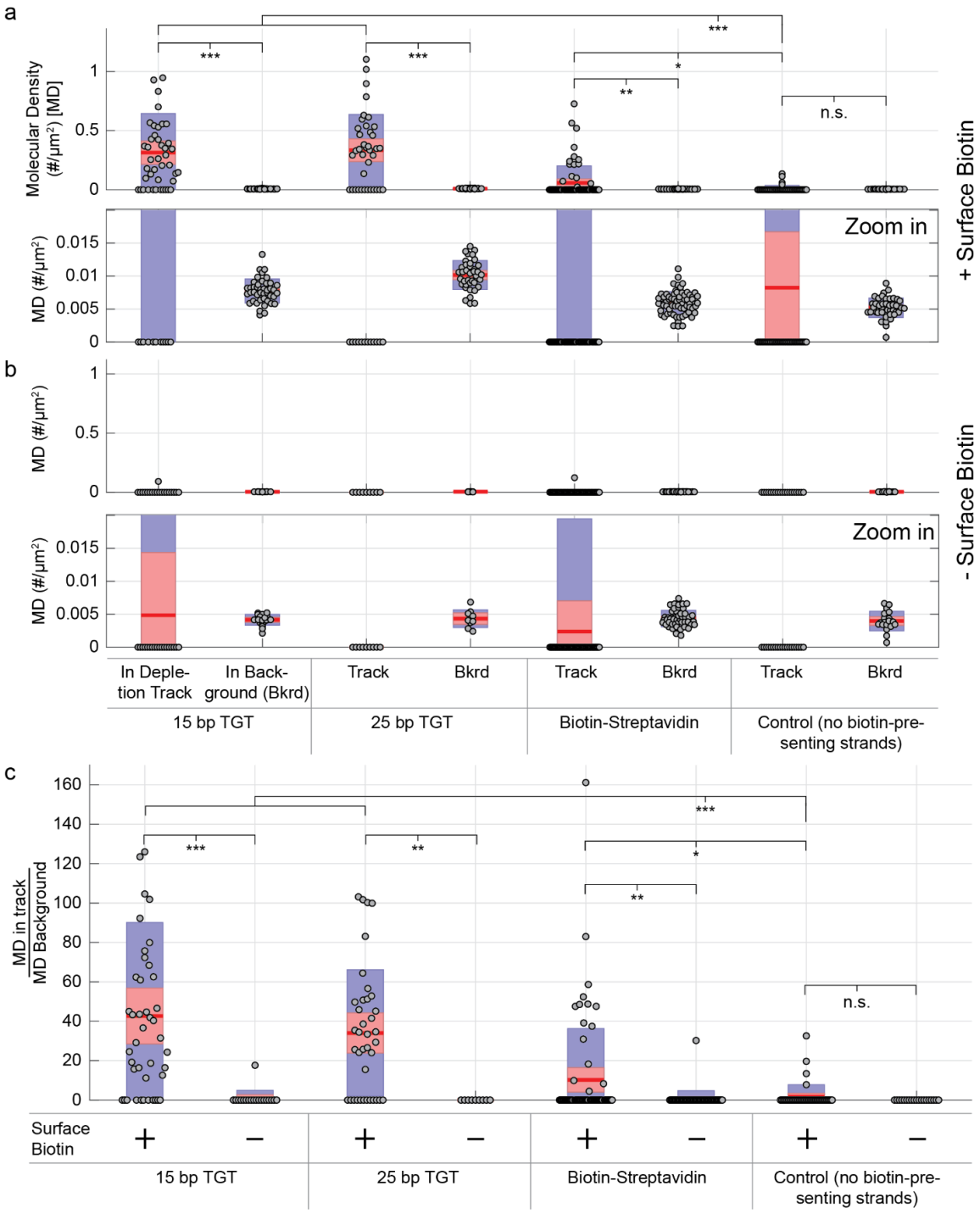

Figure 18: Population data for single molecule localization experiment

a) Molecular density (MD, e.g. the number of streptavidin localizations per μm^2) for experimental tests of HPDMs rupturing 15 bp TGTs (T_{tol} = 34 pN), 25 bp TGTs (T_{tol} =

49 pN), biotin-streptavidin bonds ($T_{tol} = 147$ pN), and a control condition where biotin-free HPDMs were subjected to the same streptavidin incubation and wash steps as the other conditions. Sample sizes were 43, 38, 68, and 43 locations, respectively. MD is shown for both depletion tracks and the background for each condition. This plot is shown at low magnification (top) and high magnification (bottom). Some very high datapoints are not shown due to axis limits. All calculations were performed using a single MATLAB code without user input. Only locations with at least 100 pixels in the depletion track are shown, and one extra location from the control condition was manually discarded due to an anomalous background fluorescence aggregate. Boxplots are shown with average (red line), standard error of the mean (pink), and 95% confidence intervals (purple), as well as all individual datapoints (gray circles). Results of statistical comparisons using the two-sample t-test (MATLAB command ttest2) are shown where n.s. denotes $p > .05$, * denotes $p < .05$, ** denotes $p < .01$, and *** denotes $p < .001$. **b)** Same as **a**, but for identical experiments on surface that lacks biotin. Sample sizes are 19, 9, 52, and 19 locations, respectively. Statistical test results are not shown. **c)** Ratio of MD in depletion track to MD in background for data shown in **a** and **b**. Some very high datapoints are not shown due to axis limits.

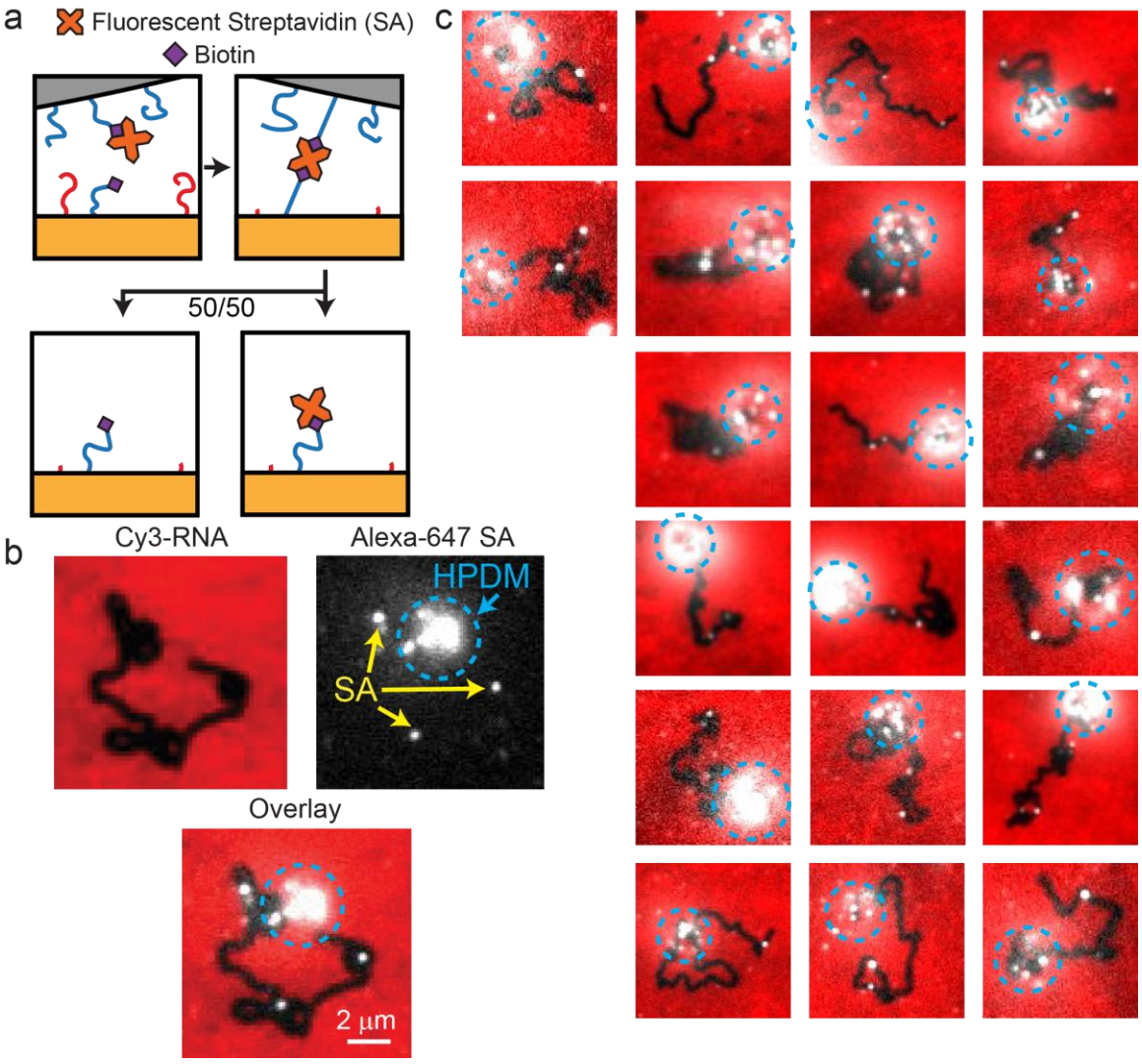

Figure 19: Single molecule biotin-streptavidin (SA) bond-rupture experiment results.

a) Cartoon depiction of the biomolecular process used to detect biotin-streptavidin bond rupture. A fluorescent streptavidin (SA) molecule is linked to HPDMs via biotin-terminated DNA strands. As the HPDM translocates, the streptavidin molecules engage with surface-tethered biotin molecules. The HPDM then moves, generating force and eventually rupturing a biotin-streptavidin bond. Because each SA is bound to two biotin molecules, there is a 50% probability that this sequence of events will result in the SA being transferred to the surface. **b)** Representative Cy3-RNA TIRF image (top left), A647-

SA TIRF image (top right), and overlay (bottom), taken ~1 hr after the addition of RNase H. Note that the SA molecules are co-localized with the depletion track in the overlay, indicating that the HPDMs rupture biotin-streptavidin bonds during translocation as shown in the cartoon. c) 20 representative overlay images, showing that the observation of SA-depletion track co-localization is common. Not all of these images are the same size and, as such, the apparent magnification can vary. However, depletion tracks, which are generally ~400 nm in width, can be used to obtain a rough understanding of image scale. Brightness scaling also varies between images, which can result in variations in the brightness of single molecule localizations. In each image, the HPDM's location is shown via a blue dotted circle.

2.7 Nanopatterning with HPDMs and unzip-mode TGTs

A TGT's T_{tol} depends not only on length and sequence, but also on the pulling geometry. All TGTs discussed thus far have been arranged in the "shear" mode, wherein force is applied to opposite ends of the DNA duplex (e.g. 5'-5' or 3'-3'). This pulling geometry maximizes T_{tol} because duplex rupture requires simultaneous denaturation of all base pairs. However, when force is applied to the same end of the duplex (e.g. 3'-5'), base pairs are unzipped one-at-a-time and, as such, T_{tol} is minimized. In other words, while $T_{tol} = 49$ pN for a 25 bp TGT in shear-mode, $T_{tol} = 12$ pN for the same 25 bp TGT in unzip-mode[43] (**Figure 20**a). Our previous results suggest that flipping the orientation of the TGT from shear-mode to unzip-mode (**Figure 20**b) should enable HPDMs to continue translocating even when bound to several (e.g. 10 or more) TGTs. As such, we predicted that we would observe processive HPDM motion at much higher χ' values, which would enable the deposition of much more dense layers of streptavidin molecules (rather than periodic, isolated molecules) within HPDM depletion tracks.

As expected, HPDMs with unzip-mode TGTs displayed highly processive motion with $\chi' = 5.3\%$ (**Figure 20**c, **Figure 21**). In contrast, HPDMs coated with shear-mode TGTs with $\chi' = 4.4\%$ displayed no motion (**Figure 21**). Furthermore, fluorescence microscopy revealed that unzip-mode TGT-coated HPDMs left dense trails of fluorescent streptavidin in their depletion tracks (**Figure 20**b, **Figure 22**). Quantitative analysis revealed that ~23% of all depletion track area was associated with high streptavidin fluorescence signal, compared with 0.7% of the background area (~30-fold enhancement – this is likely also an underestimate, see **Figure 23**). We used area coverage for this

analysis, rather than the surface density of single molecule localizations, because the high density of streptavidin molecules generally made it impossible to discriminate individual molecules. Applying the same analysis to shear-mode depletion tracks at the highest χ' where substantial HPDM motion was observed ($\chi' = 0.5\%$) revealed a more modest ~6% coverage (~10-fold enhancement over background, **Figure 23**). While these two datasets were collected on different days with different χ' values, we also performed a side-by-side comparison of data collected on the same day with similar χ' values and found that the depletion tracks of HPDMs with unzip-mode TGTs were significantly brighter in the A647 channel than those of HPDMs with shear-mode TGTs (p<0.001, **Figure 24**).

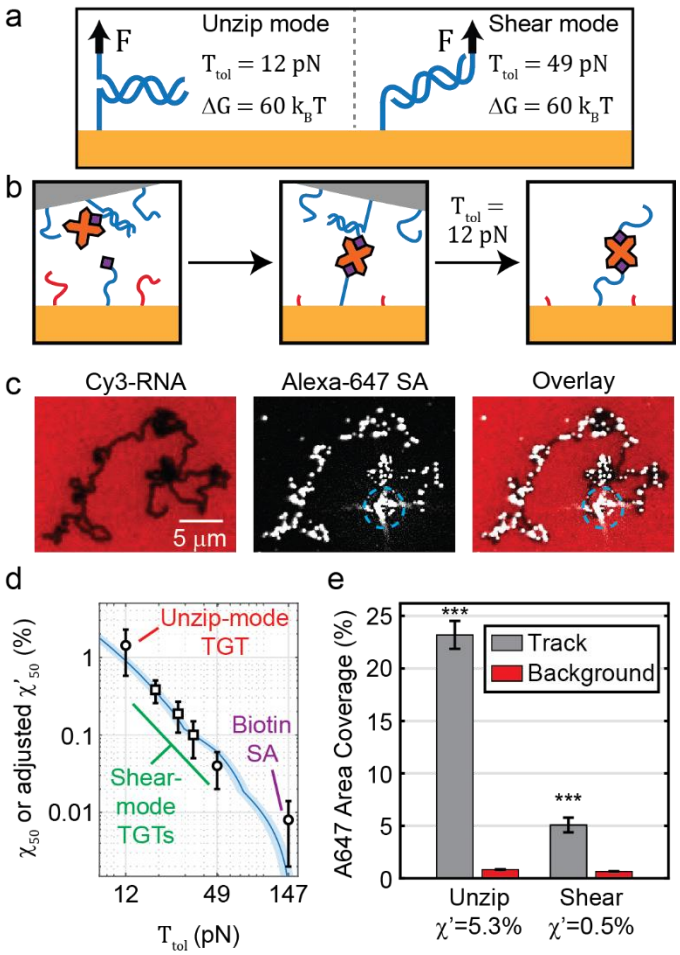

Figure 20: HPDM-mediated nanopatterning enabled by unzip-mode TGT rupture

a) Cartoon illustration of the difference between shear-mode and unzip-mode TGTs. While the two types of TGTs have the same free energy of hybridization (ΔG), they have different T_{tol} due to differences in the kinetic pathways of dehybridization. **b)** Cartoon depicting unzip-mode TGTs in the context of our experiment. **c)** Representative fluorescence microscopy images showing that HPDMs leave a dense trail of SA in their depletion tracks. The SA image was processed with rolling ball background subtraction, and both images were contrast-enhanced for clarity. **d)** Log-log plot of best-fit χ_{50} (squares) or χ'_{50} adjusted by dividing by 10 (circles) as a function of T_{tol}. Circle and squares denote best-fit values

obtained from fits to experimental data, bounds denote 95% confidence interval of the fit, and the blue curve and shading represent the global fit to the N-TGT simulation output corresponding to $F_{HPDM} = 157 \pm 14$ pN.

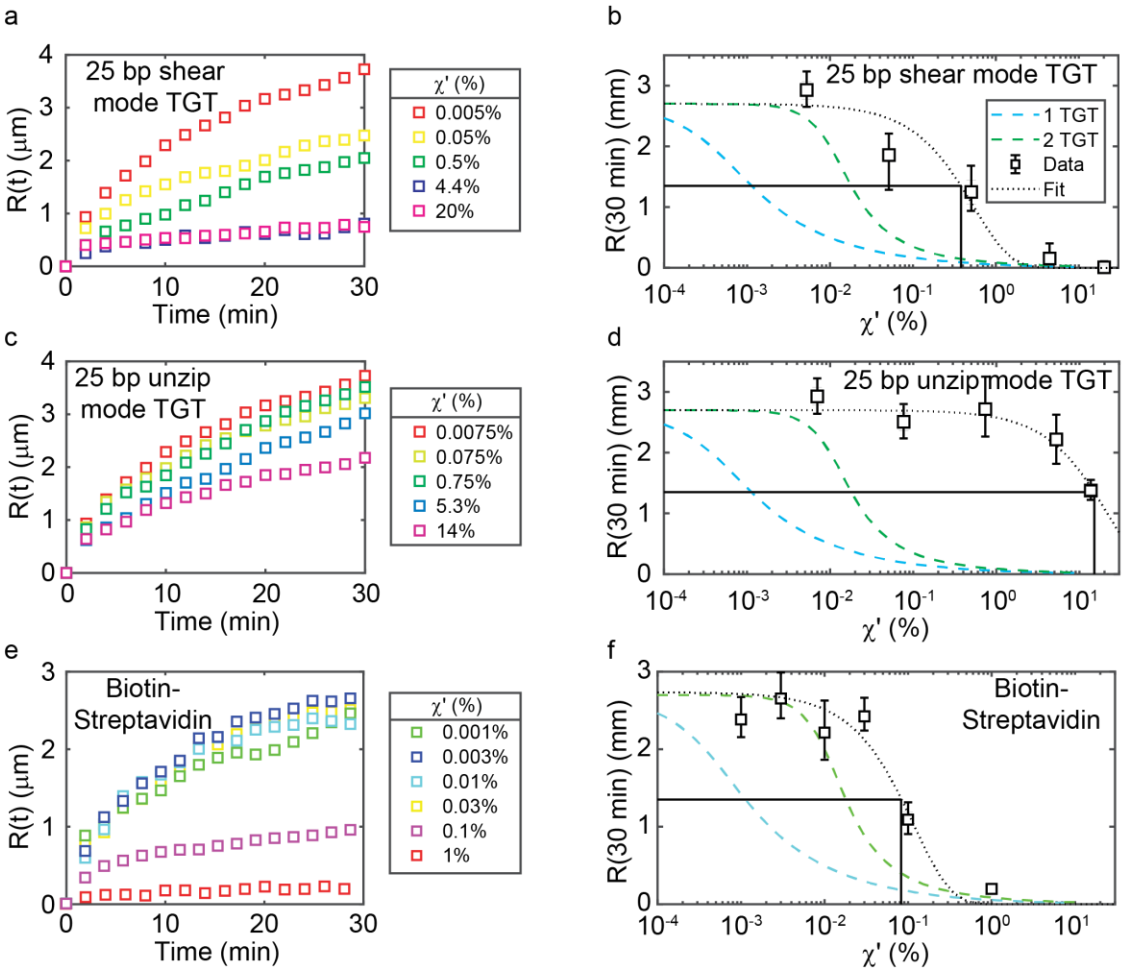

Figure 21: Ensemble HPDM tracking experiments for 25 bp shear- and unzip-mode TGT and biotin-SA bond rupture experiments

a) Average displacement vs. time curves, R(t), for ≥ 100 HPDMs rolling on substrates with 25 bp shear-mode TGTs with χ' ranging from 0.0001% to 20% (see legend, not all datapoints can be seen due to overlap). **b)** R(30 min) vs. χ' data (squares, errorbars are the 95% confidence interval of the estimate of the mean) and best-fit curve $R(30\,\text{min}) = (2.7\,\mu\text{m})\exp\left(-\frac{\ln(2)}{\chi'_{50}}t\right)$ where χ'_{50} is the only fit parameter. The best-fit curve is denoted by the dotted gray curve, and χ_{50} is denoted by the solid black line. Results of 1-TGT and 2-TGT model are shown, but note that χ'_{50} was subsequently divided by 10 to reflect the

10% surface coverage of biotin presenting strands prior to N and F_{HPDM} estimation. **c)** same as **a**, but for 25 bp unzip-mode TGTs with different χ' values. **d)** same as **b**, but for 25 bp unzip-mode TGTs. **e)** Same as **a**, but for biotin-streptavidin bond rupture with different χ' values. **f)** Same as **b**, but for biotin-streptavidin bond rupture.

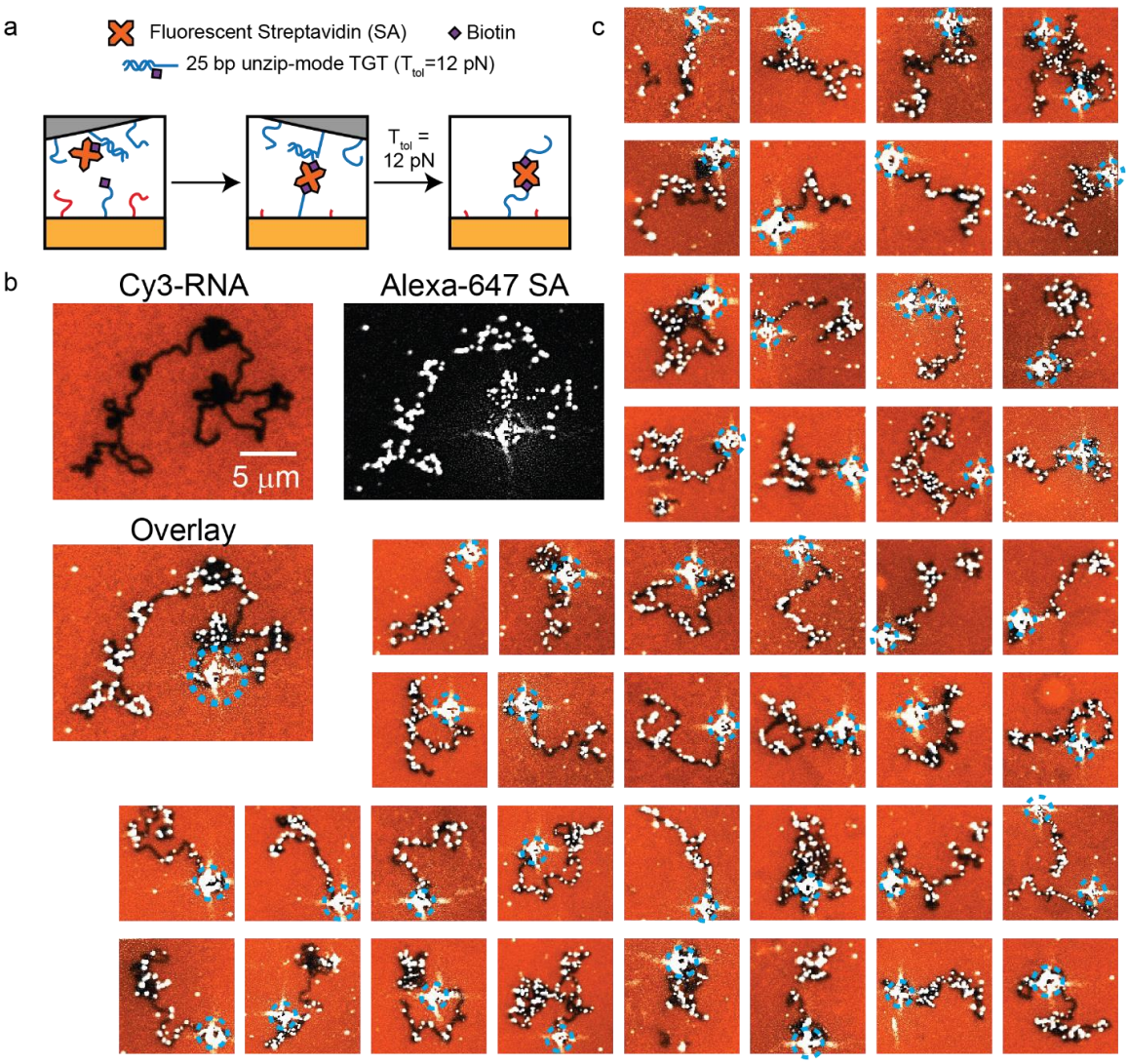

Figure 22: Nano-patterning via unzip-mode TGT rupture.

a) Cartoon depiction of the biomolecular process used to detect TGT rupture, same as in **Figure 17**, but with the geometry of the TGT switched from shear-mode to unzip-mode. **b)** Representative Cy3-RNA TIRF image (top left), A647-SA TIRF image (top right), and overlay (bottom), taken ~1 hr after the addition of RNase H. **c)** 44 representative overlay images, showing that the observation of dense SA coating within depletion tracks is highly reproducible. Not all of these images are the same size and, as such, the apparent magnification can vary. However, depletion tracks, which are generally ~400 nm in width,

can be used to obtain a rough understanding of image scale. In each image, the HPDM's location is shown via a blue dotted circle.

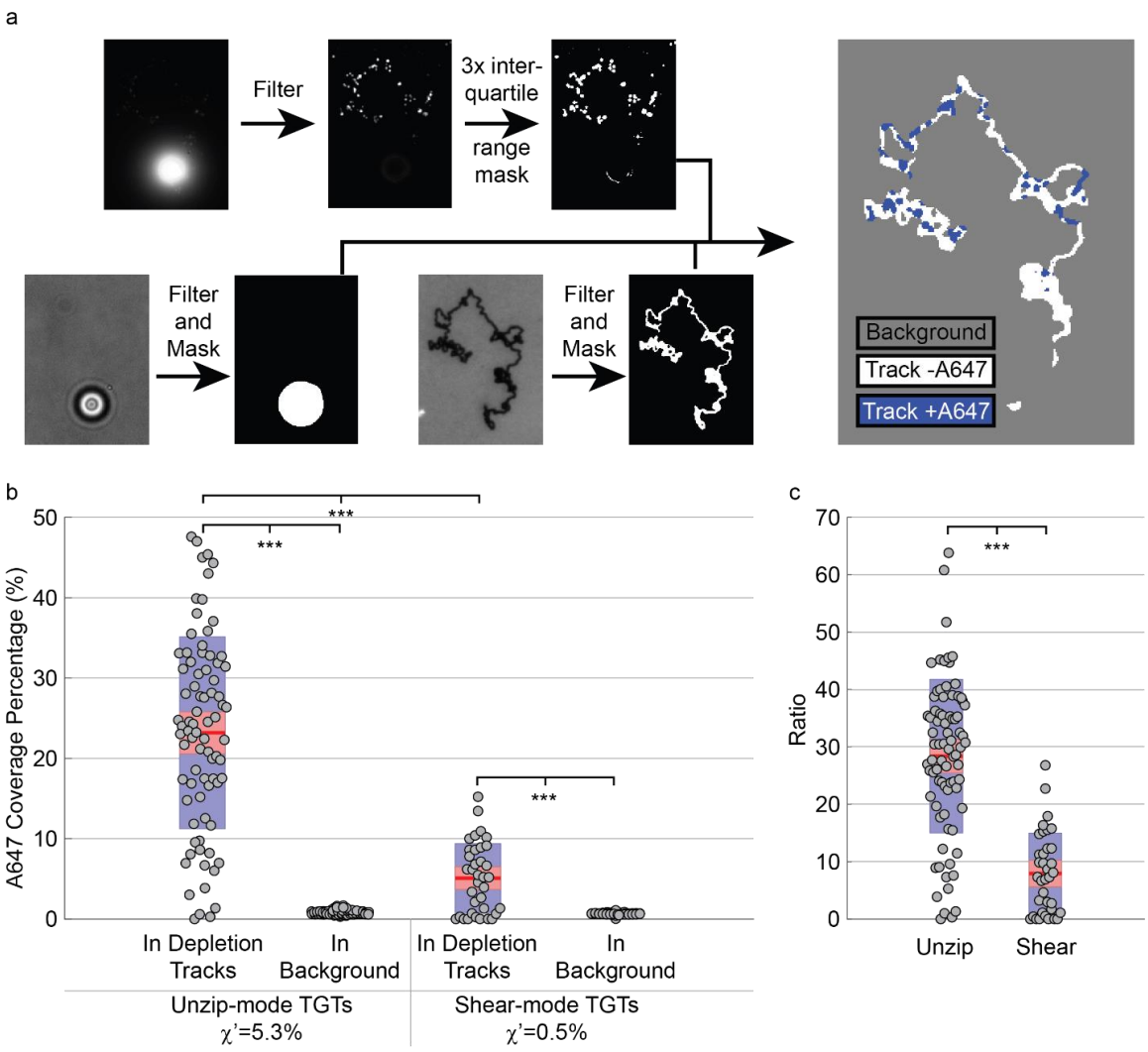

Figure 23: Depletion track streptavidin coverage fraction.

a) Depiction of automated image processing algorithm, modified from that shown in **Figure 15**. Bightfield and Cy3 images were processed as before to locate HPDMs and depletion tracks. A647 images were filtered as before, but A647 masks were generated using a threshold of 3 multiplied by the interquartile range of the filtered image (calculated using MATLAB's iqr fuction). In this example, of the 3,420 pixels that were identified as being associated with depletion tracks were also identified as having high A647 intensity, which corresponds to ~25% coverage. This subfigure also shows that the bright A647

background from the HPDM overwhelms deposited streptavidin signal that extends beyond the range of the brightfield mask. When HPDM A647 background signal is filtered out, this source of noise appears to result in an overall reduction in the observed coverage fraction. **b)** Box plots comparing A647 coverage percentage in depletion tracks and in the background for 80 separate locations with unzip-mode TGTs ($\chi' = 5.3\%$) and 40 separate locations with shear-mode TGTs ($\chi' = 0.5\%$). **c)** Ratio of depletion track A647 coverage to background A647 coverage for the two datasets shown in **b**. In both **b** and **c**, *** denotes $p < 0.001$ as calculated using a non-parametric median comparison test (MATLAB's ranksum function).

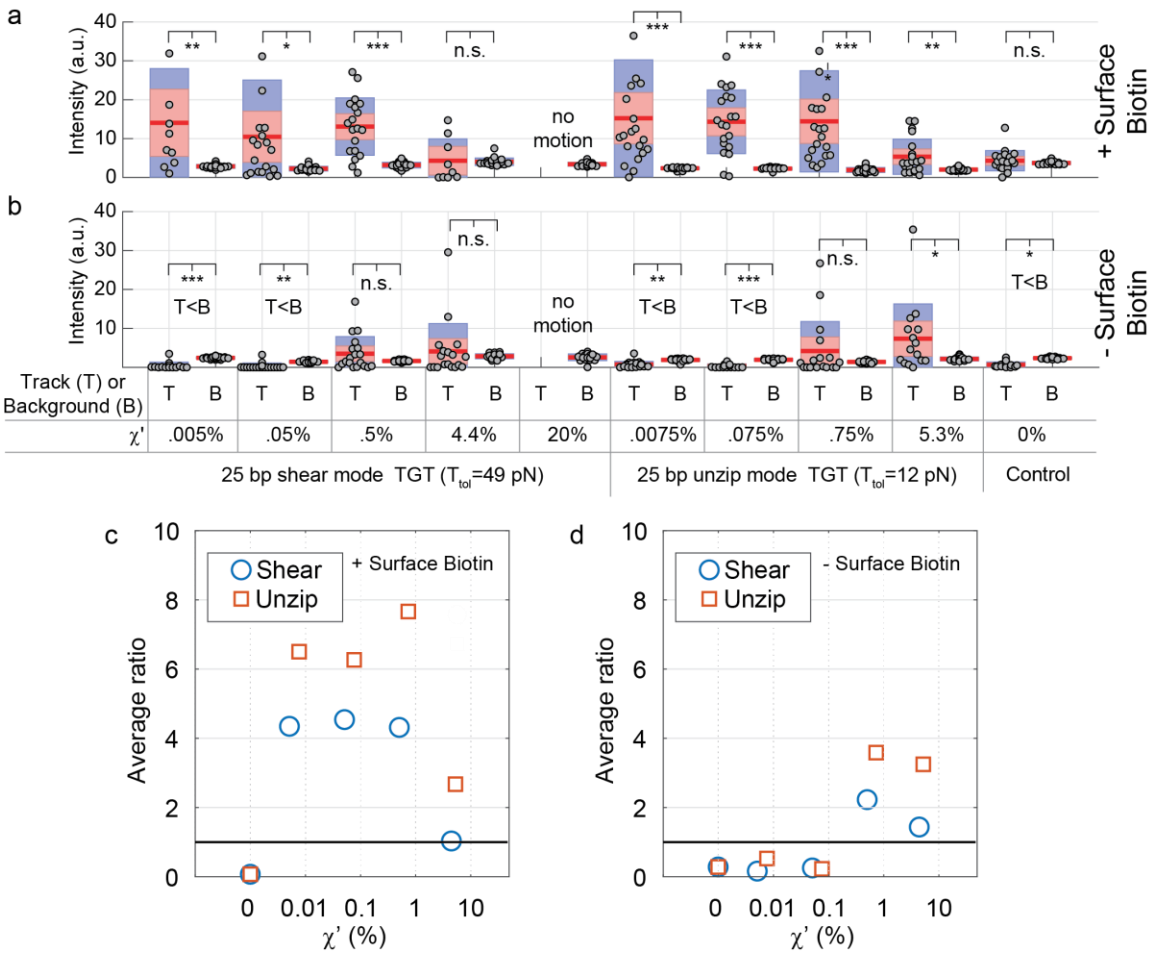

Figure 24: Streptavidin intensity in TGT-coated HPDM depletion tracks.

a) Boxplots showing average A647 intensities within depletion tracks (T) and in background (B) for ~20 representative locations per condition for HPDMs coated with shear-mode (left) or unzip-mode (right) 25 bp TGTs on substrates functionalized with 10% biotin-presenting strands for a range of χ' values spanning ~3 orders of magnitude. Results of non-parametric statistical tests (performed using MATLAB's ranksum function) show statistically significant differences in median intensity between tracks and background, where *** denotes $p < .001$, ** denotes $p < .01$, * denotes $p < .05$., and n.s. denotes $p > .05$. **b)** Same as **a**, but for HPDMs rolling on surfaces without biotin. The label "T<B" was

used to indicate when statistically significant differences were observed because the track intensity was lower than the background intensity. These results were obtained using a process similar to that shown in **Figure 15**, with the exception being that only pixels with nonzero intensity values were set to zero following A647 image filtering, rather than all pixels with intensity values below the ten standard deviation cutoff. These two plots show that depletion tracks are significantly brighter in the A647 fluorescence channel than background for shear-mode TGTs with $\chi' < 4.4\%$ (negligible motion was observed for $\chi' \geq 4.4\%$) and for all unzip-mode χ' values tested, but not for the $\chi' = 0\%$ control. The plots also show that depletion track brightness is not an artifact caused by the inherent high brightness of HPDMs; surfaces lacking biotin had depletion tracks that were generally not significantly brighter than background. In fact, depletion tracks were significantly dimmer than background on surfaces lacking biotin when $\chi' < 0.5$, which indicates that our automated image processing algorithm actually leads to an underrepresentation of depletion track intensity (possibly due to suppression of track-bound streptavidin signal due to the bright background from the HPDM). However, at $\chi' \geq 0.5\%$, track intensity appears to increase, which indicates that our algorithm fails to adequately remove background signal in some cases. **c)** The average ratio of track intensity to background intensity, plotted as a function of χ' for HPDMs rolling on substrates with 10% biotin. **d)** Same as **c**, but for HPDMs rolling on surfaces without biotin. These plot shows that depletion tracks of unzip-mode TGT-coated HPDMs are generally brighter than the depletion tracks of shear-mode TGT-coated HPDMs. We expect that this observation is the result of self-selection, because we only select and image relatively long depletion tracks for this analysis. In other words, we expect that there is a TGT surface density threshold

that is specific to each TGT geometry over which HPDMs stall. Therefore, the depletion tracks that we do observe are likely from HPDMs that happened to have TGT surface densities below this threshold. This may explain why the intensity ratio is relatively constant for χ' values spanning three orders of magnitude, but different between the shear- and unzip-modes. We pooled the ratios from $\chi = 0.05\%$ and $\chi' = 0.5\%$ (shear-mode) and compared them to the pooled ratios of the $\chi = 0.075\%$ and $\chi = 0.75\%$ (unzip mode) using MATLAB's ranksum function and found that the ratios were significantly higher ($p < 0.001$) for unzip-mode TGT-coated HPDMs than shear-mode TGT-coated HPDMs. Due to the relative invariance of intensity ratio across three orders of magnitude for χ', we expect that this conclusion should be insensitive to small differences in χ' between datasets or errors in our estimation of χ' . Together, these results also demonstrate that our findings of force-mediated bond rupture are reproducible across a range of experimental parameters.

We also performed high-throughput tracking and parameter fitting of HPDMs coated with shear- and unzip-mode 25 bp TGTs and found that $\chi'_{50} = 0.4\% \pm 0.2\%$ and $14.3\% \pm 8.5\%$, respectively. If we divide these quantities by 10 and perform global fitting to the combined datasets as described above (**Figure 9**e, **Figure 21**) we found that $N = 3.3 \pm 1.1$ for shear-mode TGTs, while $N = 13.4 \pm 4.6$ for the unzip-mode TGTs, with $F_{HPDM} = 160 \pm 55$ pN. These quantitative estimates are consistent with those obtained throughout this work, and the 230-fold difference in χ'_{50} between the two TGT modes is consistent with the notion that F_{HPDM} is consistent between experiments and is sufficient to drive TGT and biotin-streptavidin rupture. Adding these datasets to the 11 bp, 13 bp, and 15 bp TGT datasets described above yielded an (unchanged) global fit of $F_{HPDM} = 157 \pm 14$ pN.

These results demonstrate conclusively that SA-deposition is indeed a result of force-induced bond rupture. Furthermore, these results demonstrate the potential of HPDMs to serve as autonomous nanopatterning machines; nanopatterning is commonly performed using externally controlled motors (e.g. by using an atomic force microscope to perform dip-pen nanolithography[97] or cut-and-paste surface assembly[98]), but HPDMs can autonomously create nanoscale patterns of "molecular ink" via force-induced bond rupture without an externally controlled motor.

An HPDM is a rigid scaffold connecting many independent DNA feet that autonomously coordinate to generate substantial forces while translocating on non-directional substrates. To better understand how HPDMs generate such large forces, we revisit the BBBR framework discussed above. However, for this discussion, rather than focusing on the

biased Brownian motion of the microparticle, we slightly reframe our discussion to focus on individual tethers and the effect that they have on the microparticle. We define "backwards" and "forwards" HPDM movement as motion towards and away from the depletion track, respectively, and define "leftward" and "rightward" motion as opposing 90° turns from the forward and backward directions.

Considering each tether to act as an entropic spring (e.g. using the worm-like-chain model[23,32,33]) with a thermodynamic drive to minimize its end-to-end extension reveals a mechanical driving force that we had not previously considered; when a new tether forms, the tether immediately begins exerting an entropic tensile force on the HPDM. Force balance principles dictate that this new force creates a force-imbalance that is only resolved upon movement and reorientation of the HPDM (**Figure 25**). In other words, when a tether forms it immediately shifts the HPDM's energetic minimum position and orientation. Because this is the step at which chemical energy (released from the hybridization interaction) is converted into mechanical work that moves the HPDM, we contend that tether formation represents the force-generating powerstroke of HPDM motion. Note that we use the term powerstroke in its broadest definition (meaning "the stroke of a cyclic motor which generates force"). This broad definition applies to motors across all length scales (e.g. macroscopic to molecular-scale), so the use of the term powerstroke here should not to be interpreted as strictly relating to powerstroke model of cytoskeletal motor proteins.

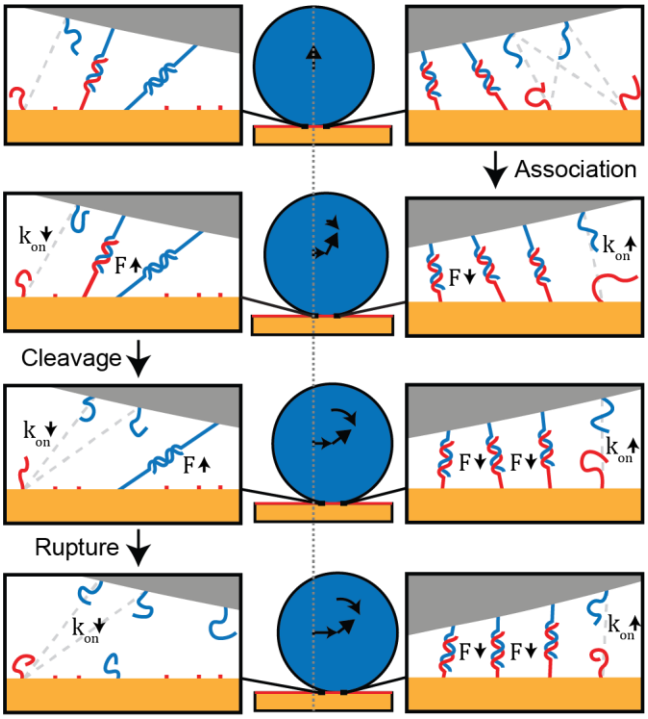

Figure 25: HPDMs generate force through autochemophoresis.

When a new tether forms, it begins exerting an adhesive force on the HPDM, resulting in movement and re-orientation that results in the extension of resistive tethers. Tether formation is biased away from the depletion region due to the RNA surface density gradient, which is self-propagated by the HPDM. Forward HPDM movement increases the on rate (k_{on}) of strands in the direction of movement (shown on the right) while decreasing k_{on} for strands at the back end of the HPDM (shown on the left), creating a positive feedback loop that promotes further forward motion. Cleavage of resistive tethers also releases stored mechanical strain energy that allows further forward motion of the particle. The repetition of many of these events can cause the force (**F**) on a TGT to eventually increase to the point of bond rupture.

Force-balance principles also dictate that HPDM movement following tether formation necessarily results in the extension of some "resistive" tethers, such that the work performed by the new tether is converted into mechanical strain energy and stored in these resistive tethers. The eventual cleavage of these resistive tethers releases the mechanical strain energy stored within them in a manner that resembles the release of energy after a stretched rubber band is cut, thus resulting in additional motion of the HPDM (**Figure 25**). Because there is a surface density gradient of RNA fuel in the HPDM's vicinity (e.g. there is more RNA fuel in front of the HPDM than behind it), tether formation is more likely to occur at the forward-facing edge of the particle and result in forward motion. In contrast, because there is generally no surface density gradient of RNA fuel from left to right (or vice-versa), sideways motion is less favorable than forward motion. Because forward motion is generally favored, resistive tethers will generally be stretched in a manner that causes them to resist forward motion. As such, it follows that the cleavage of tethers also generally favors forward motion. Forward motion also decreases the distance between unpaired DNA feet and RNA fuel at the front-edge of the HPDM, thus increasing the rate of tether formation at the front edge (**Figure 25**). The reverse is also true; forward motion increases the distance between feet and fuel strands at the backward-facing edge of the HPDM and thus decreases their association rate. This framework also leads to the prediction that these interacting chemical and mechanical processes result in a positive feedback loop that allow the tethers to spontaneously cooperate to generate relatively large collective forces (**Figure 25**). These processes also likely contribute to the persistence observed by HPDMs (**Figure 4**) and have been discussed previously in relation to the

bacterial partition system in other works. In particular, we refer readers to work by Hu et. al.[99], in which detailed simulations are used to illustrate many of the points discussed here in greater detail.

We have principally discussed our conceptual understanding of how tethers control the energetic minimum position and orientation of an HPDM. While we have largely ignored the effect of thermal (Brownian) fluctuations of the microparticle body, we argue that it is reasonable to do so because the Brownian motion of the microparticle body is highly restricted at high polyvalency; calculations suggest that when the particle is only bound to 1 tether, it can diffuse freely within a ~22 nm-wide volume (**Figure 26**). However, when an HPDM is bound to ~100 tethers, diffusion is restricted to a ~3.5 nm-wide volume (**Figure 26**). Regardless of polyvalency, the RNA and DNA oligonucleotides themselves undergo thermal fluctuations that allows them to stretch out and pair with strands within a binding cutoff distance (the separation distance below which a foot strand and fuel strand can hybridize) of ~10 nm (**Figure 26**). Put another way, at low polyvalency motion is driven by ratcheted Brownian fluctuations of the particle body as well as the oligonucleotides, but at high polyvalency Brownian fluctuations of the particle body are quenched and motion is primarily driven by ratcheted Brownian fluctuations of the oligonucleotides. In "**Supplemental Note 5 – Effect of polyvalency on HPDM mobility**", we perform calculations that suggest that the transition between these two types of motion occurs gradually with increasing polyvalency, with a crossover point at which the two types of Brownian fluctuations contribute equally occurring at a polyvalency of ~50 tethers.

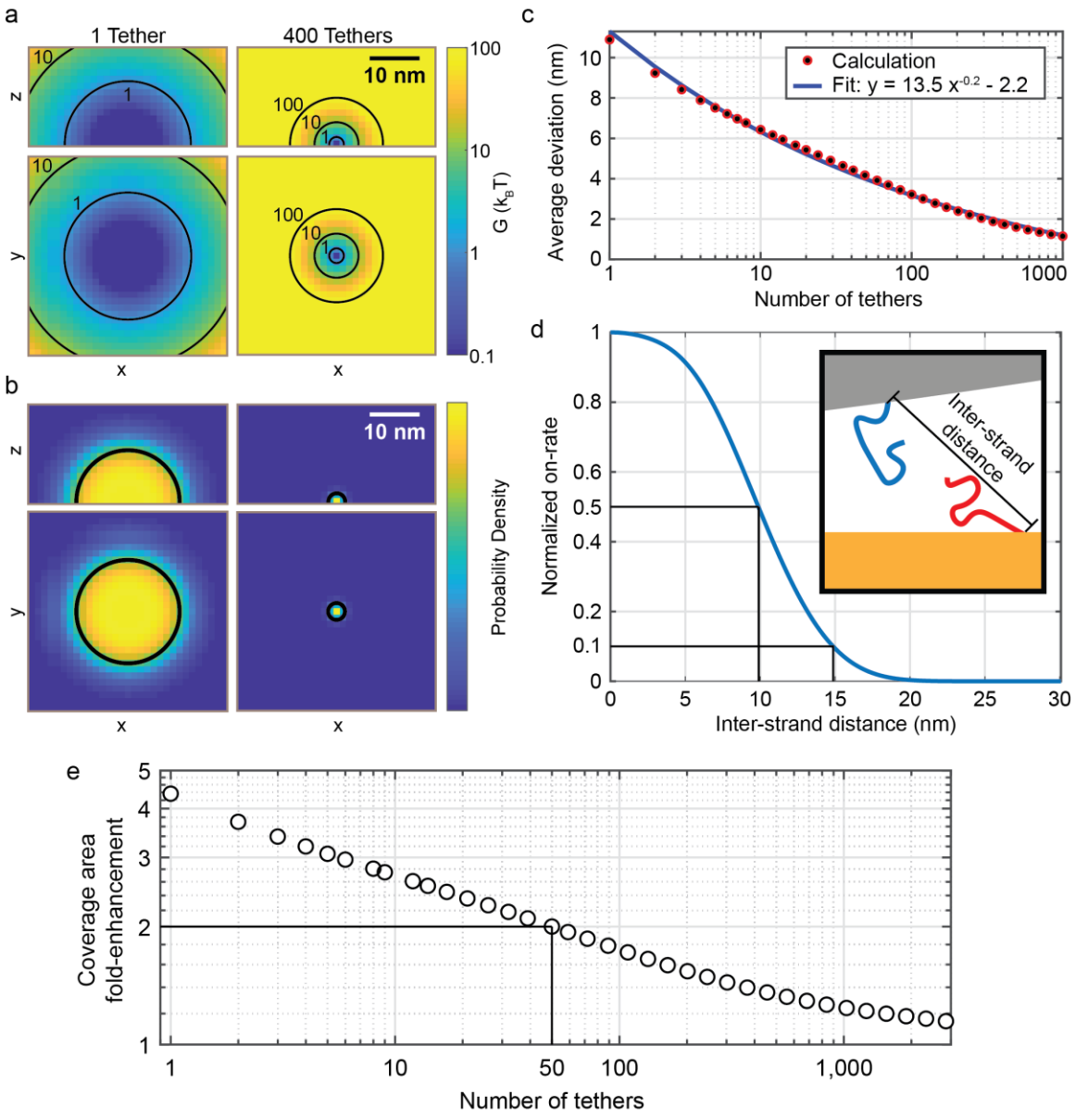

Figure 26: HPDM mobility decreases with increasing polyvalency

See "**Supplemental Note 5 – Effect of polyvalency on HPDM mobility**" for accompanying discussion. **a)** Energy (G) landscape in multiples of k_BT from x-z view with y=0 (top) and x-y view with z=0 (bottom) when an HPDM is bound to 1 tether (left) and 400 tethers (right). Black contour lines denote $G = 1$, 10, and 100 multiples of k_BT. **b)** Probability density = $\exp(-G)$ with the same layout as in **a**. Black contour lines denote the

average distance of the HPDM from the origin. **c)** Average deviation from the energetic minimum position (x=y=z=0) as a function of the number of tethers, along with a power law fit curve. **d)** Normalized association rate as a function of the inter-strand distance (illustrated in inset) as calculated according to the worm-like-chain model (see "**Supplemental Note 5 – Effect of polyvalency on HPDM mobility**"). The "binding cutoffs" of ~10 nm and ~15 nm are denoted with black lines and represent the distance at which the on rate is reduced by 50% and 90%, respectively. **e)** Fold-enhancement of the coverage area, calculated as described in "**Supplemental Note 5 –Effect of polyvalency on HPDM mobility**", as a function of the number of tethers. The crossover polyvalency of 50, which is the polyvalency at which Brownian fluctuations of the microparticle body and the oligonucleotides contribute roughly equally to HPDM motion, is denoted with a black line.

Adhesion-driven movement of cargo up a concentration gradient has previously been studied and is called chemophoresis[100]. Because an HPDM moves via a self-propagated chemophoretic energy gradient[101], we introduce the more precise term *autochemophoresis* to describe the mechanism of HPDM motion. The bacterial partition system, which plays vital roles in plasmid and chromosome replication and protein cluster positioning, can also be classified as autochemophoretic [82,99,100,102-109]. This mechanism has been called a third fundamental form of directed subcellular cargo transport (along with cytoskeletal stepping and filament polymerization) and is speculated to play roles in various biological processes such as virus-host association[82]. However, autochemophoresis has not been explicitly studied in terms of pN-scale force generation and is generally assumed to be restricted to the fN range, which is sufficient to transport nanoscale cargo through the cellular environment but not to perform many useful tasks such as cellular contraction, chromosome separation, and mechanosensation. Given the simplicity of the components required for autochemophoresis and the findings presented herein, we speculate that autochemophoresis may also be a significant mechanism of pN-scale force generation in biological systems. This means that autochemophoresis may play roles in biological processes that extend beyond cargo transport, including mechanotransduction, contraction, and protrusion. Because HPDMs are fully synthetic and have many properties that can be easily tuned, we anticipate that they will be useful in future studies aimed at understanding the fundamental principles of autochemophoresis.

To the best of our knowledge, this is the first demonstration of a DNA-based motor generating pN-scale force to perform useful tasks such as bond rupture and nanopatterning. Force generation is a fundamental aspect of biological motors that has been elusive to the

field of DNA nanotechnology. Note that HPDMs generate forces through the collective action of thousands of oligonucleotides. Therefore, our findings demonstrate that future generations of DNA walkers[29,51,57-75], other hybridization-based DNA machines[21,31,50,75,110-112], and non-DNA-based burnt bridge molecular motors[113] can be used for engineering application that require pN-scale force generation. The diversity and potential of such engineering applications is illustrated by the ubiquity of biological motors like myosin and kinesin in eukaryotes[76] and nanotechnology[4,114]. As the width of the HPDM-surface contact area is only ~400 nm, we hypothesize that the properties of autochemophoretic force generation should scale down to the nanoscale. In future works, we will test this hypothesis with the aim of developing nanoscale HPDMs that can perform previously impossible tasks such as the powering of nanomotors and deformation of nanoscale objects.

2.8 Methods for chapter 2

2.8.1 Materials:

All oligonucleotides were purchased from Integrated DNA Technologies (IDT), stored at 4 °C (-20 °C for RNA), and used without purification. Their sequences, including functional group modifications, are shown in **Table 1**. Unless otherwise stated, all other reagents were purchased from Sigma-Aldrich and used without further purification. Nanopure water (Barnstead Nanopure system, resistivity = 18.2 MΩ), was used to make stock solutions and wash surfaces and will hereafter be referred to as water. Rolling buffer, which was used for rolling experiments and washing, was custom prepared on the day of use by mixing water (77.5%), formamide (10%), 10% triton-X w/v in water (7.5%), and 10x RNase H buffer (5%). The 10x RNase H buffer was stored at 4°C for up to two years and consists of 500 mM Tris(hydroxymethyl)aminomethane hydrochloride (Tris-HCl), 750 mM potassium phosphate monobasic, and 3 mM magnesium chloride ($MgCl_2$) in water with a pH of 8.3 at room temperature. Phosphate buffer saline (1xPBS) was used for washes and dilutions and consists of 10 mM phosphate, 137 mM sodium chloride, and 2.7 mM potassium chloride in water with a pH of 7.4 at room temperature. RNase H was purchased from Takara Clontech (Product No. 2150A) and stored at -20 °C until expiration. Prior to use, 1 μL of the RNase H stock solution was diluted in 23 μL of 500 μM dithiotheitol (DTT) in 1xPBS and stored on ice for up to 2 hours. 1 μL of this dilution contains 5 units of RNase H. All computations were performed using MATLAB 2016a or later on a conventional laptop computer.

2.8.2 Preparation of custom-designed surface reaction chambers and imaging chambers:

Unless otherwise stated, all surface functionalization reactions of glass microscopy slides were carried out in custom-made Delrin reaction chambers (hereafter referred to as reaction chambers). Each reaction chamber has a large outer groove that can hold a 75 mm x 25 mm glass slide and a smaller inner groove that can hold ~750 μL of liquid such that the entire surface of the slide is in contact with the liquid (**Figure 27a,b**). We etched reaction chambers from ¼ inch-thick white Delrin (a solvent-resistant polymer, McMaster-Carr #8573K15) using a 60-watt CO_2 laser cutter (Universal Laser Systems, model VLS 4.60). Chambers were rinsed with acetone and dried with a kimwipe before the first functionalization step and rinsed with water and dried with a kimwipe between successive functionalization steps.

Custom-designed imaging chambers (**Figure 27c**) were also etched from ¼ inch-thick white Delrin and are 75 mm x 25 mm wide with a 3x10 grid of ~3 mm x 4 mm rectangular holes (with curved corners to prevent the formation of air bubbles during fluid injection). Prior to etching, one side of the Delrin was layered with solvent-resistant, double-sided sticky tape with the upward-facing tape paper still on (McMaster-Carr #7602A53). These imaging chambers were stored at room temperature for up to 1 year. Prior to use, imaging chambers were rinsed in acetone, dried with a kimwipe, further dried under a nitrogen stream, and allowed to sit at room temperature for 30 minutes to allow for complete drying. Imaging chambers were fixed to DNA-functionalized slides by unpeeling the tape paper, carefully lining the slide up with the tape, and gently pressing the slide and imaging chamber together. All air bubbles were removed from between the glass and the chamber

using a smooth thin object such as the bottom of a pen. To allow proper sealing, slide-fixed reaction chambers were allowed to sit for ~15 minutes before adding solution to the wells.

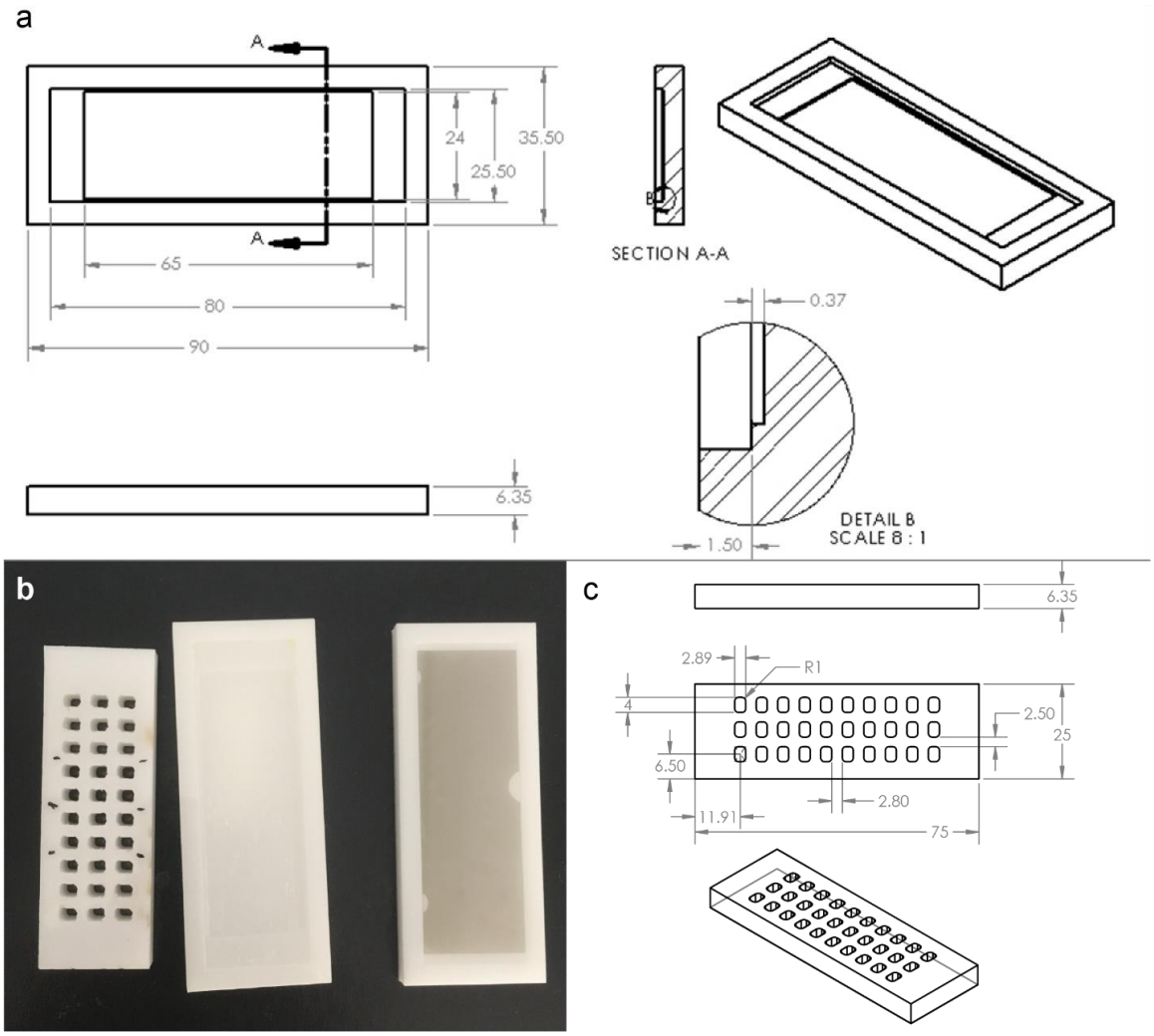

Figure 27: Delrin reaction chambers and imaging chambers.

a) Dimensions of the custom-design glass microscopy slide reaction chamber shown via side, top, and isometric views, as well as cross section view (SECTION A-A) and a zoom-in on a portion of the cross-section view (DETAIL B) to show the approximate dimensions of the grooves. Units are mm. **b)** Photograph of an imaging chamber attached to a slide (left) and reaction chambers without (middle) and without (right) a gold film-coated glass slide inserted. **c)** Dimensions of the imaging chamber shown via side, top, and isometric views. Units are mm. R1 denotes a corner curve with radius of 1 mm.

2.8.3 HPDM preparation for ensemble experiment

HPDMs were prepared using previously reported methods[29] outlined in **Figure 3a**. 1 mg of 5 μm diameter amine-modified silica particles (Bangs Labs, #SA05000) were mixed with 1 mg of azidobutyric acid NHS ester (Lumiprobe, #63720) in 100 μL of dimethyl sulfoxide (DMSO). The cycloaddition reaction was initiated through the addition of 1 μL of a mixture of 10% triethylamine and 90% DMSO. The mixture was then vortexed and left at room temperature overnight. The azide-modified particles were then washed: the particles were resuspended in 1 mL of nanopure water and pelleted via 1-minute centrifugation in a benchtop centrifuge at 2,680 rcf, and the supernatant was removed using pipette aspiration. Following five successive washes, the particles were then diluted to a final volume of 30-40 μL and stored for up to 6 months at 4 °C. Next, DNA was coupled to the azide-modified particles via a click reaction: 5 μL of azide-modified particles were mixed with 5 μL of 1 mM DNA feet, 25 μL of DMSO, 5 μL of 2 M triethylammonium acetate (TEAA) in water, 5 μL of water saturated with ascorbic acid, and 2 μL of a copper catalyst (Lumiprobe #21050). The reaction mixture was left at room temperature overnight and washed as described above twice in 1x PBS with 1% Triton-X w/v and three times in 1x PBS. The DNA-modified HPDMs were diluted to a final volume of ~40 μL and stored at 4 °C for up to 6 months.

2.8.4 Substrate preparation for ensemble experiment*:*

Substrates were prepared using previously reported methods[29], with some modifications outlined in **Figure 3b**. Surfaces were rinsed with water and dried under a nitrogen stream between all functionalization steps. Glass slides (ibidi, #1.5H ibidi Glass Coverslip) were sonicated twice in nanopure water and once in 190 proof ethanol (5 minutes each), dried under a nitrogen stream, and mounted in a home-built thermal evaporation chamber. The chamber's pressure was vacuumed to 50 μTorr and a 2 nm layer of chromium was evaporated onto the surface, followed by a 10 nm layer of gold. After a 10-minute cool-down period, the chamber was vented with air and the slides were removed. Thiol-terminated DNA anchor strands were added to the gold film via an overnight, room-temperature incubation of the gold film with 750 μL solution of 1 μM anchor in a 1 M potassium phosphate monobasic buffer. The film was then passivated via a six-hour, room temperature incubation with 750 μL of 100 μM methoxy-terminated hexa(ethylene glycol) undecane thiol (NanoScience Instruments #CMT009) in 50% water and 50% ethanol. The slide was rinsed with water, dried under a nitrogen stream, and attached to either a six-well flow chamber (ibidi, sticky-Slide VI 0.4) or a custom-made 30-well Delrin imaging chamber (**Figure 27**c). Finally, RNA fuel and TGT strands were added to the film via hybridization with the surface-bound anchor strands. The two strands were mixed at a ratio of χ in 50 μL of 1xPBS with a combined concentration of 100 nM, added to a well, and left at room temperature overnight. Prior to imaging, each well was emptied with pipette aspiration and washed three times with 50 μL of 1xPBS.

2.8.5 Microscopy:

Imaging was performed using a Nikon Eclipse Ti microscope equipped with Nikon Elements software, an automated scanning stage, a 1.49 NA CFI Apo 100× objective for high-magnification single molecule experiments, a 0.50 NA Plan Fluor 20× objective for low-magnification ensemble experiments, an Andor iXon Ultra 897 electron-multiplying charge-coupled device (EMCCD) camera for image capture, and a perfect focus system used to minimize drift during timelapse and multipoint acquisitions at 100x magnification. On gold film-coated surfaces, fluorescence imaging of the Cy3-RNA was performed at 100x using a Intensilight Hg lamp epifluorescence source (excelitas, xt120l) and a TRITC (tetramethylrhodamine isothiocyanate) filter cube set supplied by Chroma with an exposure time of 100 ms and EMCCD gain of 100. On click-functionalized glass surfaces used for single molecule experiments, fluorescence imaging of the Cy3-RNA and A647-streptavidin was performed using a total internal reflectance fluorescence (TIRF, a method used to maximize single-to-noise by only exciting fluorophores within a few hundred nanometers of the surface) laser launch, a 125 mW 647 nm excitation laser (for streptavidin, 3 s exposure time, 300 EMCCD gain, 10% power – higher power, even for short exposure times, resulted in dehybridization between the anchor and fuel due to heat accumulation), an 85 mW 561 nm excitation laser (for Cy3, 400 ms exposure time, no EMCCD gain, 20% power) (both lasers are part of a combined laser box, Agilent MLC 400B), and a Chroma quadband filter cube (ET-405/488/561/640 nm Laser Quad Band).

2.8.6 Ensemble HPDM tracking experiment for 15 bp TGTs:

Rolling buffer was prepared fresh on the day of the experiment. Following preparation, it was tested for RNA-degrading impurities by adding 50 μL to a well and recording the fluorescence intensity of the well's RNA monolayer for ~15 minutes. If any substantial

decrease was observed during this time, the rolling buffer was re-prepared with new stock solutions and the well was not used for further experiments. The RNA monolayer quality in each well was also checked for homogeneity and intensity (~10,000 intensity units is typical). Following verification of rolling buffer sterility, the stock solution of DNA-functionalized HPDMs was sonicated for 5 seconds (to disaggregate HPDMs), vortexed for ~10 seconds, and ~1-2 μL was removed and suspended in 50 μL of rolling buffer. This mixture was then vortexed for ~30 seconds (to disperse the HPDMs) and added to a well in an imaging chamber. HPDMs were given ~10 min to settle on the substrate. For data shown in **Figure 2** through **Figure 11**, experiments were performed in 6-well flow chambers (ibidi sticky-Slide VI 0.4). Prior to addition of RNase H, the glass slide was mounted on the microscope and the 20x objective was used to locate 40-50 distinct locations (a "location" is a ~410 μm x 410 μm field of view with ~10-50 HPDMs in it), which were stored in the Nikon Elements software. Next, 5 units of RNase H were mixed with 50 μL of rolling buffer and vortexed for ~10 s. The 52 μL mixture was then dropped into the well without touching the imaging chamber, initiating HPDM motion. A multipoint timelapse was then immediately initiated via the Nikon Elements software. During this timelapse, the automated scanning stage cycled between the 40-50 pre-selected locations at a speed of 1 mm/s, taking a snapshot at each location at 45 s intervals for 30 minutes. The resulting timelapse files were then saved for future analysis.

2.8.7 Ensemble HPDM tracking experiment for biotin-streptavidin and 13 bp, 11 bp, 9 bp, and 25 bp TGTs:

Experiments were performed in parallel to increase throughput. 50 μL of rolling buffer with 1-2 μL of HPDMs and 2.5 units of RNase H were added to each of ~10-15 wells (each

well had a substrate with a unique χ and TGT length). The imaging chamber was then quickly mounted on the microscope and ~10 locations were found for each well. The acquisition was typically initiated within 8 minutes of adding the RNase H- and HPDM-containing rolling buffer, and images were acquired at ~3 minute intervals for 1 hr. To compensate for the increased fraction of immobilized HPDMs at the start of acquisition, HPDMs with a final displacement of $< 1\ \mu m$ were excluded from analysis. If fewer than 100 HPDMs survived this exclusion criteria for a given well, the 100 HPDMs with the largest final displacements were analyzed. As a control, this process was also repeated with 15 bp TGTs. Results are shown in **Figure 13**.

2.8.8 Automated HPDM detection and tracking for ensemble experiment:

Automated particle tracking was performed in MATLAB 2016a or later using a custom-written code according to a process shown in **Figure 5**, **Figure 6**, and **Figure 7**. Briefly, the Laplacian of an image was taken using MATLAB's del2() function, and a threshold cutoff (10x standard deviation of the Laplacian image) was applied to the Laplacian image to generate a mask. A rectangular region of interest (ROI) was drawn around each object in this mask. Each ROI was checked across all timepoints, and only ROIs with exactly one object in each timepoint were included for analysis. For each ROI, particle tracking was then performed by using a cross correlation-based image registration algorithm[95] to measure the relative shift between the first timepoint and each subsequent timepoint. To correct for location-specific stage drift, we exploited the fact that a fraction of HPDMs (~10-30%) exhibit no motion. Immobile HPDMs exhibit nearly-identical drift profiles, so we used a custom-written code to identify HPDMs with very similar trajectories and subtracted the average of these trajectories from the trajectory of each HPDM in the

location (**Figure 8**). The displacement vs. time curve, $r(t)$, of each HPDM was then calculated by calculating the displacement at each timepoint from the first timepoint. Finally, the mean displacement vs. time curve $R(t)$ for a given condition was calculated by averaging across all $r(t)$ curves collected from all locations within the well: $R(t) \equiv \langle r(t) \rangle$. The 95% confidence interval for each $R(t)$ measurement was calculated using bootstrapping with 10,000 iterations of MATLAB's bootci() function.

2.8.9 Prediction of average displacement vs. time curves using mass action model:

Mass action models for the 1-TGT, 2-TGT, and 3-TGT models, as well as a generalized N-TGT model scheme, are depicted in flow diagrams shown in **Figure 9**a, **Figure 8**, and **Figure 11**. An N-TGT model has $N + 1$ states that an HPDM can be in, and an HPDM in the i^{th} state is bound to $i - 1$ TGTs. The $(N + 1)^{th}$ state is an immobile state and all other states are mobile states. The fraction of HPDMs in each state was calculated for 30 minutes using Euler's method with a timestep of 0.0001 min. All HPDMs were initially in the 1^{st} state, and simulation parameters included a forward rate constant (k_1) of $\frac{\chi}{100\%} * (10^4\ \mathrm{min}^{-1})$, and a backward rate constant (k_2) of $25\ \mathrm{min}^{-1}$ (except for the $(N + 1)^{th}$ state which has a backward rate constant of 0 to denote irreversible stalling). The equations used to calculate the fraction of HPDMs in each state F_i (where i is an integer denoting the states 2 through $N - 2$ and <u>not</u> the imaginary number) are:

$$\frac{dF_1}{dt} = k_2 F_2 - k_1 F_1 \tag{1a}$$

$$\frac{dF_i}{dt} = k_1 F_{i-1} + k_2 i F_{i+1} - (k_1 + (i-1)k_2) F_i \tag{1b}$$

$$\frac{dF_N}{dt} = k_1 F_{N-1} - (k_1 + (N-1)k_2)F_i \quad (1c)$$

$$\frac{dF_{N+1}}{dt} = k_1 F_N \quad (1d)$$

where the i and $(i-1)$ multipliers in equation (1b) reflect the fact that HPDMs in the $(i+1)^{th}$ and i^{th} state are bound to i and $(i-1)$ TGTs, respectively, and each TGT is independently subject to stochastic rupture. $R(t)$ was also calculated using Euler's method, by integrating the derivative of the $R(t)$ curve when $\chi = 0$ multiplied by the fraction of HPDMs that are still mobile at time t:

$$\frac{dR(t)}{dt} = bAx^{b-1}(1 - F_{N+1}) \quad (2)$$

where b and A are best-fit parameters from the power-law fit ($y = Ax^b$) for the $\chi = 0$ curve (**Figure 10**a, $A = 0.97$ and $b = 0.46$) and F_{N+1} is the time-dependent fraction of HPDMs that are immobilized obtained from equation (1). We obtained best-fit χ_{50} values by linearly interpolating into simulated χ vs. $R(30\ min)$ curves at the point where $R(30\ min)$ is 50% of the $R(30\ min)$ value calculated when $\chi = 0$.

2.8.10 Parameter fitting to estimate $\boldsymbol{F_{HPDM}}$ and calculation of $\boldsymbol{T_{tol}}$**:**

Best-fit parameters and 95% confidence intervals were calculated using the "fit()" command in MATLAB 2016a or later. χ_{50} was calculated by fitting experimentally measured $R(t)$ vs. χ data to an exponential decay function:

$$R(T, \chi) = C \exp\left(-\frac{\ln(2)\,\chi}{\chi_{50}}\right) \quad (3)$$

where C is a user-specified scaling constant and T is the final time point (5.27 and 30 min, respectively, for the 15 bp TGT data presented in **Figure 9**; 3.5 and 1 hr, respectively, for the varying length TGT data shown in **Figure 13**) and χ_{50} is the only fit parameter. The best-fit N was calculated by substituting χ_{50} in equation (3) for $f_\chi(N)$, which is a linear interpolant function used to calculate χ_{50} directly from N according to the "N-TGT" simulation output (plotted in Fid. S9c,d). Finally, the best-fit F_{HPDM} was obtained using the approximation $F_{HPDM} = N * T_{tol}$ and substituting into equation (3):

$$R(T, \chi) = A \exp\left(-\frac{\ln(2)\,\chi}{f_\chi(\frac{F_{HPDM}}{T_{tol}})} \right) \quad (4).$$

where T_{tol} is defined as the magnitude of force which, when applied constantly to a duplex of known length for 1 s, has a 50% probability of rupturing the duplex[83]. T_{tol} was calculated using an equation presented by Mosayebi et. al. that simplifies to:

$$T_{tol} = \left(\frac{69.7M - 574.6}{M - 1}\right) pN \quad (5)$$

where M is the length of the TGT in base pairs. Using this equation, $T_{tol} = 48.7$, 33.6, 27.6, 19.2, and 6.6 pN for 25, 15, 13, 11, and 9 bp TGTs, respectively. For the 25 bp unzip-mode TGT, we used $T_{tol} = 12$ pN according to literature precedent[43].

2.8.11 Substrate preparation for single molecule imaging experiments

The gold film used for the ensemble experiments hinders single-molecule imaging by quenching and scattering emitted light and preventing TIRF. As such, we used a click chemistry-based surface functionalization process that does not require the gold film as

shown in **Figure 3e**. Glass slides were mounted in a teflon Wash-N-Dry slide rack (Sigma-Aldrich Z758108) and placed in a 150 mL beaker. The beaker was filled with water, sonicated for five minutes, and then emptied. This process was repeated, and then the beaker was filled with Piranha solution (a 3:1 mixture of 2M sulfuric acid and 70% hydrogen peroxide, CAUTION: Piranha solutions are VERY DANGEROUS) for 1 hr in order to expose silane surface groups. The slides were then rinsed with water, dried under a nitrogen stream, and aminated via a 2 hr incubation in ethanol with 3% v/v (3-aminopropyl)triethoxysilane (APTES). The amine-functionalized surfaces were then rinsed with ethanol, rinsed with water, dried under a nitrogen stream, and incubated at 60 °C in an oven for 20 minutes. The slides were then functionalized with azide groups by incubating for 2 hrs with 750 μL of 4.4 mM (10 mg/mL) azidobutyric acid NHS ester (Lumiprobe, #63720) in water with 10% w/v sodium bicarbonate. The slide and reaction chamber were then washed in water and dried. DNA strands were added to the surface by incubating with a click reaction mixture (732 μL of 1 M potassium phosphate monobasic, 8 μL of saturated ascorbic acid acqueous solution, 4 μL of 20 mM copper sulfate, 8 μL of 50 μM Tris(3-hydroxypropyltriazolylmethyl)amine (THPTA), 7.2 μL of 1 mM anchor DNA, and 0.8 μL of 1 mM biotin strand) for 4 hrs. The resulting surface, which is functionalized with 90% DNA anchor strands and 10% biotin strands, was then rinsed with water and attached to custom-made 30-well Delrin imaging chamber. Finally, RNA strands were added to the surface by adding 50 μL of 100 nM RNA fuel in 1xPBS to each well. The wells were then incubated at room temperature overnight to allow maximal hybridization, resulting in a final density of ~30,000 RNA strands/μm^2. Prior to imaging, each well was emptied with pipette aspiration and washed three times with 50 μL of 1xPBS.

2.8.12 Preparation of fluorescent streptavidin:

100 μg of streptavidin was suspended in 100 μL of 1xPBS and mixed with 1) 10 μL of 1 M sodium bicarbonate and then 2) a 5-fold molar excess of Alexa 647 (A647) NHS-ester dissolved in 10 μL of DMSO. The mixture was incubated for 10 minutes at room temperature on a rotary platform. Unreacted dye was removed via P4 gel filtration. Successful functionalization was verified using UV-vis spectroscopy.

2.8.13 HPDM preparation for single molecule imaging of TGT rupture:

HPDMs were prepared as described in "*HPDM Preparation for ensemble experiment*" but the DNA feet were replaced with extended DNA feet to enable increased complementarity. 1-2 μL of the HPDMs were incubated overnight in rolling buffer with 10 pM (for shear-mode TGTs) or 300 pM (for unzip-mode TGTs) 25 bp biotin-TGT strand (or 10 pM 15 bp biotin-TGT strand) in a total volume of 100 μL. These concentrations were found to be optimal because higher concentrations resulted in stalling but lower concentrations resulted in a lower frequency of TGT formation. The biotin-terminated TGT strands were then saturated with streptavidin by adding 11 μL of 100 nM streptavidin to achieve a final streptavidin concentration of ~10 nM (multiple orders of magnitude above the biotin-streptavidin dissociation constant). After a 1 hr incubation at room temperature, the HPDMs were washed five times in rolling buffer and incubated for two days at 4 °C to allow nonspecifically-bound streptavidin molecules and DNA strands to dissociate from the HPDMs. Finally, the HPDMs were washed twice in rolling buffer and suspended in a final volume of 100 μL. See **Figure 3c**.

2.8.14 HPDM preparation for single molecule imaging of biotin-streptavidin bond rupture:

HPDM were prepared as described in "*HPDM preparation for ensemble experiment*", but 0.03% or 0.01% of DNA feet were replaced with a biotin-terminated particle strand (both conditions were tested, and the two datasets were combined). This change was achieved by preparing the 5 μL saturated ascorbic acid solution with 30 nM or 100 nM biotin strand before adding it to the reaction vessel. HPDMs were then saturated with streptavidin and washed as described in "*HPDM preparation for single molecule imaging of TGT rupture*". See **Figure 3d**.

2.8.15 Single molecule imaging experiment:

Following washing of streptavidin-linked HPDMs, 5 units of RNase H were added to the 100 μL solution and the mixture was vortexed for ~10 s. 50 μL of the mixture was then added to a well. Multiple different conditions were tested in parallel. 50 locations with 1 or more HPDMs were located in each well. After at least 45 minutes of HPDM motion a multipoint, multichannel acquisition was initiated at 100x magnification with an additional 1.5x magnification lens. Three images were acquired at each location: one brightfield, one Cy3 TIRF image, and one A647 TIRF image.

2.8.16 Automated detection of single streptavidin molecules and measurement of colocalization with depletion tracks*:*

Streptavidin molecules and depletion tracks were automatically detected using a custom-written MATLAB code outlined in **Figure 15**. Briefly, HPDMs, depletion tracks, and

streptavidin molecules were automatically localized using rolling ball filtering and standard-deviation threshold cutoffs. Because HPDMs are coated with streptavidin molecules they produce substantial background that can skew analyses. To account for this, regions overlapping with HPDMs (detected in brightfield) were excluded from analysis. Locations with fewer than 100 pixels in depletion tracks were excluded from analysis to prevent data skewing.

2.8.17 Calculation of biotin-streptavidin rupture force:

The effective T_{tol} of the biotin-streptavidin bond was calculated using the Bell model[115], where the force (F)-dependent rupture rate (k_{rup}) is given by:

$$k_{rup} = k_0 \exp\left(\frac{F\, x_{tst}}{k_B T}\right) \tag{6}$$

where k_0 and x_{tst} (recently reported as $10^{-6}\ s^{-1}$ and 0.38 nm, respectively[116]) are the off-rate at zero-force and difference in extension between the bound-state and the transition state for separation, respectively. We then set $k_B T = 4.114$ pN nm and, using the definition of T_{tol} given in "*Parameter fitting to estimate* $\mathbf{F_{HPDM}}$ *and calculation of* $\mathbf{T_{tol}}$" (T_{tol} is the magnitude of force that has a 50% probability of rupturing a bond after 1 second), set $k_{rup} = \frac{\ln(2)}{1\ s}$ according to the relation between half-life and rate constant for an exponential decay process. We then solved for F to obtain $T_{tol} = 147$ pN.

2.8.18 Estimation of χ' for TGT-coated HPDMs:

First, a complementary biotin-terminated strand was incubated with the HPDMs in rolling buffer at a selected concentration (denoted [TGT]) overnight at room temperature on a

shaker. Fluorescent streptavidin was then incubated with the HPDMs at a concentration of 10 nM or $10 * [\mathrm{TGT}]$ (whichever is higher) for one hour in order to ensure that all available biotins were saturated with streptavidin. We then washed these HPDMs 7 times in rolling buffer and imaged them with brightfield and A647 fluorescence. We next used an automated MATLAB brightfield script to detect particles in brightfield and measure the average A647 intensity for at least 200 HPDMs per condition (**Figure 14**). Finally, we fit this average intensity vs. [TGT] data simultaneously to a pair of hyperbolic functions:

$$\mathrm{I_{shear}} = \frac{\mathrm{I_{max}}[\mathrm{TGT}]_{\mathrm{shear}}}{[\mathrm{TGT}]_{\mathrm{shear}} + \mathrm{K_D}} + 200 \tag{7a}$$

$$\mathrm{I_{unzip}} = \gamma \frac{\mathrm{I_{max}}[\mathrm{TGT}]_{\mathrm{unzip}}}{[\mathrm{TGT}]_{\mathrm{unzip}} + \mathrm{K_D}} + 200 \tag{7b}$$

where $\mathrm{K_D}$ is the dissociation constant for TGT strands binding to the HPDM (we assume it is the same for both the shear- and unzip-modes), 200 is the background signal of the camera, and $\gamma < 1$ is a constant. We included γ because we expected that biotin molecules on the unzip-mode TGT would be less accessible to streptavidin binding than the biotin molecules on the shear-mode TGTs because they are closer to the HPDM surface and hidden behind a layer of DNA. In other words, we assume that 100% of biotin molecules on shear-mode TGTs are available for streptavidin binding, but only a fraction (γ) of biotin molecules on unzip-mode TGTs are available.

We performed two separate experiments. For this first experiment, we obtained best-fit parameters of $\mathrm{I_{max}} = 2{,}200$, $\mathrm{K_D} = 9\ \mathrm{nM}$, and $\gamma = 0.42$, and for the second

experiment, we obtained best-fit parameters of $I_{max} = 1{,}500$, $K_D = 4$ nM, and $\gamma = 0.53$. As such, we chose to use $K_D = 6$ nM and $\gamma = 0.5$ for our calculations, which are given by

$$\chi'_{shear} = \frac{[TGT]_{shear}}{[TGT]_{shear} + 6\ \text{nM}} \tag{8a}$$

$$\chi'_{unzip} = \frac{[TGT]_{unzip}}{2\left([TGT]_{unzip} + 6\ \text{nM}\right)} \tag{8b}.$$

Table 1: Oligonucleotide Sequences

Name	Sequence (5'-3')
Anchor (for gold)	/5AmMC6/*GAGAGAGATGGGTGC*TTTTTTTTTTTTTTT/3ThiolMC3-D/
RNA Fuel	*GCACCCATCTCTCTC*rCrCrCrCrC**rCrUrGrUrGrArUrUrGrArUrUrArCrU**/3Cy3Sp/
DNA Foot	/5Hexynyl/TTTTTTTTTTTTTTT**AGTAATCAATCACAG**
15 bp TGT strand	*GCACCCATCTCTCTC*CCCCCCTGTGATTGATTACT/36-FAM/
13 bp TGT strand	*GCACCCATCTCTCTC*CCCCCCTGTGATTGATTATC
11 bp TGT strand	*GCACCCATCTCTCTC*CCCCCCTGTGATTGATATTC
9 bp TGT strand	*GCACCCATCTCTCTC*CCCCCCTGTGATTGTTATTC
Extended DNA foot	/5Hexynyl/TTTTTTTTTTTTTTTTAGTAATCAATCACAGGAATGACTG
25 bp biotin-TGT (shear-mode)	/5Biosg/CAGTCATTCCTGTGATTGATTACTA
25 bp biotin-TGT (unzip-mode)	CAGTCATTCCTGTGATTGATTACTA/3Bio/
15 bp biotin-TGT	/5Biosg/CAGTCATTCCTGTGA
Anchor (for glass)	/5AmMC6/*GAGAGAGATGGGTGC*TTTTTTTTTTTTTTT/35OctdU/
Biotin strand	/5Biosg/TTCTACTTCTACTTCTTCTACTACTACTAC/35OctdU/

Italicized bases denote anchor-binding regions, **bold** bases denote foot-fuel binding regions, underlined bases denote foot-TGT binding regions.

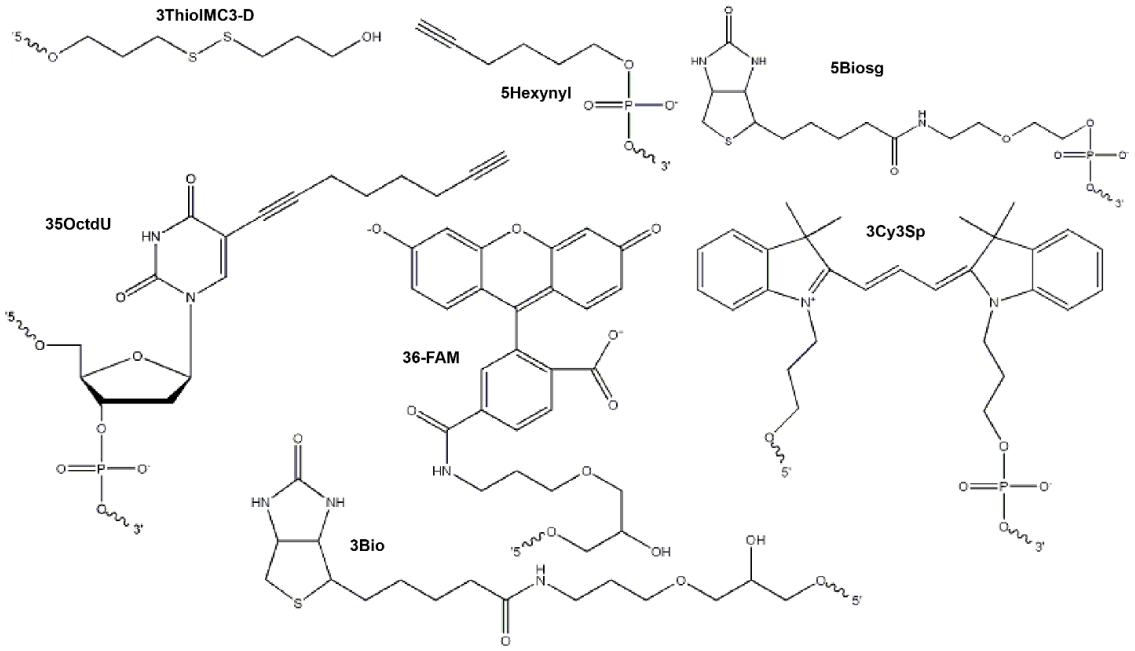

Figure 28: Oligonucleotide modifications

This figure shows the chemical structures of modifications listed in **Table 1**.

2.9 Supplemental Note 1 – Calculation of RNA fuel exchange rate

The exchange rate of RNA fuel strands is the product of the four parameters measured in ref. [29].

1) the surface density of RNA fuel strands (50,000 strands/μm^2).

2) the average particle velocity (~1 $\mu m/min$).

3) the depletion track width (~400 nm).

4) the percent of RNA that is depleted from the depletion track (~50%).

Taking the product of these four parameters yields:

$$\left(50{,}000\,\frac{\text{strands}}{\mu m^2}\right)\left(1\,\frac{\mu m}{\text{min}}\right)(0.5)(0.4\ \mu m) = 10{,}000\,\frac{\text{strands}}{\text{min}} \tag{9}$$

While these parameter estimates are only approximate, we note that the conclusions of this work are insensitive to the exchange rate of $10{,}000\,\frac{\text{strands}}{\text{min}}$ across at least an order of magnitude (data not shown).

2.10 Supplemental Note 2 – Justification of the approximation $F_{HPDM} = T_{tol}N$

Intermolecular bond rupture is a thermally-activated, time-dependent stochastic process. As such, the typical rupture force of a given intermolecular interaction depends on the timescale over which tension is applied and/or the loading rate of the applied force. Accordingly, the use of T_{tol}, which is defined in this work as the constantly-applied force that has a 50% probability of rupturing a bond after 1 second, is not always appropriate in all contexts. However, we use mathematical models in this supplemental note to argue that T_{tol} is a good approximation for the actual force at which bonds are ruptured by HPDMs. By extension of this argument, we argue that $F_{HPDM} = T_{tol} * N$ is a reasonable approximation for the actual stall force of an HPDM.

The rate of bond rupture (k_{rup}) can be approximated using the Bell model[4] (see methods), in which k_{rup} increases exponentially with the force applied to the bond. The force applied to a tether can be approximated using the worm-like-chain model, which relates the entropic force on a polymer chain to the end-to-end extension of the chain. To calculate the extension of a tether as a function of time (t), we consider a simplified abstraction of an HPDM that consists of a circle of diameter D rolling on a one-dimensional substrate. The bottom of the circle is always in contact with the substrate, and we consider a single tether formed at this point of contact at $t = 0$. The circle rolls forward with velocity v without slip, such that the end-to-end extension of the tether (d) is described by the equation:

$$d = \sqrt{\left(v * t - \frac{D}{2} * \sin\left(v * t * \frac{2}{D}\right)\right)^2 + \left(\frac{D}{2} - \frac{D}{2}\cos\left(v * t * \frac{2}{D}\right)\right)^2} \qquad (10)$$

The relationship between d and force, F, experienced by a polymer chain with persistence length P and contour length L_0 can be calculated with <1% error using the worm-like-chain (WLC) approximation developed by Petrosyan[32]:

$$d_{WLC}(F, L_0, P) = L_0 \left(\frac{4}{3} + \frac{4}{3\sqrt{\frac{FP}{k_B T}} + 1} - \frac{10 e^{\sqrt[4]{900 \frac{k_B T}{FP}}}}{\sqrt{\frac{FP}{k_B T}} \left(e^{\sqrt[4]{900 \frac{k_B T}{FP}}} - 1 \right)^2} + \frac{\left(\frac{FP}{k_B T} \right)^{1.62}}{3.55 + 3.8 \left(\frac{FP}{k_B T} \right)^{2.2}} \right) \quad (11)$$

where $k_B T = 4.114$ pN nm is the Boltzmann constant at room temperature. A TGT tether is composed of both double stranded DNA (dsDNA) and single stranded DNA (ssDNA). P and L_0 are 53 nm and $n * 0.34$ nm, respectively, for dsDNA (where n is the number of double-stranded basepairs), and 1.07 nm and $m * 0.60$ nm, respectively, for ssDNA (where m is the number of single stranded nucleotides). Therefore, the relationship between F and d for a tether composed of both ssDNA and dsDNA can be calculated using the equation:

$$d = d_{WLC}(F, n * 0.34 \text{ nm}, 53 \text{ nm}) + d_{WLC}(F, m * 0.60 \text{ nm}, 1.07 \text{ nm}) \quad (12)$$

The inverse of this function can then be used to calculate F as a function of d, meaning that F can be calculated as a function of t. Next, we use a variant of the Bell model developed by Moyosabi et. al.[3] to calculate k_{rup} as a function of F (and therefore as a function of t) that simplifies to:

$$k_{rup} = (6.86 * 10^7 s^{-1}) \exp\left(-(M - 1) \left(2.53 - (0.15 \text{ nm}) * \frac{F}{k_B T} \right) \right) \quad (13)$$

where M is the length of the TGT's double stranded region in units of basepairs. Using a kinetic theory-based framework, duplex rupture is a stochastic process that becomes more

rapid with increasing t due to the positive relationship between k_{rup} and t. We therefore consider an ensemble of circles rolling on an ensemble of one-dimensional substrates and used Euler's method to calculate the fraction of TGTs remaining bound as a function of time. We then calculated the most probable rupture force and repeated these calculations for a range of velocity values spanning five orders of magnitude centered on the typical velocity of 1 $\frac{\mu m}{min}$ using $D = 5\ \mu m$ for TGTs 9, 11, 13, and 15 bp in length. Because each TGT contains three ssDNA spacers (two of them 15 nucleotides in length and one of them 5 nucleotides in length) as well as a 15 bp dsDNA anchor region and a M-dependant TGT binding region, we used $n = 50 - M$ and $m = 15 + M$.

Our results, summarized in **Figure 29**, show that the most probable rupture force at $v = 1\ \mu m/min$ is quite similar to T_{tol} for the 15 bp TGT (38.0 pN compared to $T_{tol} = 33.6$ pN), 13 bp TGT (31.9 pN compared to $T_{tol} = 27.6$ pN), and 11 bp TGT (22.7 pN compared to $T_{tol} = 19.2$ pN), corresponding to relative errors of 12.3%, 14.5%, and 16.7%, respectively. According to these calculations, T_{tol} should accurately reflect the typical rupture force of TGTs in the context of HPDM-induced rupture. These calculations also suggest that T_{tol} underreports TGT rupture force, which would suggest that the approximation of $F_{HPDM} = N * T_{tol}$ under-estimates (rather than over-estimates) F_{HPDM}. Furthermore, our results show that rupture force is relatively insensitive to v across five orders of magnitude; fitting the most probable rupture force vs. v curves to the form $y=a*\log_{10}(x)+b$, revealed that the most probable rupture force only changes by roughly 4.6 pN, 5.6 pN, and 8.0 pN per order of magnitude change in velocity for 15, 13, and 11 bp TGTs, respectively. For example, the most probable rupture force for the 15 bp TGT increased from 38.0 pN to 42.7 pN when increasing v 10-fold to 10 $\mu m/min$ and decreased

to 33.4 pN when decreasing v 10-fold to $0.1\ \mu m/min$. As such, T_{tol} serves as a reasonable approximation across the entire range of expected HPDM velocities for the 15, 13, and 11 bp TGTs that our F_{HPDM} estimates are based on. Our results also indicate that 9 bp TGTs spontaneously denature due to thermal fluctuations before HPDMs can stress them to pN-scale force magnitudes, which is consistent with our findings that HPDMs continue rolling substantially on 9-bp TGT surfaces with $\chi = 1\%$ (**Figure 13**e,h).

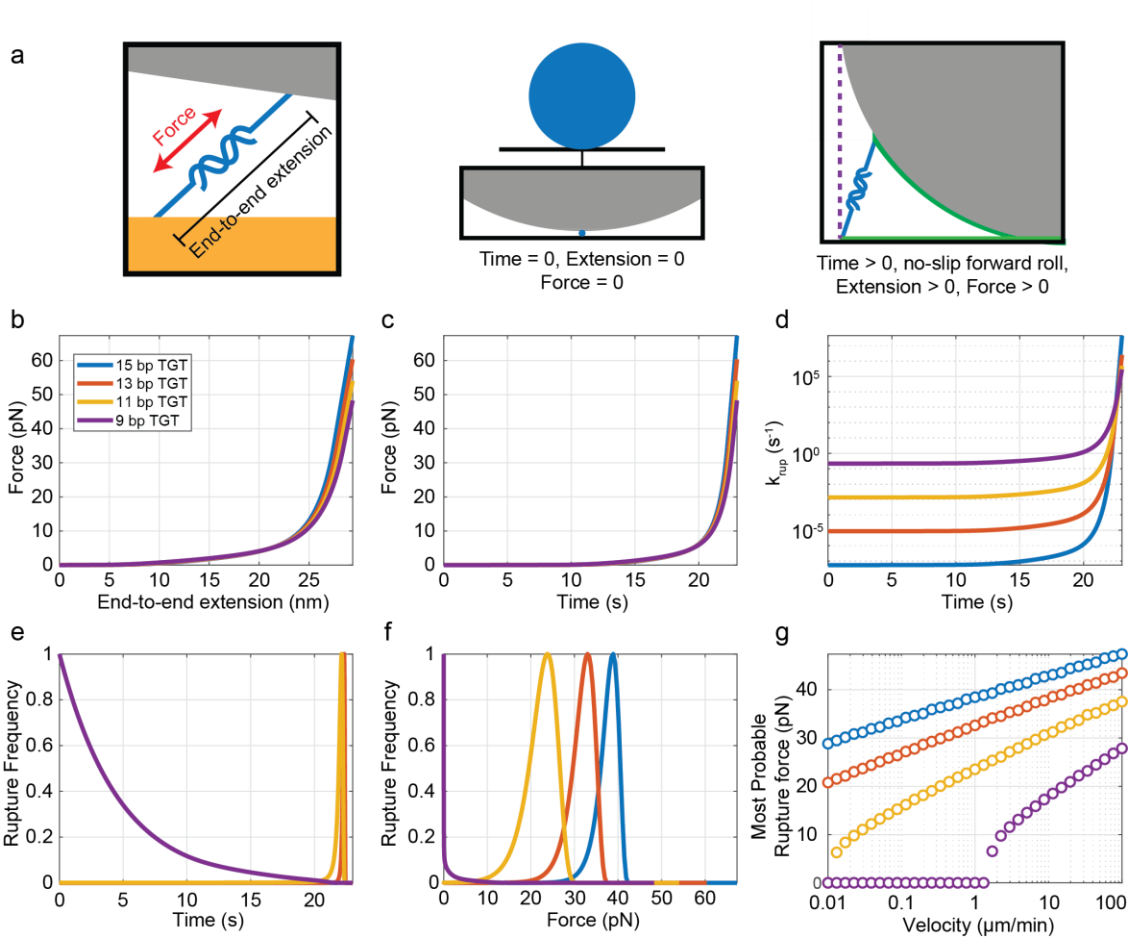

Figure 29: Time dependence of duplex rupture

a) Cartoon illustration of the relationship between TGT end-to-end extension and force (left) and the simulation method used to verify that T_{tol} is an accurate representation of the true rupture force of TGTs in this work (middle and right). A simulated HPDM at time=0 is shown (middle) bound to a TGT with an extension of zero. The HPDM then rolls forward and, in doing so, extends the TGT (right) until the point of rupture. **b)** Force-extension curves of 9 (blue), 11 (orange), 13 (yellow), and 15 bp (purple) TGTs calculated using the worm-like chain model (see "**Supplemental Note 2 – Justification of the approximation $\mathbf{F_{HPDM} = T_{tol}N}$**" for details). **c)** TGT force as a function of simulation time when assuming zero extension at $t = 0$ and no-slip forward rolling at a transverse velocity of $v = 1\ \mu m/s$.

d) Off rate (k_{rup}) as a function of time, as calculated using curves shown in **b** and **c** and the Bell model (see "**Supplemental Note 2 – Justification of the approximation $F_{HPDM} = T_{tol}N$**" for details). **e)** Normalized probability functions showing TGT rupture frequency as a function of time according to our simulations. While rupture occurs predominantly at early timepoints for the 9 bp TGT due to low stability, rupture for the 11, 13, and 15 bp TGTs all occur within a narrow time-window near 22 seconds **f)** Same as in **d**, but with rupture frequency shown as a function of force rather than time. TGT rupture occurs at low force for the 9 bp TGT, but longer TGTs rupture within a narrow force range far from zero. The most probable rupture forces (corresponding to the peak positions of the curves) for the 11, 13, and 15 bp TGTs are all quite similar to their respective T_{tol} calculations (see "**Supplemental Note 2 – Justification of the approximation $F_{HPDM} = T_{tol}N$**" for a quantitative comparison). **g)** The most probable rupture force as a function of HPDM velocity, varying across five orders of magnitude. For 11, 13, and 15 bp TGTs bond rupture is weakly dependent on HPDM rolling velocity, which demonstrates that the T_{tol} is an accurate metric for true rupture force regardless of the selected velocity parameter.

2.11 Supplemental Note 3 – multiple TGTs must form within a short time span to contribute cooperatively towards HPDM stalling

In our N-TGT simulation models we assume that TGTs are ruptured at a rate of $k_2 = 25\ \text{min}^{-1} = 0.4\ \text{s}^{-1}$, which is the experimentally measured maximum RNase H-mediated cleavage rate[29]. However, in "**Supplemental Note 2 – Justification of the approximation $\mathbf{F_{HPDM} = T_{tol}N}$**" we showed that it should take an HPDM somewhere near ~22-23 seconds to extend a TGT to the point of rupture, which is much longer than $(k_2)^{-1} = 2.5\ \text{s}^{1}$. Here we argue that, while this estimate is likely an overestimate of the true rupture rate, it should not be problematic when used in our N-TGT models because it and $k_1\chi$ (which we use to estimate the rate of TGT formation) should be accurate representations of the rate of exit and entry of TGTs out of and into what we call the "force regime of cooperativity".

In "**Supplemental Note 2 – Justification of the approximation $\mathbf{F_{HPDM} = T_{tol}N}$**" we showed that the force on a TGT due to HPDM translocation at $v = 1\frac{\mu m}{s}$ is likely low for the majority of the TGT's bound lifetime and then spikes abruptly and induces rupture within a short timescale roughly 20 seconds after tether formation. For example, the force on a simulated 15 bp tether 20 seconds after tether formation is only 6.1 pN, but in the following two seconds the force spikes to 26.5 pN. After one additional second, the force is 67.3 pN, well above $T_{tol} = 34$ pN. Therefore, our simulations show that bond rupture occurs almost entirely within a short time regime and that the force on a TGT is very low before this regime is reached; 99.8% of 15 bp TGT rupture occurs between 21.9 s and 22.4 s, while 99.8% of 13 bp TGT rupture occurs from $t = 21.2$ s to $t = 22.4$ s and 95% of 11 bp TGT rupture occurs from $t = 19.7$ s to $t = 22.3$ s.

Because our N-TGT models are intended to predict the number of TGTs that are required to stall an HPDM, we argue that it is important to consider the relative timing between TGT formation events; if two TGTs form ten seconds apart in time, then one of them will be extended and rupture before the other has even reach $F = 1$ pN and, as such, the two TGTs will not act cooperatively and the peak resistive force experienced by the HPDM will be $\sim T_{tol} + 1$ pN. However, if two TGTs form simultaneously they will be extended and ruptured together, and the peak resistive force experienced by the HPDM will be $\sim 2T_{tol}$. Viewed another way, TGTs can only contribute to stalling the HPDM when they are sufficiently extended to a high-force regime, which we call the force-regime of cooperativity. While we initially defined $k_1\chi$ as the rate of TGT formation, if we assume that no TGT rupture occurs before entry into the regime of cooperativity then $k_1\chi$ is also equivalent to the rate at which TGTs enter into the force-regime of cooperativity. Using this definition, the use of $k_2 = 0.4\ s^{-1} = (2.5\ s)^{-1}$ becomes more reasonable because it accurately reflects the rate at which TGTs will leave the regime of cooperativity. For example, if we define the regime of cooperativity as the force regime where $F \geq 5.6$ pN, then 50% of bond rupture will occur within ~2.5 seconds for a 25 bp TGT. Of course, the models used in discussion are limited in their ability to represent true scenarios, but they help show that our use of $k_2 = 0.4\ s^{-1}$ is moderately reasonable based on the information we have.

2.12 Supplemental Note 4 – Calculation of power conversion efficiency

In supplementary discussion 2 of our previous work (ref. [29]), we estimated the power conversion efficiency (η) of HPDMs by taking the ratio of the mechanical power output ($P_{mechanical}$) and the chemical power input ($P_{chemical}$):

$$\eta = \frac{P_{mechanical}}{P_{chemical}} \tag{14}$$

For the latter, we used

$$P_{chemical} = k_1 * \Delta G_{clvg} * n_{clvg} \tag{15}$$

where $k_1 = 10^4\ min^{-1}$ is the consumption rate of RNA fuel strands, $\Delta G_{clvg} = 30 \frac{kcal}{mol} = 209.1$ pN nm is the energy released from RNase H-mediated cleavage of a phosphodiester bond in an RNA strand's backbone, and n_{clvg} is an integer between 1 and 14, which denotes the fact that the RNA strand in the DNA-RNA region of a tether has 14 phosphodiester bonds, all of which are susceptible to cleavage. As such, $P_{chemical}$ ranges from $2.1 * 10^6 \frac{pN\ nm}{min}$ when $n_{clvg} = 1$ to $29.3 * 10^6 \frac{pN\ nm}{min}$ when $n_{clvg} = 14$. To estimate $P_{mechanical}$, we originally used

$$P_{mechancial} = F_{drag} * v \tag{16}$$

where $F_{drag} \approx .02$ pN is the drag force experienced by a 5 μm-wide sphere undergoing Brownian motion, and $v = 1 \frac{\mu m}{min}$ is the typical velocity of an HPDM. This yielded η in the range of 10^{-6} to 10^{-5}. However, in this work we show that $F_{HPDM} \approx 150$ pN. As such, when replacing F_{drag} with F_{HPDM}, we obtain:

$$P_{mechanical} = F_{HPDM} * v \quad (17)$$

we obtain $P_{mechanical} = 1.5 * 10^5 \frac{pN\ nm}{min}$. Using this updated estimate, we find that $\eta = 7.2\%$ when $n_{clvg} = 1$ and $\eta = 0.5\%$ when $n_{clvg} = 14$. While the true value of n_{clvg} is unknown, we estimated n_{clvg} using a Monte Carlo simulation method that applies stochastic cleavages to the phosphodiester backbone of a simulated tether and discards segments shorter than a set cutoff length until the tether is fully dissociated (**Figure 29**). Because the 9 bp TGT showed minimal capacity to stall HPDMs (**Figure 13e,h**), we used 10 bp as the cutoff length and found that, on average, $n_{clvg} \approx 2$. While it is unlikely that v remains constant regardless of F (v should reduce to zero as F approached the 157 pN stall force), we note that our calculation of η is independent of v because $P_{mechanical}$ depends linearly on v and $P_{chemical}$ depends linearly on k_1, which also depends linearly on v (**Supplemental Note 1 – Calculation of RNA fuel exchange rate**).

As a final note, these calculations depend on the geometry of rolling; these calculations were performed using v of the particle translocation. However, it may be more accurate to use the speed of tether extension along. The relationship between v and tether extension speed depends on the extent to which the HPDM rolls as it translocates. If the HPDM does not roll, then tether extension velocity is very similar to translation velocity. However, if the HPDM rolls with no slip, then tether extension is much slower (100-10x slower) and is applied nearly perpendicular to the surface. Based on simulations (data to be shown in forthcoming publications), we estimate that the angular velocity is roughly 1/3rd of the translation velocity. If this prediction is true, then tether extension occurs at roughly 2/3rd the speed of HPDM translation and η should be reduced by a factor of 1/3.

2.13 Supplemental Note 5 – Effect of polyvalency on HPDM mobility

As outlined in the main text, HPDM motion can be described using a burnt-bridge Brownian ratchet (BBBR) mechanism. In other words, motion of the HPDM is driven by Brownian fluctuations that are "ratcheted" by the formation and destruction of tethers. However, there are two types of thermal fluctuations that contribute to HPDM motion: Brownian motion of the microparticle body, and thermal fluctuations of the DNA and RNA oligonucleotides. In this note, we conduct a theoretical examination of the effect of polyvalency on the relative contributions of these two types of Brownian fluctuations. We start by examining the effect of polyvalency on Brownian motion of the microparticle body. We then quantify the expected effect of thermal fluctuations of the DNA and RNA oligonucleotides. Finally, we quantitatively examine the relative contributions of these two types of fluctuations as a function of polyvalency.

Because the microparticle body is rigid, movement of the HPDM body requires extension of many tethers at once. As such, the Brownian motion of the microparticle body depends on the amount of energy required to extend the bound tethers. The energy associated with tether extension can be quantified using the WLC model as described in "**Supplemental Note 2 – Justification of the approximation $\mathbf{F_{HPDM} = T_{tol}N}$**"; the energy associated with extending a tether (G_{teth}) by distance δ can be calculated by taking the integral of the tether's force-extension curve. As stated in "**Supplemental Note 2 – Justification of the approximation $\mathbf{F_{HPDM} = T_{tol}N}$**", the force-extension curve can be calculated by taking a weighted average of the WLC force (F)-extension curves calculated for the different segments within the tether. A DNA-RNA tether contains 30 ssDNA nucleotides, 5 ssRNA nucleotides, 15 dsDNA base pairs, and 15 DNA-RNA hybrid base pairs. Each of these four

polymer types can be accurately approximated using the WLC model using different parameters[117,118]. As such, the force extension curve can be calculated using an analog of equation (12), which depends on equation (11):

$$\delta = d_{WLC}(F, 15 * 0.34\ \text{nm}, 53\ \text{nm}) + d_{WLC}(F, 30 * 0.60\ \text{nm}, 1.07\ \text{nm}) + d_{WLC}(F, 5 * 0.67\ \text{nm}, 0.75\ \text{nm}) + d_{WLC}(F, 15 * 0.33\ \text{nm}, 100\ \text{nm}) \quad (18)$$

and the energy, in units of $pN * nm$ can be calculated by integrating F with respect to extension from 0 to δ:

$$G_{teth} = \int_0^{\delta} F(\delta')\, d\delta' \quad (19)$$

where δ' is an integration variable and $F(\delta')$ in this context is used to show that F is a function of δ' that is the inverse of equation (18). The energy landscape (e.g., energy as a function of x, y, and z) of an HPDM bound to one tether can thus be calculated by assuming that the energetic minimum occurs at the origin, where d_{teth}=x=y=z=0 (**Figure 21**a, left). The probability density, which is proportional to the amount of time that the HPDM spends at each position, can also be calculated as exp(-G_{teth}) (**Figure 21**b, left). These landscapes show that, when only bound to 1 tether, an HPDM can diffuse freely within a region 10s of nm wide. We can quantify the mobility using $\langle\delta\rangle$, which we define as the average distance of the HPDM from the origin, using the Boltzmann relation:

$$\langle\delta\rangle = \frac{\int_0^{\infty} \delta * (2\pi\delta^2) * \exp\left(-\frac{G_{teth}}{k_B T}\right) d\delta}{\int_0^{\infty} (2\pi\delta^2) * \exp\left(-\frac{G_{teth}}{k_B T}\right) d\delta} \quad (20)$$

where the relation $2\pi\delta^2$ reflects the surface area-radius relationship of a hemisphere and $k_BT = 4.114$ pN nm is the Boltzmann constant at room temperature. Performing this calculation with numerical integration, we find $\langle\delta\rangle = 10.9$ nm when the HPDM is bound to 1 tether. In reality, the HPDM is likely bound to 100s or 1,000s of tethers simultaneously at any given point in time. To understand how HPDM mobility changes as a function of the number of tethers (N_{teth} – also referred to here as "polyvalency"), we start by assuming that the extension of each tether is zero at the origin and HPDM motion results in extension of all tethers simultaneously. Setting $N_{teth} = 400$ (which is the minimum polyvalency that could be expected with a RNA fuel consumption rate of 10^4 min^{-1} and $k_{cat} = 25min^{-1}$, i.e. $10^4/25 = 400$) and calculating the energy landscape where $G = G_{teth}N_{teth}$ reveals a sharply increasing energy landscape (**Figure 21**a, right) with diffusion that is restricted to a region that is only a few nm wide (**Figure 21**b, right). To quantify the relationship between N_{teth} and mobility, we introduce a slight modification to equation (20):

$$\langle\delta\rangle = \frac{\int_0^\infty \delta * (2\pi\delta^2) * \exp\left(-\frac{N_{teth}G_{teth}}{k_BT}\right) d\delta}{\int_0^\infty (2\pi\delta^2) * \exp\left(-\frac{N_{teth}G_{teth}}{k_BT}\right) d\delta} \quad (21)$$

Running this calculation with N_{teth} values ranging from 1 to 1,000 reveals a monotonic decrease in the mobility of the HPDM, wherein $\langle\delta\rangle \propto N_{teth}^{-0.2}$ (**Figure 21**c). When $N_{teth} = 400$, $\langle\delta\rangle = 1.8$ nm. We note that for these calculations we assumed that all tethers have an extension of zero at the energetic minimum of x=y=z=0. However, in reality this is not the case and almost all tethers will have a nonzero extension. Because F is a convex function with respect to δ, accounting for heterogeneity in tether extension should cause G to

increase in an even steeper manner than we have represented here. As such, our estimate for $\langle\delta\rangle$ should represent an upper-bound for $N_{teth} > 1$.

Next, we consider Brownian fluctuations of unpaired oligonucleotides. In contrast to the microparticle body, single-stranded oligonucleotides are highly flexible, and the atoms that constitute these molecules undergo substantial Brownian fluctuations that do not depend on the mobility of the microparticle body. Brownian fluctuations of the oligonucleotides allow pairs of RNA fuel and DNA feet to stretch out and hybridize to each other even when they are not immediately next to each other. In other words, the association rate of a foot-fuel pair depends on the distance between the two strands and is related to the energy required to stretch the strands to a point where they can hybridize with each other. This distance-dependent energy relationship can also be calculated from the force-extension curve using the WLC model with a slightly modified version of equation 18 wherein the WLC parameters for the DNA-RNA duplex are replaced with parameters that are specific to the transition state of DNA-RNA hybridization[118]:

$$\delta_{tst} = d_{WLC}(F_{tst}, 15 * 0.34\ \text{nm}, 53\ \text{nm}) + d_{WLC}(F_{tst}, 30 * 0.60\ \text{nm}, 1.07\ \text{nm}) + d_{WLC}(F_{tst}, 5 * 0.67\ \text{nm}, 0.75\ \text{nm}) + d_{WLC}(F_{tst}, 15 * 0.53\ \text{nm}, 2.7\ \text{nm}) \quad (22)$$

the association rate (k_{on}) will then be related to the energy of the transition state for hybridization (G_{tst}), which can be calculated using an equation similar to equation (19):

$$G_{tst} = \int_0^{\delta_{tst}} F_{tst}(\delta')\, d\delta' \quad (23)$$

Our calculation for k_{on} is thus:

$$k_{on} = k_{on,0} \exp\left(-\frac{G_{tst}}{k_B T}\right) \quad (24)$$

where $k_{on,0}$ is the association rate when there is no separation between the strands. Without knowing $k_{on,0}$, we can estimate the binding cutoff (δ_c) as the distance where $k_{on} = \frac{k_{on,0}}{2}$ (e.g., where $\exp\left(-\frac{G_{tst}}{k_B T}\right) = 0.5$). **Figure 21**d shows our calculation of the normalized association rate ($\frac{k_{on}}{k_{on,0}}$) vs. δ and shows that $\delta = 10$ nm. At δ_{tst} =15 nm, $k_{on} = \frac{k_{on,0}}{10}$. At $\delta_{tst} = 20$ nm, $k_{on} \approx 0$. In other words, thermal fluctuations of the tether contribute meaningfully to HPDM motion within a length regime below ~10-20 nm. This length scale is comparable to the Brownian diffusion radius of the HPDM at low polyvalency, but is several times larger than the Brownian diffusion radius of the HPDM at high polyvalency.

As a means of roughly quantifying the relative contributions of the two types of Brownian motion, we define the "coverage area" as $\pi(\langle\delta\rangle + \delta_c)^2$. This quantity is roughly equivalent to the area of the substrate that a single DNA foot can access for strand hybridization via the combined Brownian fluctuations of the microparticle body and the oligonucleotides. With $\delta_c = 10$ nm, the coverage area is 1,372 nm^2 and 437 nm^2 for $N_{teth} = 1$ and $N_{teth} = 400$, respectively. Finally, we calculate the coverage area fold-enhancement as $\frac{(\langle\delta\rangle+\delta_c)^2}{\delta_c^2}$, which is a metric that quantifies the increase in coverage area that results from accounting for Brownian diffusion of the microparticle body of the HPDM. When the area coverage fold-enhancement is equal to 2, the two types of Brownian motion contribute equally. This fold-enhancement is 4.4 and 1.4 at $N_{teth} = 1$ and $N_{teth} = 400$, respectively. Calculating the area coverage fold-enhancement with N_{teth} ranging from 1 to ~3,000 reveals a

"crossover polyvalency" of 50 tethers at which the fold-enhancement is equal to 2 (**Figure 21**e). In other words, Brownian diffusion of the microparticle body is dominant below a polyvalency of 50 tethers and Brownian diffusion of the oligonucleotides is dominant above a polyvalency of 50 tethers. Because HPDMs are expected to be bound to 100s or 1,000s of tethers simultaneously, we thus conclude that HPDM motion is predominantly driven by thermal fluctuations of the oligonucleotides, rather than Brownian motion of the microparticle body.

Note that if we use $\delta_c = 15$ nm, the crossover polyvalency decreases to 12. Furthermore, as stated above $\langle\delta\rangle$ is likely an over-estimation and, as such, the contribution of Brownian fluctuations of the microparticle is likely even lower then reported here. We also note that these calculations do not account for many factors such as gravity, surface-surface interactions, molecular crowding, and limitations of the WLC model at low extensions. Nonetheless, we conclude that a soft crossover occurs from conventional BBBR motion (where random diffusion of the cargo dominates) to an autochemophoretic variant of BBBR motion when polyvalency is on the order of 10s of tethers.

CHAPTER 3. PROPERTIES OF HIGHLY POLYVALENT DNA MOTORS REVEALED WITH ADHESIVE DYNAMICS SIMULATIONS

This chapter is a (first author) manuscript that is in preparation. This work builds on the HPDM work discussed in the previous chapter.

3.1 Introduction to adhesive dynamics

To understand the mechanism of force generation, we developed RoloSim, a simulation package used to simulate autochemophoretic HPDM translocation. RoloSim can be described as a type of adhesive dynamics[119] (AD) simulation.

AD has been used to simulate the adhesive and/or transport properties of nanoscale biological adhesion structures[120,121] and whole cells[122] interacting with boundaries through specific receptor ligand interactions. AD-like simulations have also been used extensively to study the transport properties of multi-legged burnt bridge molecular motors[77-79,123-127], and the autochemophoretic bacterial partition system [99,108].

In AD, a "body" (such as a cell, plasma membrane, a colloidal particle, or an infinitesimal point) is decorated with multiple adhesive molecules. The body is close to a surface that itself is decorated with a second type of adhesive molecule. We can call these two types of molecule B (adhesive molecule on the body) and S (adhesive molecules on the surface). The two types of molecule interact with each other to form tethers (SB). Each tether then

acts as a spring that exerts force on the body such that the position and orientation of the body are controlled by the set of tethers that are bound to it.

Generally, AD is the recursive iteration of two steps:

1) **Apply stochastic changes:** tethers are formed and degraded using the kinetic Monte Carlo method with kinetic rate constants k_{on} and k_{off}. In the kinetic Monte Carlo method, the probability, p, of a single event with kinetic rate constant k occurring within a timestep of duration Δt is equal to $p = 1 - \exp(-k\,\Delta t)$. Generally, k_{on} is negatively correlated with the distance, d, between S and B such that pairs that are closer together are more likely to associate than pairs that are farther away. Similarly, k_{off} may also depend on the tether's end-to-end extension, r, to reflect force-induced rupture. In the case of burnt-bridge motor modeling, k_{off} has an extension-independent, constant component that reflects irreversible "consumption" of the S species. Following consumption, these "burnt" molecules can no longer form new tethers (although in some cases, burnt molecules can undergo time-dependent regeneration[99,108]).

2) **Calculate new energetic minimum of the system** – the position and orientation of the body (and, in some cases, deformation of the body and surface) are then calculated using energy minimization methods. Energy, E, can be broken up into two terms:

$$E = E_{sys} + \sum_{i=1}^{N} E_{teth,i}$$

Where $E_{teth,i}$ represents the mechanical strain energy of the i^{th} tether, N is the number of tethers, and E_{sys} encompasses all other energetic terms of the system that can include 1)

gravity, 2) body-surface repulsion, 3) externally-applied biasing forces, and 4) strain energy terms that govern deformation of the body and/or surface. In some cases, random thermal energy terms may be added in to reflect tethered Brownian motion of the body. The energetic minimum of the system may have an analytic solution (generally true when tethers are modeled as linear springs), but numerical methods (e.g. gradient descent) can be used when an analytical form is not available. RoloSim adheres to this AD framework.

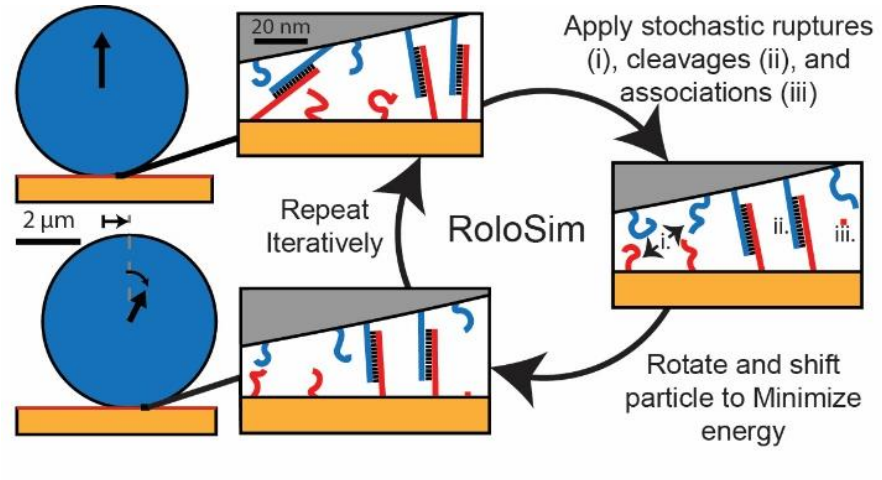

Figure 30: Schematic depiction of the iterative RoloSim simulation method.

The simulation method is an iterative process which alternates between 1) calculating distance dependent rate constants and stochastically associations, cleavages, and ruptures, and 2) minimize the system's spring potential energy via rigid body motion.

3.2 Description of RoloSim

In this section, we describe the simulation method and the mathematical relationships that we used to model the tethers. Generally, parameter quantities may not be discussed until the "optimizing RoloSim" subsection.

3.2.1 Overview

In RoloSim, DNA strands are randomly scaffolded on a microsphere at the previously measured density of $91{,}000\,\frac{strands}{\mu m^2}$ and RNA fuel strands are randomly patterned on an underlying planar surface (which we call the "substrate") at a density of $50{,}000\,\frac{strands}{\mu m^2}$. Specific hybridization interactions between the particle-bound DNA and the surface-bound RNA form "molecular tethers", each of which exerts an extension (r)-dependent force on the microsphere. Every single strand is explicitly modeled, such that the simulated HPDM acts as a "virtual twin" of a real HPDM. RoloSim allows for the simulation of spherical particles, as well as more complex geometries including dimers and trimers of spheres, rods with spherical caps, and polygonal prisms (not shown). RoloSim faithfully reproduces many characteristics of HPDM motion that we have observed experimentally. A 30 min simulation with a 30 ms timestep can be completed in ~24 hours. We generally run hundreds of RoloSim simulations in parallel using a computing cluster.

3.2.2 Energy minimization

At each timestep, the position (encoded by the vector $\boldsymbol{P} = [P_x, P_y, P_z]^T$, which describes the particle's geometric centroid) and orientation of the HPDM is adjusted to minimize E. The coordinates of all DNA strands are rigidly linked to the HPDM's surface, such that any rotation or translation of the particle are also propagated to the DNA strands' coordinates. The simulation operates in an x-y-z Cartesian coordinate system where the z-direction is perpendicular to the substrate. Energy minimization is performed by accounting for the energy of the tethers, as well as a few additional terms that represent forces acting on the HPDM body:

$$E = E_g + E_{el} + E_B + \sum_{i=1}^{N} E_{teth,i}$$

where E_g accounts for gravity and buoyancy, E_{el} accounts for electrostatic repulsion between the particle and the substrate, and E_B accounts for an externally applied biasing force that is generally set to zero.

We found that spherical particles of radius R, we could model E_g as:

$$E_g = (R - P_z)R^3(9.92 * 10^{-12}\ nm^{-4})$$

In addition, when using parameters that best-matched our experimental conditions, E_{el} could be described as:

$$E_{el} = R(3.21\ nm^{-1}) \exp\left(-\frac{P_z - R}{\lambda_D}\right)$$

Each tether is modeled as a nonlinear elastic spring with a force-extension relationship that was calculated using the worm-like-chain (WLC) model[32,33]. The details of our calculations are written in the supplemental notes of chapter 2. Briefly, the WLC model has no closed-form solution so we used a sophisticated approximation developed by Petrosyan[32] to calculate the force-extension curve (**Figure 31**). We later found that this representation could accurately represent tether mechanics as large extensions, but would fail to report resistance to compression at very small compression. To compensate for this issue, we adapted a Monte Carlo simulation method presented by Becker, Rosa, and Everaers[128]. Ultimately, we developed a simple, accurate approximation that accurately fits the Monte Carlo simulation data (**Figure 32**) for E_{teth} as a function of the tether's end-to-end extension, d:

$$E_{teth} \approx \kappa_t \exp(\mathrm{K}\, d^2) + \frac{\kappa_c}{d_z}$$

where κ_t and κ_c are spring constants for tension and compression, K is a fit parameter that is related to the length of the contour length of the tether, and d_z is the tether's extension in the z-direction. While the first term reflects an energetic cost for extending the tether, the second term reflects an energetic cost for compressing the tether into a small volume between the particle and the substrate. In both cases, the energetic cost is entropic in nature because extension and compression both reduce the tether's mobility.

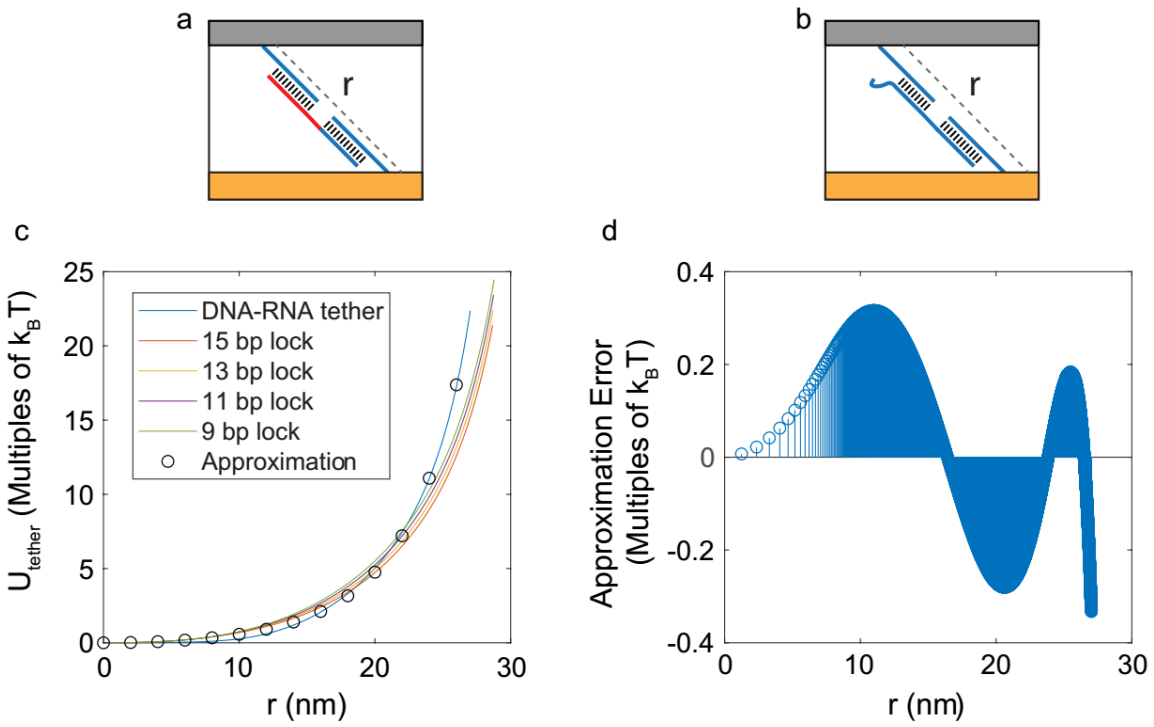

Figure 31: Tether WLC calculation and approximation

a) Depiction of a tether with end-to-end extension, r. **b)** Depiction of a DNA-DNA lock with a shorter duplex. **c)** Tether energy (U_{tether}, referred to as E_{teth} elsewhere in this text) as a function of r. Calculations for various DNA-DNA locks are also shown. Calculations were performed using the Petrosyan approximation[32]. Circles show simple approximation used in this work:

$$E_{teth} = (0.91\ k_B T)(\exp(0.0045 r^2) - 1)$$

d) Absolute error of the simple approximation (with respect to the Petrosyan approximation), showing that the error does not exceed $0.35\ k_B T$ at relevant extensions of $r \leq 25\ nm$.

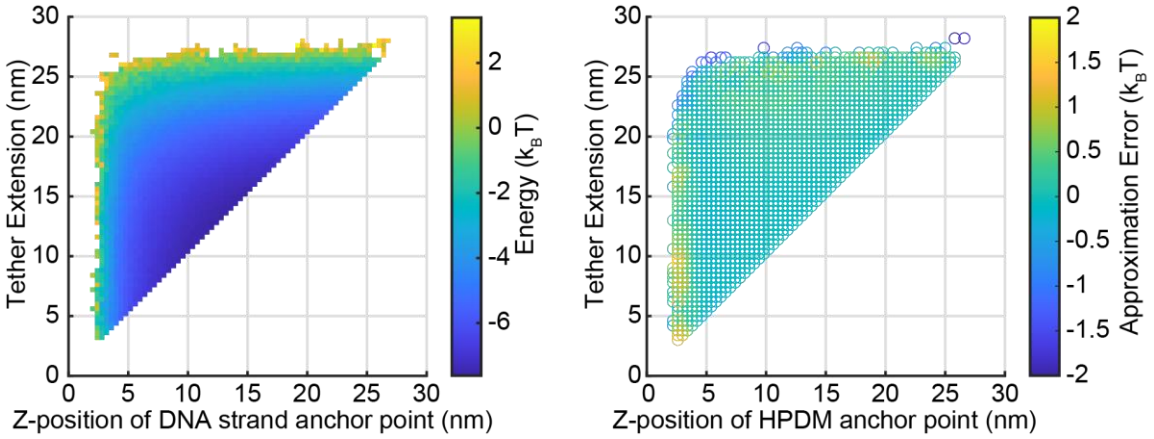

Figure 32: E_{teth} measured using WLC Monte Carlo simulations

Monte Carlo simulations[128] were performed with 100,000 timesteps of the Metropolis-Hastings algorithm. At each timestep, tether extension (r) and the z-position of the DNA-strands anchor part on the particle (d_z) were recorded at each timepoint. Datapoints were grouped into $1\,nm \times 1\,nm$ bins and the energy of each bin was calculated as $E = \log(n/r^2)$ (where r^2 accounts for the increasing surface area with respect to r). We found that our result (left) fit accurately to a simple computationally-efficient approximation:

$$(0.36\,k_BT)(\exp(0.0045r^2) - 1) + \frac{(1.4k_BT\,nm)}{d_z}$$

We performed energy minimization using simulated annealing with six free parameters: three components of a translation vector denoted by $\boldsymbol{D} = \left[D_x, D_y, D_z\right]^T$ and three components of a rotation vector denoted by $\boldsymbol{\rho} = \left[\rho_x, \rho_y, \rho_z\right]^T$ (using the rotation vector representation, $|\boldsymbol{r}|$ denotes the magnitude of the rotation while the orientation of $\boldsymbol{r}$ denotes the axis around which the rotation is performed). Specifically, we used MATLAB (2019b)'s built-in simulannealbnd function (which performs simulated annealing, allowing the system to escape local energetic minimums) with MaxFunctionEvaluations set to 1,000 and an fminun hybrid function (which performs local gradient descent, allowing the system to find the nearest local energetic minimum following simulated annealing) and otherwise default settings. We performed energy minimization after each timestep in which at least one tether forms or breaks.

3.2.3 Stochastic application of changes to tether set

In each timestep, changes to the set of tethers are applied via the kinetic Monte Carlo method. There are three types of transitions: 1) association between a DNA strand and an RNA fuel strand, which occurs with r-dependent rate constant of k_{on}, 2) irreversible cleavage of the tether's fuel strand, which occurs with with d-independent rate constant k_{clvg}, and 3) duplex rupture, which occurs with the d-dependent rate constant k_{rup}. Cleavage and rupture both break the tether, but only cleavage renders the fuel strand unavailable for future binding.

The details of our calculation of k_{on} are described in detail supplemental notes of chapter 2. Briefly, we utilize the Petrosyan approximation[32] of the WLC model and WLC parameters specific to the RNA-DNA transition state for hybridization[118] to calculate the

energy of the transition state tether, E_{tst}, as a function of d. We found that E_{tst} takes a similar form to E_{teth}:

$$E_{tst} \approx \kappa_t^*(\exp(\mathrm{K}^* \, d^2) - 1)$$

From this value, we calculate k_{on} as:

$$k_{on} = k_{on,0} \exp\left(-\frac{E_{tst}}{k_B T}\right)$$

where $k_{on,0}$ is an unknown scaling constant that we later optimize and $k_B T = 4.114 \; pN$ is Boltzmann's constant at room temperature (**Figure 33**).

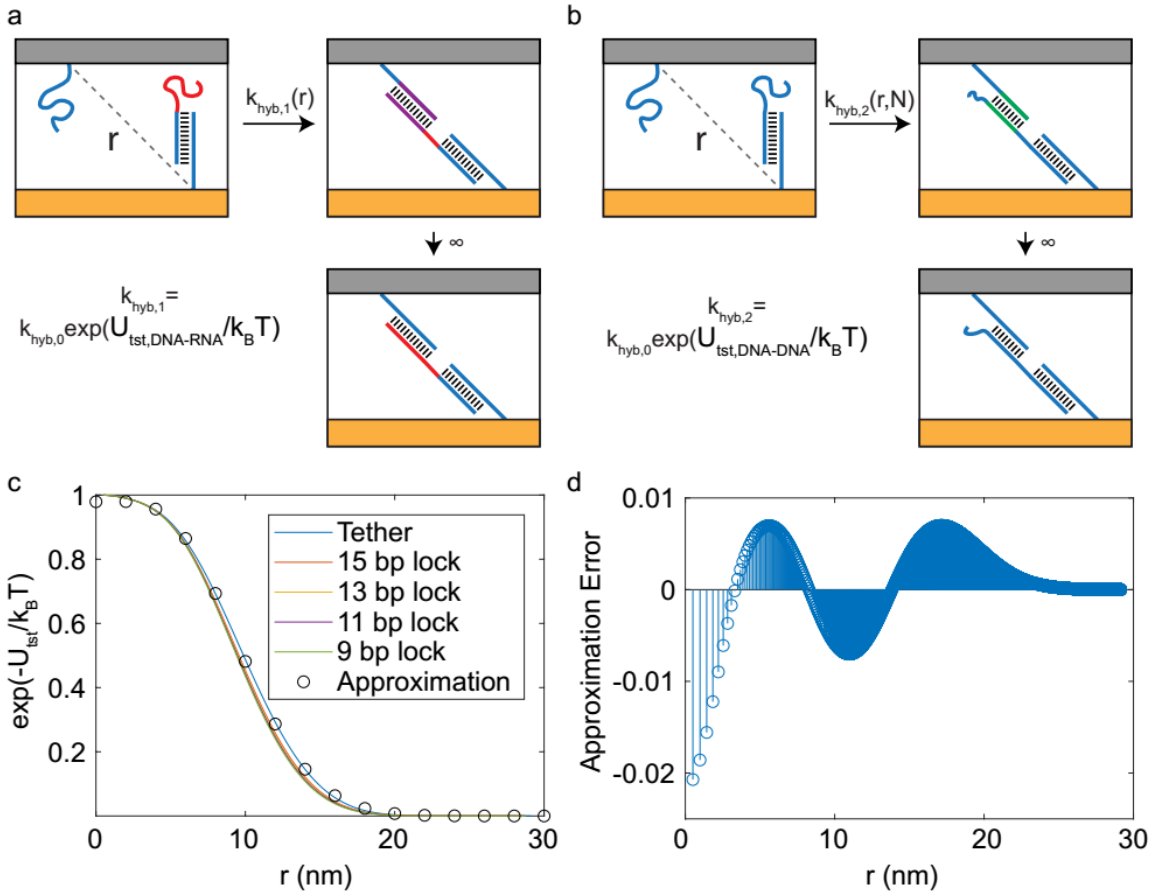

Figure 33: Depiction and calculation of association

a,b) Depiction of strand association, with transition state duplex shown in purple (for DNA-RNA) or green (for DNA-DNA). **c)** WLC calculation of the exponent of tether energy (which is proportional to the tether association rate) as a function of the distance between strands. Calculation is shown for tethers of various lengths. A simple approximation described above is shown with black circles. **d)** Error of approximation as a function of r, showing less than 1% error at all relevant distances.

We calculate the rate of bond rupture us a function of tether force (F) using a model previously developed by Mosayebi *et al.*[83], which we subsequently[1] simplified to:

$$k_{rup} = k_{rup,0} \exp\left(-(\mathrm{M}-1)\left(2.53 - (0.15\ \mathrm{nm}) * \frac{\mathrm{F}}{\mathrm{k_B T}}\right)\right)$$

where M is the length of the duplex ($M = 15$ unless otherwise stated) and $k_{rup,0} = 6.86 * 10^7 \mathrm{s}^{-1}$. (See the supplemental notes of chapter 2 for more information).

3.3 Goals

We had four specific goals that we sought to use RoloSim to accomplish. The first one is broad while the second, third, and fourth focus on specific potential applications of HPDMs.

1) **To understand the scaling properties of autochemophoretic HPDM motion.** HPDMs have potential to be versatile tools for molecular recognition, nanopatterning, and force generation. In order to engineer HPDMs to serve specific roles, it is important to know how controllable HPDM properties – such as diameter, RNase H concentration, guide and fuel strand surface density, and tether duplex and spacer length – on HPDM translocation properties such as force and velocity. RoloSim offers the opportunity to measure this scaling properties *in silico*. While there is no guarantee that RoloSim results are experimentally-relevant, RoloSim does have value in that it offers a pure environment that is free of experimental error, heterogeneity between experiments, and measurement noise. RoloSim also allows for the exploration of HPDM properties in high-throughput (i.e. the testing of large numbers of conditions in parallel), which can generate hypotheses that can later be tested experimentally.

2) **To determine under what conditions HPDMs can be used for single molecule sensing.** The ability to perform molecular detection in a rapid, reliable, manner in resource limited settings is critical for responding to disease outbreaks, assessment of food and water quality, and for medical decision making. However, molecular detection in the field (e.g. outside of the lab) often require samples to be transported to dedicated laboratories with specialized equipment for testing. Conversely, most field-based sensors

do not provide appropriate molecular sensitivity. HPDMs have potential to address these issues, by serving as single molecule biomarker sensors. In principle, if F_{HPDM} can be reduced while preserving HPDMs' processivity and speeds, they could be stalled by individual biomarkers. rapid, sensitive, on-site molecule detection using smart phone-based readers. We sought to use RoloSim to understand how to reduce F_{HPDM} to levels that would make HPDMs suitable for single molecule sensing.

3) **To measure force generation by non-spherical HPDMs.** HPDMs have significant potential to serve as motors powering nano- and micromachines. However, the large size of existing HPDMs is a hindrance that will prevent future nanoscale applications. The specific importance of pN-scale force generation at the nanoscale is clearly illustrated by biological systems; molecular motors such as myosin and kinesin power countless tasks by generating and sustaining 1-10 pN of force via ATP-fueled powerstrokes. Currently, we do not have the means to engineer similar functionalities from the bottom-up, and so nanotechnological tools are largely viewed from a chemical rather than mechanical paradigm. The field of nanorobotics is still quite new and there is a large need for demonstrations of technology that can perform fundamental tasks such as force generation. By miniaturizing force-generating HPDMs to the nanoscale we can push the field forward and pave the way for the next generation of rationally-designed nanoscale mechanical systems. By designing RoloSim to allow for non-spherical HPDM geometries, we can understand how rod-shaped HPDMs can be used to scale the large force-generating potential of HPDMs down to the nanoscale (**Figure 34**).

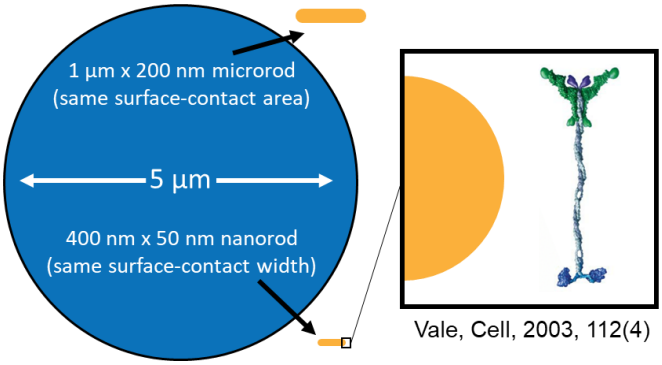

Figure 34: Depiction of the size difference between rod-shaped and spherical HPDMS

4) **To understand how to "steer" HPDMs in a massively parallel fashion:** The HPDM-substrate contact zone is restricted to <400 nm and this could potentially be reduced. This narrow, sharply bounded footprint suggests that HPDMs can serve as highly selective tools for "writing" nanoscale patterns with high precision. Furthermore, the ability to deposit streptavidin into depletion tracks using mechanical bond rupture as a selection mechanism[1] also demonstrates that HPDMs can perform additive, in addition to subtractive, lithography. If HPDM motion can be controlled using an externally controlled force field, then all HPDMs can, in principle, be directed to follow the same path in parallel. Given the small size of an individual depletion track – 400 nm, which can be reduced to ~100 nm by reducing HPDM size – HPDMs may be capable of performing relatively high-resolution nanolithography and may be well-suited towards addressing this problem. By designing RoloSim to allow for the incorporation of externally-applied forces, we can understand how to steer HPDMs for massively parallel nanolithography.

3.4 Optimization of RoloSim

We initially sought to obtain optimal parameters that would create the greatest resemblance between the RoloSim result and experimental observation. To summarize the process, we first sought to obtain a set of mechanical parameters (k_c, k_t, and k_t^*. We always used $K = 0.0045$) as well as the $k_{on,0}/k_{clvg}$ ratio in order to reproduce "equilibrium" quantities of HPDM translocation. We then scaled $k_{on,0}$ and k_{clvg} together to accurately reproduce the dynamic properties of HPDM translocation.

3.4.1 Metrics

We sought to optimize the following observable quantities:

1. Depletion track width: depletion track width was previously quantified[29] by taking linescans of depletion tracks and quantifying the full-width half maximum (FWHM) of the tracks. Previously, we utilized structured illumination microscopy (SIM, a superresolution imaging technique) to obtain an estimate of $FWHM = 380\ nm$. As a best-attempt to replicate this scenario, we used an automated process in which simulated data is used to create a mimic SIM image and then linescans are taken at defined intervals along the simulated HPDM's trajectory (**Figure 35**).

2. Depletion track depth: we generally find that roughly 50% of the fuel strands beneath the HPDM are cleaved[1,29]. While this estimate is not as precise as the FWHM measurement, the finding that a substantial fraction (~50%) of fuel strands in depletion tracks remain uncleaved is reproducible. We quantify width and depth together by fitting linescans of simulated SIM images to inverted Gaussian functions (see methods). We then calculate the FWHM and depth directly from the parameters of the best-fit Gaussian (**Figure 35**).

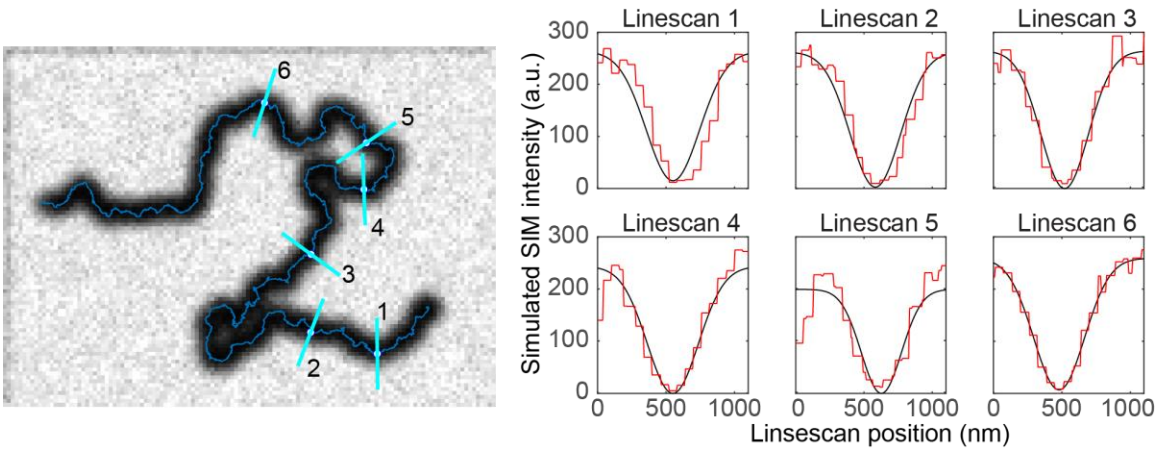

Figure 35: Automated analysis of depletion tracks

An automated analysis method was used to analyze depletion track properties. Briefly, The trajectory was queried at an interval of every 2,000 timepoints. The first and last query points were then excluded to avoid sampling the track at the ending or beginning of the image. For each query point, all trajectory points within a 550 nm radius were collected. From these trajectory points, two durations were recorded: the time between the first and the last point, and duration of the continuous set of trajectory points that the query point belongs to. If the ratio of these durations is greater than 1.1, the query point is discarded. This process is intended to exclude query points where the track switched back on itself (linescans of such query points could artificially bias the width measurement upwards). Each of the remaining query points was then used to draw a linescan 733 nm in length and with an orientation that is perpendicular to the major axis of the set of trajectory points within the 550 nm radius cutoff. This linescan was then fit to an Gaussian function, which was then analyzed to extract the track depth (depth of the Gaussian) and width (FWHM of the Gaussian).

3. Path persistence length: we previously found that HPDMs exhibit persistent motion at intermediate timescales (i.e. HPDMS tend to travel in the same direction for tens of seconds)[1]. At longer timescales of several minutes or more, the directionality of spherical HPDMs is randomized. Our simulated trajectory should also exhibit these properties. This intermediate timescale persistence can be quantified using the path persistence length (L_{traj}) metric[129], which is analogous to the persistence length parameter of the WLC model and denotes the distance across which a trajectory's directionality remains correlated with itself. We generally find that L_{traj} is on the order of 1-2 μm (**Figure 36**). However, because this quantification of L_{traj} includes contributions from some HPDMs that are stalled due to nonspecific interactions between the HPDM and the surface, we take 2 μm as our lower-bound cutoff

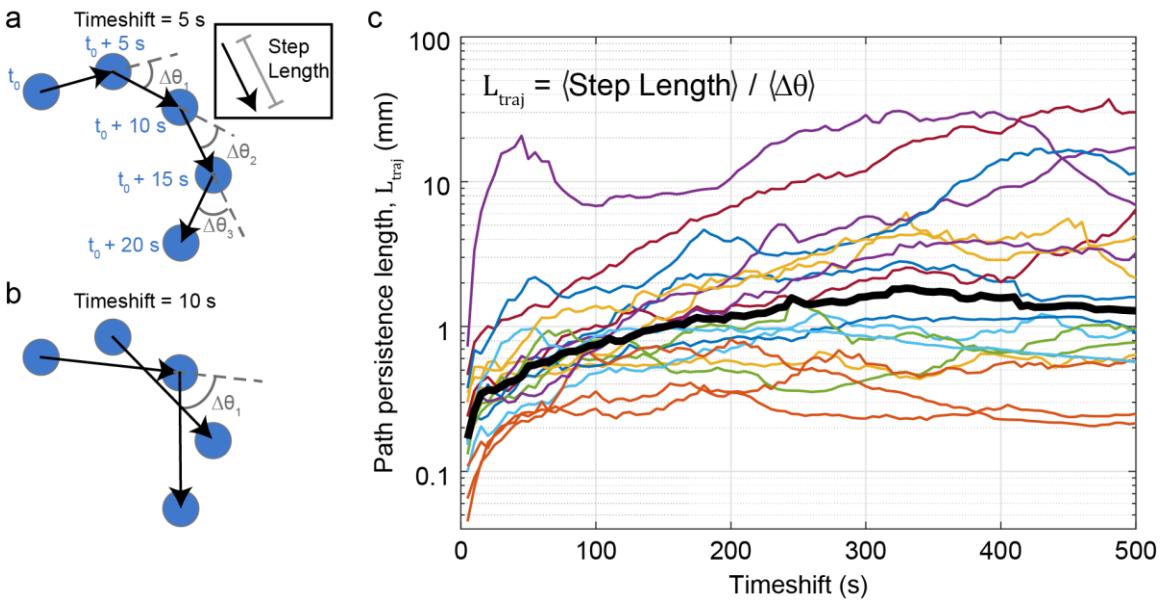

Figure 36: Experimental measurement of path persistence (L_{traj}).

a) Depiction of $\Delta\theta$ and step length (inset) for a timeshift of 5 seconds when the HPDMs are imaged at a 5-second interval. Five representative HPDM positions are shown, along with four "steps" and. **b)** Same as **a**, but for a timeshift of 10 seconds. **c)** L_{traj} as a function of timeshift for 18 individual HPDMs, as well as the median of the 18 HPDMs (thick black curve). At short timescales, L_{traj} appears to be artificially low, which is an expected result of localization error. At intermediate timscales (~1 to 5 minutes) the median L_{traj} value converges to a range of $\sim 1-2\,\mu m$. Trajectories were calculated by re-analyzing supplemental movie 1 from ref. [29] using an improved particle tracking presented in ref. [1] (and used in this work).

4. Stall force: in previous experiments[1], we quantified the force generated by HPDMs (F_{HPDM}) as $F_{HPDM} \approx 150\,pN$. This measurement was obtained using high throughput particle tracking experiments involving hundreds of individual HPDMs. Because this level of throughput is not practical for RoloSim, we adopted an alternative approach. Briefly, we restart a completed RoloSim simulation at a random timepoint and "pin" the HPDM by making one random tether unbreakable. The simulation is then allowed to continue until the HPDM "stalls". Stalling is determined to have occurred when the polyavalency (the number of tethers) drops to five, which we have found is too low to ever occur under normal conditions. A 1-second smoothing average is then applied to the force vs. time curve, and the maximum force of this smoothed curve is then determined to be the stall force. This process is repeated several dozen times to obtain an average estimate of F_{HPDM} (**Figure 37**).

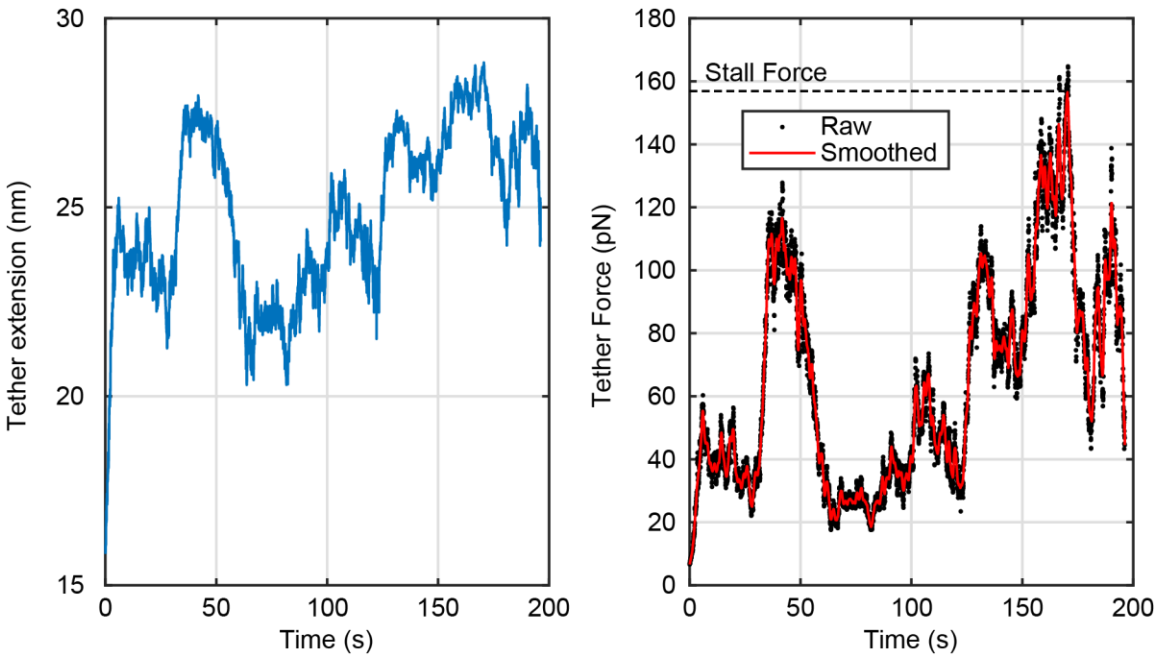

Figure 37: RoloSim-based estimation of F_{HPDM}

Because the previous experimental methods for F_{HPDM} estimation require very high throughput, we developed an alternative method to estimate F_{HPDM} using RoloSim. In this method, a completed simulation is restarted at a random timepoint, and then a random tether is selected from the set of existing tethers at that time point. That tether is set as an indestructible tether, that can be neither cleaved nor ruptured. The simulation is then allowed to continue until the polyvalency drops below five. The tether's extension vs. time curve is stored (left). This curve is then used to calculate a force vs. time curve (right), which is then smoothed with a 1-second rolling average. The maximum value of the smoothed curve is then recorded as the stall force. This process is repeated ~100 times per condition to obtain a robust estimate of F_{HPDM}.

5. Average velocity (v_{avg}): we generally find that the average HPDM velocity is roughly 1.3 $\mu m/min$. This estimate lumps contributions from mobile HPDMs as well as low-mobility HPDMs that have become “entrapped” within their own depletion tracks (**Figure 38**).

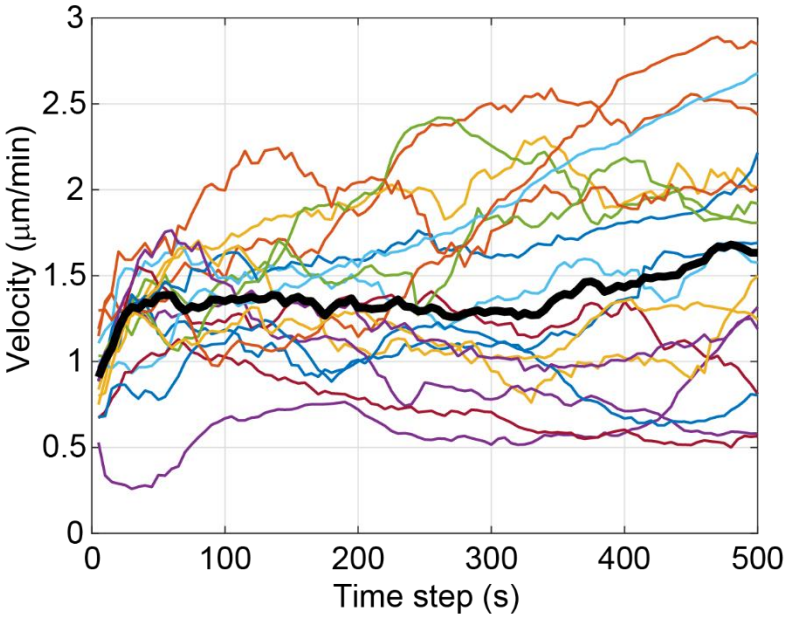

Figure 38: Experimental measurement of average velocity, v_{avg}

Average HPDM velocity (v_{avg}) as a function of timeshift for 18 individual HPDMs, as well as the median of the 18 HPDMs (thick black curve). At short timescales, v_{avg} appears to be artificially low, which is an expected result of localization error. At intermediate timscales (~1 to 5 minutes) the median v_{avg} value converges to $\sim 1.3\,\mu m/min$. Trajectories were calculated by re-analyzing supplemental movie 1 from ref. [29] using an improved particle tracking presented in ref. [1] (and used in this work).

6. The kinetic rate constant for RNase H-mediated hydrolysis (k_{clvg}): through experiments, we previously estimated $k_{cat} = 25\ \text{min}^{-1} = 0.4\ s^{-1}$, where k_{cat} is the maximal kinetic rate constant for RNase H-mediated cleavage according to the Michalis Menten kinetic framework (i.e. $k_{clvg} = k_{cat}$ where $[RNase\ H] = \infty$. Accordingly, the k_{clvg} value obtained from our optimization process should not exceed this value.

These six metrics can be divided into three categories: depletion track width and depth are timescale-independent, meaning that they are equilibrium properties that are calculated without any consideration of the dynamics of HPDM translocation; path persistence length and F_{HPDM} both exhibit a light timescale-dependence but can be assumed to be largely timescale independent (L_{traj} depends slightly on the selected step length and the simulated F_{HPDM} calculation depends on a 1-second smoothing average); and v_{avg} and k_{clvg} are completely timescale-dependent quantities.

3.4.2 Optimization of mechanical parameters

We started the optimization process by using parameters calculated according to the WLC model. Specifically, we found that $K = 0.0045$ allowed for an accurate representation of the tether's force-extension curve. While the Petrosyan approximation yielded best-fit values of $\kappa_t = 0.91\ k_BT$ and $\kappa_c = 0\ k_BT$, our Monte Carlo WLC simulations produced best-fit values of $\kappa_t = 0.36\ \ k_BT$ and $\kappa_c = 1.4\ k_BT\ nm$. This result suggested that tethers, when bound on either end to two surfaces, are easier to extend than would be expected from the conventional WLC model. The conventional WLC model calculation for the association transition state also yielded a best-fit of $k_t^* = 0.88\ k_BT$ and $K^* = 0.0036$. The

disparity between the conventional and Monte Carlo WLC results suggested that a similar disparity may exist for the transition state tether. Therefore, we varied κ_t^* across two orders of magnitude (from 0.088 to 8.8). We also varied $k_{on,0}/k_{clvg}$ across two orders of magnitude. In total, we ran one 60 minute simulation for most combinations of 13 k_t^* values and 13 $k_{on,0}/k_{clvg}$ values (several simulations were not run according to user choice, particularly in the extremes of the parameter space). Of these simulations, a total of 110 finished successfully. For each condition that finished successfully, we quantified track width and depth, L_{traj}, and F_{HPDM} and then adjusted the timescale of the simulation (by adjusting $k_{on,0}$ and k_{clvg}, and Δt post-hoc) to obtain $v_{avg} = 1.3\ \mu m/min$ (we started by arbitrarily setting $k_{clvg} = 60\ min^{-1} = 1\ s^{-1}$). Following timescale adjustment, we also quantified k_{clvg}. Finally, we quantified the steady-state polyvalency of each HPDM by measuring the number of tethers at 1-second intervals throughout the simulation.

The results of these simulations, shown in **Figure 39** and **Figure 40**, show three general behaviors. At low $k_{on,0}/k_{clvg}$ and high κ_t^*, tether association is much slower than cleavage, which results in a low steady-state polyvalency, very low force ($F_{HPDM} < 1\ pN$) diffusive motion (i.e. $L_p < 0.4\ \mu m$) and no depletion track. At high $k_{on,0}/k_{clvg}$ and low κ_t^* association is much faster than cleavage, resulting in a wide, deep depletion track (with 100% consumption of all strands in the HPDM's path), high force ($F_{HPDM} > 10\ pN$), and high persistence ($L_p > 2\ \mu m$). The third category exhibited intermediate properties, with depletion track depths between 10% and 90%, $FWHM$s close to 400 nm, and L_{traj} within the ideal range of $1\ \mu m < L_{traj} < 2\mu m$.

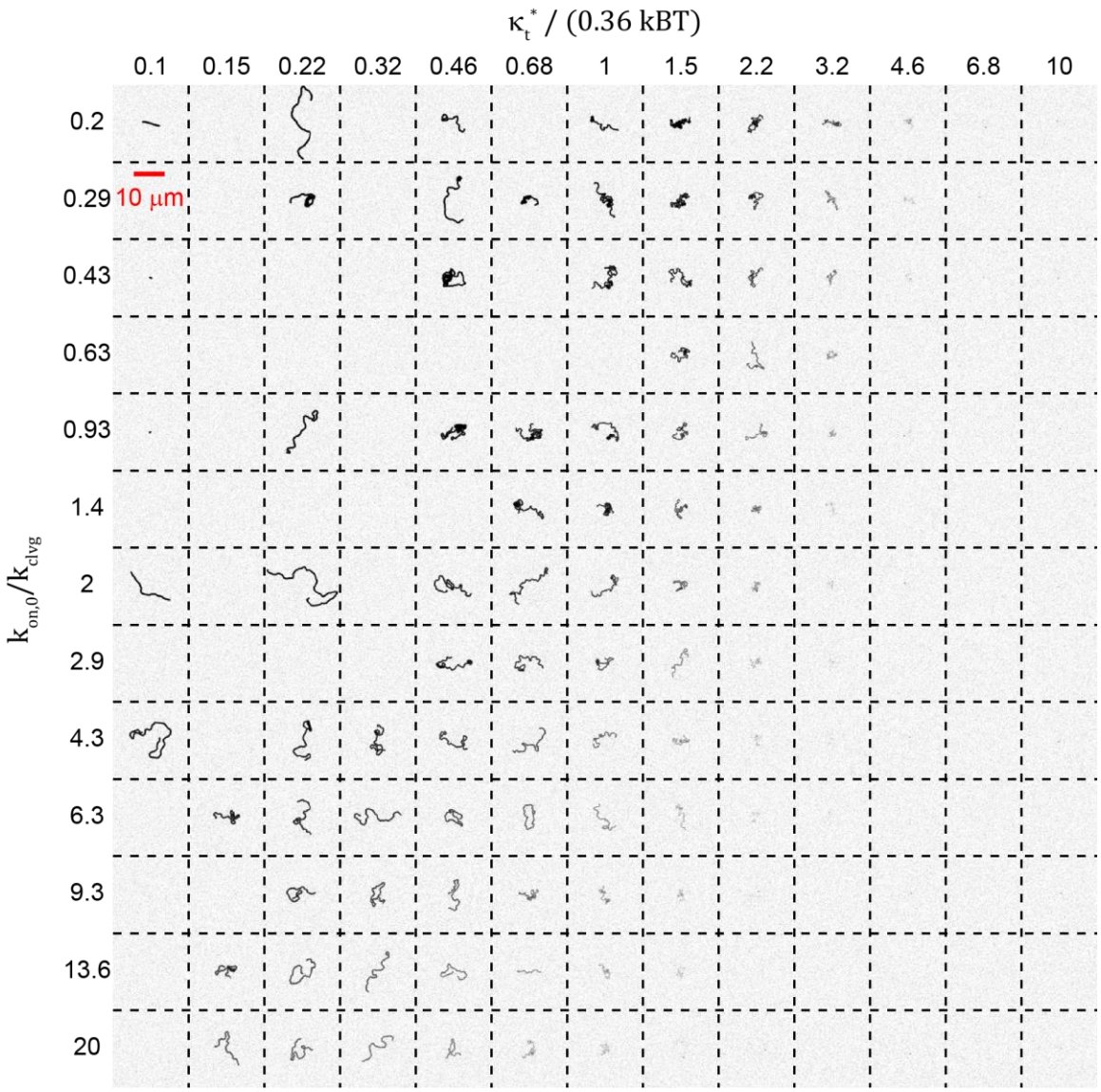

Figure 39: Depletion tracks from simulations run with varying κ_t^* and $k_{on,0}/k_{clvg}$ values

A 13x13 grid of simulated depletion track images. Not all conditions are represented due a combination of 1) early termination of a small number of simulations due to various computational errors (some of which were corrected following this round of optimization), and 2) efficient selection of condition to conserve computational resources.

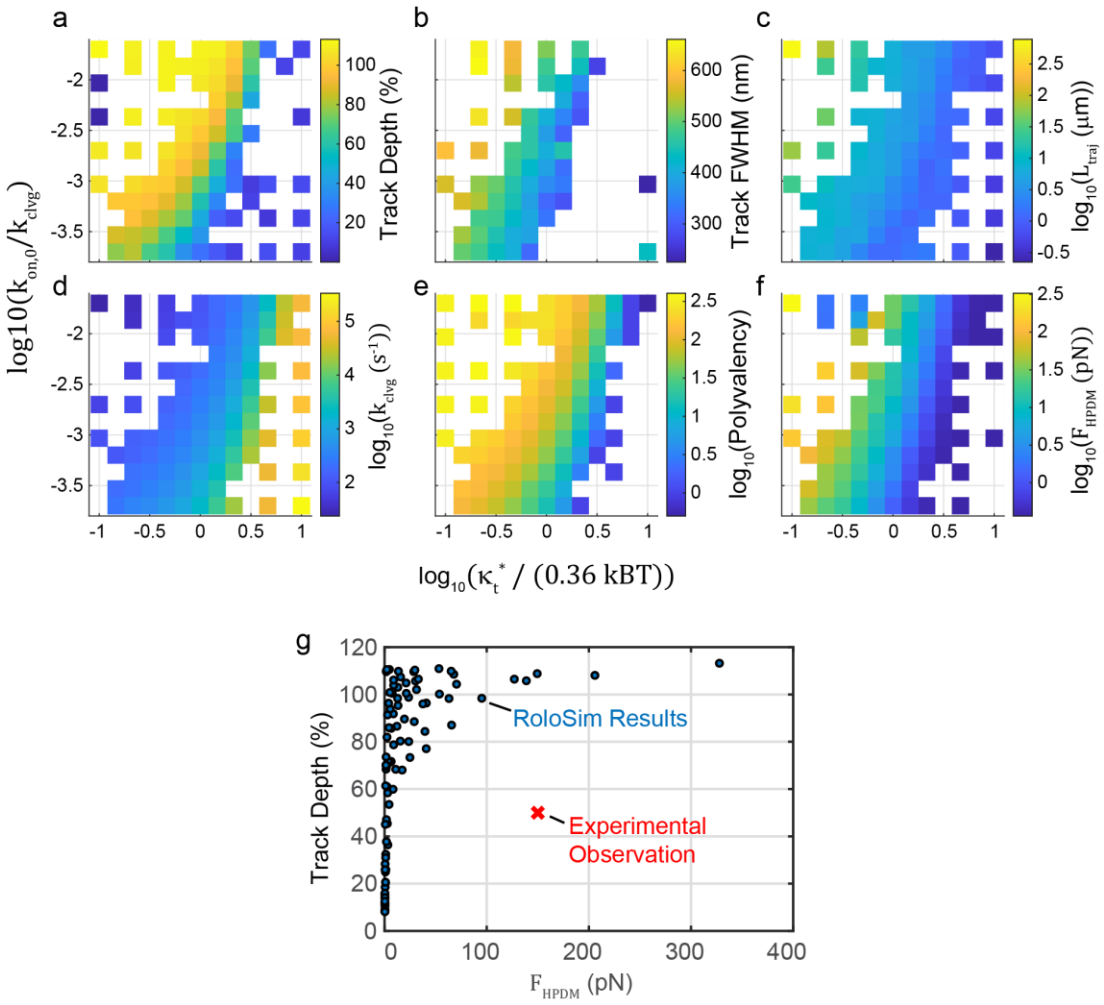

Figure 40: Metrics for first round of optimization

a-f) Various metrics quantified from the results shown in **Figure 39**. The key takeaway for the purposes of optimization is **g)** that no pair of parameters results in the experimental observation of a 50% track depth and $F_{HPDM} = 150\ pN$ (or even $F_{HPDM} > 10pN$).

Unfortunately, no condition produced a depletion track depth below 100% and $F_{HPDM} > 10\,pN$ (**Figure 40g**). This finding contrasts starkly with experimental observations, wherein the track depth is ~50% and $F_{HPDM} \approx 150\,pN$. Instead, conditions that produced a depletion track depth of between 10% and 90% resulted in low force magnitudes that would not be capable of rupturing even a single DNA-DNA duplex, as previously observed in extensive and unambiguous detail[1].

While the reason for this disparity from experimental observation is unclear, we think the primary cause of this issue may be RoloSim's failure to account for potential heterogeneity of the activation energy of tether association; if strands have different levels of accessibility and/or nonspecific association with their underlying surfaces, then different strands could have different on rates. We believe that a method that allows for heterogeneity in association activation energy could allow for simulated HPDMs to achieve higher steady-state polyvalency (and thus higher F_{HPDM} measurements) while still producing a track depth of ~50%. However, the exploration of such hypotheses will be the subject of future work.

Having failed to obtain a pair of κ_t^* and $k_{on,0}/k_{clvg}$ values that accurately reproduce all of our experimentally-observed metrics simultaneously, we sought to obtain a reasonable set of parameters that could be used for this initial study. Specifically, we relaxed our constraint on track dimensions and sought a condition in which $F_{HPDM} \approx 150\,pN$ and $L_p > 1\,\mu m$. We started by increasing κ_c and κ_t ten-fold, with the reasoning that increasing tether stiffness would result in increased force generation. (Ideally, future versions of RoloSim

will include more rigorous parameterization). We then varied $k_{on,0}/k_{clvg}$ across two order of magnitudes, as before. We ran seven independent simulations for each of seventeen $k_{on,0}/k_{clvg}$ values ranging from 0.0001 to 0.01 and quantified L_{traj} and F_{HPDM} for each (**Figure 41**). We found that $L_{traj} > 2\mu m$ at all conditions (**Figure 41**d). At no condition was $FWHM \leq 380\ nm$ (this may potentially be an artifact of the automated track analysis method, which down not always result in linescans being taken perpendicular to the depletion track, leading to over-estimation of $FWHM$) (**Figure 41**b). Across the range of conditions tested, F_{HPDM} increased from ~10 pN to ~300 pN (**Figure 41**e). Similarly, track depth increased from ~10% to 100% (**Figure 41**c). Finally, at no condition was k_{clvg} lower than the previously measured $k_{cat} = 0.4\ s^{-1}$ (**Figure 41e**). This result likely stems from the same issues that require the 10-fold scaling of κ_t and κ_c – which we hope to resolve with future iterations of RoloSim. Ultimately, we chose the condition of $k_{on,0}/k_{clvg} = 0.0042$, which produced $F_{HPDM} \approx 170\ pN$ and $L_{traj} \approx 7\ \mu m$. Temporal scaling to obtain $v_{avg} = 1.3\ \mu m/min$ resulted in. $k_{on,0} = .0091\ s^{-1}$ and $k_{clvg} = 2.2\ s^{-1}$.

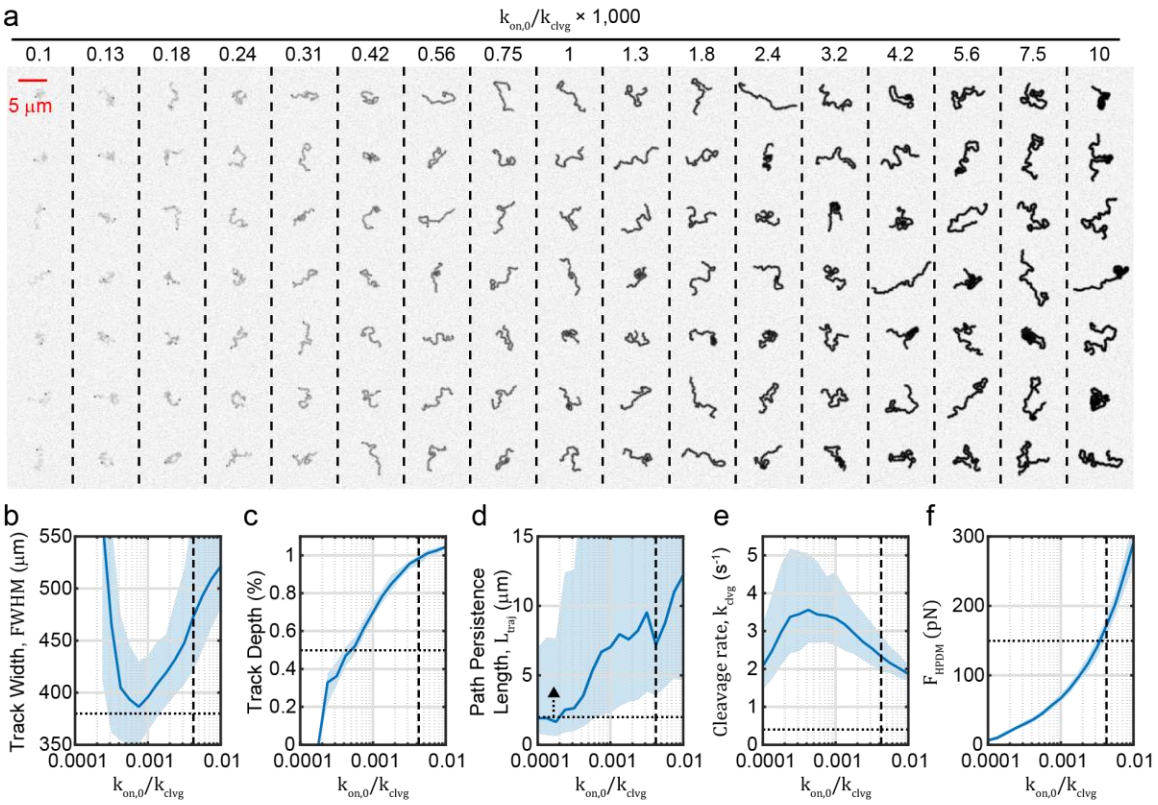

Figure 41: RoloSim optimization results, round 2

a) Montage of depletion tracks depicting results of seven simulations at each of seventeen $k_{on,0}/k_{clvg}$ values. Image brightness is scaled to 0% to 100% RNA fuel depletion. **b-f)** Median +/- inter-quartile range of several quantifiable metrics shown as a function of $k_{on,0}/k_{clvg}$. Horizontal dotted line denotes experimental observation, while vertical dashed line denotes the selected condition.

3.4.3 Assumptions

RoloSim treats the HPDM as static through the duration of each individual timestep. In reality, thermal fluctuations should result in random, rapid variations in particle position and orientation. We argue that this approximation is reasonable based on our previous calculations of the effect on high polyvalency on HPDM mobility[1]. These calculations revealed that the Boltzmann average angular deviation at high polyvalency (50+) was on the order of one or a few nanometers. This length scale is substantially smaller than the length scale of typical tether formation (<25 s). Accordingly, the effect of thermal fluctuations on $k_{on,0}$ should be negligible. Because particle valency rarely dipped below 30, thermal fluctuations in HPDM position and orientation can reasonably be ignored.

At the end of each timestep, the particle's position and orientation is instantaneously updated. We reason that this is a reasonable approximation of particle behavior: generally we find that HPDMs consume ~500 RNA fuel strands per second, meaning that there are roughly 1,000 events per second (with an event being defined as a cleavage or an association). This yields an average inter-event time of 1 ms. By contrast, the relaxation time constant of an immersed microsphere $\tau_p = \frac{m}{6\pi\mu R}$ (where $M \approx 10^{-13}\ kg$ and $R = 2.5 * 10^{-6}\ m$ are particle mass and radius respectively and $\mu \approx .001\ kg/(m * s)$ is the viscosity of the surrounding solution) is roughly equal to $2\ \mu s$. Finally, due to high polyvalency the effect of any single tether on HPDM position and orientation is minimal. As such, we posit that a particle spends ~99.9% of its time at static equilibrium with rapid sub-angstrom shifts that are caused by individual strand associations and dissociations. Furthermore, because

each individual shift is so small, we reason that using a timestep length that is several times that of the inter-event timescale does not significantly alter the behavior.

3.5 Results

3.5.1 Mean squared displacement analysis

We started our analysis of the RoloSim outputs by analyzing the condition that we elected to move forward with as our optimal condition. Specifically, we analyzed the mean-squared displacement (MSD) properties of the simulated HPDMs' trajectories. We previously found that, when MSD was recorded on a timescale of ~5 seconds to ~1 minute, MSD scaled as a function of $t^{1.5}$. This behavior is a feature of superdiffusive motion, owing in this case to the self-avoiding behavior of HPDM translocation. if the scaling exponent (generally called α) is equal to 1, behavior is diffusive. Ballistic motion results in $\alpha = 2$, subdiffusive motion results in $\alpha < 1$, and superdiffusive motion results in $\alpha > 1$. We found that HPDMs simulated using RoloSim would also exhibit superdiffusive motion, with $\alpha \approx 1.5$ when analyzed on experimentally-relevant timescales (**Figure 42**).

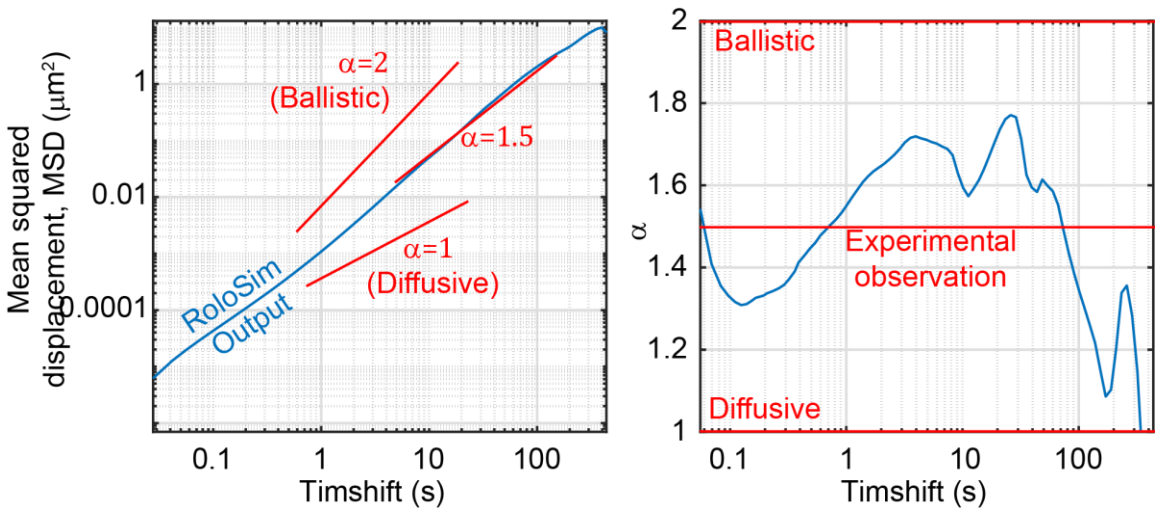

Figure 42: MSD analysis of optimized RoloSim results

A log-log plot of MSD vs. timeshift (τ) exhibits a slope that is equal to the α coefficient when $MSD \propto \tau^{\alpha}$. Running an MSD analysis for the optimized RoloSim output shows that at experimentally relevant timescales (τ ranging from 5 seconds to ~2 minutes), $\alpha \approx 1.5$. This finding is consistent with experimental observation.

3.5.2 Use of RoloSim to parameterize RNase H kinetics

We previously observed[29] that v_{avg} increases with [RNase H] in a hyperbolic manner; at the standard concentration of $[RNase\ H] = 144nM,\ v_{avg} = 1.3\ \mu m/min.$ Decrease $[RNase\ H]$ 10-fold to $[RNase\ H] = 14.4nM$ resulted in a near-complete abrogation of motion, while increasing $[RNase\ H]$ 10-fold to $[RNase\ H] = 1{,}440nM$ resulted in a ~2-fold increase in v_{avg} to $v_{avg} = 2.4\ \mu m/min.$ We fit these v_{avg} values to a hyperbolic function:

$$v_{avg} = \frac{v_{avg,max}[RNase\ H]}{[RNase\ H] + [RNase\ H]_{50}}$$

where $v_{avg,max}$ is the maximum HPDM velocity when $k_{clvg} = k_{cat}$ (i.e. when $[RNase\ H] = \infty$) and $[RNase\ H]_{50}$ is the concentration of RNase H that causes $v_{avg} = v_{avg,max}/2$. We obtained best-fit values of $v_{avg,max} = 2.7\ \mu m/min$ and $[RNase\ H]_{50} = 170\ nM$ (**Figure 43**c).

One mechanistic interpretation for this scaling behaviour is that RNase H-mediated tether cleavage can be described by a two-step sequential reaction (**Figure 43**a). The first step, which is $[RNase\ H]$-dependent, reflects association of the RNase H with the tether and is described by the first order rate constant k_1. The second step is $[RNase\ H]$-independent and reflects cleavage of the RNA background of the tether. This step is described by the zero-order rate constant k_{cat}. In this scenario, k_{clvg} can be described in terms of these two rate constants as:

$$\frac{1}{k_{clvg}} = \frac{1}{k_1[RNase\ H]} + \frac{1}{k_{cat}}$$

Because the second round of optimization produced RoloSim results with varying $k_{on,0}/k_{clvg}$ ratios, we next sought to recycle these optimization results to investigate the effect of tuning k_{clvg} on F_{HPDM}. Perhaps more importantly, we sought to use RoloSim to understand how F_{HPDM} would scale with $[RNase\ H]$ (which is a controllable quantity, while k_{clvg} is not). To accomplish this, we temporally re-scaled each simulation's output such that $k_{on,0}$ would equal the optimized condition of $k_{on,0} = .0091$ and calculated v_{avg} at each condition. We found that eight of the seventeen conditions exhibited $v_{avg} < v_{avg,max}$ (**Figure 43**b). We then used these eight v_{avg} values and least-squared-residuals fitting to find a combination of k_1 and k_{cat} that resulted in the simulated $[RNase\ H]$ vs v_{avg} values producing best-fit values of $v_{avg,max} = 2.7\ \mu m/min$ and $[RNase\ H]_{50} = 170\ nM$ (**Figure 43**c). The result of this process revealed that $k_1 = 0.044\ s^{-1}nM^{-1}$ and $k_{cat} = 13.5 s^{-1}$ (**Figure 43**d).

This best-fit k_{cat} value is 33-fold higher than the previous k_{cat} value that was measured experimentally of $0.4\ s^{-1}$. While it is possible that the experimental measurement resulted in an underestimation of k_{cat}, we find it much more likely that the simulation-based estimate is less accurate. We therefore caution against over-interpretation of this finding. Nonetheless, these extracted values can offer some insight into the potential scaling between F_{HPDM} and $[RNase\ H]$, which could potentially allow F_{HPDM} to be tuned up or down depending on the application.

3.5.3 Relationship between $[RNase\ H]$ and F_{HPDM}.

To understand how $[RNase\ H]$ could be adjusted to tune F_{HPDM}, we utilized our fit results from the previous subsection. Our results reveal a negative correlation between $[RNase\ H]$ and F_{HPDM} Specifically, we found that F_{HPDM} could be fit to a simple relationship:

$$F_{HPDM} = \left(\frac{6{,}757\ nM}{[RNase\ H]}\right)^{5/6} pN + 87.5pN$$

However, according to this model, k_{clvg} can only be tuned as high as k_{cat}, at which point F_{HPDM} converges to $87.5\ pN$. Therefore, F_{HPDM} can only be reduced – to a point – by increasing $[RNase\ H]$. While extrapolation of our model to low $[RNase\ H]$ does suggest that F_{HPDM} can be tuned to arbitrarily high levels, this interpretation is clearly incorrect. Nonetheless, our results suggest that F_{HPDM} can potentially be increased by decreasing $[RNase\ H]$.

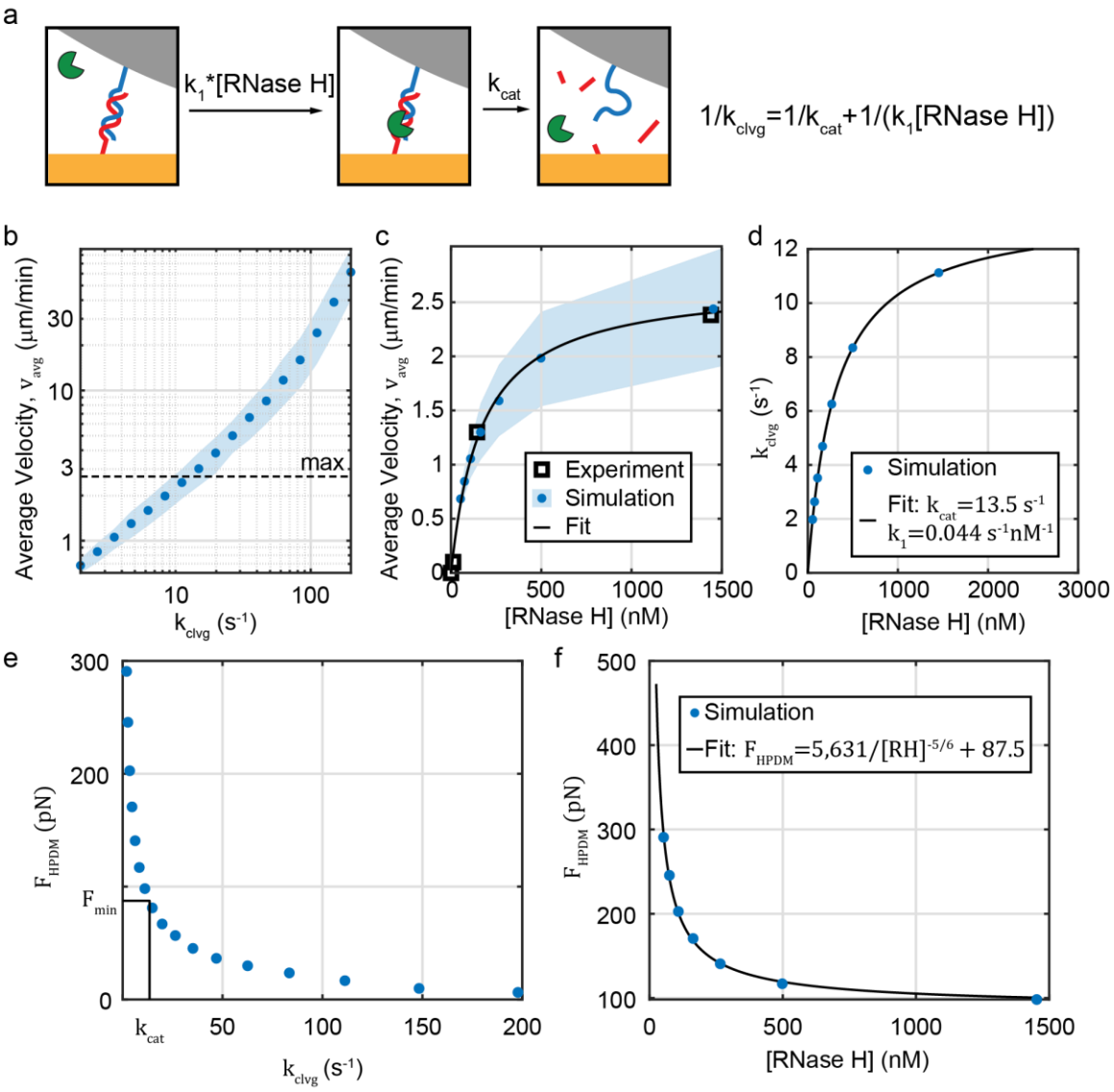

Figure 43: [RNase H]-dependence of F_{HPDM} and v_{Avg}

a) Simple sequential reaction scheme used to model RNase H-mediated tether cleavage. Equation demonstrates how k_{clvg} depends on $[RNase\ H]$, k_1 (the rate constant for the [RNase H]-dependent association step), and k_{cat} (the rate constant of the [RNase H]-independent cleavage step). **b)** Simulated v_{avg} (median +/- 25%-75% bounds) vs. k_{clvg} on a log-log scale. Dashed line denotes the cutoff velocity corresponding to maximum v_{avg}

according to fit to experimental data. c**)** v_{avg} vs RNase H showing both experimental averages from ref [29] (black boxes) and simulation results (median +/- 25%-75% bounds) following parameter optimization. Black curve shows hyperbolic function fit with $v_{avg,max} = 2.7\ \mu m/min$ and $[RNase\ H]_{50} = 170\ nM$. **d)** k_{clvg} vs $[RNase\ H]$ following parameter fitting to match the hyperbolic fit (shown in **c**) from the simulation to the hyperbolic fit from the experiment. Black curve shows fit and blue points show calculations at the k_{clvg} values that were used. **e)** Simulated F_{HPDM} as a function of k_{clvg}. **f)** F_{HPDM} as a function of $[RNase\ H]$. The power-law fit curve shows an asymptote of $F_{min} = 87.5$, suggesting that tuning [RNase H] can only be used to decrease F_{HPDM} by a limited amount.

3.5.4 The effect of HPDM diameter on F_{HPDM} and v_{avg}

To understand how HPDM force and speed scale with HPDM diameter, D_{HPDM}. we simulated HPDM motion with HPDM diameters ranging in 500 nm increments from 500 nm to 6,000 nm. Our results (**Figure 44**) show a near linear dependence of F_{HPDM} (**Figure 44c**) on D_{HPDM}, fitting accurately ($R^2 > 0.99$) to the relationship:

$$F_{HPDM} = (0.19\ pN)(D_{HPDM}\ nm^{-1})^{4/5}$$

In contrast, we found that v_{avg} exhibited sub-linear scaling (**Figure 44b**) with respect to D_{HPDM}, fitting well to the relationship:

$$v_{avg} = \left(0.16\frac{\mu m}{min}\right)(D_{HPDM} nm^{-1})^{1/4}$$

The nature of this scaling suggests that reduction of HPDM diameter may be one means of improving HPDMs' utility as molecular sensors; If HPDM mobility is used as a readout with stalling corresponding to the detection of a target molecule of interest, then it is desirable to have 1) high baseline velocity, which both ensures that the stalling event results in a larger change in the readout metric and also ensures that target molecules are sampled at a higher rate, and 2) low force, which ensures that a smaller number of target molecules (ideally 1) can stall an HPDM without being ruptured. These results suggest that decreasing diameter decreases F_{HPDM} to a larger extent than it decreases v_{avg}. Put another way, a 50% reduction in diameter results in a 50% reduction in F_{HPDM} but only decreases v_{avg} by ~10-20%. However, HPDM diameter must remain large enough for them to be seemed using a brightfield microscope, and low polyvalencies (which can result from decreased diameter)

increase the possibility of spontaneous bond rupture. Therefore, future efforts to use decreased-diameter HPDMs as more sensitive molecular sensors will likely need to balance these tradeoffs.

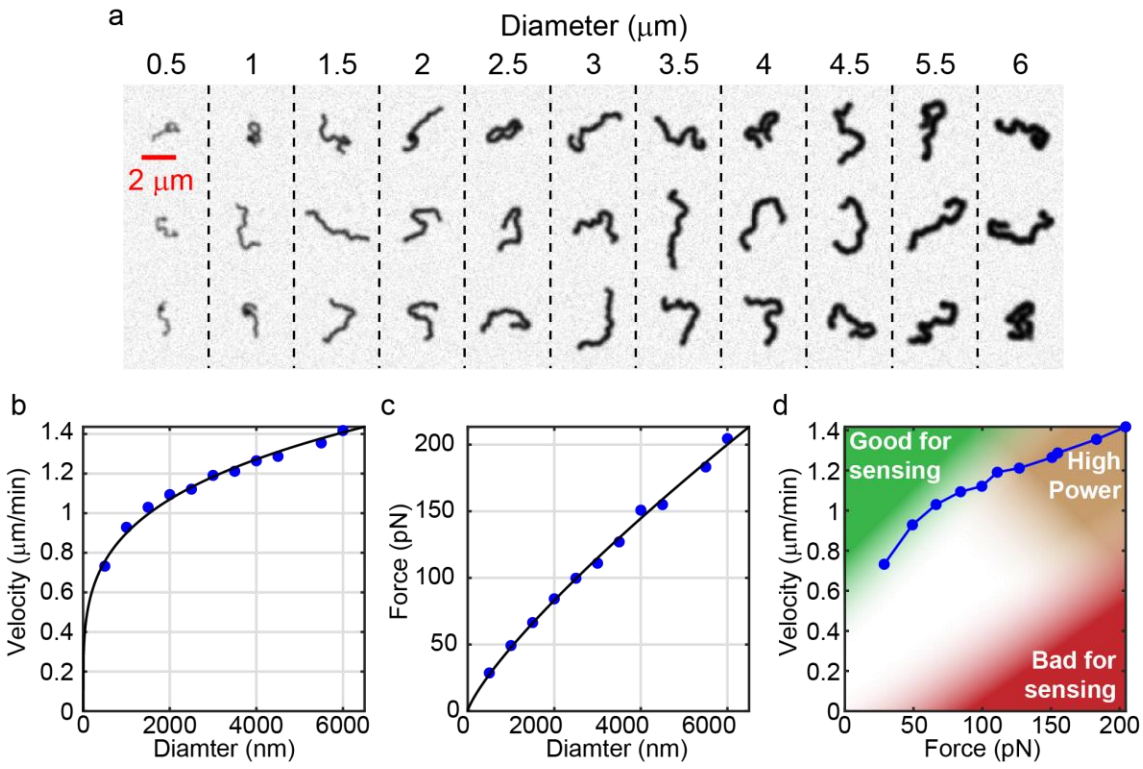

Figure 44: Dependence of F_{HPDM} and v_{avg} on HPDM diameter

a) Montage of depletion tracks obtained with ten different HPDM diameters ranging from 500 nm to 6,000 nm. **b,c)** Plots of average velocity (b) and F_{HPDM} along with power-law fit curves. **d)** Plot of Velocity vs. force, along with color depiction of regimes on this plot that are good/bad for molecular sensing or that provide a high mechanical power output.

3.5.5 The effect of RNA fuel and DNA guide density on F_{HPDM} and v_{avg}

We next investigated the effect of RNA fuel and DNA guide strand density on HPDM translocation and force-generation. We ran 100 simulations – one at each combination of fuel and guide densities (ρ_{fuel} and ρ_{guide}) ranging in 10% increments from 10% to 100% of the experimentally measured density (**Figure 45**). Our results reveal a near-linear dependence of F_{HPDM} on both ρ_{fuel} and ρ_{guide}, and fit well ($R^2 = 0.975$) to the relationship:

$$F_{HPDM} = (10^{-5} pN)\left(\rho_{guide} * \rho_{fuel}\left(\frac{\mu m^2}{strands}\right)^2\right)^{3/4}$$

However, the dependence of v_{avg} on both ρ_{fuel} and ρ_{guide} was not quite as straightforward; v_{avg} was positively correlated with ρ_{guide} and negatively correlated with ρ_{fuel}. v_{avg} can be approximated with moderate accuracy ($R^2 = 0.91$) with the function

$$v_{avg} = \left(2\frac{\mu m}{min}\right)\left(\frac{\left(\rho_{guide}\frac{\mu m^2}{strands}\right)^{\frac{1}{5}}}{\left(\rho_{fuel}\frac{\mu m^2}{strands}\right)^{\frac{1}{4}}}\right)$$

These results suggest that decreasing ρ_{fuel} and ρ_{guide} have different overall effects; while decreasing ρ_{guide} decreases both F_{HPDM} and v_{avg}, decreasing ρ_{fuel} decreases F_{HPDM} and increases v_{avg}. In the latter case, both effects drive the HPDM towards a parameter space that we identified in the previous section as favorable for molecular sensing purposes (high speed, low force). In fact, decreasing ρ_{fuel} from $50{,}000\ strands/\mu m^2$ 10-fold to

5,000 $strands/\mu m^2$ while preserving ρ_{guide} at 91,000 $strands/\mu m^2$ reduces F_{HPDM} to ~23 pN – which is sufficient for single molecule detection of high-affinity bonds such as DNA duplexes or high-affinity antibody-antigen interactions – and almost double v_{avg} from 1.3 μm to 2.5 μm.

As mentioned at the close of the previous section, anything that reduces the average polyvalency of the HPDM may also result in an increase in the rate of spontaneous HPDM detachment – which is bad. Furthermore, RoloSim does not model nonspecific interactions between the HPDM and the substrate, but the persistent presence of immobile particles in HPDM tracking experiments suggest that some fraction of HPDMs stick to the surface via nonspecific interactions. It is possible that reducing ρ_{fuel} may alter the nature of these interactions. Furthermore, it is possible that, as with all results presented here, these results are simple not accurate due to discrepancies between experimental observation and our simulation results. This is particularly important to keep in mind when considering for these ρ_{fuel}-dependent results because the experimentally measured track depth is ~50%, while here it is ~100%. Nonetheless, our results suggest that reducing ρ_{fuel} while maintaining high ρ_{guide} may be an effective strategy for using HPDMs as effective molecular sensors.

d

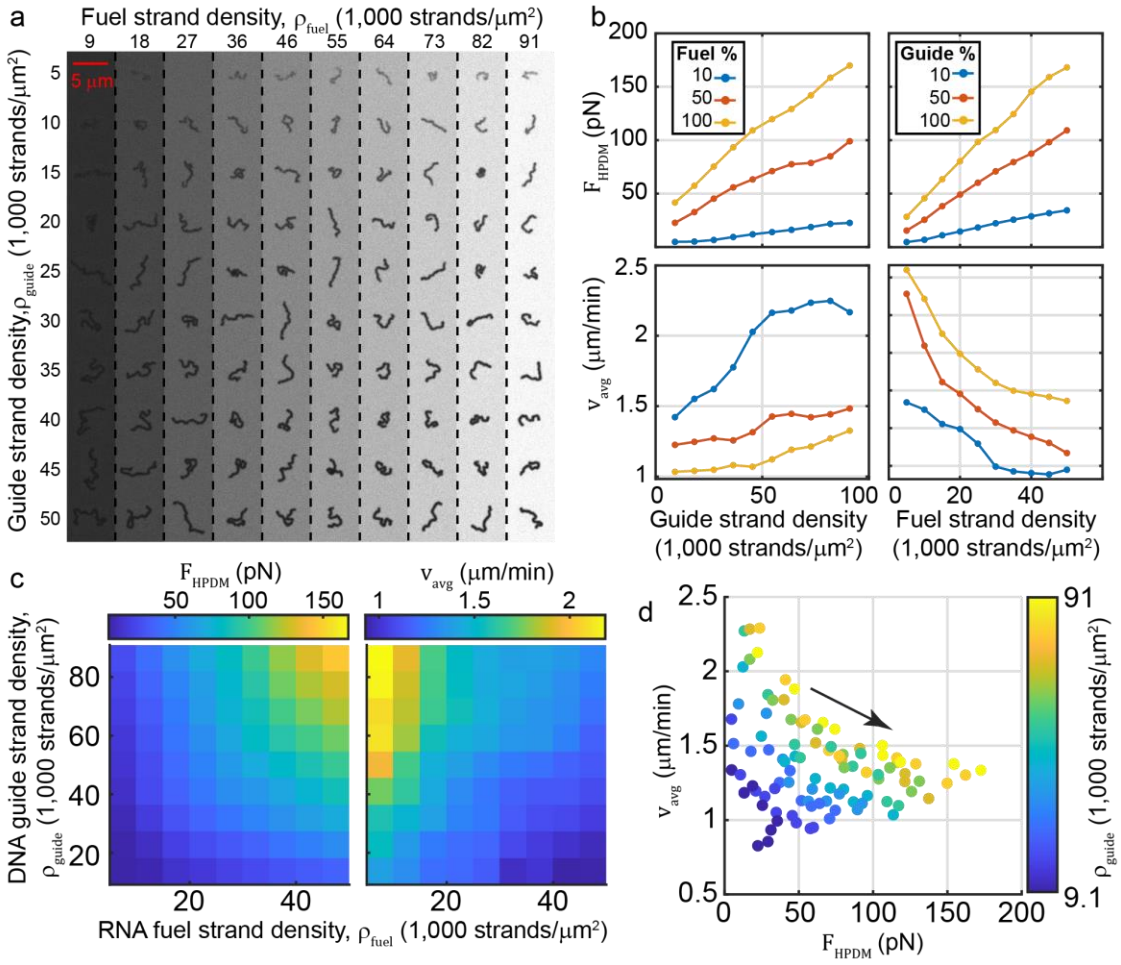

Figure 45: Dependence of F_{HPDM} and v_{avg} on RNA fuel and DNA guide density

a) Montage of simulated depletion tracks obtained with varying DNA guide and RNA fuel strand surface densities. **b)** F_{HPDM} and v_{avg} as a function of guide strand density (left) and fuel strand density (right) at three representative fuel strand and guide strand densities, respectively. **c)** Surface plots showing F_{HPDM} and v_{avg} as a function of guide and fuel strand density. **d)** Plot of v_{avg} vs. F_{HPDM}, with color depicting guide strand density and a

black arrow showing the general direction along which fuel strand density generally increases.

3.5.6 Simulations of rod-shaped HPDMS (rHPDMs)

Our studies of HPDMs thus far have focused on sphereical HPDMs, but rod-shaped HPDMs (rHPDMs) offer a means of substantially reducing HPDM size. To understand the characteristics (v_{avg} an F_{HPDM} in particular)) of rHPDMs, we used RoloSim to simulate rods (specifically, cylinders with spherical tips) with diameters (D_{rod}) ranging from 100 nm to 1,000 nm and lengths L_{rod}) ranging from 200 nm to 2,000 nm (**Figure 46**). Interestingly, our results suggest that rod diameter is much more important than rod length in determining both v_{avg} an F_{HPDM}; while increasing diameter increased both F_{HPDM} and v_{avg} in a near linear manner, increasing rod length decreased v_{avg} and had a very mild effect on F_{HPDM}. We found that F_{HPDM} could be accurately described ($R^2 = 0.986$) by the equation

$$F_{HPDM} = (0.5\ pN)\left((D_{rod}\ nm^{-1})^{4/5}(L_{rod}\ nm^{-1})^{1/14}\right) - 11.4\ pN$$

Which illustrates the minimal dependence of F_{HPDM} on L_{rod} but the strong dependence on D_{rod}. We found the v_{avg} could be accurately described ($R^2 = 0.957$) by the equation:

$$v_{avg} = \left(0.1466\,\frac{\mu m}{min}\right)\left(\frac{(D_{rod}\ nm^{-1})^{3/5}}{(L_{rod}\ nm^{-1})^{1/3}}\right)$$

Importantly, rHPDM offer a means of taking the force-generating properties of autochemophoresis to a much smaller length scale than is currently possible. For example, the rHPDM with $D_{rod} = 700\ nm$ and $L_{rod} = 600\ nm$ is generates a similar level of force ($F_{HPDM} = 150\ pN$) to 5 μm spherical HPDMs, but is ~160x smaller by volume (or 280x if the spherical caps – which largely do not contribute to rHPDM motion – are removed).

These initial findings provide a pessimistict outlook for the possibility of creating nanoscale autochemophoretic motors that can generate force in the high pN range (e.g. <100 nm in their smallest dimension). Because rods with $D_{rod} = 100\,nm$ never generate more than ~20 pN of force, long thin rods do not appear to be capable of producing arbitrarily high forces. In theory, short wide "rods" (e.g. $L_{rod} = 100\,nm,\ D_{rod} = 1{,}000\,nm$) may be capable of generating high forces, but such "cheese-wheel" type rods would have very large volumes because they'd be micron-scale in two dimensions, which essentially defeats the purpose. In theory, F_{HPDM} could be increased for thin rods by decreasing $[RNase\ H]$ (**Figure 43**), at the cost of v_{avg}.

Finally, it's important to note that this discussion would likely be slightly different if rHPDMs had been simulated without spherical caps (this will be the subject of future work).

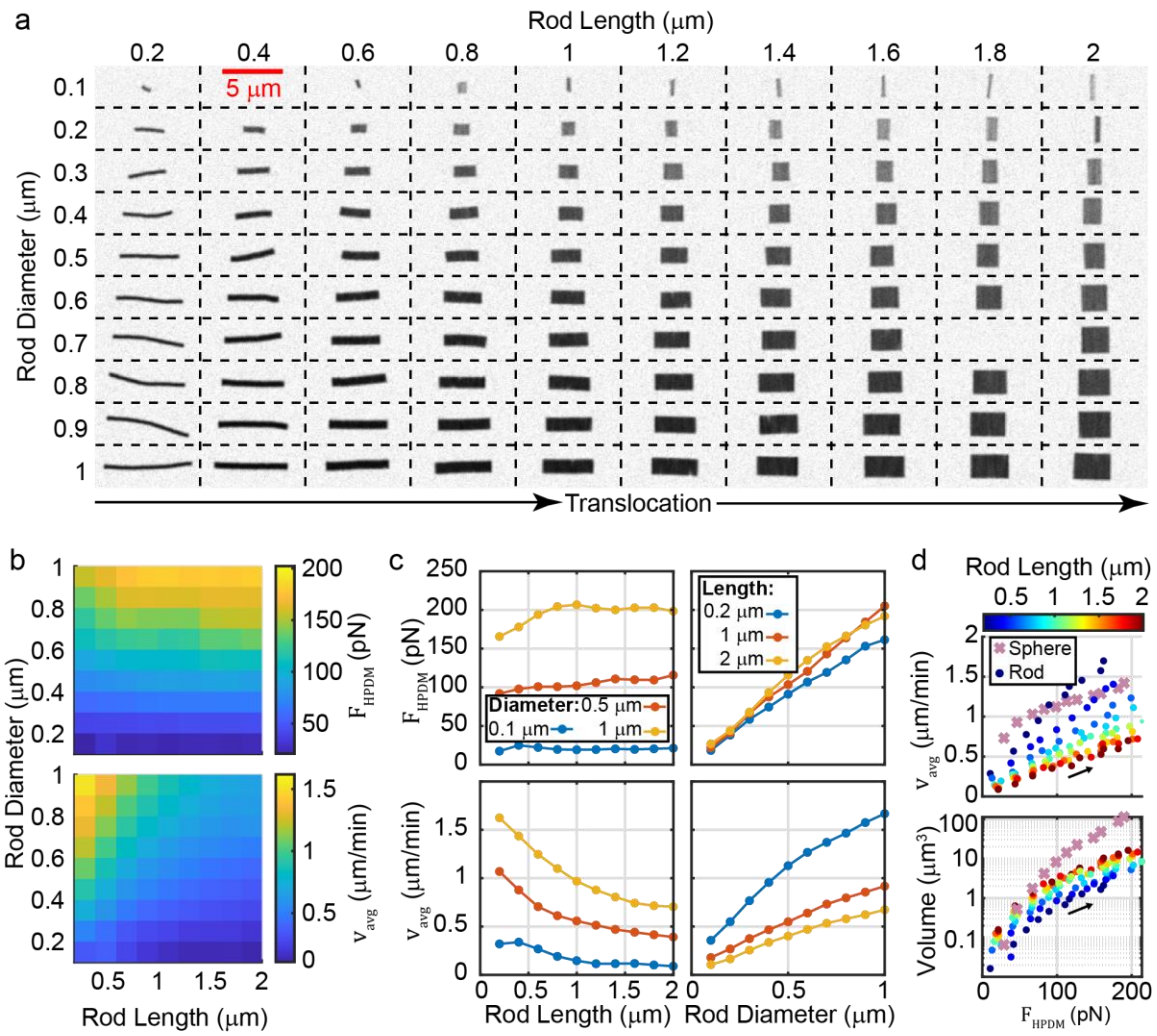

Figure 46: Results of simulations of rod-shaped HPDMs (rHPDMs)

a) Montage of simulated depletion tracks obtained with varying rHPDM lengths and diamters. The direction of translocation is generally right to left or left to right (not up/down). **b)** Surface plots showing F_{HPDM} and v_{avg} as a function of rod length and rod diameter. **c)** F_{HPDM} and v_{avg} as a function of rod lengths (left) and rod diameters (right) at three representative rod diameters and rod lengths, respectively. **d)** Scatterplots of v_{avg} and HPDM volume vs. F_{HPDM} with color depicting rod length and black arrows showing the general direction along which rod diameter increases. The results of spherical HPDMs are

shown as x's. Note the high difference between the volume of spheres and rods (plotted on a log-scale) at similar force levels.

3.5.7 HPDM motion with a biasing force

To complete this initial adhesive dynamics study of HPDM translocation, we investigated the effect of a biasing force on HPDM translocation. Because HPDMs "write" as they translocation by removing RNA fuel (or by depositing molecules through mechanical bond rupture[1]), the ability to control HPDM direction would enable a new form of highly parallel nanolithography. However, it is unclear whether HPDM directionality can be controlled using an external biasing force. To address this question, we used RoloSim to evaluate the effect of an externally applied biasing force on HPDM motion. We ran seven iterations at each of 11 biasing force magnitudes, ranging from 0 pN to 100 pN. At each condition, we quantified L_{traj} and v_{avg} to assess the extent to which the biasing force directs and speeds HPDM translocation.

Our results (**Figure 47**) suggest that HPDM motion can be directed using a biasing force. A force of 1 pN results in no discernable change in directionality, L_{traj}, or v_{avg}. However, a force of 3 pN creates a clear bias in HPDM motion towards the direction of the force. This bias magnitude does not result in a notable increase in v_{avg} and tracks still exhibit many notable deviations from the most favorable direction of translocation, but there is an notable increase in L_{traj}. A biasing force of 6 pN further increases L_{traj} and further increases the directional appearance of the depletion track. A biasing force of 10 pN results in a notable increase in L_{traj} and v_{avg} and also appears to result in periodic detachment from the depletion track. Forces above 10 pN result in exponentially increasing L_{traj} values, linearly increasing v_{avg} values, and an increased frequency of apparent detachment events.

The apparent detachment events appear to be an artifact of the manner in which RoloSim handles detachment; when the polyvalency reduces to zero, the HPDM undergoes planar Brownian motion until a new tether forms. In other words, the HPDM is not allowed to detach and irreversibly flow away from the surface following detachment of the final tether, as would be expected to happen in reality. Accordingly, our RoloSim results suggest that as little as 10 pN can result in complete detachment of HPDMs from the surface. Nonetheless, our results suggest that there may be a biasing force range that can steer HPDMs without causing them to detach from the surface.

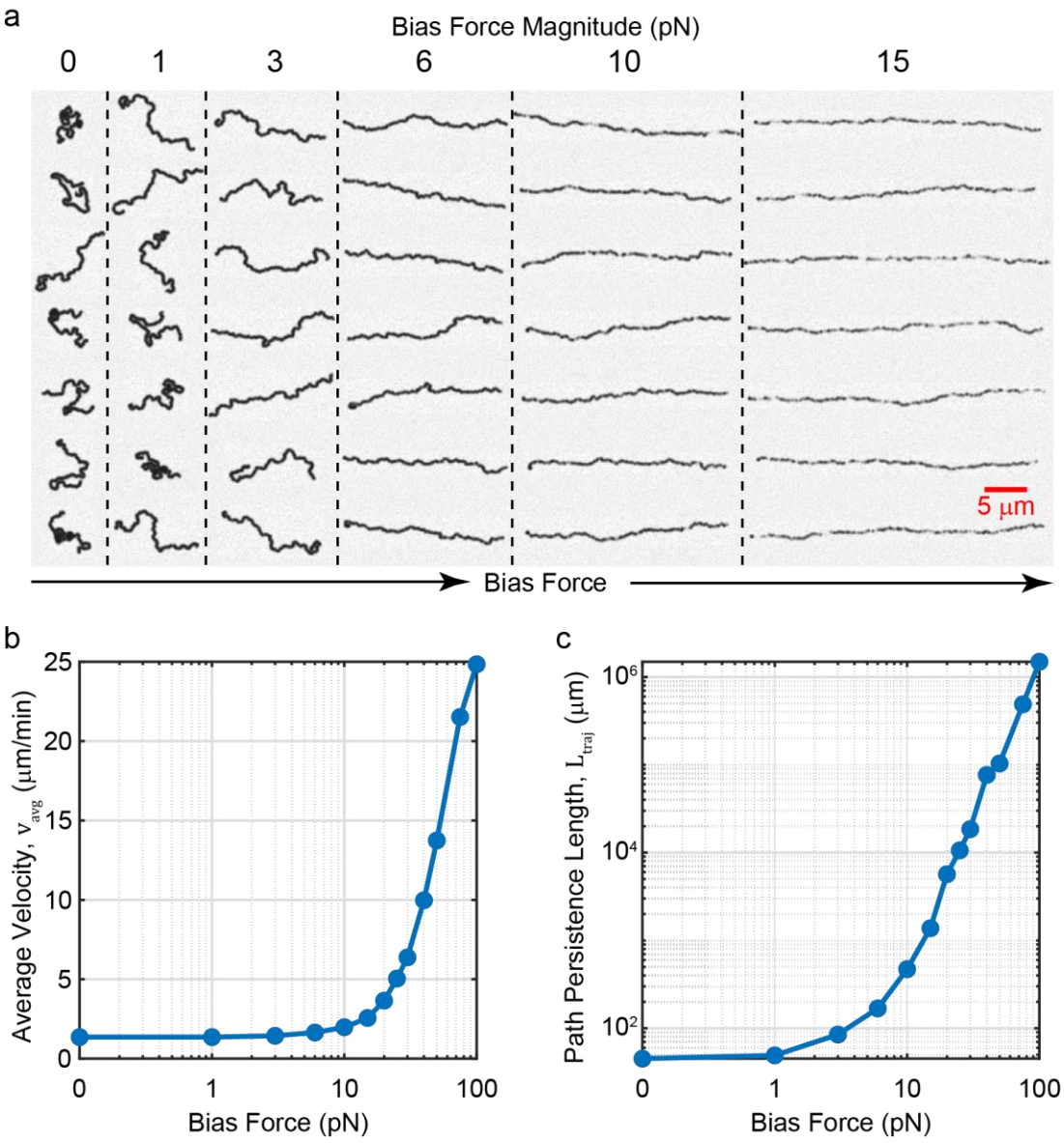

Figure 47: Simulation results of HPDM translocation in the presence of a biasing force

a) Montage of simulated depletion track images from simulations of HPDMs rolling in the presence of biasing forces (pointing to the right) at varying force magnitudes. **b,c)** Quantification of v_{avg} and L_{traj} as a function of the bias force magnitude.

To assess the accuracy of this final prediction, we imaged HPDMs rolling under standard conditions ([RNase H]=144 nM, 100% RNA fuel and DNA guide, 5 μm diameter sphereical HPDMs) while applying a biasing force using flow. We applied flow rates (Q) ranging from 200 $\mu L/min$ to 1,000 $\mu L/min$ and imaged HPDMs for 10 minutes.

At the condition of $Q = 1{,}000\ \mu L/min$, we found that HPDM motion was biased towards the direction of flow in a parallel fashion. To illustrate this, we imaged depletion tracks after 10 minutes of flow followed by 10 minutes of rolling in the absence of flow. We used ibidi µ-Slide VI 0.4 for this study, which has rectangular channels 3.8 mm in width and 0.4 mm in height. This cross sectional area and flow rate results in an average flow velocity of ~11 mm/s. Assuming parabolic flow, (which is reasonable given the channel's small aspect ratio[130]), the velocity at a height of 2.5 microns is

$$v_{flow} = \left(.011\frac{m}{s}\right)\left(1 - \left(\frac{200\mu m - 2.5\mu m}{200\mu m}\right)^2\right) = .00041\frac{m}{s}$$

Which, using Stokes law:

$$F_{bias} = 6\pi(.0000025\mu m)\left(1\frac{N\,s}{m^2}\right)\left(.00041\frac{m}{s}\right) = 19\ pN$$

Yields $F_{bias} = 19\ pN$.

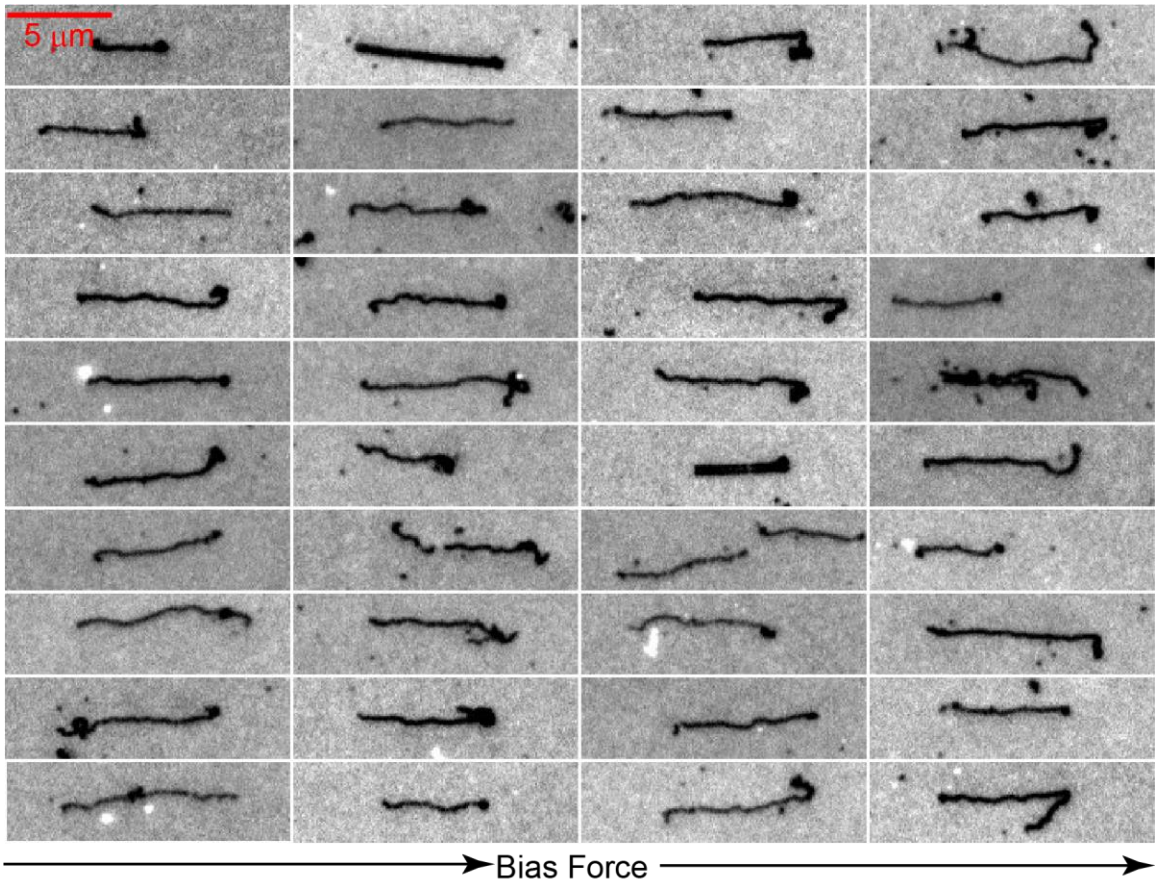

Figure 48: Images of depletion tracks following HPDM translocation with flow-based bias force

This figure show 40 depletion tracks collected after ten minutes of HPDM translocation in the presence of flow, followed by ten minutes of HPDM translocation in the absence of flow. The direction of flow was from left to right, and it was performed at a flow rate of 1,000 $\mu L/min$. According to our calculations above, this flow rate corresponds to a force of $F_{bias} = 19pN$. The depletion tracks generally reveal ~5-10 μm of translocation from left to right, followed by random self-avoiding translocation.

CHAPTER 4. FLUORESCENCE POLARIZATION-BASED TRACTION FORCE ORIENTATION MAPPING WITH DNA MECHANOTECHNOLOGY AND STRUCTURED ILLUMINATION MOLECULAR FORCE MICROSCOPY

This chapter is an adaptation of a manuscript that I am preparing (as first author) at the time of this writing. While previous chapters have focused on DNA mechanotechnology for generating forces, this work focuses on DNA mechanotechnology tension probes for mapping pN-scale traction forces. The work builds on my co-first author manuscript from the early part of my PhD[45], in which we presented the first technique for mapping the orientation of molecular traction forces with fluorescence polarization microscopy.

4.1 Summary

Piconewton (pN)-scale mechanical forces regulate many cellular processes via mechanosensitive receptor proteins at the plasma membrane. Molecular tension probes are central tools for the visualization and control of these molecular forces. We recently presented molecular force microscopy (MFM) which combines fluorescence polarization microscopy with DNA hairpin-based molecular tension probes to report on the 3D orientation of receptor forces. MFM enables mapping of pN-scale cellular traction force orientation with the highest spatial and temporal resolution presented to date. However, fluorescence microscopes are generally not equipped to perform the polarization modulation necessary for MFM. Some microscopes may be customized to incorporate polarizing components, but such modifications are not always possible and require a level

of technical expertise that may be prohibitive. Here, we present one solution to this challenge by demonstrating that MFM can be implemented using conventional structured illumination microscopy (SIM). SIM microscopes are relatively common and are maintained by core facilities at many research institutions. We show that SIM-MFM leverages the inherent polarization modulation associated with SIM imaging to report on force orientation. Our results of cellular experiments show that SIM-MFM can reproduce our previous observations while increasing the temporal resolution of image acquisition ~3.6-fold. In addition, our results reveal novel insight into the dynamics of platelet traction and the nature of T-cell receptor traction forces. Because SIM was originally designed as a superresolution technique, we also show that SIM-MFM can produce superresolution force orientation maps with ~2-fold higher spatial resolution than conventional MFM. Furthermore, we demonstrate the integration of SIM-MFM with single molecule imaging to report force PAINT (fPAINT), which allows for the measurement of the orientation of forces applied through integrins at the single molecule level. Importantly, no modifications to existing SIM microscopes are necessary, thus making MFM and fPAINT available to anyone with access to a SIM microscope.

4.2 Introduction to molecular force microscopy

Forces exerted through receptor proteins at the cell-surface interface – or traction forces – regulate a wide variety of essential processes in mammalian cells, including stiffness sensing, cell migration, immune recognition, and coagulation[5]. These cellular-level processes scale up to regulate large tissue-level or even systemic responses such as tissue formation, embryogenesis, clot contraction, and the immune responsem. Accordingly, traction forces are of broad interest to mammalian biologists.

Molecular tension probes (MTPs) have recently emerged as powerful tools for quantifying and visualizing traction forces. These probes, which generally consist of an extensible "molecular spring" flanked by a fluorophore-quencher pair, are generally conjugated onto a substrate such as a glass coverslip. Cells are then cultured on top of them. The tops of the MTPs present ligands that cell receptors (e.g. integrins) can bind to, and traction forces exerted through the cell receptors open the MTPs, resulting in dequenching of the fluorophore (**Figure 49**a). Fluorescence imaging is then used to reveal where forces are being applied by the cell. This approach offers roughly an order of magnitude improvement in spatial and temporal resolution over previously-presented techniques (which generally track cell-induced deformation of soft substrates). However, until recently MTPs could only be used to report on force magnitude, without reporting on force orientation. Recent work has increasingly shown the importance of force orientation in receptor mechanosensation, with the TCR, integrins, and vinculin all acting as orientation-dependent mechanosensors[44,131,132].

We overcame this limitation with the development of molecular force microscopy (MFM)[45], the first technique for mapping molecular force orientation with MTPs. MFM is enabled by the combination of DNA mechanotechnology[133]-based tension probes, which consist of DNA hairpins flanked by organic fluorophores, with fluorescence polarization microscopy. DNA hairpins are incredibly precise because they offer a nearly-"digital" force response; a DNA hairpin MTP can exist in one of two states – folded or unfolded – and the fraction of time spent in the folded state decreases from ~95% to ~5% over a narrow force range of 2-3 piconewtons (pN) centered on the MTPs $F_{1/2}$ (defined as the force where the probe spends equal time in each state). $F_{1/2}$ can be tuned from ~2 pN to ~19 pN by

adjusting the length and GC content of the hairpin. Due to highly efficient quenching, the fluorescence intensity of the opened stated is ~30-100x brighter than that of the closed state.

The fluorophore most commonly used in DNA hairpin MTPs, cyanine 3b (Cy3b), has two properties that make MFM possible: First, Cy3b, like most fluorophores, has a transition dipole moment that can be approximated as the 3-dimensional (3D) vector **μ** (**Figure 49**b)[45]. The intensity (*I*) of a fluorophore excited by plane-polarized excitation light (which has a fixed polarization vector denoted by **E**) can be described by the relationship:

$$I \propto \langle \cos^2(\psi) \rangle \quad (1)$$

where ψ is the angle between **μ** and **E** and ⟨ ⟩ denote ensemble averaging across the probability distribution of orientations that **μ** adopts over time. When **E** is rotated (e.g. by placing a rotatable half wave plate in the path of the excitation beam) and multiple images of a sample are taken with different ***E*** orientations, the set of *I* values for each pixel that can be used to calculate the average fluorophore orientation in that pixel.

Second, when Cy3b is covalently coupled to the terminus of a DNA duplex, it inherently stacks perpendicular to the duplex's long-axis[134]. This property, and the nature of our MTP design, cause Cy3b to align itself such that ***μ*** is perpendicular to the long axis of the opened probe (**Figure 49**b). Because probe orientation is controlled by force orientation, ***μ*** is therefore perpendicular to the force vector ***F***. Assuming the MTP can freely rotate around its long axis, then **μ** can take an ensemble "disk" of orientations perpendicular to ***F***. As such, fluorescence intensity can be described by the equation:

$$I = A\sin^2(\alpha - \phi) + c \quad (2)$$

where ϕ and α are the in-plane angles of the $\boldsymbol{F}$ and $\boldsymbol{E}$, respectively (**Figure 49**b) and A and c are scaling constants that depend on the tilt angle of the force, θ (**Figure 49**b) and the number of opened MTPs. We previously derived[45] an equation to roughly calculate θ:

$$\theta = \cos^{-1}\left(\sqrt{\frac{\frac{c}{A+c} - 0.069}{0.931}}\right) \quad (3).$$

In our initial implementation of MFM[45], we utilized a rotating HWP to vary α continuously and recorded a series of 73 images over the course of ~3.2 seconds. We then used least-squares residuals fitting to fit the intensity values for each pixel to equation (2). However, because eqn. (4) has three unknown fit parameters (ϕ, θ, and A), three unique α values (e.g. $\alpha = 0°$, $60°$, and $120°$) would technically be sufficient to obtain a unique best-fit curve analytically (**Figure 49**c).

The diffraction-limited resolution of MFM is an order of magnitude improvement over previous techniques such as traction for microscopy. However, many physiologically-important force-bearing structures – such as focal adhesions[135], lamellipodial protrustions[44], t-cell receptor clusters[46], and podosomes[136] – are only a few hundreds or tens of nanometers (nm) in their smallest dimensions. Accordingly, tools for superresolution MFM are desirable.

An additional limitation of MFM is the requirement for a microscope setup where α can be modulated freely. The modifications necessary for MFM can easily be made to many custom-built microscopes with free-standing laser lines. However, the addition of an

adequate polarization modulator to the excitation path is impossible using many common commercially available microscopes that eliminate free-standing optical components to ensure compaction and reliability. Accordingly, MFM as a technique is technologically inaccessible to a large proportion of researchers that could otherwise tap into the power of the technique.

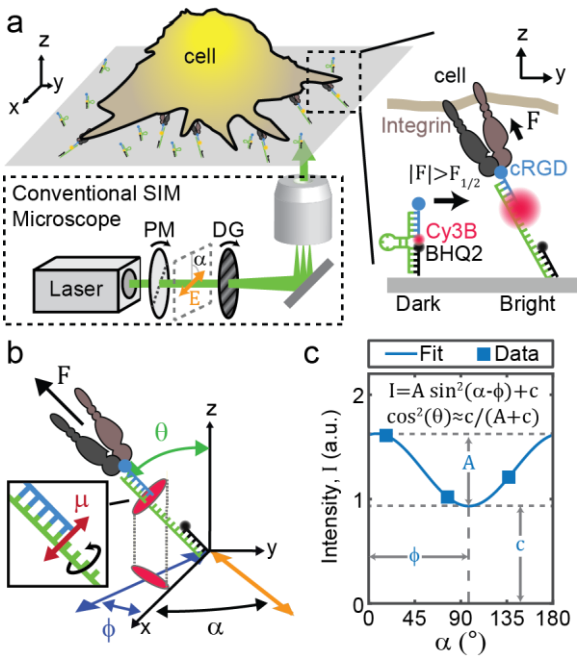

Figure 49: SIM-MFM concept

a) Diagram showing simple microscope setup and DNA hairpin-based tension probe function. We show the basic components of a SIM microscope excitation line: a linear polarized laser passes through a polarization modulator (PM) and diffraction grating (DG). These two components rotate together such α (the angle of the laser beam's electric field vector, $\boldsymbol{E}$) is the same as the orientation of the striping pattern created by the DG. Inset shows a DNA hairpin-based tension probe (blue, green, and black DNA strands) transitioning from a closed state to an opened state upon application of tension (of magnitude F) exceeding the probe's $F_{1/2}$ value. Cell receptor (brown and gray) is an integrin and the ligand (blue circle) is cRGD. **b)** Illustration of $\boldsymbol{F}$ (black arrow) and $\boldsymbol{E}$ (orange dipole) angles used in this work. Inset shows Cy3b transition dipole moment ($\boldsymbol{\mu}$) perpendicular to the long axis of the tension probe. **c)** Representative data and curve fit

from a pixel indicated in **Figure 51**c. A, c, and ϕ are illustrated and equations used to obtain curve fit from data are shown.

In this work, we demonstrate a new method for implementing MFM using conventional structured illumination microscopy (SIM). SIM is an increasingly-utilized superresolution fluorescence imaging modality that achieves a two-fold increase in spatial resolution by exciting fluorescent samples with a structured pattern of excitation light. Many research institutions maintain SIM microscopes within core facilities or within a small number of research labs. Importantly, SIM-MFM can be implemented without any modification to properly-maintained SIM microscope setups because a central property of SIM is polarization modulation (**Figure 49**a).

SIM works by using diffraction grating to create an excitation beam illumination pattern that varies sinusoidally in one dimension. The sinusoidal interference pattern is then shifted back and forth, generally for a total of three or five images with different phase shifts. The orientation of the illumination pattern is then rotated and this process is repeated at two or more distinct illumination pattern angles, resulting in a minimum of nine images (if three phases per stripe orientation are used) or fifteen images (if five phases per stripe orientation are used). These images are then processed using a reconstruction algorithm to produce a single image with a two-fold improvement in spatial resolution when compared to widefield epifluorescence. Importantly, the sinusoidal diffraction pattern can only form properly when excitation light is linearly polarized with **E** parallel to the striping orientation. Therefore, when the striping orientation is modulated, so is α (**Figure 49**a). Accordingly, polarization modulation is a fundamental characteristic of SIM. Recently, Zhanghao *et al.* leveraged this property of SIM to measure the orientation of samples of oriented fluorophores[137] in super resolution. We hypothesized that we could use the same approach to implement superresolution MFM.

To test whether SIM could be used to implement MFM, we first verified the inherent polarization modulation of our SIM microscope by imaging a standard sample: microspheres coated with tetramethylindocarbocyanine (DiI)-doped supported lipid bilayers (SLBs). DiI is a cyanine dye (similar to Cy3b) linked to two lipid tails that spontaneously insert into SLBs, such that $\boldsymbol{\mu}$ should be parallel to the microsphere's surface. As expected, we observed a sinusoidal variation in I around the perimeter of the microsphere, with maximal intensity corresponding to the spot where $\boldsymbol{\mu}$ was aligned with the striping pattern. As α varied during each SIM acquisition, the sinusoid shifted by a commensurate amount, thus confirming that the polarization modulates with the direction of the stripe pattern for our SIM microscope at an interval of ~60° .

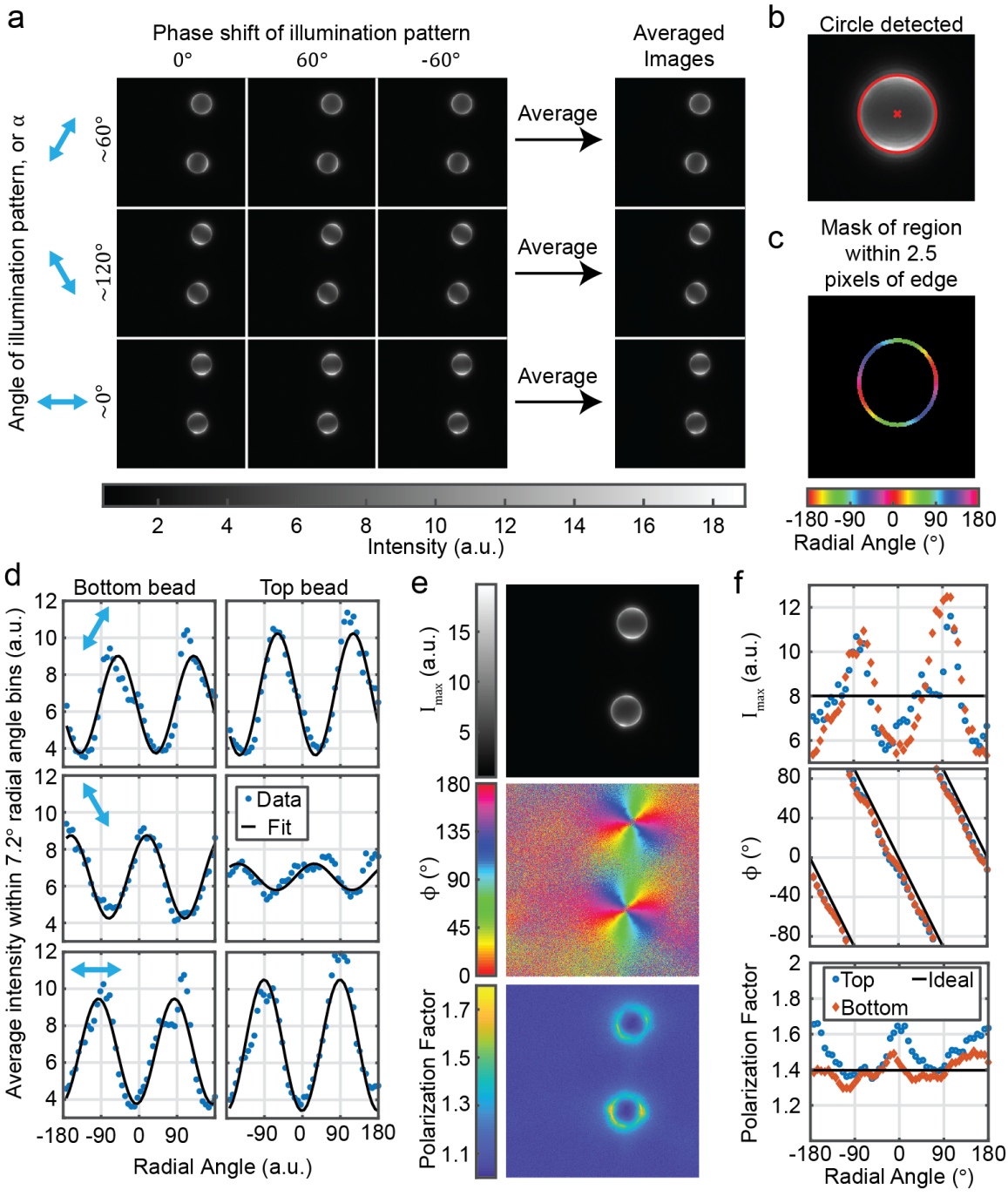

Figure 50: Analysis of DiI-doped SLB-coated microspheres imaged using SIM microscope.

a) Raw 2D SIM images of DiI-doped supported lipid bilayer (SLB)-coated silica microspheres. **b)** Automatic detection of spheres using MATLAB's imfindcircles()

command. **c)** Mask used for subsequent analysis. Mask is colored by the radial angle, which is used as a coordinate for subsequent analysis (in this scenario, ϕ should be equal to the radial angle). **d)** fluorescence intensity as a function of radial angle for each of the two beads in the image. Each blue point represents the average value within one of 50 bins. **e)** I_{max}, ϕ, and the polarization factor ($(A + c)/c$) calculated for every pixel in the image. **f)** Quantities in **e** calculated as a function of radial angle is in **d**. I_{max} and the polarization factor should not exhibit variations with respect to radial angle, but do – likely an artifact due to the index of refraction mismatch between the bead and the surrounding buffer.

We next tested whether SIM could be used to implement MFM. We prepared a typical DNA hairpin-based MTFM experiment by conjugating DNA tension probes ($F_{1/2} = 4.7$ pN) presenting cyclic arginine-glycine-asparagine (cRGD, a peptide that binds $\alpha_v\beta_3$ integrin receptors with high affinity[138]) to a glass coverslip through biotin-streptavidin binding. Previous surface density calibration of surfaces prepared in this manner[45] revealed a density of ~700 tension probes per square micron. We cultured human platelets – an easy-to-work-with model system – on top of these surfaces. Within ~10-20 minutes, platelets sedimented onto the surface. Contact between the platelets' integrins and the cRGD ligands promoted integrin activation and initiated platelet spreading and contraction, resulting in tension probe opening[44]. We then collected SIM images of well-spread platelets within ~45 minutes. Typically, platelets spread out over an area $\sim 2 - 5$ μm in width and their MTFM maps generally exhibited two distinct features: an outer ring of tension, which arises from actin polymerization-based protrusion of the actin cortex, and a large inner region with lobes of tension, which arises from actomyosin contraction in the body of the platelet. We observed the same features in this experiment (**Figure 51**), confirming successful reproduction of typical MTFM experiment.

We next tested to see whether the polarization modulation of the SIM microscope could be used to measure force orientation. For our initial assessment, we used the built in "3D-SIM" function of our Nikon Eclipse Ti-based commercial SIM microscope to acquire three sets of five images (**Figure 51**a – five phase shifts at each of three striping orientations). We then simply took the average of the images acquired at each striping orientation (this

is mathematically valid due to the specific phase shifts used in SIM), resulting in three images each corresponding to a unique α value such that each pixel has three intensity values associated with it (**Figure 49**c). We then loaded the image into fairSIM[139] (an open-source ImageJ plugin for facile analysis of SIM data), which revealed striping orientations (and therefore α values) of 77°, 137°, and 17°. Accordingly, for a given pixel we designate the three intensity averages as $I_{17°}$, $I_{77°}$, and $I_{137°}$. Rather than applying least squares residuals fitting to the I vs. α curve as previously[45], we derived analytical equations (Supplemental Note 1) to rapidly obtain a unique fit to equation 2 for each pixel:

$$\phi = \frac{1}{2}\tan^{-1}\left(\frac{I_{avg} - I_{137°} - \left(I_{avg} - I_{77°}\right)\cos(120°)}{\left(I_{avg} - I_{137°}\right)\sin(120°)}\right) + 77° \qquad (4a).$$

$$A = \frac{2\left(I_{avg} - I_{137°}\right)}{\cos\left(2(77° - \phi)\right)} \qquad (4b).$$

$$c = I_{77°} - A\sin^2(77° - \phi) \qquad (4c).$$

$$\theta = \cos^{-1}\left(\sqrt{\frac{\frac{I_{max}}{c} - 0.069}{1 - 0.069}}\right) \qquad (4d),$$

Where I_{max} is the maximum intensity of the fit sinusoid:

$$I_{max} = A + c \qquad (5)$$

which is a better metric for total brightness than I_{avg} because I_{max} is (very nearly) proportional to the number of opened probes regardless of force orientation. We then

applied these calculations to the entire image set. Our initial results demonstrate successful recapitulation of force patterns that are expected for platelets, demonstrating that SIM-MFM is viable (**Figure 51**b-e).

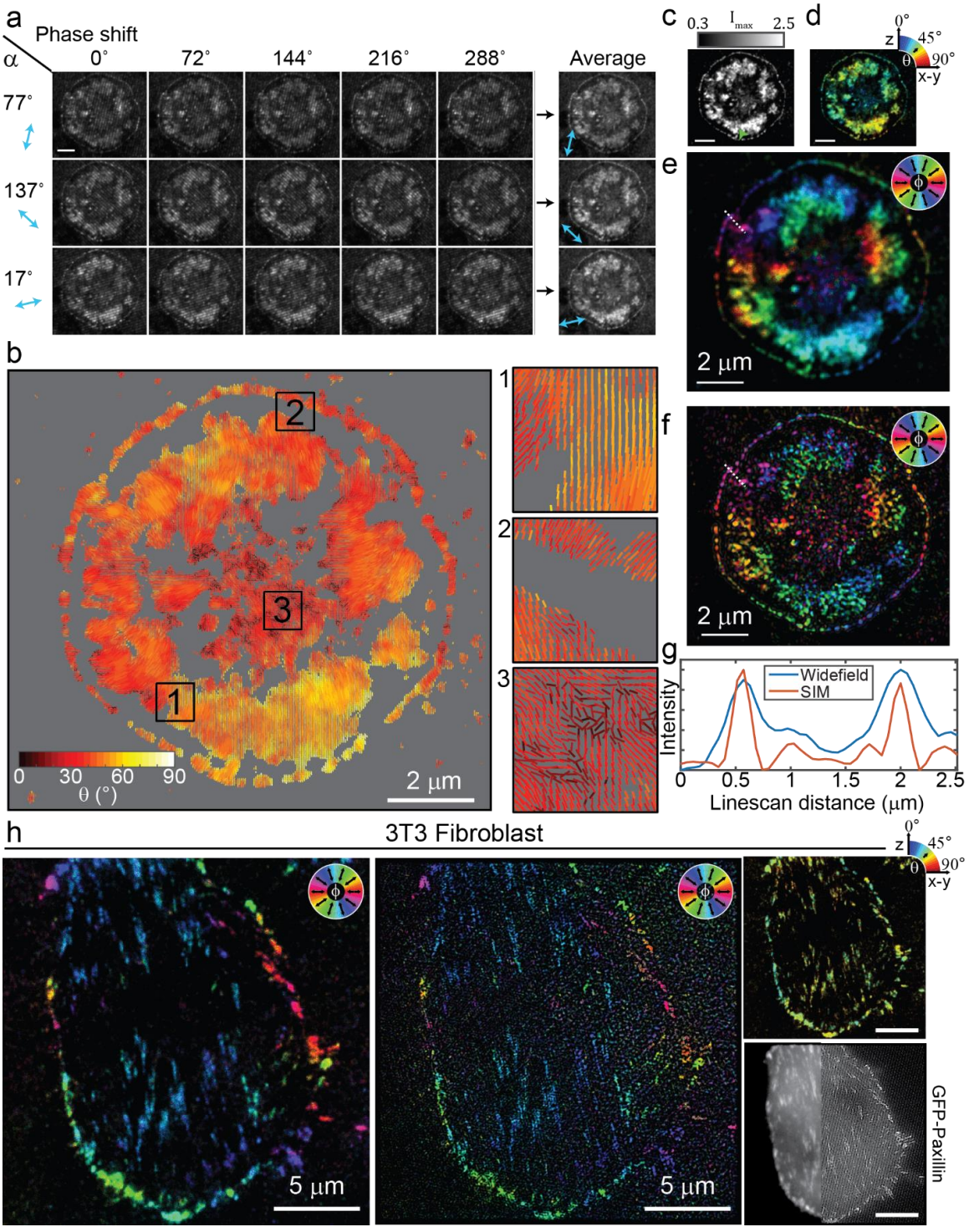

Figure 51: Representative SIM-MFM data

a) Representative raw images of a platelet imaged using SIM-MFM. Fifteen images – one at each of 5 phase shifts and 3 illumination pattern orientations – are shown. The sinusoidal diffraction pattern can be seen upon careful inspection. Scale bar is $2\,\mu m$. **b)** Dipole orientation map of the platelet, wherein each pixel with I_{max} greater than a threshold (in this case, the 60% quantile of the image) has a dipole associated with it. For each dipole, ϕ is encoded in the dipole's orientation, θ is encoded in the dipole's color, and I_{max} is encoded in the dipole's length. Insets 1-3 show zoom-ins on specific regions of the dipole map. This display method was developed in our previous work. **c-e)** Alternative colormap-based display style used in this work showing **c)** I_{max}, **d)** θ, and **e)** ϕ for each pixel. For d and e, the color reflects the measured force orientation. For all three colormaps, the brightness of each pixel is scaled to the I_{max} value shown in **c** (scale bar is $2\,\mu m$). The images were also contrast adjusted such that the brightness is bounded to the 35th and 99th percentiles of the pixels' I_{max} values. **f)** Super resolution reconstruction of the platelet. **g)** A linescan of the platelet's lamellipodial edge for both widefield (**c-e**) and superresolution (**f**), showing a ~2-fold enhancement in spatial resolution when using the SIM reconstruction. **h)** Similar to **c-f**, but for a NIH 3T3 fibroblast cell. A fluorescence image (both widefield and superresolution) of GFP-tagged paxillin (a focal adhesion protein) is shown. Scale bars are $5\,\mu m$.

We utilized two methods for displaying orientation data, both of which are shown in **Figure 51**. First, we utilized a colormap-based approach to simultaneously display I_{max} and ϕ by linking pixel color to ϕ (using the circular HSV colormap) and linking pixel brightness to I_{max} (**Figure 51**e,). To reduce the apparent magnitude of background signal for this display method, we scaled the minimum and maximum pixel brightness to the 35% and 99% quantiles, respectively, of the entire image. For this display method, θ is not represented and so we display accompanying images where pixel color is linked to θ and brightness is calculated in the same way (**Figure 51**d). Our second display method sacrifices some spatial detail in order to simultaneously show I_{max}, ϕ, and θ; we mask the image to the 60% quantile of the image and, for each pixel, plot a dipole (on a grey background) with orientation related to ϕ, length proportional to I_{max}, and color related to θ (**Figure 51**b, **Figure 52**).

The platelets that we imaged with SIM-MFM displayed many characteristics that we observed in our original MFM study. The platelets display the two distinct regions of tension; the lamellipodial edge and the inner lobe(s). As previously observed the lamellipodial edges generally display a highly isotropic radial pattern (i.e. ϕ values are generally perpendicular to the platelet's edge and point towards the centroid of the platelet) while the platelets' inner regions generally display (with a few exceptions) two to four "lobes" that appear to act as independent and internally-homogenous mechanical units. For example, **Figure 53** shows a platelet with two lobes in its inner region and a clearly visible lamellipodial edge. While the outer ring of lamellipodial tension points isotropically inward, the inner lobes display highly anisotropic contraction, with all dipoles within the lobes pointing to the central axis that bisects them. SIM-MFM also faithfully recapitulates

previously-recorded θ values; an analysis of θ values across many platelets ($n = 17$ platelets) also revealed that the average θ value, $\langle\theta\rangle$, is $47 \pm 3°$ which is similar to the value of $39 \pm 2°$ that we measured previously[45].

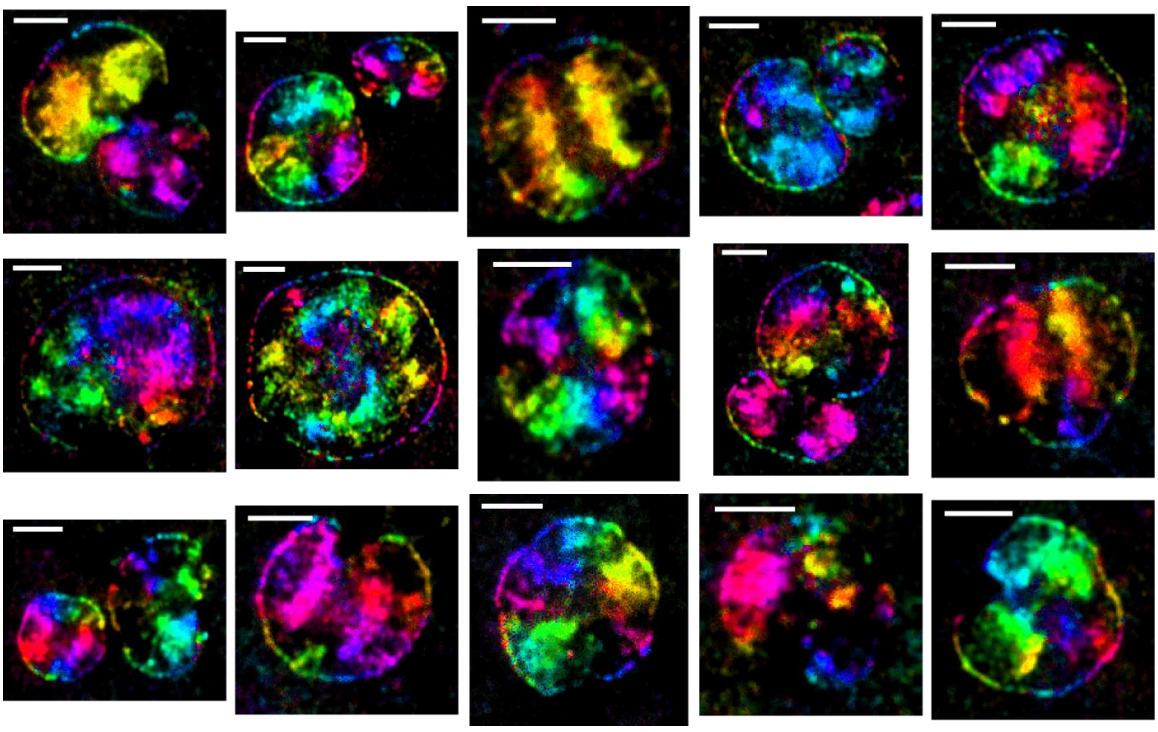

Figure 52: Azimuthal angle maps of 15 representative platelets.

Colormap-based display style. The scale bar for each image denotes 2 micrometers.

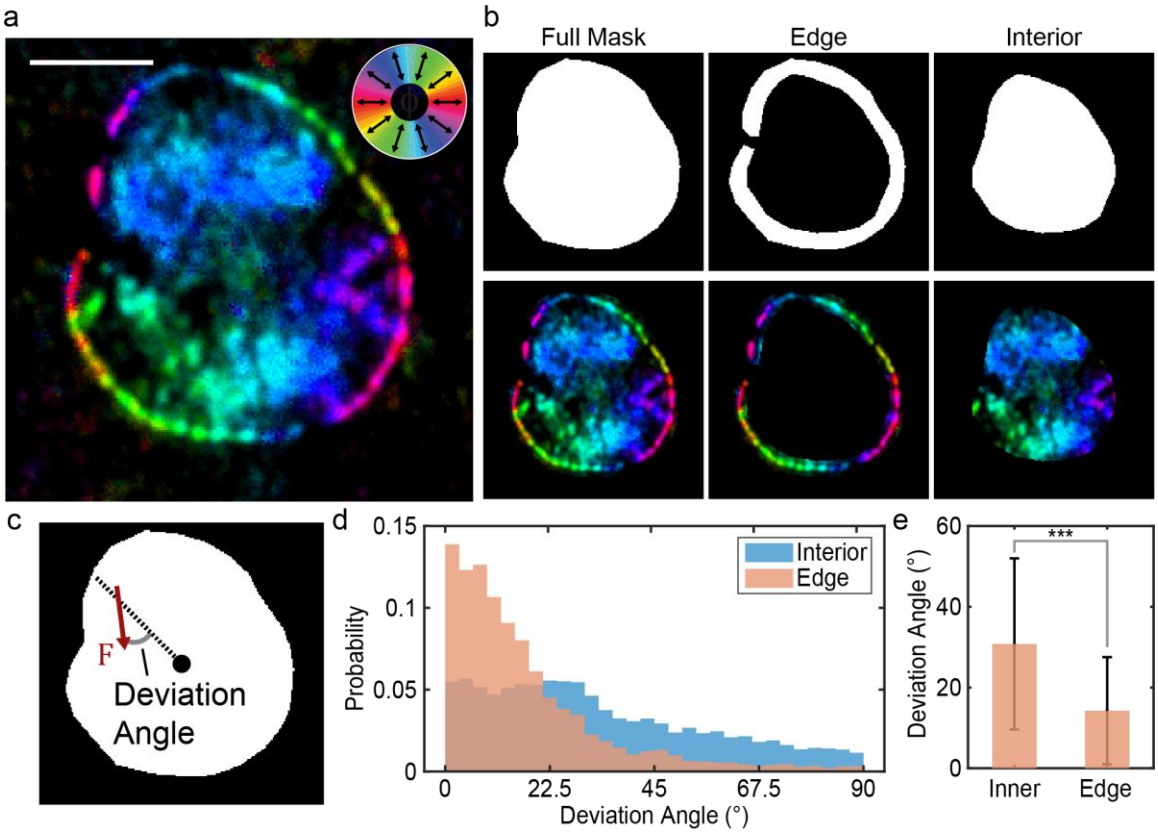

Figure 53: Reproduction of previous finding that platelets exhibit two distinct zones of force orientation.

a) Colormap-based ϕ-map of a platelet. Scale bar denotes 2 micrometers. **b)** Hand drawn masks of the full cell, lamellipodial edge, and cell interior (top) with correponsing masked ϕ-maps (bottom). **c)** Depiction of "deviation angle" used to quantify cellular alignment (deviation angle for a given pixel is the angle between the force and the axis that links the mask's centroid to the pixel's centroid). **d)** Probability istogram of deviation angle in the interior and cell edge. **e)** Comparison of the two populations for this cell. *** denotes $p<0.05$, Wilcoxon rank-sum test.

We were initially concerned that the use of only 3 α angles (compared to 73, as previously used) could potentially lead to systematic errors in θ and ϕ measurements due to inconsistencies in the effect of measurement noise on different force orientations. To examine this effect, we performed two validations. First, we conducted Monte Carlo simulations to evaluate the effect of true ϕ, θ, and I_{max} values on the accuracy of ϕ and θ measurements (**Figure 56**a). In these simulations, we generate ideal data for a given (ϕ, θ, I_{max}) combination using eqns. (2) and (4), add in noise, and then calculate ϕ^*, θ^*, and I^*_{max} (where $*$ denotes the value measured using least-squared residuals fitting). We repeat this process ~30,000 times, using randomly generated noise values each time. We then quantified systematic error (σ) and random error (ε) for θ and ϕ, as follows:

$$\varepsilon_\phi = \langle|\phi - \phi^*|\rangle \tag{6a}$$

$$\sigma_\phi = \phi - \langle\phi^*\rangle \tag{6b}$$

$$\varepsilon_\theta = \langle|\theta - \theta^*|\rangle \tag{6c}$$

$$\sigma_\theta = \theta - \langle\theta^*\rangle \tag{6d}$$

This process is described in greater detail in the online methods section in the supplementary information. Our results at the experimentally relevant signal level of $I_{max} = 1{,}000\ photons$ displayed small systematic errors in ϕ (less than half a degree across all orientations). As we observed in previous work[45], random error in ϕ was high at low θ, and systematic error in θ was high at very low and high θ. Importantly, we did not observe a substantial dependence in any form of error on ϕ. While ε_ϕ, σ_ϕ, ε_θ, and σ_θ all exhibited slight periodic variations with respect to ϕ, these variations were all smaller than

1°. This was also true when increasing I_{max} to $3{,}000\,photons$ or decreasing it to $300\,photons$. Thus, we can conclude that the use of only three α values introduces small ϕ-dependent orientation measurement errors.

To test this prediction, we plotted a histogram of ϕ values from 81 different platelets (**Figure 56**b). Ideally, all ϕ values will be measured with equal probability resulting in a flat histogram. However, consistent with the simulation predictions we observed slight systematic biases that resulted in a non-flat histogram with local minima close to $\phi = 17°$, 77°, and 137°. This small systematic error resulted in at most a 7% deviation from the ideal.

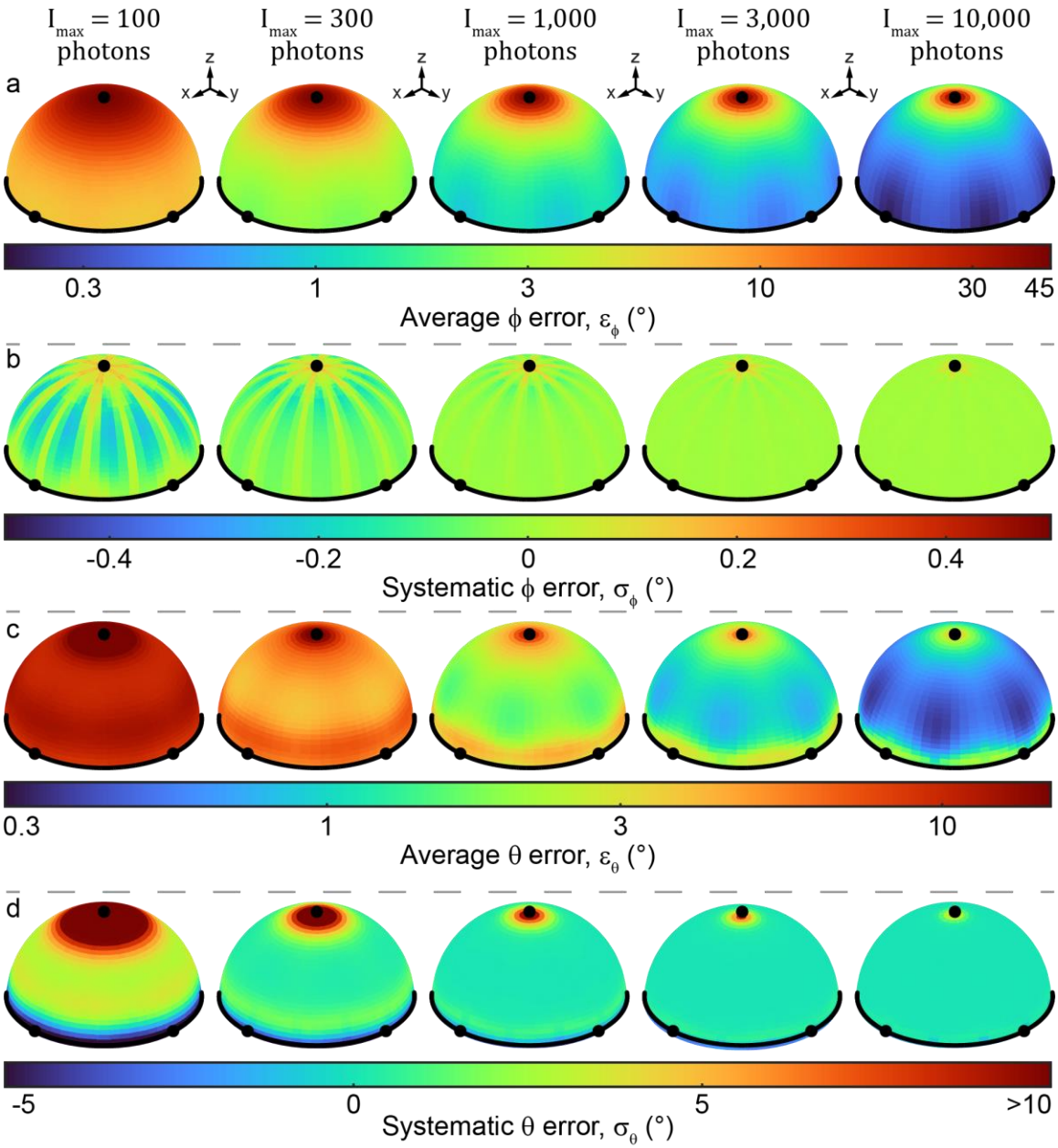

Figure 54: Results of Monte Carlo simulations of force orientation measurement.

Several unit hemispheres are shown. Each hemisphere has three dots denoting the points where the x-, y-, and z-axes intersect with the hemispheres. A black curve also shows the plane of intersection between each hemisphere and the x-y plane. The color of each point on a hemisphere denotes the error of the orientation that passes through that point. Average error and systematic error are shown for ϕ and θ at five different signal to noise ratios.

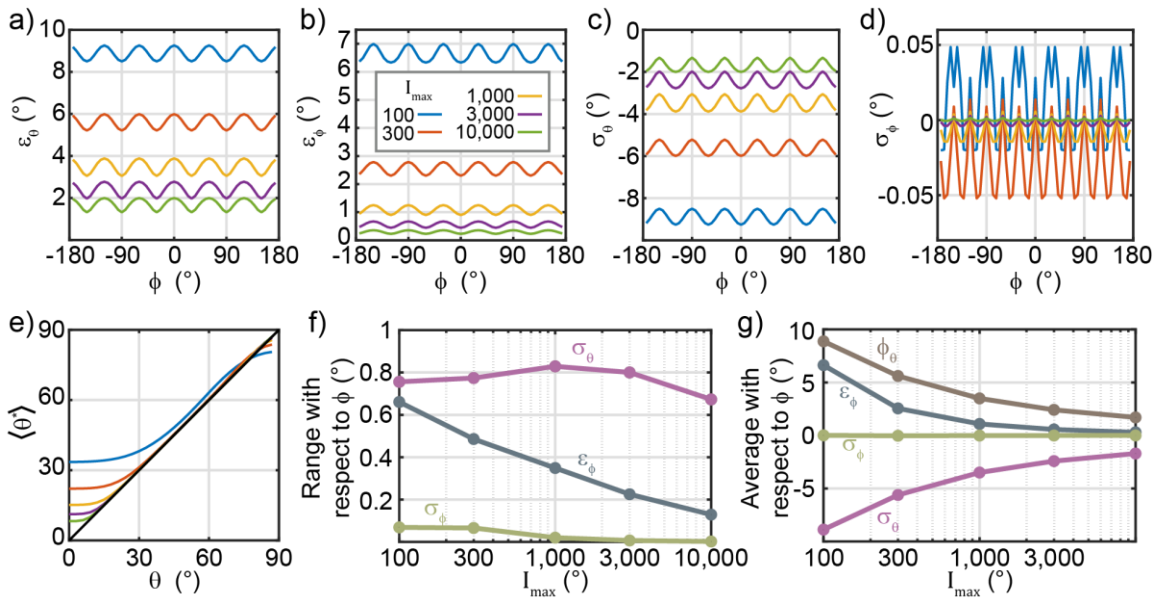

Figure 55: Extended analysis of Monte Carlo simulation results.

a-b) ε_θ, ε_ϕ, σ_θ, and σ_ϕ as a function of ϕ with $\theta = 90°$ at five different signal-to-noise levels. These results show that all four metrics exhibit small periodic variations with respect to ϕ. **e)** The average measured θ value, $\langle\theta^*\rangle$, as a function of the true θ value. These results show a previously-observed result: θ is biased systematically towards higher values when θ is very low because noise generally causes an increase in the best-fit sinusoid's amplitude. This effect decreases with increasing signal-to-noise. f) Range of curves shown in **a-d** showing the amplitude of the variation with respect to I_{max}. The curve for ε_θ is not shown because $\sigma_\theta = -\varepsilon_\theta$ when $\theta = 90°$, making the two range curves equivalent. **g)** Average of ε_θ, ε_ϕ, σ_θ, and σ_ϕ curves shown in **a-d** as a function of I_{max}, showing that all four types of error decrease with increasing signal-to-noise.

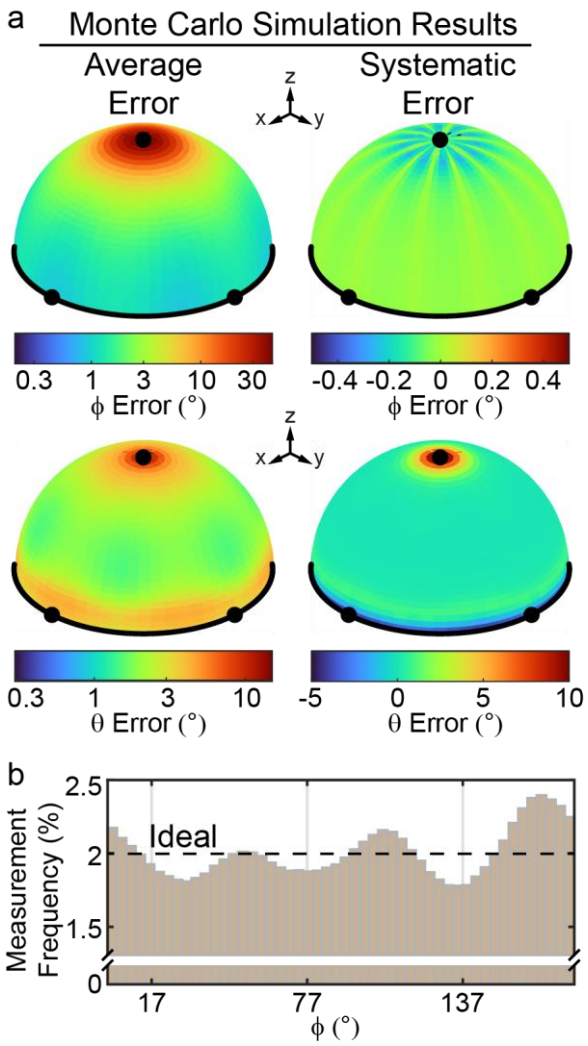

Figure 56: Analysis of measurement errors

a) Results of Monte Carlo simulations of force orientation measurement. Four unit hemispheres are shown. The color of each point on a hemisphere denotes the error of the orientation that passes through that point. Average error (left) and systematic error (right) are shown for ϕ (top) and θ (bottom). **b)** Histogram of all ϕ values accumulated from 81 platelet timelapses. Dashed line shows the ideal behavior (2% measurement frequency in each of 50 bins). Small variations (from 1.81% to 2.16%) reveal a small effect of systematic errors. Only the brightest 50% of pixels were included in the analysis.

As a second means of investigating potential sources of systematic error in orientation measurement, we evaluated the ϕ dependence of θ measurements. To accomplish this, we assembled data from several platelets and calculated $\langle\theta\rangle$ values as a function of ϕ (**Figure 57**). Ideally, $\langle\theta\rangle$ should not depend on ϕ in the compiled dataset. We found that $\langle\theta\rangle$ was constrained to a narrow range of $\sim 43 - 50°$. The small scale of this variation (~7°) serves as a validation for SIM-MFM-based orientation measurement. However, ideally this variation would be on the order of $< 1°$. This result, as well as the slight discrepancy between the $\langle\theta\rangle$ measured here and previously[45] suggest that there may be slight measurement errors that were not fully corrected for in image pre-procession (e.g. variations in the illumination profile of the microscope).

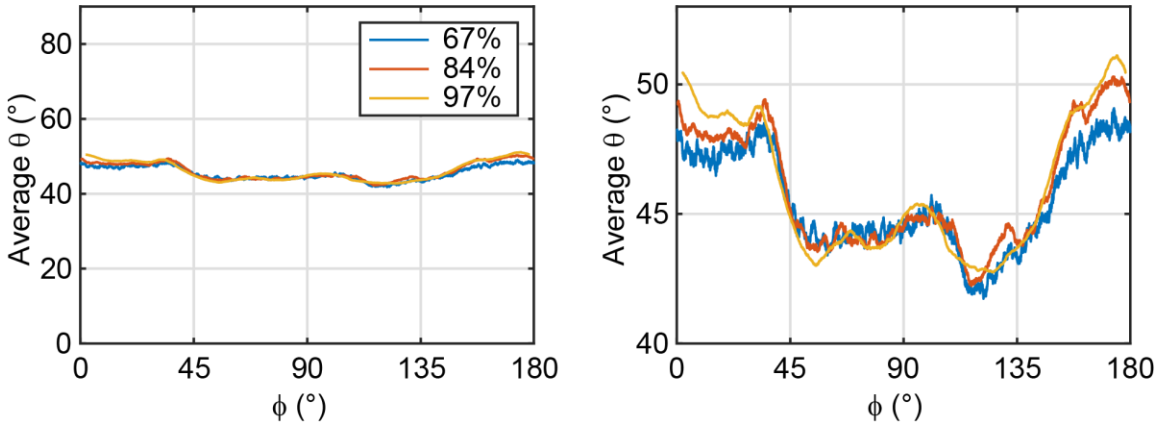

Figure 57: Dependence of measured $\langle\theta\rangle$ on measured ϕ values.

A 500-point rolling average of θ values accumulated from 17 platelet images as a function of ϕ. Plot is shown with the y-axis spanning the full range of potential θ values (left) and a zoom in on the curves (right). Three curves are shown, with thresholds cutoffs set as the 67th, 84th, and 97th percentiles of the accumulated dataset's intensity values. The similarity between the curves shows that the slight variation with respected to ϕ is not an artifact of the selected signal threshold cutoff.

SIM-MFM is a versatile technique that can be implemented without substantial photobleaching. We took advantage of this feature to investigate the dynamics of platelet spreading and adhesion. Our analysis, described below, reveals that, under our experimental conditions, platelet traction force align over time in a manner that can only be resolved using MFM. We added platelets to the solution over a tension probe-functionalized surface and imaged several locations on the surface at 2-minute intervals for 82 minutes. Over the course of this acquisition, we identified 81 platelets interacting with the surface. For each of these platelets, we segmented a small region-of-interest containing the platelet out of the imagestack (**Figure 58**a). For each timepoint, we quantified the "tension area" (T), which is the surface area of the tension signal created by the platelet and a measure that we call the "alignment parameter" (**Figure 58**b). The alignment parameter, R, is a measure for the dispersion of all ϕ angles measured under a platelet. If all ϕ angles are aligned perfectly along the same axis, $R = 1$. If all ϕ angles are oriented randomly, $R = 0$. In the context of directional statistics, the alignment parameter is equal to one minus the circular variance of the ϕ angles[45].

We found that, generally, tension area spiked sharply, quickly plateaued within a few minutes, then gradually or sharply dropped to zero within 10-30 minutes. The T vs. time, t, curve for almost every platelet could be accurately described by the equation:

$$T \approx T_{max} u(t - t_{attach}) \left(\left(1 - \exp\left(-\frac{t - t_{attach}}{\tau_{spread}} \right) \right) - \left(\frac{1}{1 + \exp\left(-\frac{t - t_{attach} - t_{detach}}{\tau_{retract}} \right)} \right) \right) + T_0 \quad (7)$$

where T_{max} is the maximum tension area of the platelet, t_{attach} approximate the times at which the platelet attaches to the surface, t_{detach} approximates the duration between

platelet adhesion and detachment, τ_{spread} and $\tau_{retract}$ are time constants for platelet spreading and retraction, respectively, T_0 is the basal T value measured (typically a noise-induced artifact) and $u(t - t_{attach})$ is the unit step function that denotes initiation of spreading at $t = t_{attach}$ (**Figure 58b,c**). We set T_{max}, t_{attach}, t_{detach}, $\tau_{retract}$, and τ_{spread} all as fit parameters and used simulated annealing to fit eqn (6) to each platelet's T vs. t data. We found that $T_{max} = 18 \pm 14\ \mu m^2$ (median ± inter-quartile range). Of the 81 platelets, 79 (97.5%) exhibited $T_{max} > 5\ \mu m$. Of these, 46 had best-fit t_{attach} and t_{detach} values that fell within the range of the acquisition.

Of the 46 platelets in which the full process of attachment, spreading, retraction, and detachment was recorded, we quantified alignment, R, from t_{attach} to $t_{attach} + t_{detach}$. We found that roughly half ($N = 20$, 43.5%) exhibited no significant correlation between R and t (**Figure 58d**). Of the remainder, alignment decreased over time for 4 (8.7%) and 22 (47.8%) exhibited a gradual, asymptotic increase in alignment (**Figure 58e**) that could generally be fit to the relationship:

$$R \approx R_{max} - \Delta R \exp\left(-\frac{t - t_{attach}}{\tau_{align}}\right)$$

where R_0 and R_{max} are the minimum and maximum alignment parameters, and τ_{align} is the time constant for force alignment (only R_{max}, R_0, and τ_{align} were set as fit parameters; t_{attach} from the T vs. t fit was used as a fixed parameter) (**Figure 58b,c**). We split these cells into two groups (22 increasing alignment cells and 24 cells with non-increasing alignment) and compared the sets of fit parameters. The 22 increasing-alignment platelets exhibited significantly different R_0, and R_{max} values than the 24 cells with non-increasing

R ($p < 0.01$, Wilcoxon rank-sum test). The dynamics of spreading were the same between the two groups ($p > 0.05$ for τ_{spread}, $\tau_{retract}$, and $t_{detatch}$) (**Figure 58f,g**). Platelets with non-increasing alignment were slightly larger than cells with increasing alignment (median $T_{max} = 21$ vs. $14\,\mu m^2$, $p = 0.015$, Wilcoxen rank-sum test) (**Figure 58f**). This last finding may have arisen because larger platelets are more likely to form more than two lobes, which could result in low, unchanging R measurements even when three or more lobes are each undergoing alignment internally.

Table 2: Timelapse fit parameters for platelet spreading and tension alignment: Median (Inter-quartile range) with Wilcoxen rank-sum test p-values

	T_{max} (μm^2)	τ_{spread} (min)	$\tau_{retract}$ (min)	$t_{detatch}$ (min)	ΔR	R_{max}	τ_{align} (min)
Increasing alignment platelets (N=22)	14.3 (11.4, 20.6)	1.7 (0.2, 2.6)	3.8 (1.8, 5.5)	24.6 (19.8, 34.3)	0.32 (0.20, 0.45)	0.97 (0.94,1.00)	7.0 (2.9, 12.2)
Non-increasing alignment platelets (N=24)	21.1 (13.6, 30.6)	1.7 (0.3, 3.0)	4.6 (2.4, 10.5)	25.1 (21.3, 32.5)	0.10 (-0.28, 0.27)	0.87 (0.59, 0.96)	-
p-value	0.015	0.831	0.127	0.634	<0.001	0.008	-

An interesting finding of this analysis is that spreading occurs on a significantly faster timescale than alignment; $\tau_{spread} = 1.7\,min$, while $\tau_{align} = 7.0\,min$ ($p < 0.001$, Wilcoxen rank-sum test) (**Figure 58g**). This result suggests that, in our experimental conditions, platelets have a mechanical progression that involves three phases. In the first phase, the platelet spreads across the surface, and eventually its spread area and total traction force plateau. In the second phase, forces within the platelet begin to re-align along an axis, allowing the platelet to maximize the mechanical efficiency of its contraction. Finally, the platelet eventually exhausts itself and detaches from the surface. We previously observed all of these phases[44,53]. However, this work shows that the second phase, which was previously thought to be largely static (because we previously only quantified tension signal and not force orientation), is actually a highly dynamic stage wherein the orientation (but perhaps not the overall magnitude) of force is gradually changing over time.

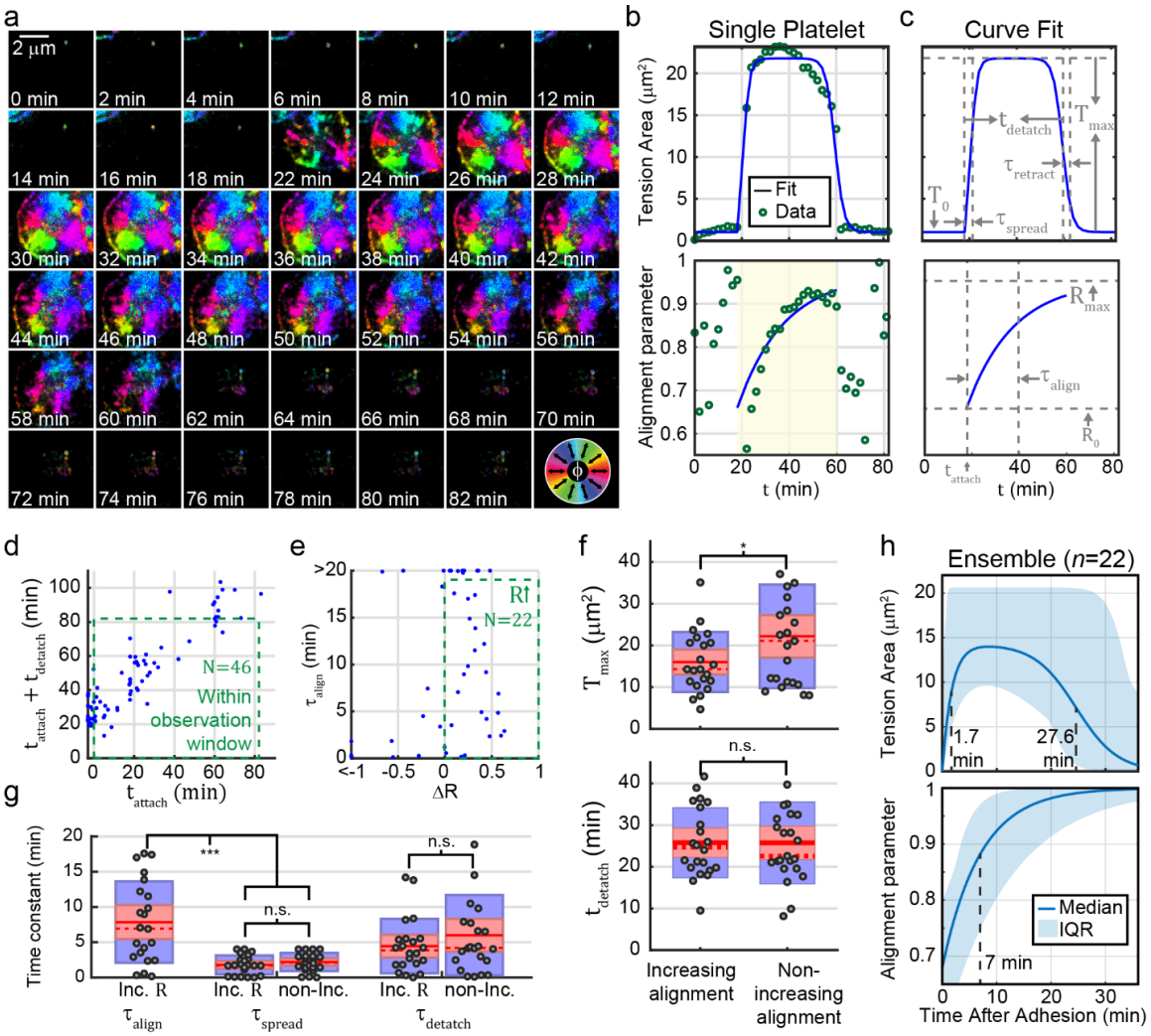

Figure 58: Dynamic properties of human platelets revealed using SIM-MFM.

a) Timelapse of a platelet spreading on a surface, shown using the ϕ colormap display method (see color wheel in bottom right corner). Gradual tension alignment can be seen via careful inspection; greens and cyans are common at early timepoints, but gradually transition to purple and dark blue due. **b)** Tension area (top) and the alignment parameter (bottom), R, quantified as a function of time, t, with curve fits shown (blue). Yellow shading denotes time window of platelet attachment. **c)** Best fit curves from **b** with annotations depicting fit parameters. **d)** scatterplot of best-fit $t_{attach} + t_{detatch}$ (the

timepoint at which platelet detachment occurs) and t_{attach} (the timepoint at which attachment occurs) values. Green dashed line shows the parameter space in which attachment and detachment both occurred within the duration of the timelapse. **e)** Scatterplot of best-fit τ_{align} (the time constant for tension alignment) and ΔR (the change in alignment) values for the platelets selected from **d**. Green line shows selected population with increasing alignment. **f)** Boxplots of T_{max} (the max platelet spread area – top) and t_{detach} (the duration of platelet attachment – bottom) for the 22 cells selected in **e**. Solid red line indicates mean, dashed red line indicates median, red boxes show standard error of the mean and blue boxes shows 95% confidence interval of the mean. Grey circles indicated individual datapoints. **g)** Boxplots for τ_{align}, τ_{spread} (the time constant for platelet spreading), and τ_{detach} (the time constant for platelet retraction). * denotes $p<0.05$, *** denotes $p<0.001$, and n.s. denotes $p>0.05$ (Wilcoxon rank-sum test for difference in population medians). h) Depiction of ensemble behavior. Blue curves denote reconstruction with median best-fit parameters and blue shading denote range of values obtained using all possible combinations of 25th, 50th, and 75th percentile best-fit parameters.

As a final experiment in our proof-of-concept SIM-MFM study, we investigated the anisotropic mechanosensor hypothesis of T-cell receptor (TCR) activation[131]. Previous work has suggested that application of lateral tension to the TCR is more likely to stimulate an immune response than tension that is applied perpendicular to the plasma membrane[131]. In that investigation, optical tweezers were used to apply tension to T-cells. However, in reality TCR traction forces are applied by the T-cells themselves. SIM-MFM offers an opportunity to measure the orientation of tension applied directly with T-cells. The observation of lateral forces applied by the TCR would lend credence to the anisotropic mechanosensor hypothesis.

We cultured primary mouse CD8+ T-cells on DNA hairpin tension probes that present antibodies to CD3 (a TCR co-receptor). As observed previously[46,140], the T-cells spread on the tension probe-functionalized surface and opened tension probes to produce bright tension fluorescence signal. We then imaged several cells (N=26 cells from 3 independent experiments) and found that T-cells did not exhibit any notable polarization-dependent response (**Figure 60**). To quantify this finding, we measured the ratio $\langle A \rangle / (\langle c \rangle + 1)$ (where A is a measure of the polarization-dependent fluorescence intensity signal and c is a measure of the polarization-independent fluorescence intensity signal – see **Figure 60**b) under cells and in the background. As a control, we also quantified $\langle A \rangle / (\langle c \rangle + 1)$ for platelets. Higher $\langle A \rangle / (\langle c \rangle + 1)$ means that the polarization-dependent component of fluorescence intensity is strong, indicating the presence of temporally stable forces with a substantial in-plane component ($\theta \gg 0°$). Conversely, low $\langle A \rangle / (\langle c \rangle + 1)$ means that the polarization dependent component of fluorescence intensity is weak, which can have multiple interpretations discussed below.

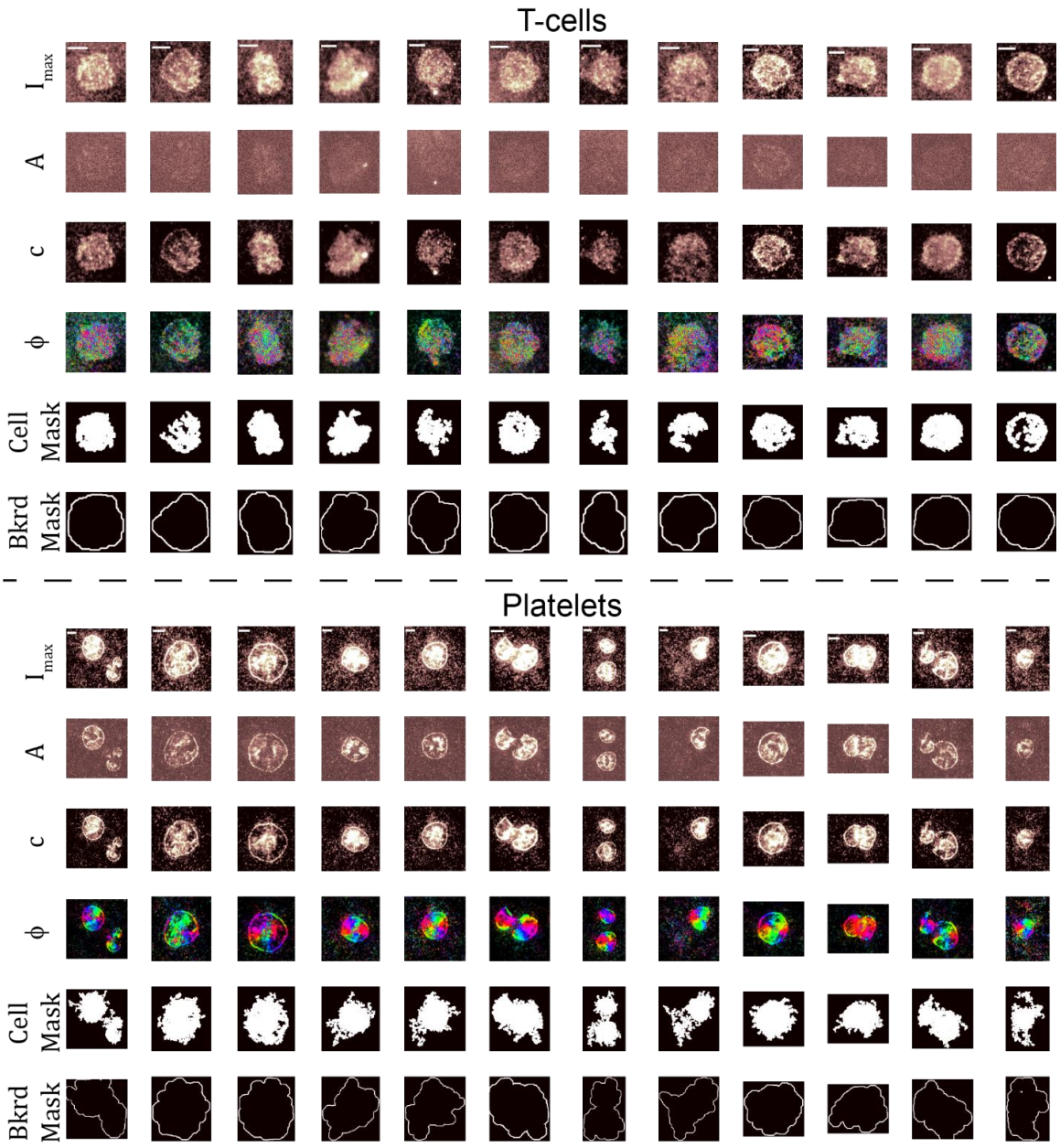

Figure 59: Analysis of T-cell receptor tension does not reveal a polarization-dependent response.

This figure is divided in two sections that have the same structure. The top half of the figure shows representative T-cell data, while the bottom half shows representative data for platelets, which serve as a control. Each panel shows twelve representative cells (one in each platelet) and has 6 rows corresponding to I_{max}, A, c, ϕ, and the cell and background

masks used to quantify $\langle A \rangle$ and $\langle c \rangle$ within the cells and the cell-free background. Notably, the T-cell A images show signal that is barely distinguishable from background, while platelet A images show substantially brighter signal than background. Additionally, the ϕ images for the T-cells show no distinguishable spatial pattern because the low A values result in ϕ values that are noise-dominated.

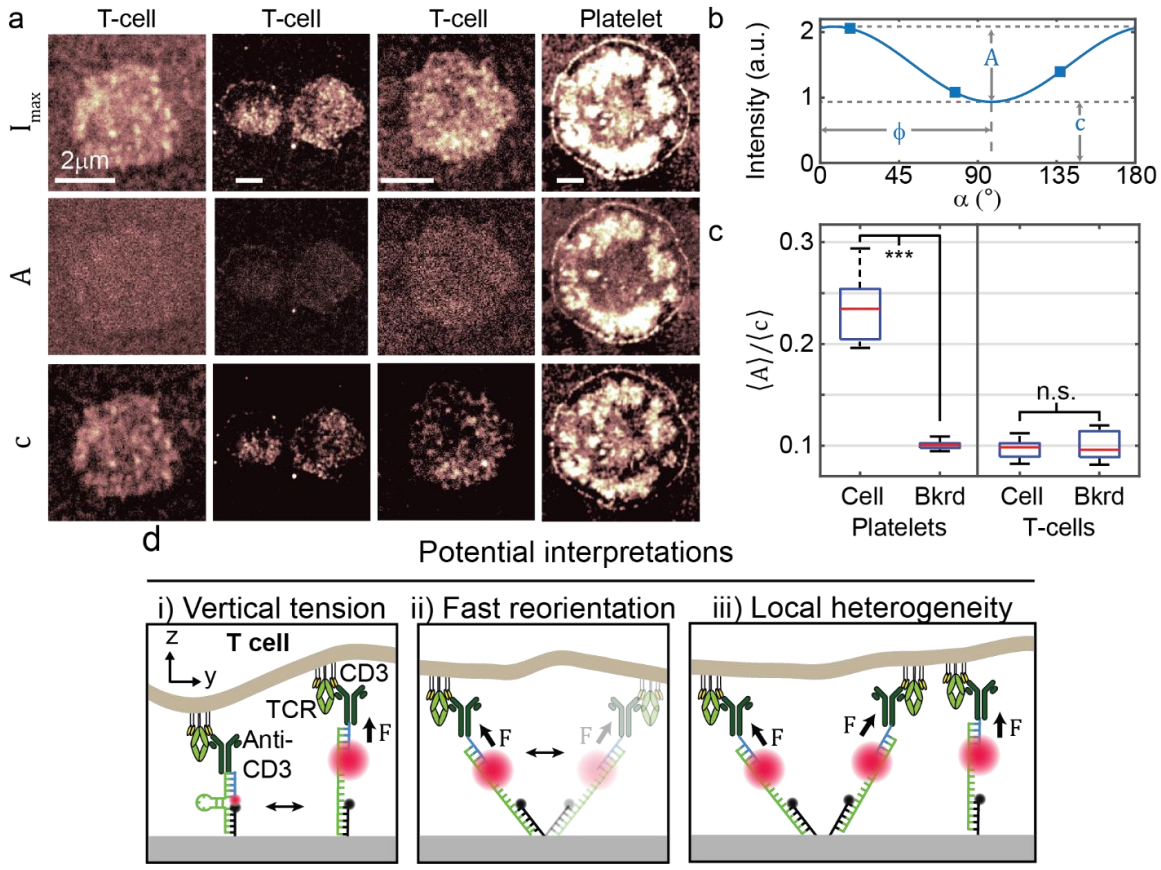

Figure 60: Analysis of T-cell receptor tension reveals no polarization-dependence

While platelets exhibited large $\langle A\rangle/(\langle c\rangle + 1)$ values (median of ~0.24), T-cells exhibited a low $\langle A\rangle/(\langle c\rangle + 1)$ (median of ~0.1) – see **Figure 60**c. Measurement of $\langle A\rangle/(\langle c\rangle + 1)$ values in the cell-free background for both cells types exhibited values similar to that measured under T-cells (median ~0.1). Inspection of maps of A and c show that virtually all T-cell signal is orientation-dependent (**Figure 60**a). Together, these results suggest that tension is not oriented in a manner that results in the polarization response needed for MFM to map orientation. Specifically, our results suggest that TCR forces are not organized, temporally stable, and lateral as they are with platelet integrins. Instead, our results can be interpreted to suggest that TCR forces exhibit one of (or a combination of) three properties, all of which can lead to polarization-independence in MFM signal; i) vertical tension, wherein $\theta \approx 0°$, ii) fast reorientation, wherein individual open tension probes rapidly reorient within the timescale of an individual image, or iii) local heterogeneity, wherein neighboring tension probes exhibit vastly different force orientations. In cases ii and iii, ensemble averaging results in signal that resembles vertical tension. We made similar observations while conducting a previous study[45] (data not shown), but did not include them because of the inconclusive nature of our results. However, we have chosen to include them here primarily to demonstrate the need for further development in this area to answer certain questions about the role of molecular force orientation.

One potential improvement to SIM-MFM would be to adapt it for the measurement of forces exerted by individual receptors. We recently developed a method that combines DNA point accumulation for imaging in nanoscale topography (DNA-PAINT) with molecular tension probes to map forces exerted by single integrins in living cells[141]. We named the technique tension PAINT (tPAINT). Here, we close this report with a proof-of-

principle demonstration that tPAINT can be integrated with SIM-MFM to enable mapping of the orientation of forces applied by individual integrins in a high-throughput manner. In keeping with our previous nomenclature, we name this combined tPAINT-SIM-MFM approach force PAINT (fPAINT).

fPAINT builds upon tPAINT by adding in the ability to measure the orientation of individual integrin forces (**Figure 61**). In fPAINT, fluorphores and quenchers are removed from the tension probes such that hairpin opening produces no enhancement in fluorescence signal. However, a soluble 10 nt, Cy3b-tagged "imager" is added to solution. The imager is complementary to the stem region of the hairpin, such that it can hybridize to opened hairpins. Due to competition with the other half of the stem, imagers cannot hybridize to closed hairpins. Accordingly, fluorescence microscopy reveals the sites in which imagers are bound to opened hairpins.

Using TIRF-SIM (which only illuminates a thin volume near the surface), single molecules can be imaged with adequate signal-to noise. Continuous TIRF-SIM imaging, wherein one nine-image SIM acquisition is taken every 1.27 seconds, allows continuous cycling between three polarization in a manner that was used by Backer, Lee, and Moerner[142]. Each nine-image set was averaged into three polarization-specific images as described above. These images were then assembled into a continuous timelapse, which was processed using previously developed single molecule localization software. Localizations that were detected in at least five continuous frames were then analyzed to estimate force orientation for that specific localization. Specifically, the first and last frame were discarded (because intensity in these frames will depend on the unknown timing of imager hybridization,

dehybridization, and/or photobleaching) and the single molecule intensity vs. α values were fit to a sinusoid as described above.

The 10 bp length of the imager ensures that the imager remains bound to the opened tension probe for a duration of ~1-10 seconds[118], which is long enough to ensure that most imagers stay bound for long enough to be imaged for at least five consecutive frames, but short enough to prevent imagers from irreversible locking probes in an opened state[140]. At appropriate imager concentrations (in this work we used 10 nM), imagers will hybridize to opened tension probe with a frequency that is low enough to observe individual localizations, but high enough to construct a cell-wide map of integrin traction within a reasonable timeframe.

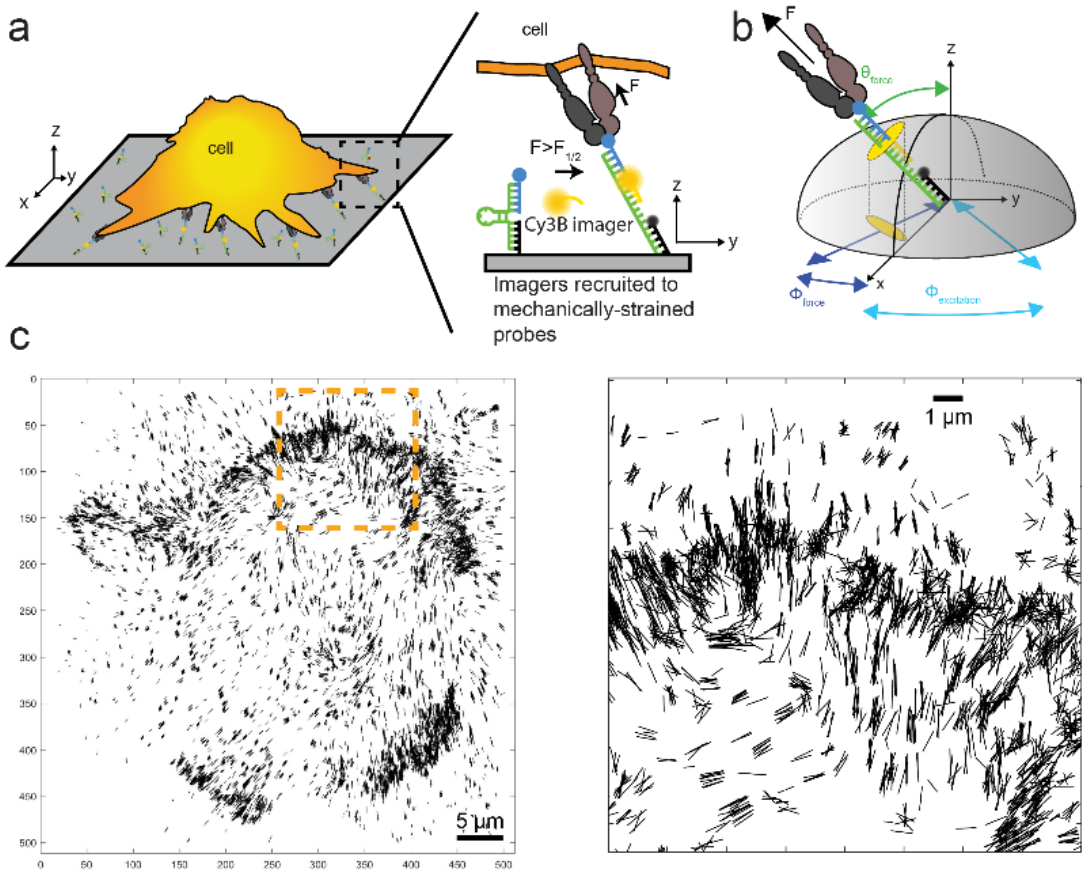

Figure 61: fPAINT reveals the orientation of forces applied by individual integrins.

A) Scheme shows how fPAINT works; a non-fluorescent DNA tension probe is pulled open by an integrin, exposing a binding site that a soluble fluorescent "imager" can bind to. The imager's dye is oriented perpendicular to the force, so polarized SIM fluorescence can be used to measure the orientation of the dye – which yields force orientation. **B)** Depiction of force orientation. **C)** Representative fPAINT image showing orientation of several thousand accumulated events.

For this preliminary proof-of-concept demonstration of fPAINT with an NIH-3T3 fibroblast, we display the ϕ orientations of individual localizations using black dipoles. Our results are in line with expectations based on previous studies; integrin tension is aligned towards the cell centroid, and is concentrated at the lamellipodial edge of the fibroblast. There is a striking lack of tension in the middle of the cell – typically, we would expect to see microns-long focal adhesions. This finding may be a result of the different tension magnitudes transmitted in focal adhesions and in lamellipodial structures and the tension magnitude-dependence of imager hybridization; the imager binds to a strained region of the opened tension probe. Our previous tPAINT study showed that integrin tension can exceed 20 pN in focal adhesions, which is expected to completely inhibit imager hybridization and greatly accelerate imager off-rates[141]. In contrast, lamellipodial tension is confined to the 5-20 pN range, in which imagers can effectively hybridize and remain bound for the ~2 seconds required for analysis.

fPAINT offers a new type of measurement, but has substantial room for future improvement due to multiple limitations, including those discussed in the previous paragraph. The ~2 seconds of continuous acquisition required for orientation measurement is one issue that may prevent the study of receptor-ligand pairs with short lifetimes (including the TCR). One solution to this issue would be to use fast SIM[143], a fast non-SIM microscope[142] or emission resolved polarization[144] (although the SIM illumination does potentially offer a further doubling of resolution[145] beyond the 20 nm resolution previously achieved with tPAINT[141]). Another limitation of fPAINT is that it requires continuous imaging for ~20 minutes to construct a full high-resolution image. Because SIM-MFM can map whole-cell force orientation with a single acquisition, both techniques should be

treated as individual tools within a growing toolbox of techniques for mapping molecular force orientation.

In conclusion, we demonstrate that a SIM microscope can be used to implement MFM and the new technique fPAINT. We used SIM-MFM to image platelets, fibroblasts, and T-cells. In our proof-of-concept studies, we have demonstrated that platelets undergo traction force realignment on a timescale that is substantially longer than the timescale of platelet spreading. We have also shown that TCR forces are, in contrast to the integrin traction forces that we generally study with MFM, not temporally stable, homogenously aligned, and lateral. We expect that SIM-MFM and fPAINT will be used in several future applications in cellular biology and for the investigation of force generation by active nanomaterials, which is an emerging application area of DNA mechanotechnology tension probes[1,93].

4.3 Methods

4.3.1 Preparation of supported lipid bilayer (SLB) functionalized microparticles.

SLB-functionalized microparticles were prepared as previously described (REF MFM). Small unilamellar vesicles (SUVs) with (average diameter of 100 nm) were prepared via lipid extrusion. Briefly, 4 mg mL−1 of 1,2-dioleoyl-sn-glycero-3-phosphocholine lipid (DOPC) (Avanti Polar Lipids Inc., Alabaster, Alabama) was diluted in ∼1 mL chloroform in a round-bottom flask. The chloroform was removed via rotary evaporation, resulting in the formation of a thin lipid film. The lipid film was then dried under a steam of N2 and subsequently hydrated with 2 mL of milli-Q water. The film was then dissolved via three freeze–thaw cycles. The lipid solution was then extruded ∼10 times through a 100 nm polycarbonate filter. Upon proper formation of SUVs ~100 nm, the solution became clear. The SUVs were stored at 4 °C and then used within 4–6 weeks.

To prepare SLB-coated microparticles, 100 μL 1 mg mL−1 5 μm silica beads (product #: SS06N, Bangs Laboratories, Fishers, Indiana) were mixed with 100 μL of SUVs and equilibrated on a rocker for 15 min at room temperature. The supported lipid bilayer (SLB) beads were purified via three successive 5 min spin in a benchtop centrifuge at 2,000 r.p.m. After each spin, the supernatant was removed via pipette aspiratoin and replaced with 1 mL of 1× PBS. The SLB-functionalized beads were then incubated with 5 μM DiI for 15 min. The DiI-loaded SLB functionalized beads were separated from free DiI with three successive 5 min spins, with each spin followed by supernatant aspiration and replacement with 1x PBS as before. The final volume was 100 μL. The mixture was vortexed, and 2 μL of SLB-functionalized beads were then diluted in 1 mL of 1x PBS to ensure that particles

would be spatially isolated. The diluted beads were then vortexed and 100 µL were transferred to one clean well of a flow chamber (product #: µ-Slide VI 0.4, Ibidi, Verona, Wisconsin).

4.3.2 Isolation and handling of platelets

Experiments were performed with platelets drawn from human volunteers. Blood was drawn from volunteers according to IRB-approved protocols (Emory University, Institutional Review Board) in complete compliance with ethical regulations. Informed consent was obtained prior to blood draw from all subjects. Venous blood was drawn from the arm of human volunteers in two 3 mL portions. The first portion discarded, and 0.75 mL of Anticoagulant citrate dextrose (ACD) solution (0.75 mL) was added to the second portion. The mixture of whole blood and ACD was then spun at 150 RCF for 15 min. The lowest centrifuge acceleration and braking settings were used to avoid platelet activation. The platelet-rich plasma was removed, combined with 10% ACD (v/v), and spun at 900 RCF for 5 min (again, with the lowest centrifuge acceleration and braking settings). The platelet-poor plasma was aspirated following the spin. Then, the platelets were suspended gently in 2 mL 1× Tyrodes with 0.1% BSA *w/v*. Finally, platelets were allowed to settle for ∼1 h before the start of each experiment, which allowed them to return to a resting state.

4.3.3 Culture and handling of 3T3 fibroblast cells

NIH 3T3 cells – which were a kind gift from Dr. Andres Garcia's Lab at the Georgia Institute of Technology – were cultured to 75% confluency in Dulbeccos modified essential medium (DMEM) supplemented with 10% (v/v) fetal bovine serum and 2.1 mM L-

Glutamine, 1000 µg/L streptomycin, and 10000 IU/L penicillin G. Cells used in different experiments were derived from different subcultures. Cells were removed from culture flasks and replated to DNA hairpin-functionalized surfaces within 20 min. For removal from flasks, cells were removed using a trypsin solution (Corning) containing 0.25% (wt/vol) trypsin, sodium bicarbonate, and 2.21 mM EDTA. The cells were then centrifuged at 218 rcf, pelleted and resuspended in the same medium. Finally, the cells were transferred to and plated on DNA hairpin-functionalized surfaces at a density of 20,000 cells/cm^2. Cells were imaged between 10 and 60 min after plating.

4.3.4 Surface preparation

Glass coverslips with thicknesses of 0.17 mm – either 25 mm x 75 mm rectangular covorslips (product #: 10812, Ibidi, Verona, Wisconsin) or 25 mm diameter round coverslips (PRODUCT) – were cleaned via sonication in ethanol for 10 min and then dried in an oven at a temperature of 100 ˚C for 20 min. The dried coverslips were then exposed in piranha acid (a solution of 30% (v/v) H2O2 in concentrated H2SO4) (Caution! This solution is extremely corrosive and explosive in contact with organics!) for 10 min. Coverslips were then rinsed six times with water and then rinsed three times with ethanol. The rinsed coverslips were then functionalized with amine groups. This was achieved by incubating slides in 3% (v/v) (3-aminopropyl)triethoxysilane in ethanol for one hour. Next, the slides were washed three times with ethanol, baked in an oven at 100 ˚C for 20 min, and then washed 3 times with ethanol. The slides were then baked in a 100 ˚C oven (again) for 20 min. A solution of 2 mg/ml Biotin-NHS in anhydrous DMSO was then placed onto the dried slides, which were then sealed with parafilm in plastic petri dishes and stored at room temperature for 12 hours or longer. These surfaces were then used within two weeks

of preparation. On the day of use, the biotinylated coverslips were sonicated in ethanol for 15 seconds, rinsed with ethanol, and dried with N_2. Round slides were then mounted into round imaging chambers (PRODUCT #) and immedeately immersed in 1xPBS. Rectangular slides were attached to Ibidi sticky slides (PRODUCT), and each of the six wells were immediately immersed in 1x PBS. Next, the mounted surfaces were rinsed 5 times with 1xPBS, passivated for 45 min with a solution of 1 mg/ml BSA in 1xPBS, washed again with 1xPBS, incubated in 0.05 mg/mL streptavidin in 1xPBS for 1 hr, and washed once more with 1xPBS. Finally, the streptavidin-functionalized surfaces were incubated with 20 nM hybridized DNA hairpin probes in 1xPBS for 1 hr, washed again with 1xPBS, and washed with 3 volumes of imaging buffer. Cells were then plated onto the surfaces for imaging.

4.3.5 DNA strand hybridization

Modified DNA oligonucleotides were hybridized together at concentrations of 200 nM (for the hairpin strand) and 220 nM (for two handle strands) in 1xPBS, representing a molar ratio of 1.1:1.0:1.1 anchor-strand/hairpin-strand/ligand-strand. Annealing was carried out by heating to 75˚C, then cooling to 25 ˚C at a rate of 1.3 ˚C/min in a Perkin-Elmer GeneAmp 2400 ® thermocycler. Annealed probes were diluted in 1xPBS before being added to streptavidin-functionalized surfaces.

4.3.6 Structured illumination microscopy

SIM images were acquired on a Nikon N-SIM system equipped with a CFI Apo ×100 1.49 NA objective and an Andor iXon EMCCD (60 nm per pixel). For each N-SIM image,

fifteen images of a 3′-Cy3-RNA sample were acquired in different phases using a 561 nm laser as an excitation source.

4.3.7 Standard resolution image processing

Raw nd2 Files from SIM acquisitions were opened in MATLAB 2018b using the bfopen MATLAB function (part of the Bioformats package). Raw images were originally in a 3x5 montage form, wherein the 15 images that make up a single acquisition are concatenated directly together. (Reconstruction was only performed on 3D SIM acquisitions, which exhibited clearer striping patterns than 2D SIM on our microscope). Each raw montage was loaded into MATLAB, and the CCD background of 200 intensity units was subtracted from it. The background-subtracted montage was then divided by a background correction montage to account for intensity variations between and within individual images (see below). Finally, the 1% quantile of the montage (calculated using MATLAB's quantile function) was subtracted from the entire montage, and all negative values were set to zero. (This background-corrected montage was then saved into a text file for subsequent superresolution image processing see **Super resolution image processing** below). Next, the montage was split into 15 individual images. Each set of five images acquired at a common polarization angle was then averaged, resulting in three images – one corresponding to each of the three polarization angles (α_1, α_2, and α_3). These three images were then used to calculate I_{max}, ϕ, and θ using equation 6.

4.3.8 Preparation of illumination profile correction images

Background correction images were generated on the day of the experiment by collecting at least six SIM acquisitions with the microscope focused onto the bottom of a Chroma

slide or a surface with 100% open tension probes (which were prepared by adding a "locking strand" during the DNA strand hybridization step). Each acquisition produced a 3x5 montage of images. All montages were opened into MATLAB, baseline (200 a.u.) subtracted, and smoothed with a rolling ball filter (using MATLAB's imfilter command) with a 3-pixel radius. The filtered montages were then averaged together. Finally, the montage was normalized to the mean value of the entire montage. This process was repeated each time an experiment was performed.

4.3.9 Super resolution image processing

Background-corrected montages (see **Standard resolution image processing** above) were opened in Fiji – a version of ImageJ that includes several additional built-in plugins – for SIM reconstruction. The text file was then imported as a montage into ImageJ (File>Import>Text Image…). The montage was then separated into an imagestack using ImageJ's "montage to stack" function (Image>Stacks>Tools>Montage to Stack…). SIM reconstruction was then performed on the stack using the fairSIM plugin (fairSIM is a separate ImageJ plugin that must be installed separately because it is not included in Fiji). A new fairSIM reconstruction was opened (Plugins>fairSIM>New Reconstruction) with the following settings: Type/Img.Seq=p,z,a (OMX); beams=3; angles=3; phases=5. The imagestack was then imported into the fairSIM reconstruction with the following settings: Pixel size=41.7 nm (or 83.4 nm if images were acquired with 2x2 binning); background subtraction: no. Next, an optical transfer function (OTF) approximation was run using the following settings: NA=1.4; $\lambda = 561$ (or 488 for GFP); Comp: a=0.30.

Parameter estimation was then run using an iterative process: First, the default settings were used (Band to use for shift vector est.=2; Region to exclude from fit=0.6) to run parameter estimation. Following parameter estimation, fairSIM outputs three modulation estimates (mod. est.) in the parameter fit summary. A mod. est. of 1 denotes perfect parameter estimation, while lower numbers denote poorer parameter estimations. If all three mod. est. values were greater than 0.7, then the parameter estimation was used. If not, the parameter estimation settings were adjusted and parameter estimation was re-run iteratively. First, "Band to use for shift vector" (which can either be 1 or 2) was changed to 1. Then, Region to exclude from fit (which can be 0.2, 0.3, 0.4, 0.5, 0.6, 0.7, or 0.8) was altered. If any of the 14 setting combinations resulted in all three mod. est. values being greater than 0.7, then the parameter estimation was used SIM reconstruction. If none of the combinations resulted in all three mod. est. values exceeding 0.3, the dataset was deemed inadequate for superresolution reconstruction. Otherwise the parameter estimation that maximized the minimum of the three mod. est. values was used.

Reconstruction was then run using the following settings: OTF attenuation=off; Intermediate results=full; Output=raw values; Filter type=Wiener filter; Wiener parameter=0.05; APO cutoff=2; APO bend=0.9; RL iterations=5. The reconstruction output includes three stacks of images, one of which is titled "Spatial Images", which includes 16 images corresponding to various final and intermediate results of the reconstruction. Four of the images in this image stacked were saved as text images (File>Save As>Text Image…): "(a0: band 0)"; "(a1: band 0)"; "(a2: band 0)"; and "(full result)".

4.4 Supplemental Note I – derivation of equations for analytical orientation measurement

To obtain a method for calculating force orientation analytically for each set of three intensity measurements (I_1, I_2, and I_3), we consider equations that can be used to represent fluorescence intensity:

$$I_1 = A\sin^2(\alpha_1 - \phi) + c \quad (1a)$$

$$I_2 = A\sin^2(\alpha_2 - \phi) + c \quad (1b)$$

$$I_3 = A\sin^2(\alpha_3 - \phi) + c \quad (1c)$$

where α is the polarization angle of the excitation beam, ϕ is the azimuthal angle of the force vector, and and A and c are scaling constants that are related to the background intensity, number of open tension probes, and the tilt angle of the force (θ). Because the three α angles are related to each other by rotations of $60°$, we can re-write these equations simply as:

$$I_1 = A\sin^2(\alpha_1 - \phi) + c \quad (2a)$$

$$I_2 = A\sin^2(\alpha_1 + 60° - \phi) + c \quad (2b)$$

$$I_3 = A\sin^2(\alpha_1 - 60° - \phi) + c \quad (2c)$$

Applying the half-angle formula yields:

$$I_1 = \frac{A}{2}(1 - \cos(2\alpha_1 - 2\phi)) + c \quad (3a)$$

$$I_2 = \frac{A}{2}(1 - \cos(2\alpha_1 + 120° - 2\phi)) + c \quad (3b)$$

$$I_3 = \frac{A}{2}(1 - \cos(2\alpha_1 - 120° - 2\phi)) + c \quad (3c),$$

and rearranging yields:

$$I_1 = \bar{I} - \frac{A}{2}\cos(2\alpha_1 - 2\phi) \quad (4a)$$

$$I_2 = \bar{I} - \frac{A}{2}\cos(2\alpha_1 + 120° - 2\phi) \quad (4b)$$

$$I_3 = \bar{I} - \frac{A}{2}\cos(2\alpha_1 - 120° - 2\phi) \quad (4c),$$

where

$$\bar{I} = \frac{A}{2} + c = \frac{I_1 + I_2 + I_3}{3} \quad (5)$$

Applying the identity $\cos(a + b) = \cos(a)\cos(b) + \sin(a)\sin(b)$ yields:

$$I_1 = \bar{I} - \frac{A}{2}(\cos(2\alpha_1)\cos(2\phi) + \sin(2\alpha_1)\sin(2\phi)) \quad (6a)$$

$$I_2 = \bar{I} - \frac{A}{2}(\cos(2\alpha_1 + 120°)\cos(2\phi) + \sin(2\alpha_1 + 120°)\sin(2\phi)) \quad (6b)$$

$$I_3 = \bar{I} - \frac{A}{2}(\cos(2\alpha_1 - 120°)\cos(2\phi) + \sin(2\alpha_1 - 120°)\sin(2\phi)) \qquad (6c).$$

If we rotate our coordinate system such that $\alpha_1 = 0°$ and re-arrange, we obtain:

$$\bar{I} - I_1 = \frac{A}{2}\cos(2\phi) \qquad (7a)$$

$$\bar{I} - I_2 = \frac{A}{2}(\cos(120°)\cos(2\phi) + \sin(120°)\sin(2\phi)) \qquad (7b)$$

$$\bar{I} - I_3 = \frac{A}{2}(\cos(-120°)\cos(2\phi) + \sin(-120°)\sin(2\phi)) \qquad (7c).$$

Merging equations $(7a)$ and $(7b)$ yields:

$$\bar{I} - I_2 = (\bar{I} - I_1)\cos(120°) + \frac{A}{2}\sin(120°)\sin(2\phi) \qquad (8)$$

Re-arranging, we obtain

$$\frac{\bar{I} - I_2 - (\bar{I} - I_1)\cos(120°)}{\sin(120°)} = \frac{A}{2}\sin(2\phi) \qquad (9).$$

Dividing equation (9) by equation $(7a)$ rearranging yields

$$\tan(2\phi) = \frac{\bar{I} - I_2 - (\bar{I} - I_1)\cos(120°)}{(\bar{I} - I_1)\sin(120°)} \qquad (10)$$

and finally, rearranging the equation and adjusting the coordinate system to allow for arbitrary α_1 yields:

$$\phi = \frac{1}{2}\tan^{-1}\left(\frac{\bar{I} - I_2 - (\bar{I} - I_1)\cos(120°)}{(\bar{I} - I_1)\sin(120°)}\right) + \alpha_1 \quad (11).$$

Now that ϕ is known, A can be solved for by re-arranging equation $(4a)$:

$$A = \frac{2(\bar{I} - I_1)}{\cos(2\alpha_1 - 2\phi)} \quad (12).$$

Next, c can be obtained by re-arranging equation $(1a)$:

$$c = I_1 - A\sin^2(\alpha_1 - \phi) \quad (13).$$

Finally, θ can be estimated using an equation that we previously derived:

$$\theta = \cos^{-1}\left(\sqrt{\frac{\frac{I_{max}}{c} - 0.069}{1 - 0.069}}\right) \quad (14),$$

where

$$I_{max} = A + c \quad (15).$$

CHAPTER 5. VARIABLE INCIDENCE ANGLE LINEAR DICHROISM (VALID): A TECHNIQUE FOR UNIQUE 3D ORIENTATION MEASUREMENT OF FLUORESCENT ENSEMBLES

This chapter is an adaptation of Blanchard, Brockman, Salaita, and Mattheyses *Optics Express* 2020, 28 (7), 10039–10061 (ref. [146]). While this work doesn't explicitly deal with DNA mechanotechnology, it sets up the work presented in the following chapter.

5.1 Introduction

5.1.1 Summary

A fundamental challenge with fluorophore orientation measurement is degeneracy, which is the inability to distinguish between multiple unique fluorophore orientations. Techniques exist for the non-degenerate measurement of the orientations of single, static fluorophores. However, such techniques are unsuitable for densely labeled and/or dynamic samples common to biological research. Accordingly, a rapid, widefield microscopy technique that can measure orientation parameters for ensembles of fluorophores in a non-degenerate manner is desirable. We propose that exciting samples with polarized light and multiple incidence angles could enable such a technique. We use Monte Carlo simulations to validate this approach for specific axially symmetric ensembles of fluorophores and obtain optimal experimental parameters for its future implementation.

5.1.2 Introduction to fluorescence polarization microscopy

Fluorophores absorb and emit polarized light in an orientation-dependent manner. Fluorescence polarization microscopy (FPM) techniques can be used to calculate fluorophore orientation from fluorescence intensity measurements. Widefield FPM can enable diffraction-limited orientation mapping across fluorescence microscopy images, which is particularly useful for characterizing molecular organization within living cells. One of the most common orientation-mapping techniques is fluorescence detected linear dichroism (FDLD) [147], which leverages the orientation-dependence of the intensity (I) of a fluorophore excited by plane polarized light:

$$\mathrm{I} = \mathrm{Q}(\mathbf{E} \cdot \boldsymbol{\mu})^2 = \mathrm{Q}|\mathbf{E}|^2|\boldsymbol{\mu}|^2 \cos^2(\Psi) \qquad (1)$$

where $\mathbf{E}$ is the excitation light's dipolar electric field vector (which we interchangeably refer to as the "measurement vector"), $\boldsymbol{\mu}$ is the fluorophore's absorption transition dipole moment, Ψ is the angle between $\boldsymbol{\mu}$ and $\mathbf{E}$, and Q is a scaling constant that combines terms such as quantum yield and detection efficiency. The observed intensity of a static (e.g. translationally and rotationally immobile) fluorophore thus depends on the orientation of $\mathbf{E}$ and, as such, the fluorophore's orientation can be measured by recording fluorescence intensity with multiple distinct measurement vectors.

FDLD is most commonly employed by using simple polarization optics to rotate $\mathbf{E}$ by angle α around a fixed optical axis that, as is standard in epifluorescence microscopy, is perpendicular to the sample plane (i.e. the x-y plane) and parallel to the z-axis. In this context:

$$I_{FDLD} = Q|\mathbf{E}|^2|\boldsymbol{\mu}|^2 \sin^2(\theta)\cos^2(\varphi - \alpha) \quad (2)$$

where θ and φ are the polar and azimuthal angles of **μ** in the microscope coordinate system**.** (In this work, azimuthal angle is the clockwise angle from the x-axis of the projection of **μ** onto the x-y plane, and polar angle is the angle between **μ** and the z-axis – see **Figure 62**C). A series of at least three images are recorded using different α angles (e.g. $\alpha = 0°, 60°$, and $120°$, where $\alpha = 0°$ denotes **E** parallel to the x-axis) such that each pixel in the image stack has at least three intensity measurements associated with it. The measurements in each pixel can then be fit to Eq. (1), enabling pixel-by-pixel azimuthal-angle mapping. This method is robust to ensemble averaging, such that the best-fit φ value reports on the ensemble-average φ value when fluorophores are overlapping and/or rotationally mobile. In addition, information about the best-fit sinusoid's amplitude can be used to infer properties about a fluorophore's (or fluorescent ensemble's) orientational heterogeneity and, in certain scenarios, average θ value.

FDLD is a technologically accessible and versatile technique that has been used to image the orientation of fluorescent ensembles [45,147-155] and single fluorophores [142]. One limitation of FDLD is that it cannot be used to image fluorophores that are perpendicular to the sample plane (when $\theta = 0°$, $\Psi = 90°$ and, therefore, $I = 0$ for all α). Furthermore, and critically for this work, measurements of φ are strictly two-dimensional because they are confined to the x-y plane. Any effort to measure three-dimensional orientation is thwarted by a fundamental limitation of this implementation of FDLD: All measurement vectors are co-planar with the x-y plane, which causes measurement degeneracy. In other words, any given **μ** cannot be distinguished from its reflection across the sample plane. To use an

example, an orientation measurement of $\varphi = 45°$, $\theta = 30°$ is indistinguishable from $\varphi = 45°$, $\theta = 120°$ because the two orientations produce the same intensity at all α values. This can generally be expressed mathematically using Eq. (2):

$$Q|\mathbf{E}|^2|\boldsymbol{\mu}|^2 \sin^2(\theta)\cos^2(\varphi) = Q|\mathbf{E}|^2|\boldsymbol{\mu}|^2 \sin^2(180° - \theta)\cos^2(\varphi) \qquad (3).$$

A second degree of degeneracy arises from negation of $\boldsymbol{\mu}$, as can be illustrated using a modification of Eq. (1):

$$Q\big(\mathbf{E} \cdot (-\boldsymbol{\mu})\big)^2 = Q|\mathbf{E}|^2|-\boldsymbol{\mu}|^2 \cos^2(\Psi) = Q|\mathbf{E}|^2|\boldsymbol{\mu}|^2 \cos^2(\Psi) \qquad (4).$$

As such, FDLD is a "four-fold degenerate" technique. For any given set of measurements, four possible $\boldsymbol{\mu}$ orientations exist on two distinct axes; one axis is parallel to $\boldsymbol{\mu}$ and $-\boldsymbol{\mu}$, and the other axis is parallel to the reflections (across the x-y plane) of $\boldsymbol{\mu}$ and $-\boldsymbol{\mu}$. Similar degeneracies hinder alternative FPM approaches, such as emission splitting [144] and polarized total internal reflection fluorescence (TIRF) [156,157]. Eliminating the degeneracy described in Eq. (3) would reduce the degree of degeneracy from four-fold to two-fold and is an attractive development because it would enable measurement of a unique axis that is parallel to $\boldsymbol{\mu}$. For the purposes of this work, we will henceforth refer to two-fold degenerate techniques that yield a unique axis simply as "non-degenerate".

Several previously presented techniques that use the orientation dependence of emission and/or excitation for the measurement of individual fluorophores' orientations are non-degenerate [91,142,158-168]. However, these techniques generally require fluorophores to be spatially and rotationally static and spatially isolated from each other. (While some techniques allow for limited rotational mobility [91,167,168], they still require individual

fluorophores to be spatially isolated). These conditions are not always possible; there are many situations in which samples are densely labeled with fluorophores that exhibit localized organization. There are many applications in which it would be useful to measure the average 3D orientation of semi-ordered spatiotemporal ensembles of fluorophores. However, orientation mapping of densely labeled samples has thus far only been accomplished using, at best, four-fold degenerate techniques.

For example, we recently developed molecular force microscopy (MFM). MFM employs FDLD and DNA mechanotechnology [133] tension sensors to measure the orientation of traction preventing direct mapping of force vectors; each measurement represents two distinct force orientations with equal likelihood, each of which has a distinct biological meaning. This limitation prevents useful forms of inquiry (such as force-balance analysis) that would be illuminating considering the increasingly apparent importance of force orientation in molecular biophysics research [44,53,131,132] and the increasing use of techniques like MFM in the development in active force generating nanomaterials [1,93].

Herein, we present the first non-degenerate technique, to the best of our knowledge, for ensemble fluorophore orientation mapping on densely labeled samples. This technique is a variant of FDLD that leverages a variable incidence polarized excitation beam and, as such, we call it variable incidence angle linear dichroism (VALiD).

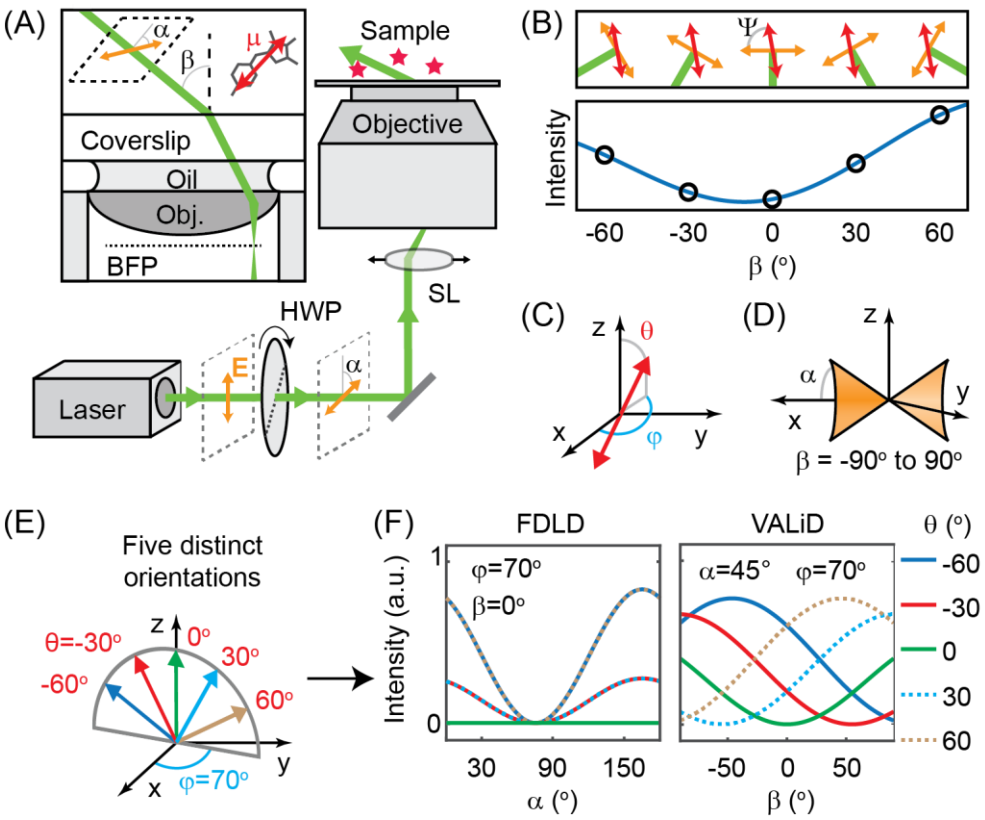

Figure 62: VALiD concept

(A) VALiD microscope setup showing excitation laser beam (green), **E** (orange), **μ** (red, superimposed on the chemical structure of an example fluorophore), rotating half wave plate (HWP) sliding lens (SL), and objective back focal plane (BFP) (B) I as a function of β calculated using Eq. (1) with $\alpha = 45°$, $\phi = 60°$, and $\theta = 45°$ and illustrated for five distinct β values. (C) Fluorophore azimuthal angle (φ) and polar angle (θ) shown in cartesian coordinate system. (D) Bisected cone of E orientations achievable when $\alpha = 45°$. (E) Five distinct fluorophore orientations and (F) corresponding intensity curves calculated using conventional FDLD (left) and VALiD (right).

- VALiD eliminates measurement degeneracy by rotating **E** in three-dimensions. This rotation can only be achieved by tilting the excitation beam with respect to the sample plane. One possible VALiD microscope setup is illustrated in Need to carefully discuss this apparant discrepancy between stall force and biasing force
- Critically overdamped system - microsecond response time may be inaccurate because mass should drop out at theis length scale

A: a rotatable half wave plate (HWP) is used to vary α of a linearly polarized, collimated excitation laser beam. A sliding lens is then used to laterally shift the position of the excitation beam's focal point on the objective lens's back focal plane (BFP), which tilts the laser beam as it leaves the objective such that it enters the sample at angle β. While there are many ways to implement VALiD within this framework, we start by considering the simplest implementation (which we call **configuration 1**): α is fixed at a constant value ($\alpha = \alpha_0$) and multiple images are acquired at different distinct β values. Setting $\alpha_0 = 90°$ makes **E** invariant with changing β and setting $\alpha_0 = 0°$ re-introduces degeneracy by restricting **E** to y-z plane (thus making the y-z plane a new plane of symmetry). As such, an intermediate value of α_0 (such as $45°$) must be used.

- The expected intensity of a single static fluorophore imaged with $\alpha_0 = 45°$ and varying β angles is shown in Need to carefully discuss this apparant discrepancy between stall force and biasing force
- Critically overdamped system - microsecond response time may be inaccurate because mass should drop out at theis length scale
- B. Note that varying β rotates **E** through a bisected cone with half angle α_0 centered on the x-axis (Need to carefully discuss this apparant discrepancy between stall force and biasing force
- Critically overdamped system - microsecond response time may be inaccurate because mass should drop out at theis length scale
- D). The measurement vectors in this cone are not coplanar, ensuring that each orientation of **μ** will produce a unique set of intensity measurements

(Need to carefully discuss this apparant discrepancy between stall force and biasing force
- Critically overdamped system - microsecond response time may be inaccurate because mass should drop out at theis length scale
- E,F). Theoretical VALiD curves for five static fluorophores with the same φ but different θ calculated using $\alpha_0 = 45°$ and $\beta \in [-90°, 90°]$ are shown in Need to carefully discuss this apparant discrepancy between stall force and biasing force
- Critically overdamped system - microsecond response time may be inaccurate because mass should drop out at theis length scale
- F (right). For reference, we also show intensity curves for the same orientations calculated according to conventional FDLD, where $\beta = 0$ and $\alpha \in [0°, 180°]$ (Need to carefully discuss this apparant discrepancy between stall force and biasing force
- Critically overdamped system - microsecond response time may be inaccurate because mass should drop out at theis length scale

F left). Note two key distinctions: first, in VALiD, all five curves are unique while curves generated from FDLD are degenerate; second, VALiD generates a curve for the $\theta = 0°$ case while FDLD does not. In practice, three-dimensional fluorophore orientation can be calculated from experimental intensity measurements via least-squares residual fitting to Eq. (1).

5.2 Mathematical modeling and computational methods

In this work, we will use computational methods to predict the experimental conditions under which VALiD can be correctly implemented. We first derive idealized equations for the fluorescence intensity of axially symmetric distributions of fluorophores. We then perform Monte Carlo simulations of VALiD measurements to model the effect of noise on orientation measurements and understand the effects of various experimental conditions and parameters on measurement quality. Throughout this text, we use non-bold type for scalars (e.g. φ, θ, A) and bold type for vectors (e.g. $\boldsymbol{\mu}$, **E**). Vectors are described

conventionally as 3x1 matrices. Unit vectors are defined with a hat; $\mathbf{v}/|\mathbf{v}| = \hat{\mathbf{v}}$. We use the standard **x**-**y**-**z** coordinate system to define the microscope coordinate system and a local **k**-**l**-**m** coordinate system to describe fluorophore ensembles. Within this local coordinate system, we denote polar angle as δ and azimuthal angle as γ. These quantities are matched to specific vectors using subscripts (e.g. δ_μ and δ_E). Finally, we will use rotation matrices; $R_{\mathbf{v}}(\tau)$ is a 3x3 matrix that, when multiplied by a vector, rotates the vector by τ degrees around the axis parallel to **v**. We can define the orientation of **E** and $\boldsymbol{\mu}$ with rotation matrices:

$$\hat{\mathbf{E}} = R_{\mathbf{y}}(\beta)R_{\mathbf{z}}(\alpha)\hat{\mathbf{x}} = R_{\mathbf{m}}(\gamma_E)R_{\mathbf{l}}(\delta_E)\hat{\mathbf{m}} \quad (5)$$

$$\hat{\boldsymbol{\mu}} = R_{\mathbf{z}}(\varphi)R_{\mathbf{y}}(\theta)\hat{\mathbf{z}} = R_{\mathbf{m}}(\gamma_\mu)R_{\mathbf{l}}(\delta_\mu)\hat{\mathbf{m}} \quad (6)$$

5.2.1 Fluorescence intensity of a conical ensemble

To enable the measurement of ensemble average orientation, we first derive equations for the expected fluorescence intensity of an ensemble of fluorophores that are uniformly distributed around a "symmetry axis". The orientation of the symmetry axis is defined by the unit vector $\hat{\mathbf{m}}$ (**Figure 63**A), which has polar angle Θ and azimuthal angle Φ such that

$$\hat{\mathbf{m}} = R_{\mathbf{z}}(\Phi)R_{\mathbf{y}}(\Theta)\hat{\mathbf{z}} \quad (7).$$

We will derive mathematical equations that can be used to calculate orientation from intensity values using two simplifying assumptions. We will later relax these assumptions to understand the extent to which they reduce the accuracy of this technique.

Assumption 1: We first assume that δ_μ is a fixed constant such that fluorophore orientation is restricted to a cone centered on $\hat{\mathbf{m}}$ (**Figure 63**D). In this scenario, the ensemble average δ_μ value, which we denote in this work as Δ, is the same as the half angle of the cone (**Figure 63**D). This assumption, which simplifies the forthcoming mathematics, is a reasonable approximation of many physically-relevant scenarios. For example, the commonly used fluorophore DiI has two lipid tails that readily insert into plasma membranes such that the transition dipole moment can rotate freely parallel to the plasma membrane. In this scenario, $\hat{\mathbf{m}}$ is normal to the plasma membrane and $\Delta \approx 75°$ [157,169].

Assumption 2: Second, we assume that each fluorophore's rotational time constant is much shorter than the fluorescence lifetime. This assumption simplifies mathematics by removing the orientation dependence of fluorescence emission on the measured ensemble intensity. Put another way, if a fluorophore's orientation within the cone is randomized between excitation and emission, then the effects of the orientation-dependence of emission will be equivalent for all orientations of **E**. It follows that, under this assumption, changes in fluorescence intensity will result strictly from changes in the orientation of **E**.

We also make three minor assumptions: first, we assume that photobleaching is negligible – which is reasonable for densely labeled samples that are excited with low power. Second, we assume that other time-dependent photophysical effects such as blinking are negligible, which is reasonable for ensembles of fluorophores where these effects can be averaged out and lumped in with the orientation-independent Q term. Finally, we assume and that the transition dipole moment for emission is parallel to the transition dipole moment for excitation ($\boldsymbol{\mu}$), which is reasonable for most fluorophores. Unlike with **assumptions 1** and

2, we do not study the effect of these assumptions within this work. However, we do note that photobleaching corrections can be applied to densely labeled samples that do undergo meaningful photobleaching. We also recommend avoiding the use of fluorophores with non-parallel emission and excitation transition dipole moments for future implementations of this technique.

Using these assumptions, the intensity of an ensemble of fluorophores can be expressed in a relatively simple manner:

$$I_{ens} = A \int_{\Omega} P_{ens} I \, d\boldsymbol{\mu} \tag{8}$$

where P_{ens} is a probability density function describing the relative contributions of all possible orientations of $\boldsymbol{\mu}$ to the ensemble, A is a scaling constant that combines factors such as the average detection efficiency, quantum yield, the number of fluorophores, and the intensity of the excitation light, and $\int_{\Omega} d\boldsymbol{\mu}$ denotes integration across all possible orientations of $\boldsymbol{\mu}$.

Next, we consider the local **k**-**l**-**m** coordinate system centered on $\hat{\mathbf{m}}$ (**Figure 63**B,C). The **k**-**l**-**m** unit basis vectors can be obtained by rotating the unit basis vectors of the global **x**-**y**-**z** coordinate system:

$$[\mathbf{k}\ \mathbf{l}\ \mathbf{m}] = R_{\mathbf{z}}(\Phi) R_{\mathbf{y}}(\Theta) [\mathbf{x}\ \mathbf{y}\ \mathbf{z}] \tag{9}$$

Within this coordinate system we can re-write Eq. (1) using the angular representation of the dot product and apply ensemble averaging as shown in Eq. (8):

$$I_{ens} = A\int_{\Omega}\left(\cos(\delta_E)\cos(\delta_\mu) + \sin(\delta_E)\sin(\delta_\mu)\cos\left(\gamma_\mu - \gamma_E\right)\right)^2 d\boldsymbol{\mu} \qquad (10)$$

where δ_μ, γ_μ and δ_E , γ_E are the local polar and azimuthal angles of $\boldsymbol{\mu}$ and **E**, respectively (**Figure 63**B,C). Expanding the square in Eq. (10), we obtain

$$I_{ens} = A\int_{\Omega}\left(\begin{matrix}\cos^2(\delta_E)\cos^2(\delta_\mu) + \cos(\delta_E)\cos(\delta_\mu)\sin(\delta_E)\sin(\delta_\mu)\cos(\gamma_\mu - \gamma_E) \\ + \sin^2(\delta_E)\sin^2(\delta_\mu)\cos^2(\gamma_\mu - \gamma_E)\end{matrix}\right) d\boldsymbol{\mu}\,. \quad (11)$$

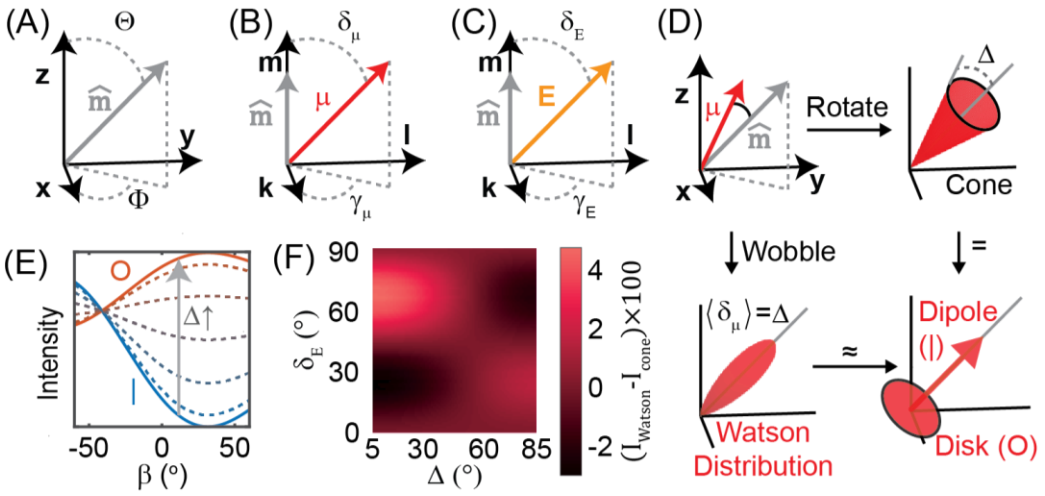

Figure 63: Coordinate system used in this work

(A) Global coordinate system showing orientation of symmetry axis $\hat{\mathbf{m}}$ denoted with polar angle Θ and azimuthal angle Φ. (B,C) Local coordinate system centered on $\hat{\mathbf{m}}$ showing orientation of (B) $\boldsymbol{\mu}$ with local polar angle δ_μ and local azimuthal angle γ_μ and (C) $\mathbf{E}$ with local polar angle δ_E and local azimuthal angle γ_E. (D) Depiction of ensembles of fluorophores distributed uniformly around symmetry axis $\hat{\mathbf{m}}$ via conical and Watson distributions. These ensembles can respectively be exactly and approximately decomposed into a dipole and a disk. (E) Intensity curves of disk (blue) and dipole (orange) components of ensemble and dashed lines showing weighted averages for 15° increments of δ_0 with $\Theta = \Phi = \alpha_0 = 45\circ$, and $A = 1$. (F) Surface plot showing the error (multiplied by 100 so that it loosely represents the percent error) of Eq. (12) when used to represent the Watson distribution (with $A = 1$). Because the error is low (<5%) for all combinations of Δ and δ_E, we conclude that Eq. (12) is a reasonable approximation for the intensity of Watson-distributed fluorescent ensembles.

Consider **assumption 1** in which a cone of fluorophores is centered on $\hat{\mathbf{m}}$ such that δ_μ is a fixed constant Δ. In this scenario, P_{ens} is an impulse function that is nonzero only when $\delta_\mu = \Delta$. Because **E** is static during an acquisition and Δ is constant, γ_μ is the only variable in Eq. (11) which must be integrated over to calculate the intensity of a conical ensemble (I_{cone}). When integrating γ_μ from 0° to 360°, the second term becomes zero and the third term becomes $\sin^2(\Delta)\sin^2(\delta_E)/2$, yielding:

$$I_{cone} = A\left(\cos^2(\Delta)\cos^2(\delta_E) + \frac{\sin^2(\Delta)\sin^2(\delta_E)}{2}\right) \quad (12).$$

Note that δ_E represents the angle between **E** and $\hat{\mathbf{m}}$ and, as such, is analogous to Ψ in Eq. (1). Additionally, note that this equation denotes separation of the ensemble into two simple components: a uniformly sampled disk perpendicular to $\hat{\mathbf{m}}$ and a dipole parallel to $\hat{\mathbf{m}}$ (**Figure 63**D). These two components are combined in a weighted average wherein the weights depend strictly on Δ (**Figure 63**E). Accordingly, Eq. (12) can be re-written as:

$$I_{cone} = I_{dipole}\cos^2(\Delta) + I_{disk}\sin^2(\Delta) \quad (13)$$

where I_{dipole} is the ensemble intensity (for given orientations of **E** and $\hat{\mathbf{m}}$) when $\Delta = 0$ and I_{disk} is the ensemble intensity when $\delta_0 = 90°$. Note that this last point assumes equal detection efficiencies of the two ensembles, which will not always be true even with **assumption 2**.

5.2.2 Fluorescence Intensity of a Watson ensemble

We next tested the necessity of **assumption 1** by testing whether Eq. (12) is reasonable for the description of other axially-symmetric distributions. Specifically, we evaluated the use

of Eq. (12) to represent fluorophores with orientations distributed according to the Watson distribution. The Watson distribution is an angular analog of the Gaussian distribution (**Figure 63**D) and is defined by the probability density function (P_{watson}):

$$P_{Watson} = C\exp(\kappa(\hat{\boldsymbol{\mu}} \cdot \hat{\mathbf{m}})^2) = C\exp\left(\kappa\cos^2(\delta_\mu)\right) \tag{14}$$

where κ is the concentration parameter and C is a normalization constant:

$$C = \frac{1}{\int_\Omega \exp\left(\kappa\cos^2(\delta_\mu)\right) d\boldsymbol{\mu}} \tag{15}.$$

Vectors randomly sampled from a Watson distribution will be concentrated around the axis $\hat{\mathbf{m}}$ when $\kappa > 0$ or around the equator perpendicular to $\hat{\mathbf{m}}$ (in what is called a "girdle" distribution) when $\kappa < 0$. The extent to which the distribution is concentrated parallel to or perpendicular to $\hat{\mathbf{m}}$ depends on the magnitude of κ. According to Eqs. (8) and (14), the intensity of fluorophores distributed via the Watson distribution can be computed using integration:

$$I_{Watson} = A\int_\Omega P_{Watson}\cos^2(\Psi)\, d\boldsymbol{\mu} \tag{16}$$

The parameter κ is directly related to Δ in a manner that can also be calculated through integration:

$$\Delta = A\int_\Omega \delta_\mu P_{Watson}\, d\boldsymbol{\mu} \tag{17}.$$

Performing this integration reveals a direct relationship between κ and Δ that can be used to assess the extent to which Eq. (12) can be used to approximate the intensity of Watson-

distributed fluorescent ensembles. While the integrations in Eqs. (15)-(17) are not easy to perform analytically, they are trivial to perform numerically. We accomplished numerical integration by generating 30,000 unit vectors that are roughly equally sampled from a unit sphere (using the SpiralSampleSphere technique [170]) and replacing $\int_{\Omega} \mathrm{d}\boldsymbol{\mu}$ in Eqs. (15)-(17) with the summation operator. Taking the difference between Eqs. (12) and (16) with $\mathrm{A} = 1$ (**Figure 63**F) reveals a very small difference (<5%) across the entire range of possible δ_{E} and Δ combinations, thus revealing that Eq. (12) is, in fact, a reasonable approximation for Watson-distributed fluorescent ensembles. In section 3.4, we will further test the truth of this conclusion using Monte Carlo simulations. We will also consider the effect that arises from relaxing **assumption 2** for both the Watson and conical distributions.

While we will not go into more sophisticated axially-symmetric distributions in this work, we also note that the intensity of any arbitrary axially-symmetric distribution can be calculated by treating the distribution as a summation of many cones and integrating over Eq. (5).

$$\mathrm{I}_{\mathrm{ax}} = \mathrm{A}\int_{0}^{\frac{\pi}{2}} \Gamma_{\mathrm{cone}}(\Delta, \Theta)\mathrm{I}_{\mathrm{cone}}(\delta_{\mathrm{E}}, \Delta)\mathrm{p}(\Delta)\mathrm{d}\Delta \tag{18}$$

Where $\Gamma_{\mathrm{cone}}(\delta_0, \Theta)$ is a scaling factor that accounts for the Δ- and θ_0-dependence of ensemble detection efficiency and $\mathrm{p}(\Delta)$ is a probability density function denoting the shape of the orientation distribution.

In addition, we note that when $\Delta = \tan^{-1}\sqrt{2} \approx 54.7$ (also known as the "magic angle") intensity ceases to depend on **E**'s orientation because $\mathrm{dI}/\mathrm{d}\Psi = 0$. We therefore predict that VALiD loses accuracy as Δ approaches the magic angle.

5.2.3 Microscope configurations

Below, we present three microscope configurations that could be used to implement VALiD. These three configurations exhibit qualitative differences in the set of measurement vectors that they can produce. We use a Monte Carlo simulation method – described below – to determine how well each configuration can be used to measure properties of simple axially symmetric fluorescent ensembles.

Configuration 1, which was described above, is the simplest implementation of VALiD, wherein α is fixed at $\alpha = \alpha_0$ and N images are acquired at β values equally spaced between $-60°$ and $60°$. We used a $60°$ cutoff because higher incidence angles will result in a large proportion of excitation light being reflected at the sample-coverslip interface and may result in distortions to the polarization state and/or spatial profile of the excitation light.

Configuration 2 is similar to config. 1; $N - 1$ images are acquired at varying β values with $\alpha = \alpha_0$. In addition, a single image is taken with $\alpha = 90°$ and $\beta = 0°$. In practice, this configuration can be implemented by adding an appropriately oriented polarization modulator that can be manually inserted into and removed from the path of the excitation beam. Config. 2 is intended to overcome some of the specific limitations of config. 1 by adding an additional measurement vector that is not restricted to the **E** cone.

Configuration 3 allows both β and α to vary freely and can be implemented using an electronically controlled polarization modulator (e.g. a HWP mounted in a rotational actuator or Pockels cell). This configuration is expected to maximize the spread of the vectors to equally cover the entire unit sphere. To simulate **E** in this configuration, we generated $4N - 3$ vectors equally distributed on the unit sphere using the

SpiralSampleSphere method [170] and then discarded all vectors except for those with polar angles between 30° and 90°. As such, this approach mimics the situation where the maximum β angle is 60°.

While these configurations are all based on a though-the-objective TIRF-style microscope wherein the excitation beam is tilted within a single plane of incidence, VALiD could also be implemented using alternative instruments such as azimuthal scanning fluorescence microscopes [171].

5.2.4 Monte Carlo simulation method

We used a Monte Carlo simulation method to evaluate each configuration over a range of experimental parameters. To summarize this method, we generate simulated intensity data for a given fluorescent ensemble and set of measurement vectors, add noise to the intensity data, and then use least-squares residual fitting to measure the best-fit orientation of the ensemble's symmetry axis (**Figure 64**A). We then repeat this process many times to measure the average accuracy of a given set of measurement vectors for a given fluorescent ensemble. This process is then repeated for a representative set of symmetry axis orientations to measure the overall performance of a set of measurement vectors. Finally, we repeated this entire process for different microscope configurations and different types of ensembles. The Monte Carlo algorithm is described in greater detail below. Least-squares residual fitting is performed using a two-layer lookup table approach. Steps 1-3 of the algorithm describe initialization of the lookup table. Steps 4-6 describe the process used for a single measurement simulation, and steps 7-9 describe various repetitions used to evaluate a wide parameter space.

1. Create the first layer of the lookup table by generating a representative set of 360 $\hat{\mathbf{m}}$ vectors equally-spaced on a unit hemisphere (using the SpiralSampleSphere function [170]) and calculating ideal intensity (I_{ideal}) values for each using Eq. (12). For each orientation, N intensity values are calculated (one for each of the measurement vectors). The set of measurement vectors is defined by the user-specified microscope configuration and the user-specified parameters N and (for configs. 1 and 2) α_0. I_{ideal} calculations also depend on the user-specified parameters A and Δ.

2. Create the second layer of the lookup table by calculating ideal intensity values for 36,000 equally spaced orientations in a similar fashion.

3. Connect the two layers of the lookup table; for each orientation in first tier, generate a list of the 200 most similar orientations in the second tier.

4. For a given orientation, add photon noise to obtain I_{noise}. Photon noise is Poisson distributed and if we assume that 1 intensity unit corresponds to 1 photon and that $I_{ideal} \gg 0$ then it can be modeled as normally-distributed with a standard deviation that is equal to the square-root of I_{ideal} due to the central limit theorem. Photon noise is also compounded by a background noise term (I_{bkrd}) that is common for fluorescence microscopy and arises due to myriad factors including thermal activation of camera photodetectors and nonspecific fluorescence from the background. As such, I_{noise} can be described using common notation for Normal distributions:

$$I_{noise} \sim \text{Normal}\left(I_{ideal}, \sqrt{I_{ideal} + I_{bkrd}}\right) \quad (19)$$

where the first argument of Normal() denotes the expected value and the second argument denotes the standard deviation of the random variable. We used $I_{bkrd} = 200$ to mimic values that we have observed in recent experiments [45].

5. Use least-square residual fitting to find the best-fit orientation in the first layer of the lookup table. Then, find the best-fit second-layer orientation from the 200 linked orientations. For both sets of calculations, the best-fit ($\hat{\mathbf{m}}^*$) is defined as the orientation that produces the lowest sum-squared error of all N intensity measurements:

$$\hat{\mathbf{m}}^* = \underset{\hat{m}}{\text{argmin}} \left(\sum_{i=1}^{N} (I_{noise} - I_{ideal})^2 \right) \quad (20)$$

where I_{ideal} is a function of $\hat{\mathbf{m}}$. In cases where multiple distinct orientations produced the exact same sum squared error, a single best-fit was randomly selected from the set. This approach enables a solid-angle resolution of $360^{\circ 2} \times (36{,}000)^{-1} = 0.01^{\circ 2}$ while only requiring $360 + 200 = 560$ comparison calculations per iteration.

6. Calculate angular error (ε) between the best-fit second tier and the true orientation:

$$\varepsilon = \cos^{-1}(|\hat{\mathbf{m}} \cdot \hat{\mathbf{m}}^*|) \quad (21).$$

7. Repeat steps 4-6 for n =30,000 Monte Carlo iterations and calculate the average angular error, $\langle \varepsilon \rangle$:

$$\langle \varepsilon \rangle = \frac{1}{n} \sum_{j=1}^{n} \varepsilon_j \qquad (22).$$

This large number of iterations ensures that the calculated ⟨ε⟩ value has converged. We also calculate the error anisotropy, as described below in 2.4.

8. Repeat steps 4-7 for each of 360 representative orientations of $\hat{\mathbf{m}}$ and calculate assessment metrics (described below) for the set of measurement vectors defined in step 1.

9. Repeat steps 1-8 for a range of parameter values. We performed several different types of parameter sweeps that will be described in greater detail below.

We evaluated the accuracy of configs. 1-3 under different fitting conditions; Θ and Φ were always treated as unknown fit parameters, but A and Δ were optional additional unknown fit parameters. The situation where A is known prior to acquisition is not experimentally practical. As such, these simulations were primarily run to isolate fundamental characteristics of the orientation measurement process. When A was an additional unknown parameter, each set of I_{ideal} lookup table values (steps 1-2) or I_{noise} values (step 4) was normalized to the average of the set. When Δ was an additional unknown parameter, step 5 was repeated 31 times (one for each 3° increment of Δ from 0° to 90°) and the best of the 31 best-fits was selected. Note that Δ could be estimated prior to VALiD acquisition using a variety of techniques or via existing reports in the research literature. For instance, fluorescence anisotropy techniques have been used to estimate Δ for DiI in supported lipid bilayers as ~75° [157,169].

To maintain a consistent SNR when comparing sets of measurement vectors with different N, we defined $A \times N$ as a proxy for the "total photon count". This definition imposes a tradeoff with increasing N between the benefit obtained by using more measurement vectors and the cost of decreasing the SNR for each individual intensity measurement.

5.2.5 Monte Carlo simulation assessment metrics

In addition to quantifying the average error for each orientation, we also quantified the error anisotropy. In this context, we define error anisotropy as the tendency of noise to bias orientation measurements preferentially towards some orientations. We agree with Chandler et al. that the ideal technique should be able to "reconstruct the orientation with a small and nearly uniform uncertainty" for all orientations [159]. Substantial error anisotropy is likely to result in systematic errors and "sink" orientations that will be measured more commonly than others. For example, estimation of θ using FDLD with Eq. (2) results in fluorescent ensembles with low θ angles being systematically over-estimated [45]. In this case, θ overestimation occurs because noise generally increases the amplitude of a best-fit sinusoid, particularly when the amplitude of the true sinusoid is very small. In other cases, high error anisotropy may have other causes. Regardless of the underlying cause, our Monte Carlo simulation method allows us to quantify error anisotropy in a context-independent manner.

Error anisotropy can be roughly visualized by analyzing the distribution on a unit sphere of 30,000 measured orientations for a given true orientation of $\hat{\mathbf{m}}$. When error is anisotropic, measurements will be concentrated along a given direction (e.g. around a given γ angle) on the unit hemisphere and the density map will resemble an elliptical Gaussian.

When error is isotropic, measurements will be uniformly distributed around the true orientation and the density map will resemble an isotropic Gaussian. **Figure 64**B, and D show examples of anisotropic and isotropic errors, respectively. Error anisotropy (σ) can be quantified by fitting the distribution of measured orientations to an uncertainty ellipse. This calculation is performed by assembling the **k** and **l** components of all measured $\hat{\mathbf{m}}^*$ values into two "component vectors", (denoted **K** and **L**, respectively, where each is a $n \times 1$ vector) calculating the covariance matrix (C) of these component vectors:

$$\mathrm{C} = \mathrm{cov}(\mathbf{K}, \mathbf{L}) \tag{23},$$

and then subtracting the ratio of the two eigenvalues of the covariance matrix (λ_1 and λ_2, where $\lambda_1 > \lambda_2$) from 1:

$$\sigma = 1 - \frac{\lambda_2}{\lambda_1} \tag{24}.$$

Measurement error that is perfectly anisotropic (with measurements lying purely on one circle of the unit sphere or, equivalently, all coincident with a single plane) results in $\sigma = 1$. In contrast, perfectly isotropic error results in $\sigma = 0$.

After calculating $\langle\varepsilon\rangle$ and σ for each of 360 representative orientations, we then calculated five assessment metrics that together reflect the performance of a given set of measurement vectors for a given pair of A and Δ parameters. Those metrics are the average and maximum of the 360 calculated $\langle\varepsilon\rangle$ values ($\langle\varepsilon\rangle_{\mathrm{mean}}$ and $\langle\varepsilon\rangle_{\mathrm{max}}$), the average and maximum of the 360 calculated σ values (σ_{mean} and σ_{max}), and finally an "overall quality" metric q, where

$$\mathrm{q} = (60°)^2(\langle\varepsilon\rangle_{\mathrm{mean}}\langle\varepsilon\rangle_{\mathrm{max}}\sigma_{\mathrm{mean}}\sigma_{\mathrm{max}}\mathrm{N})^{-1} \tag{25}$$

is the product of the four other assessment metrics and N, as well as a scaling constant. This scaling constant makes q dimensionless and normalizes q to the theoretical maximum values for $\langle\varepsilon\rangle_{\mathrm{mean}}$ and $\langle\varepsilon\rangle_{\mathrm{max}}$ (both 60°, corresponding to randomly sampled $\hat{\mathbf{m}}^{*}$ vectors). This formulation reports on the overall measurement quality because in an ideal scenario all of the multiplied terms would be minimized. N was added as a multiplier on the rationale that increasing N increases the amount of time required for a full set of acquisitions, and faster acquisitions are generally favorable. We nonetheless view $\langle\varepsilon\rangle_{\mathrm{max}}$ as the most important of the five metrics because the original objective of this work (to determine microscope configurations that can measure all orientations accurately and non-degenerately) will only be achieved if $\langle\varepsilon\rangle_{\mathrm{max}}$ is low. As such, the other four assessment metrics are only informative if $\langle\varepsilon\rangle_{\mathrm{max}}$ is low.

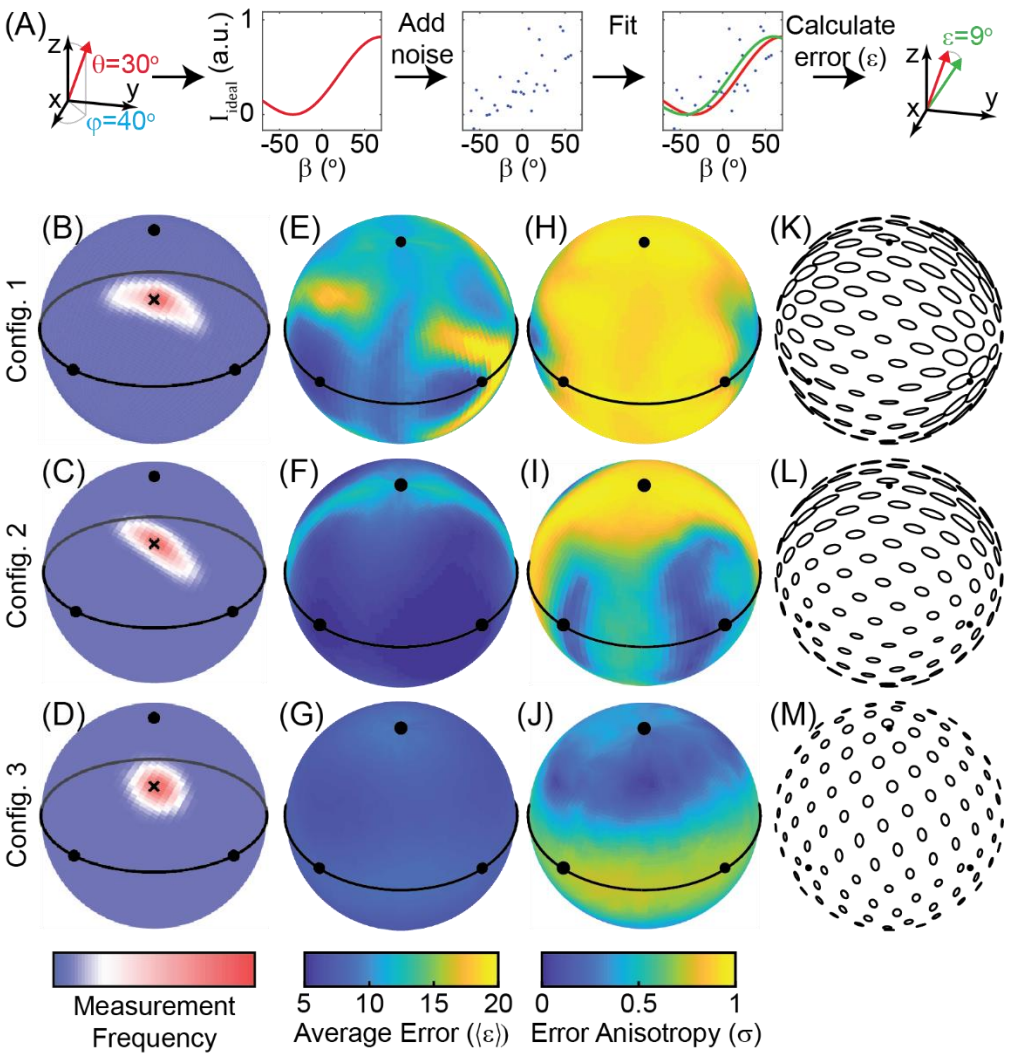

Figure 64: Monte Carlo error simulation results

(A) Depiction of a single iteration of the Monte Carlo algorithm used for error estimation: I_{ideal} is calculated with Eq. (9) for a given set of Θ, Φ, Δ, and A values (the curve shown was calculated with $\Theta = 30°$, $\Phi = 40°$, $\Delta = 0°$, and $A = 1$). Noise is then added to the calculated I_{ideal} values, and then the true orientation is fit to the noisy data. Finally, the angular error (ε) of the best-fit orientation is calculated. (B-M) Monte Carlo simulation outputs collected with $\Delta = 0°$, $\alpha_0 = 30°$ (when applicable), and A and Δ treated as known parameters. (B-D) Representative heatmaps of orientation measurements for a given true

orientation denoted by x ($\Theta = 40°$, $\Phi = 45°$) with $A \times N = 700$ for (B) configuration 1 with $N = 4$ (C) configuration 2 with $N = 4$, and (D) configuration 3 with $N = 7$. The x may appear to deviate from the maximum likelihood measurement due to artifacts associated with data display. (E-M) Surface plots showing the (E-G) average error ($\langle\varepsilon\rangle$), (H-J) error anisotropy (σ), and (K-M) error ellipses as a function of orientation with $A \times N = 1{,}000$ for (E, H, K) configuration 1 with $N = 5$, (F, I, L) configuration 2 with $N = 5$, and (G, J, M) configuration 3 with $N = 10$. All surface plots have black dots showing intersection of the unit sphere with the z-axis (top dot), x-axis (bottom left dot), and y-axis (bottom right dot) and the plots in (B-J) have a black circle showing the intersection of the unit sphere with the x-y plane.

5.3 Results

5.3.1 Initial configuration assessment

We first ran representative Monte Carlo simulations for configs. 1, 2, and 3 to obtain a qualitative understanding for the contexts in which each configuration could be reasonably used. For our initial assessment, we set $\Delta = 0$, $\alpha_0 = 30°$ (for configurations 1 and 2), $\Theta = 40°$, and $\Phi = 45°$. We also set $\mathrm{A} \times \mathrm{N} = 700$, which is an experimentally relevant value that would be expected for an ensemble consisting of a few dozen fluorophores. (This value is also somewhat low, ensuring that the effect of noise is meaningful). We treated both A and Δ as known parameters. A quick interpretation of Eq. (10) suggests that at least four measurement vectors must be used to achieve Nyquist sampling. Therefore, for configurations 1 and 2 we used $\mathrm{N} = 4$ measurement vectors. For config. 3, we used $N = 7$ measurement vectors to obtain more uniform sampling. We ran $n = 30{,}000$ iterations under these conditions and plotted errormaps showing the probability of measuring any given orientation when the true orientation is fixed (**Figure 64**B-D). As expected, we see a single node of measured orientations centered around the true orientation, thus confirming that all three configurations can achieve nondegenerate orientation measurement. (As a control, we ran the same process with $N = 4$ for FDLD and observed two nodes separated by a $180°$ rotation around the z-axis, not shown). Noise results in deviations from the true orientation such that $\langle\varepsilon\rangle$ is somewhat consistent between the three configurations ($11.0°$ for C1, $7.9°$ for C2, and $8.2°$ for C3). However, the orientational nature of these deviations vary; for config. 3, error is highly isotropic ($\sigma = 0.19$), producing measurement errors that are equally probable in all directions (**Figure 64**D). For

configs. 1 and 2, error is highly anisotropic ($\sigma = 0.85$ and 0.64 respectively – **Figure 64**B, C). These results suggest that spreading the measurement vectors across a wide variety of orientations shields against error anisotropy. These results are also in line with recent theoretical analyses [172].

We next varied $\hat{\mathbf{m}}$ across a representative set of 360 orientations and measured how σ and ⟨ε⟩ vary as a function of orientation for all three configurations. For these simulations we used $A \times N = 1{,}000$ and $\Delta = 0°$ and treated A and Δ as known parameters. For configs. 1 and 2 we used $N = 5$ and $\alpha_0 = 30°$, and for config. 3 we used $N = 10$. Unit sphere colormaps are shown in **Figure 64** E-J. To show the nature of error anisotropy across the entire unit sphere, we also plotted error ellipses for 100 representative orientations where the orientation of each ellipse shows the primary orientation of measurement error and the lengths of the major and minor axes are proportional to $\sqrt{\lambda_1}$ and $\sqrt{\lambda_2}$, respectively (**Figure 64** K-M).

These results provide a more detailed depiction of measurement error; ⟨ε⟩ depends heavily on orientation for config. 1 (**Figure 64**E), ranging from 5.4° to $\langle\varepsilon\rangle_{max} = 25.0°$ (with $\langle\varepsilon\rangle_{mean} = 11.9°$). Generally, orientations that are proximal to the half-cone of measurement vectors are measured much more accurately, while orientations that are further from the half-cone are measured less accurately because they are poorly excited. Config. 1 also produces highly anisotropic error for nearly all $\hat{\mathbf{m}}$ orientations, with $\sigma_{mean} = 0.84$ and $\sigma_{max} = 0.96$ (**Figure 64**H, K). Config. 2 generally is associated with lower error, with $\langle\varepsilon\rangle_{max} = 13.1°$ and $\langle\varepsilon\rangle_{mean} = 7.0°$ (**Figure 64**F). Config. 2 also produces lower error anisotropy, with $\sigma_{mean} = 0.60$ and $\sigma_{max} = 0.96$, than config. 1 (**Figure 64**I, L).

Measurement of many $\hat{\mathbf{m}}$ orientations is improved with config. 2, but some orientations – particularly, those that are close to the x-y plane – exhibit relatively high error and measurement anisotropy. These results suggest that the additional measurement vector parallel to the y-axis is sufficient to mitigate some, but not all, of the shortcomings associated with config. 1. In contrast, config. 3 exhibits low error ($\langle\varepsilon\rangle_{\text{mean}} = 7.4°$ and $\langle\varepsilon\rangle_{\text{max}} = 9.1°$) and relatively low error anisotropy ($\sigma_{\text{mean}} = 0.44$ and $\sigma_{\text{max}} = 0.75$) across all orientations (**Figure 64**G, J, M).

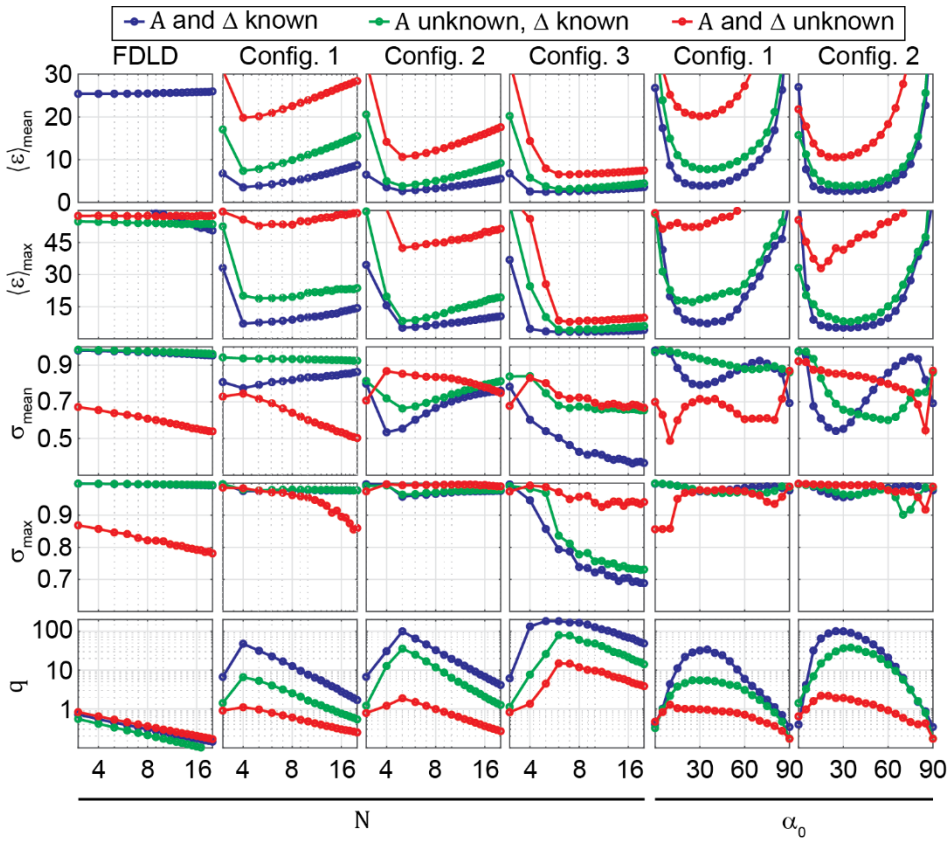

Figure 65: Optimization results

Results of Monte Carlo simulation-based optimization. We refer readers to section 3.2 for a more detailed description of the results shown here. Each subplot contains three curves showing five assessment metrics (section 2.4) as a function of the number of images (N) or the measurement vector cone angle (α_0). Blue curves show results when both A and Δ were known, green curves show results when Δ was known and A was unknown, and red curves show results when both A and Δ were unknown. Simulations were performed with $A \times N = 3{,}000$ and $\Delta = 0$ with all integer values of N ranging from 3 to 20 (left four columns) and 5° increments of α_0 ranging from 0° to 90°. When testing for optimal N, $\alpha_0 = 30°$ was used. When testing for optimal α_0, $N = 5$ was used. To summarize the

results, FDLD always fails due to measurement degeneracy, config. 3 always performs better than configs.1 or 2, and config. 2 always performs better than config 1. Configs. 1, 2, and 3 were found to have $N = 4$, 5, and 6 optimal, respectively, regardless of the number of free fit parameters. Configurations 1 or 2 were generally found to have an optimum of $\alpha_0 = 30°$, although in some cases the $\alpha_0 = 25°$ or $\alpha_0 = 35°$ exhibited an up to 1% increase in quality (q) over the $\alpha_0 = 30°$ condition.

The improved performance of config. 3 ($q = 5.10$) over config. 1 ($q = 0.83$) and config. 2 ($q = 3.82$) further demonstrates the benefits of spreading the set of measurement vectors out to cover a wider range of orientations. However, the improved performance comes at the cost of increasing complexity of the microscope system. It is worth noting that these simulations were performed with a relatively low SNR (only a few hundred photons per intensity measurement), and the issues with configs. 1 and 2 may not be as prominent at the higher SNR values that will often be accessible for densely labeled samples.

5.3.2 Optimization of VALiD parameters

We next sought to determine optimized N and α_0 values for each of the three configurations. As stated above, increasing N adds more unique measurement vectors, but also reduces the

SNR of each measurement (when $A \times N$ is held constant) and increases the amount of time required to obtain a full set of measurements. To determine optimal parameters, we used the Monte Carlo strategy described above to calculate the assessment metrics as a function N for configs. 1, 2, and 3 with $A \times N$ held constant and $\alpha_0 = 30°$ (when applicable). We also performed simulations for configs. 1 and 2 with α_0 ranging from $0°$ to $90°$ with $N = 5$. As a control, we ran simulations of FDLD with varying N, in which there are N distinct α values ranging from 0 to $(N - 1) \times 180°$ and $\beta = 0°$. For these simulations we selected $A \times N = 3{,}000$, set $\Delta = 0°$, and ran simulations with different sets of unknown parameters. Optimal N and α_0 values were defined as the values that maximized q. Our results are shown in **Figure 65**. Assessment metrics at optimized conditions are summarized Table 1.

We observed failure, which we define as occurring when $\langle\varepsilon\rangle_{\max} \geq 45°$, for FDLD in all scenarios due to the four-fold degenerate nature of FDLD measurements. This finding was expected, thus partially validating our simulation approach. Config. 1 performed well only when A and Δ were known, and the optimal condition was $N = 4$ and $\alpha_0 = 30°$. Config. 1 performed poorly when A was treated as an unknown parameter and failed when Δ was unknown. This failure was likely due to specific degeneracies that arise when constraining **E** vectors to a half-cone. One such degeneracy is between the case where $\hat{\mathbf{m}}$ is parallel to the y-axis and the case where $\Delta = 54.7°$, both of which produce intensity values that are invariant with respect to β. When A and Δ were known, performance was relatively insensitive to α_0 over a range of values from ~20° to 45°. For config. 1, error anisotropy was always high. Taken together, these results suggest that config. 1 can be used with caution when $N = 4$ and $\alpha_0 \approx 30°$ when Δ is known, but that config. 1 should not be used when Δ is unknown. While prior knowledge of A helps to improve accuracy, it does not improve error anisotropy and so results obtained using config. 1 should also be assumed to exhibit anisotropic error. Furthermore, due to inherent variability in fluorescent samples, accurate estimation of A is impractical without additional acquisitions with non-polarized light or with **E** vectors that are not restricted to the cone of measurement vectors – as is exactly the case with config. 2.

Table 3: Optimal experimental parameters and assessment metrics under optimal conditions

	Φ and Θ unknown			Φ, Θ, and A unknown			Φ, Θ, A, and Δ unknown		
Configuration #	1	2	3	1	2	3	1	2	3
Optimal N	4	5	6	4	5	6	-	-	6
Optimal α_0	30	25	-	30	35	-	-	-	-
$\langle\varepsilon\rangle_{max}$ (°)	7.1	5.1	3.3	20.2	8.3	4.3	45+	43	8.6
$\langle\varepsilon\rangle_{mean}$ (°)	3.5	2.7	2.5	7.4	3.8	3.1	-	-	6.6
σ_{max}	0.98	0.96	0.79	0.98	0.96	0.84	-	-	0.97
σ_{mean}	0.77	0.55	0.5	0.94	0.66	0.68	-	-	0.74
q	47.7	99.3	181.5	6.6	35.6	79.5	1.1	1.9	14.9

- Config. 2 demonstrated improved performance over config. 1. The optimal N value increased to 5, with $\langle\varepsilon\rangle_{\mathrm{mean}}$, $\langle\varepsilon\rangle_{\mathrm{max}}$, σ_{mean}, and σ_{max} all increasing monotonically with N when $N > 5$. This unit increase in N means that the optimal acquisition for config. 2 is the same as the optimal acquisition for config. 1, but with one additional measurement vector (with $\alpha = 90°$ and $\beta = 0°$). Unlike config. 1, config. 2 performed well when A was added as an additional unknown parameter. This finding suggests that config. 2 is inherently well-suited for simultaneous estimation of A and orientation, which is attractive for practical purposes. However, although config. 2 exhibits slightly lower error anisotropy than config. 1, it still exhibits substantial error anisotropy for all N and, as such, this configuration should also be used with a degree of caution. Config. 2 essentially failed (with $\langle\varepsilon\rangle_{\mathrm{max}}$ near 45°) when Δ and A were both unknown. Accordingly, our results suggest that config. 2 is well suited towards orientation measurement when Δ is known, but not when Δ is unknown. Optimization of α_0 showed that $\alpha_0 = 25°$ is optimal when A and Δ are known and $\alpha_0 = 35°$ is optimal when A is unknown and Δ is known. However, as with config. 1 we found that performance was relatively insensitive to α_0 over a range of values from ~20° to ~45°, and in both cases the optimal q was <1% higher than q when $\alpha_0 = 30°$. As such, we can reasonably conclude that $\alpha_0 = 30°$ is optimal for both config. 1 and config. 2. It is not immediately clear why $\alpha_0 = 30°$ is optimal, but we note that 30° is the angle that minimizes the average angular difference between all orientations and the cone of measurement vectors (shown in Need to carefully discuss this apparant discrepancy between stall force and biasing force
- Critically overdamped system - microsecond response time may be inaccurate because mass should drop out at theis length scale

D).

We observed the best performance with config. 3, for which there was another unit increment in the optimal number of measurement vectors to $N = 6$ (the specific set of $[\alpha, \beta]$ values was $[152°, -34°]$, $[20°, -12°]$, $[115°, 0°]$, $[158°, 6°]$, $[58°, 34°]$, $[118°, 59°]$). Unlike with configs. 1 and 2, config. 3 did not fail when both Δ and A were treated as unknown parameters. Config. 3 was also unique in that increasing N beyond the optimum of 6 generally caused σ_{mean} and σ_{max} to decrease. While increasing N came with the cost

of increased $\langle\varepsilon\rangle_{mean}$ and $\langle\varepsilon\rangle_{max}$, the increase in error was modest. For example, when A was unknown and Δ was known, increasing N from 6 to 20 caused σ_{max} to decrease from 0.84 to 0.73, while $\langle\varepsilon\rangle_{max}$ increased from 4.3° to 6.0°. However, the benefit of increasing N was less pronounced when both Δ and A were unknown; in the cases where Δ was known, σ_{max} trended toward ~0.7, but when Δ was unknown, σ_{max} trended towards ~0.94. The similarity in the two σ_{mean} vs. N curves when A was unknown suggests that only a small subset of orientations exhibited highly anisotropic error when Δ was unknown, potentially due to specific degeneracies that arise when Δ is added as an additional free parameter. Together, these results suggest that 1) config. 3 can be used to obtain accurate orientation measurements, 2) reasonably isotropic orientation measurements can generally be obtained when Δ is known, and 3) the error anisotropy can be decreased – to an extent – at the cost of slightly reduced accuracy by increasing N. These results also suggest that anisotropic error is a fundamental issue with VALiD that will be difficult to fully address for practical scenarios when A is unknown. However, we note that when the error is very low the fact that it is highly anisotropic has little practical relevance.

5.3.3 VALiD accuracy as a function of total photon count

To assess the manner in which the quality of VALiD-based orientation measurement scales with SNR, we measured $\langle\varepsilon\rangle_{max}$ and σ_{max} with A × N values ranging from 10^2 to 10^5 for all three configurations using optimized conditions ($N = 4$, $\alpha_0 = 30°$ for config. 1, $N = 5$, $\alpha_0 = 30°$ for config. 2, and $N = 6$ for config. 3) and $\Delta = 15°$. We ran these simulations under two fitting conditions: with A unknown and Δ known, or with both A and Δ unknown (**Figure 66**A). The results display principles discussed above: All configs. can accurately

measure orientation when Δ is known and SNR is high; config. 2 is much more accurate that config. 1; and config. 3 is substantially more accurate than config. 2; only config. 3 can measure orientation when Δ is unknown (although at extremely high SNR config. 2 appears to perform satisfactorily); and $\sigma_{\max}$ is generally close to 1, except when Δ is known for config. 3.

If we define a cutoff photon count $(\mathrm{A} \times \mathrm{N})_{\mathrm{cutoff}}$ as the $\mathrm{A} \times \mathrm{N}$ value that results in $\langle \varepsilon \rangle_{\max} \approx 10°$, we observe $(\mathrm{A} \times \mathrm{N})_{\mathrm{cutoff}} = 18{,}900$, 4,200, and 2,000 for configs. 1, 2, and 3 respectively when Δ is known. When Δ is unknown $(\mathrm{A} \times \mathrm{N})_{\mathrm{cutoff}} = 3{,}200$ for config. 3 and $(\mathrm{A} \times \mathrm{N})_{\mathrm{cutoff}} > 10^5$ for configs. 1 and 2.

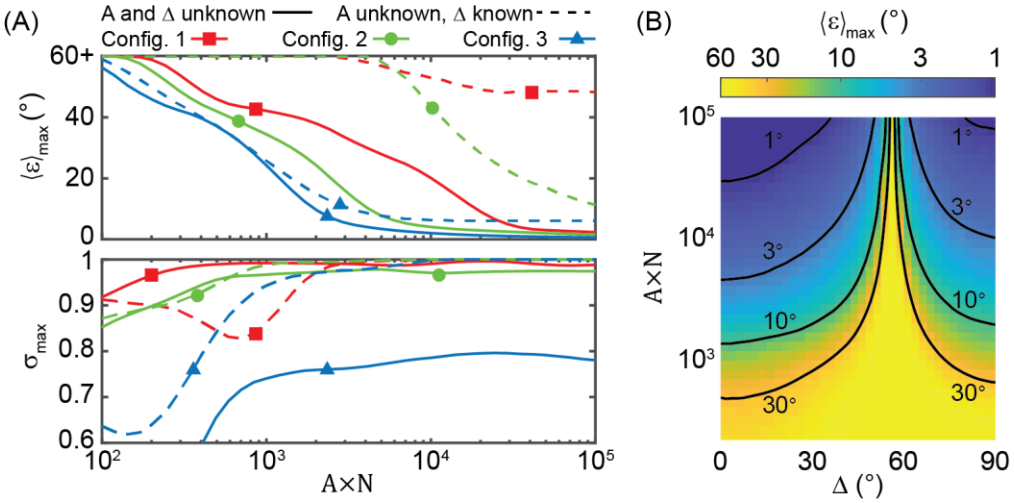

Figure 66: Comparison of different configurations

VALiD performance as a function of A × N and Δ. (A) $\langle\varepsilon\rangle_{max}$ (top) and σ_{max} (bottom) as a function of A × N with $\Delta = 15°$ for config. 1 with $N = 4$ and $\alpha_0 = 30°$ (red, squares), config. 2 with $N = 5$ and $\alpha_0 = 30°$ (green, circles), and config. 3 with $N = 6$ (blue, triangles) with A treated as an unknown fit parameter and Δ known (solid curves) or Δ unknown (dashed curves). (B) $\langle\varepsilon\rangle_{max}$ as a function of A × N and Δ for config. 3 with $N = 6$, A unknown, and Δ known. Black curves show contours where error is 30°, 10°, 3°, and 1°. Simulations were performed with Δ varying in 2.5° increments from 0° to 90°, and with 40 A × N values distributed logarithmically from 10^2 to 10^5.

For config. 3 with Δ unknown, $\langle\varepsilon\rangle_{\max}$ converges to ~6.1° (rather than 0°, as expected) with increasing $A \times N$ values. We expect that this convergence is an artifact of our lookup table-based fitting algorithm, rather than an outcome of specific degeneracies. As such, future implementations of VALiD may be improved by alternate fitting methods. For example, it may be possible to derive analytical methods for fast best-fit calculations that are stable against noise. Alternatively, following the lookup table method with gradient descent optimization may help the fitting algorithm converge to the global optimum.

We next simulated $\langle\varepsilon\rangle_{\max}$ as a function of $A \times N$ and Δ with config. 3, $N = 6$, A unknown, and Δ known (**Figure 66**B). For computational tractability, we reduced the number of Monte Carlo iterations per orientation to $n = 1{,}000$ and reduced the number of simulated orientations per condition to 120. Our results show that error is always negatively correlated with $A \times N$. As predicted, we also see that error increases monotonically as Δ approaches the magic angle of ~$54.7°$. Through parameter fitting to the 10° contour line, we find that the relationship:

$$\log_{10}((A \times N)_{\text{cutoff}}) = \frac{3.3}{\sqrt{\Delta - 54.7°}} + 2.7 \tag{26}$$

is a reasonable approximation (R^2>0.99), both when $\Delta > 54.7°$ and when $\Delta < 54.7°$. This relationship suggests that, under these conditions, a minimum of $A \approx 233$ is acceptable when $\Delta = 0°$. This level of signal (~700 total photons detected photons per set of $N = 6$ intensity measurements if $\cos^2(\delta_E)$=0.5, on average) is low enough to enable imaging even at the single molecule level.

5.3.4 Accounting for non-conical distributions and orientation-dependence of emission

We close out our simulation-based analysis by evaluating the effect that lifting **assumptions 1** and **2** has on orientation estimation. Specifically, we generated maps of $\langle\varepsilon\rangle_{\max}$ as a function of Δ and $A \times N$ as described above for **Figure 66**B under three conditions that we call "static cone", "mobile Watson", and "static Watson". For these simulations, we used config. 3 with $N = 6$, Δ known, and A unknown, and calculate I_{ideal} using condition-specific methods as described below. We assess error when reference curves are calculated either with **assumptions 1** and **2** (Eq. (12)) or with the same condition specific techniques used to calculate I_{ideal}. By running simulations in this way, we assess problems that may arise if Eq. (12) is used in situations where **assumptions 1** and **2** do not hold true, as well as the extent to which these problems can be corrected by using appropriate calculation methods for orientation fitting.

The static cone condition relaxes **assumption 2**, which states that fluorophore orientation randomizes within the probability distribution between excitation and emission. Instead, the opposite situation, wherein fluorophore orientation does not change at all between excitation and emission, is made. Under this condition, Eq. (12) no longer holds true because the orientation-dependence of emission will also modulate intensity. The mobile Watson condition relaxes **assumption 1** and assumes that fluorophores are distributed according to the Watson distribution, rather than a conical distribution, as described in section 2.2. The static Watson condition relaxes both **assumptions 1** and **2** by assuming that fluorophores are both distributed according to the Watson distribution and do not re-orient between excitation and emission.

To develop a means of calculating I_{ideal} for the static cone condition, we first calculated the expected collection efficiency (the fraction of emitted photons collected by the

microscope) for a static fluorophore as a function of θ. For these calculations, we accounted for 1) the anisotropic nature of fluorescence emission, wherein the intensity of fluorescence emission is strongest in directions perpendicular to $\boldsymbol{\mu}$ and decreases in a $\sin^2$ fashion to 0 in directions parallel to $\boldsymbol{\mu}$, 2) the limited collection angle of a microscope objective, and 3) partial reflection of emitted light at the sample-surface interface (the polarization of all emitted rays is perpendicular to the ray and parallel to the plane made by the ray and $\boldsymbol{\mu}$). We also assumed that fluorophores were far enough from the sample-coverslip interface to prevent near-field effects on emission. Running these calculations we found that the collection efficiency of a fluorophore Γ was well described by the equation.:

$$\Gamma = 0.16 + 0.05 \sin^2(\theta) \tag{27}$$

when the index of refraction for the sample was 1.33 (the same as water), the index of refraction for the coverslip was 1.515, and the numerical aperture of the microscope was 1.49 (although the same result would be obtained with numerical aperture ≥ 1.33 because any rays entering the coverslip at an incidence angle greater than $\sin^{-1}(1.33/1.51) \approx 62°$ will be totally reflected). In other words, 16% of the light emitted by a fluorophore aligned with the z-axis is collected, but for a fluorophore perpendicular to the z-axis that number increases to 21%. To calculate the intensity of a static cone for a given Δ, $\hat{\mathbf{m}}$, and $\mathbf{E}$, we generated 200 $\boldsymbol{\mu}$ vectors equally spaced in a cone centered on $\hat{\mathbf{m}}$ and then took the average of the $I = \Gamma(\mathbf{E} \cdot \boldsymbol{\mu})^2$ values. For the mobile Watson condition, we calculated I_{ideal} using Eq. (16) and numerical integration with 1,000 uniformly distributed fluorophore orientations. For the static Watson condition, we used an updated form of Eq. (16) that includes Γ:

$$I_{Watson} = \frac{A}{C}\int_{\Omega} \Gamma \, P_{Watson} \cos^2(\Psi) \, d\boldsymbol{\mu} \qquad (28).$$

The results of our simulations are shown in **Figure 67**.

We found that for the static cone condition, $\langle\varepsilon\rangle_{max}$ increased by a few degrees for all Δ and $A \times N$ when the lookup table fit values were calculated assuming a mobile cone (using Eq. (12)). This increase in error can be visualized by an outward shift of the contour lines in Figure 67A. Furthermore, error appeared to converge to non-zero values, which suggests that improper application of **assumption 2** can result in small systematic errors. Systematic errors were eliminated and $\langle\varepsilon\rangle_{max}$ reduced back to the baseline level when reference curves were properly calculated using the static cone model (Figure 67B).

Similarly, the mobile Watson condition demonstrated increased $\langle\varepsilon\rangle_{max}$ and introduced systematic errors when lookup table values were calculated using a mobile cone assumption (Figure 67C). The increase in error was more pronounced than in the static cone case and exhibited a non-monotonic dependence on $|\Delta - 54.7°|$. Again, error reduced to baseline when lookup table values were calculated using Eq. (16), which corresponds to the mobile Watson condition (Figure 67D). The same trends were observed for the static Watson condition, with the most pronounced pre-correction increases in error of all three conditions (Figure 67E,F). Interestingly, in the Watson distribution cases contour lines converged to $\Delta \approx 60°$, rather than the magic angle, when corrected reference values were used (Figure 67D,F).

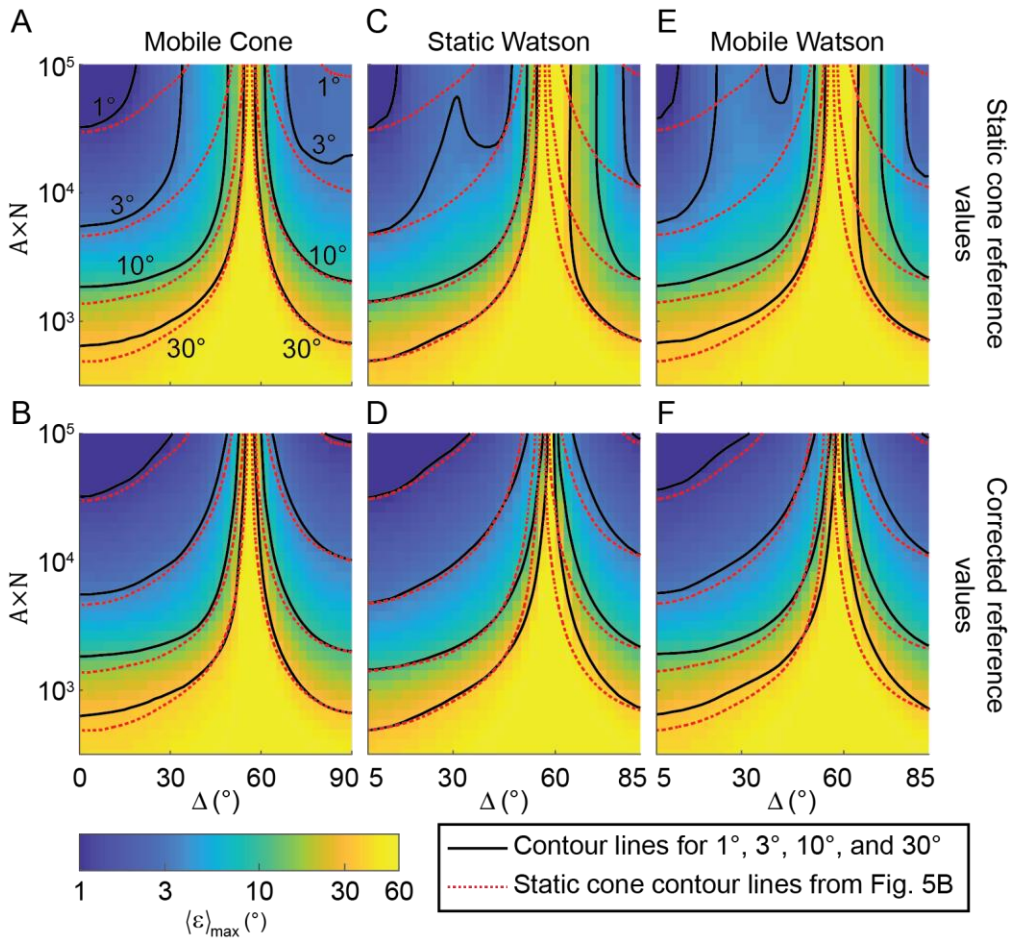

Figure 67: Comparison of different ensemble types

Surface plots showing $\langle\varepsilon\rangle_{\max}$ as a function of Δ and $A \times N$ when the underlying ensemble can be represented by (A,B) a cone of fluorophores that do not reorient between excitation and emission, (C,D) a Watson distribution wherein fluorophores re-orient between excitation and emission, and (E,F) a Watson distribution wherein fluorophores do not re-orient between excitation and emission. All simulations were performed with config. 3, $N = 6$, Δ known, and A unknown. Simulations were performed with reference intensity values (A, C, E) calculated using the static cone assumption (Eq. (12)), or (B, D, F) corrected in a manner that is specific to the true underlying distribution. Black contour lines

are specific to each surface plot, while red dashed contour lines are the same contour lines that are present in **Figure 66**B (static cone).

Together, these results show that failure to properly parameterize the fluorescent ensemble under investigation may slightly reduce the accuracy of the ensemble. However, under all three of the conditions tested systematic errors caused by improper parameterization were generally minimal ($< 5°$); the 3° contour line substantially deviated from the static cone condition (**Figure 66**B), but the 10° contour line did not. As such, we conclude that the effects of **assumptions 1** and **2** on performance are likely minimal. While efforts should generally be taken to use accurate models for calculations of I_{ideal}, in many cases the amount of information about a fluorescent ensemble is limited. In such cases, Eq. (12) can be used as a reasonable approximation for simple axially symmetric fluorescent ensembles.

5.4 Discussion and conclusions

Here we present an initial theoretical and computational exploration of a proposed technique, which we call VALiD, to perform non-degenerate measurement of fluorescent ensemble orientation. We present a mathematical model that can be used to fit the orientation of fluorescent ensembles to sets of intensity measurements acquired using the VALiD approach. We present three potential microscope configurations and optimal experimental parameters for each. We also present Monte Carlo simulation-based estimates for the SNR level necessary to implement VALiD with high accuracy.

We chose to use this Monte Carlo simulation-based approach over analytical approaches for several reasons. First, the Monte Carlo simulation algorithm described is simple and does not rely heavily on analytical formulations. This simplicity could, in the future, enable extension of the method to simulate more complex fluorophore orientation distributions that are not easy to describe analytically. Second, the least-squares residuals process used

to calculate orientation from simulated intensity measurements resembles the process that would commonly be used to process experimental data, thus allowing for an unbiased means of assessing the predicted accuracy of VALiD under different conditions. Third, this approach enables the detection of systematic errors arising from measurement degeneracies between orientations that are not similar to each other. Nonetheless, future studies would likely benefit greatly in terms of computational speed and fundamental insight from an analytical treatment. For example, analysis of axially-symmetric distributions in terms of their second moment matrices [91,173] could enable rapid matrix-based (rather than lookup table-based) orientation calculation. Similarly, Cramer-Rao lower bound estimates may yield fundamental insight into the maximal expected accuracy of VALiD under various conditions and prove crucial to optimization efforts [159,172].

The three tested configurations are only a few examples of microscope setups that can be used to implement VALiD. For example, variants of VALiD could also be implemented using light-sheet, structured illumination, and variable azimuthal incidence angle (rather than variable inclination) microscope setups. Future efforts to implement VALiD would benefit from paired error-estimation simulations, similar to those presented here, that consider specific aspects of the microscope system and account for effects such as β- and α-dependent reflection of the excitation laser at the sample surface-interface. Such simulations could help experimenters optimize their experimental apparatus to maximize performance.

Practically, it will be necessary to correct for changes in the shape of the illumination profile (i.e. by normalizing images to control images of randomly oriented fluorophores taken at corresponding α and β values). Normalization should also account for the z-

dependence of excitation beam intensity; the lateral component of the beam's propagation with nonzero β will result in a z-dependence of $|\mathbf{E}|$, particularly when the beam has a non-flat (e.g. Gaussian) profile (although flat field illumination [174] could mitigate some of these issues). It may also be necessary to account for slight changes in the $\mathbf{E}$ orientation of excitation light passing through the coverslip-sample interface due to reflection at the interface, which is polarization-dependent and can be accounted for using the Fresnel equations.

Note that a setup similar to the one we simulated is used for though-the-objective TIRF microscopy, meaning that VALiD can be implemented on many TIRF microscope with slight modifications. Variable inclination microscopy techniques have been increasingly used in recent years, including: variable-angle TIRF [175-177] and scanning angle interference microscopy [178], both of which enable enhanced z-axis localization resolution; highly-inclined thin illumination microscopy (HiLo) [179], which enhances signal-to-noise by restricting illumination to a thin slice; variable-angle near-TIRF [180], which enables refractive index image mapping; and three-dimensional optical polarization tomography, which enables orientation mapping of single static fluorophores [160]. Accordingly, the proposed design is experimentally feasible.

While we have considered four types of ensembles (mobile/static, cone/Watson) and found that the static cone assumption is somewhat reasonable for all of them, physical scenarios will likely exhibit intermediate behavior such as partial fluorophore re-orientation between excitation and emission or behave as wobbly cones. In some cases, optimization routines that incorporate additional parameters may help to account for some of these properties. Constrained optimization routines (e.g. treating Δ as unknown but restricted to the range

between 0° and 30°) and/or combination with emission-splitting optical components may offer improvements in accuracy and yield additional information about the type of fluorescent ensemble that is being investigated. We have not explored the analysis of non-axially symmetric orientation distributions, axially symmetric distributions with less simple (e.g. multi-modal) shapes, or axially-symmetric distributions with separate static and temporal components to their orientational heterogeneity [181-183]. Future theoretical investigations, and potentially combination with techniques that enhance orientational resolution (such as two-photon excitation microscopy [184,185]) may enable resolution of arbitrarily complex orientation distributions. Combination of VALiD with computational microscopy [186] or structured illumination [187] approaches may enable the reconstruction of super-resolution images from VALiD acquisitions. However, fluorophores of certain orientations will likely produce systematic biases in the observed spatial illumination pattern, particularly when they are out-of-focus [188]. Accurately reconstructing such images with high spatial resolution may require joint spatio-angular deconvolution procedures [189,190].

In conclusion, VALiD overcomes a fundamental limitation of existing fluorophore ensemble orientation mapping techniques and is therefore a promising technique for fluorescence microscopy orientation mapping applications.

CHAPTER 6. NONDEGENERATE NANOSCALE TRACTION FORCE ORIENTATION MAPPING WITH VARIABLE INCIDENCE ANGLE MOLECULAR FORCE MICROSCOPY

This final (brief) chapter illustrates the experimental technique that builds on the theoretical study in chapter 5. Specifically, I present VALiD-MFM, which allows for force vector mapping using MFM.

I had the idea for VALiD-MFM (**Figure 68, Figure 2**) as a first year student and envisioned a technique in which 3D force vectors, rather than degenerate pairs of force orientation angles, could be measured, displayed, and used for interesting biophysical calculations. Sometime in my second year, I attempted an implementation of VALiD-MFM wherein I fixed the polarization angle (α) at 45° and imaged platelets at various incidence angles (β) ranging from $-60°$ to $60°$. However, my attempts to reconstruct molecular force orientation maps using these images were unsuccessful. I put this project on the back burner until, as a fourth year, we decided to settle for a theory paper (chapter 5) that would at least present the VALiD technique. In conducting this theoretical/computational study, we found that the experimental approach that I had used in my initial study, which we refer to as "configuration 1" in chapter 5, has some fundamental limitations; while the approach can theoretically measure nondegenerate force orientation at very high signal to noise ratios (SNR), noise at experimentally-relevant SNR essentially ruins any attempt to measure force orientation.

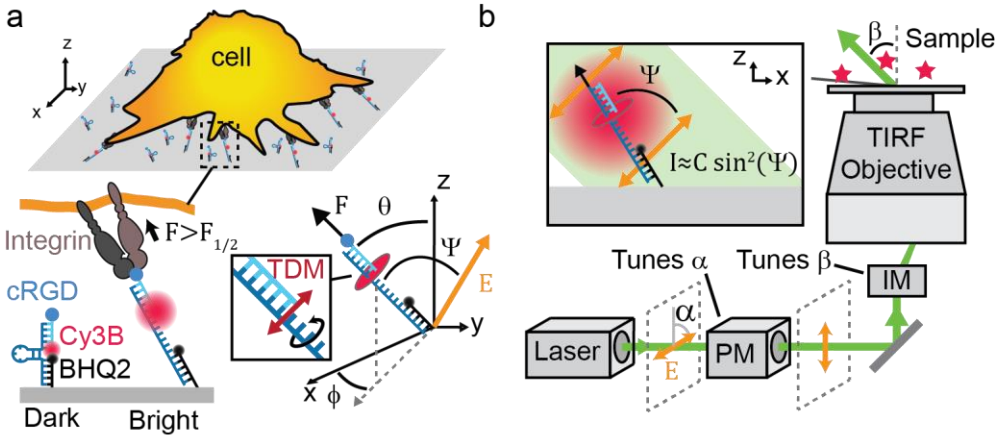

Figure 68: VALiD-MFM concept

a) Depiction of molecular tension probes with force orientation angles (θ and ϕ) as well as the excitation laser's electric field vector ($\boldsymbol{E}$) and the angle between force and E (Ψ). **b)** Excitation of fluorescent probe using an inclined laser beam with inclination angle β. The orientation of $\boldsymbol{E}$ is controlled by two modules: the polarization angle α is controlled by the polarization modulater (PM) and β is controlled by in incidence modulator (IM).

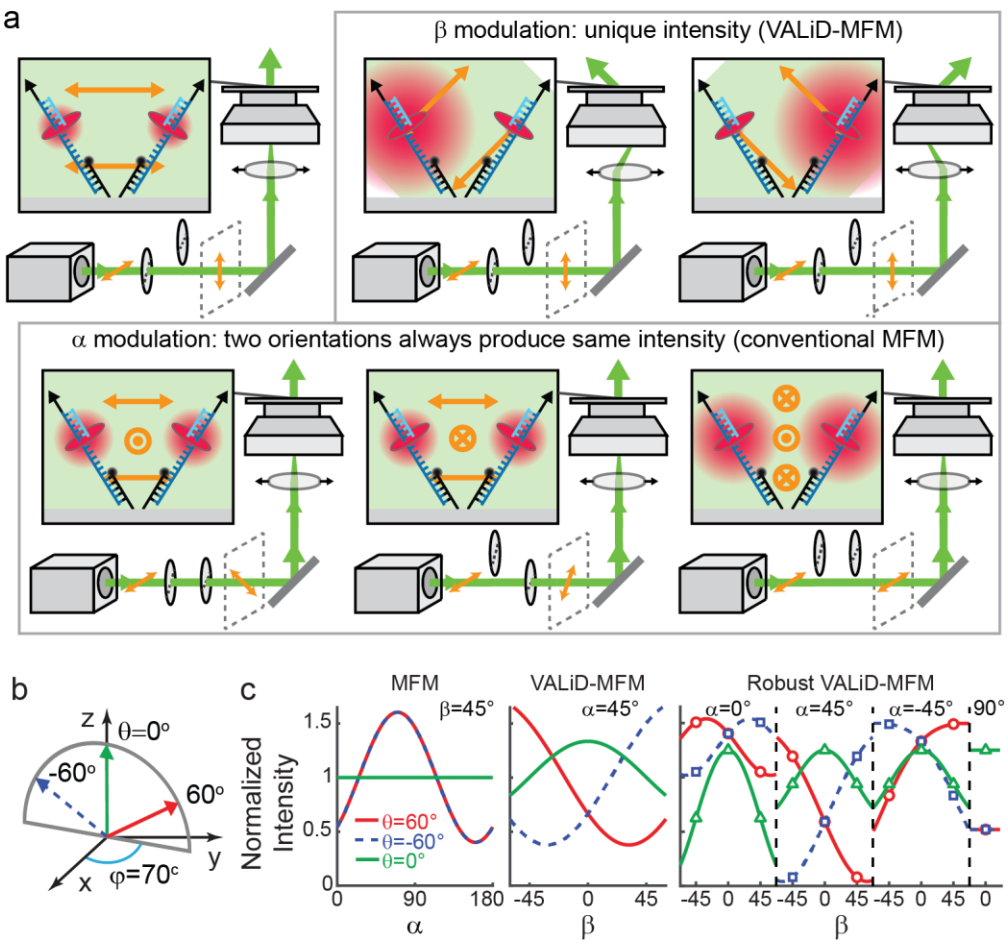

Figure 69: Depiction of VALiD-MFM-based measurement

a) Depiction of six fluorescence intensity measurements of two opened tension probes with the same θ and ϕ angles that differ by 180°. **b)** Depiction of three force orientation angles. Two have the same θ and ϕ angles that differ by 180°. **c)** Calculation of intensity using conventional MFM (varying α only), VALiD-MFM configuration 1 (varying β only), and robust VALiD-MFM (varying β at different α values. While the curves in the conventional MFM case show degeneracy between two of the orientations, the curve are nondegenerate for the VALiD-MFM and robust VALiD-MFM scenarios.

Towards the end of my fifth year, days before Emory labs shut down due to the COVID-19 pandemic, I attempted an experiment that utilized a less error-prone measurement approach. This approach involved adding a second insertable half wave plate (HWP) to the excitation laser line, which allowed for α to be fixed at four distinct angles. To calibrate the microscope, I imaged hundreds of DiI-doped SLB-coated microbeads at each combination of HWP insertions (both in, both out, one in, or the other one in) (**Figure 70**). I then used an automated algorithm to localized beads and quantify the intensity as a function of radial angle, where the minimum of the intensity vs. radial angle curve should correspond to α. This analysis confirmed satisfactory instrument setup with $\alpha = [0°, 45°, 90°, 135°]$.

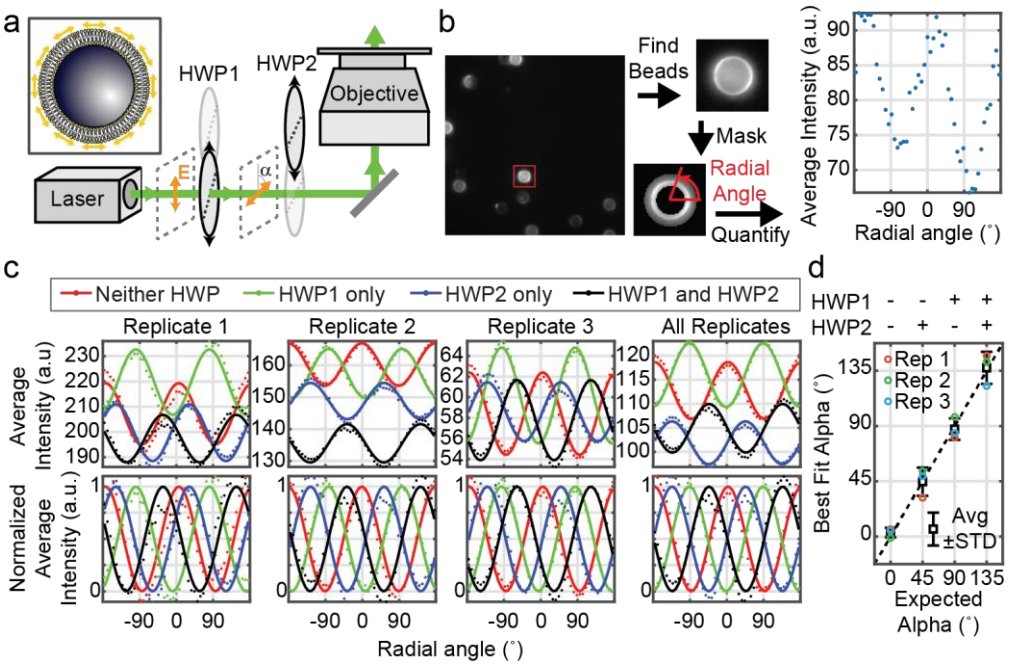

Figure 70: Experimental calibration of microscope

a) Depiction of microscope scheme, with two insertable HWPs that control the polarization angle, α. **b)** Representative SLB-coated bead fluorescence image, as well as the bead localization, masking, and radial intensity quantification. The average intensity vs. radial angle curve shows a sinusoidal profile. **c)** Ensemble average intensity vs radial angle curves for each of the four HWP insertion combinations. Bottom row shows curves and datapoints normalized to set the fit sinusoid minima and maxima to 0 and 1, respectively. **d)** Best fit α angle as a function of the expected α angle (expectation: $\alpha = [0°, 45°, 90°, 135°]$), showing strong adherence to expectation. This analysis shows that the expected α angles are indeed reflected in the context of our microscope.

As a proof-of-principle VALiD-MFM experiment I performed robust VALiD-MFM acquisitions of platelets spreading on molecular tension probe functionalized surfaces. These acquisitions entailed taking ten images: one at each combination of $\beta = [-45°, 0°, 45°]$ and $\alpha = [0°, 45°, 135°]$. A tenth image was taken at $\alpha = 90°$ and $\beta = 0°$. As a means of correcting for variations in the illumination profile due to changes in polarization and incidence, I also performed this same acquisition ten times on platelet-free regions of the surface. I then smoothed, averaged, and normalized these image sets to obtain ten background correction images, which I normalized all VALiD-MFM acquisitions to. Finally, I used least-squares residuals fitting methods described in chapter 5 to obtain molecular force orientation, as well as the heterogeneity angle (Δ) for each pixel. Preliminary results of one platelet, demonstrating the proof-of-principle, are shown in **Figure 71**.

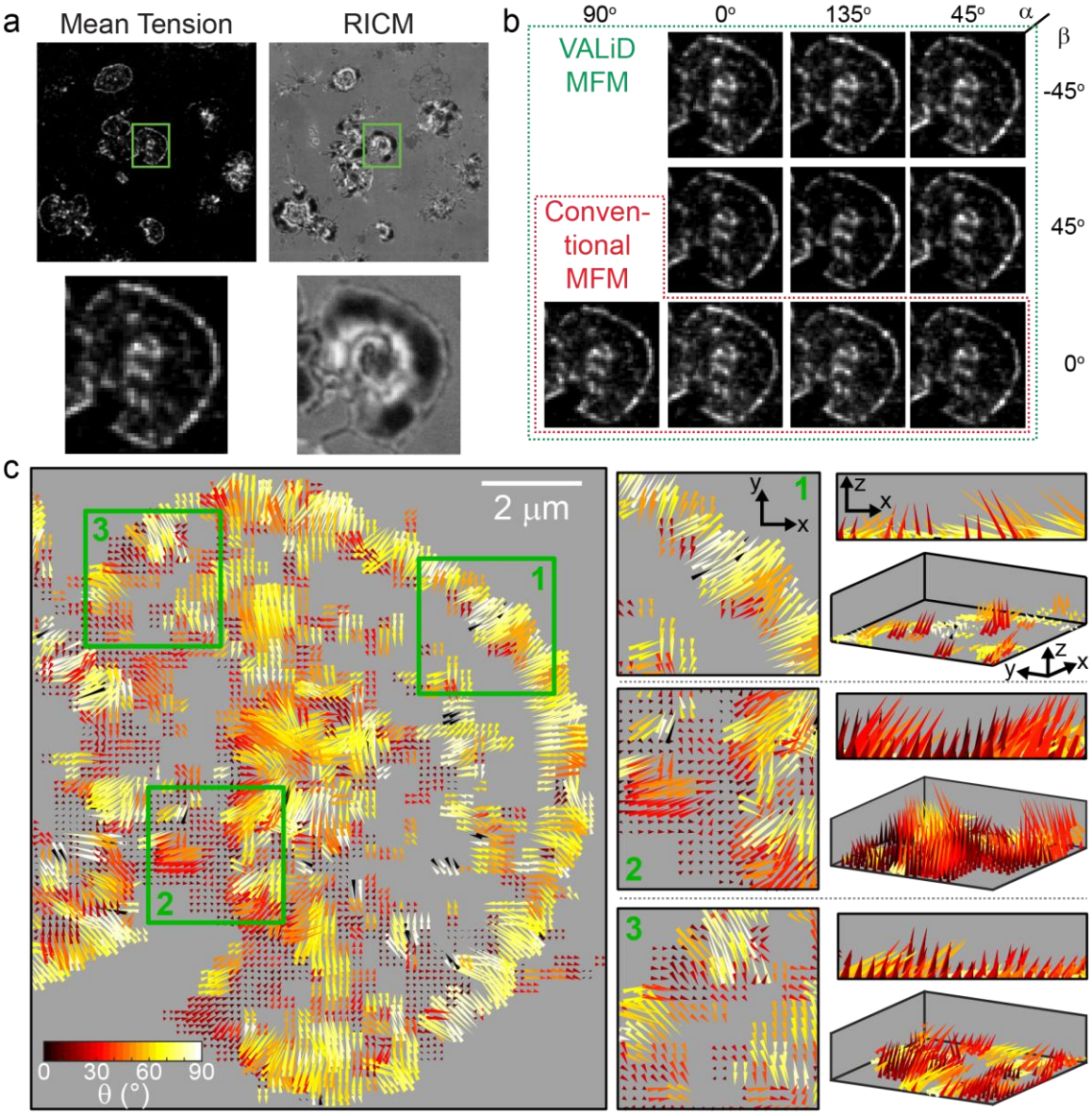

Figure 71: VALiD-MFM proof of principle experimental results

a) Mean fluorescence intensity and RICM image of a platelets spreading on a surface. Region of interest (ROI) is defined with a green box. **b)** Set of ten acquisitions, with α and β angles shown, for the ROI. Red dashed lines show the images that would constitute a conventional MFM acquisition. **c)** Force orientation map of the ROI. Force vectors are denoted using tapering lines, with color denoting tilt angle. Line length corresponds to

intensity, but force vectors with low tilt angles appear shorter in the top-down view. Accordingly, zoom-ins of three selected regions, shown with green boxes, are shown in x-y, x-z, and isometric views.

I have images of 50+ platelets taken from three independent experiments, but I have not yet processed the full dataset. However, this preliminary reveals an interesting result. While our previous study suggested that platelet integrin tilt angles (θ) were centered around $\sim 40°$, this work shows that most integrin traction force are concentrated in the $60 - 90°$ range. This result suggests that local integrin traction forces exhibit a higher degree of heterogeneity than previously thought. With conventional in, and orientational heterogeneity will systematically reduce the measured θ value. However, VALiD-MFM allows orientational heterogeneity (which is included in the Δ parameter of the fit) to be measured separately from the force orientation. Therefore, it appears that our previous measurement was systematically biased and that integrin force orientation are more highly inclined than previously thought. This conclusion is further supported by the presence of vectors with "flip-through" orientations.

Flip-through in VALiD-MFM is a phenomenon that illustrates a fundamental limitation of VALiD-MFM that will likely be impossible to resolve. VALiD works by allowing one to measure the orientation of the symmetry axis of a fluorescent ensemble. Technically, any symmetry axis can correspond to a force pointed in two different directions (either direction along the axis). Tension can only be applied upward from the planar surface, so when $\theta < 90°$ there is only one reasonable physical interpretation for a given symmetry axis orientation. However, when $\theta = 90°$ the symmetry axis is parallel to the surface, meaning that there are two possible interpretations. While the probability that θ is exactly $90°$ is infinitesimally small, noise induced error when θ is close to $90°$ (e.g. $\theta > 70°$) can result in small numbers of flip-through measurements that are off by almost exactly $90°$.

Further quantitiatvie analysis of these results is the subject of ongoing work.

REFERENCES

1 Blanchard, A. T. *et al.* Highly polyvalent DNA motors generate 100+ piconewtons of force via autochemophoresis. *Nano Lett.*, doi:10.1021/acs.nanolett.9b02311 (2019).

2 Jones, M. R., Seeman, N. C. & Mirkin, C. A. Programmable materials and the nature of the DNA bond. *Science* **347** (2015).

3 Oria, R. *et al.* Force loading explains spatial sensing of ligands by cells. *Nature* **552**, 219, doi:10.1038/nature24662

4 Hess, H. & Saper, G. Engineering with Biomolecular Motors. *Acc. Chem. Res.* **51**, 3015-3022, doi:10.1021/acs.accounts.8b00296 (2018).

5 Chen, Y., Ju, L., Rushdi, M., Ge, C. & Zhu, C. Receptor-mediated cell mechanosensing. *Mol. Biol. Cell* **28**, 3134-3155, doi:10.1091/mbc.E17-04-0228 (2017).

6 Huxley, H. & Hanson, J. Changes in the cross-striations of muscle during contraction and stretch and their structural interpretation. *Nature* **173**, 973-976 (1954).

7 Huxley, A. F. & Niedergerke, R. Structural changes in muscle during contraction; interference microscopy of living muscle fibres. *Nature* **173**, 971-973 (1954).

8 Scholey, J. M., Porter, M. E., Grissom, P. M. & McIntosh, J. R. Identification of kinesin in sea urchin eggs, and evidence for its localization in the mitotic spindle. *Nature* **318**, 483, doi:10.1038/318483a0 (1985).

9 Vale, R. D., Reese, T. S. & Sheetz, M. P. Identification of a novel force-generating protein, kinesin, involved in microtubule-based motility. *Cell* **42**, 39-50 (1985).

10 Brady, S. T. A novel brain ATPase with properties expected for the fast axonal transport motor. *Nature* **317**, 73, doi:10.1038/317073a0 (1985).

11 Olesen, S. P., Clapham, D. E. & Davies, P. F. Haemodynamic shear stress activates a K+ current in vascular endothelial cells. *Nature* **331**, 168-170, doi:10.1038/331168a0 (1988).

12 Wang, N., Butler, J. P. & Ingber, D. E. Mechanotransduction across the cell surface and through the cytoskeleton. *Science* **260**, 1124-1127 (1993).

13 Chu, S., Kron, S. E. D. O. A. S. C. C. S. & Ippen, E. in *International Quantum Electronics Conference.* QWJ5 (Optical Society of America).

14 Block, S. M., Goldstein, L. S. B. & Schnapp, B. J. Bead movement by single kinesin molecules studied with optical tweezers. *Nature* **348**, 348, doi:10.1038/348348a0 (1990).

15 Mullis, K. B. *et al.* (Google Patents, 1987).

16 McBride, L. J. & Caruthers, M. H. An investigation of several deoxynucleoside phosphoramidites useful for synthesizing deoxyoligonucleotides. *Tetrahedron Lett.* **24**, 245-248, doi:https://doi.org/10.1016/S0040-4039(00)81376-3 (1983).

17 Kallenbach, N. R., Ma, R.-I. & Seeman, N. C. An immobile nucleic acid junction constructed from oligonucleotides. *Nature* **305**, 829, doi:10.1038/305829a0 (1983).

18 Mao, C., Sun, W., Shen, Z. & Seeman, N. C. A nanomechanical device based on the B–Z transition of DNA. *Nature* **397**, 144, doi:10.1038/16437 (1999).

19 Rothemund, P. W. K. Folding DNA to create nanoscale shapes and patterns. *Nature* **440**, 297-302, doi:10.1038/nature04586 (2006).
20 Cecconi, C., Shank, E. A., Marqusee, S. & Bustamante, C. in *DNA Nanotechnology: Methods and Protocols* (eds Giampaolo Zuccheri & Bruno Samorì) 255-271 (Humana Press, 2011).
21 Castro, C. E., Su, H.-J., Marras, A. E., Zhou, L. & Johnson, J. Mechanical design of DNA nanostructures. *Nanoscale* **7**, 5913-5921, doi:10.1039/C4NR07153K (2015).
22 Bryant, Z., Oberstrass, F. C. & Basu, A. Recent developments in single-molecule DNA mechanics. *Curr. Opin. Struct. Biol.* **22**, 304-312, doi:https://doi.org/10.1016/j.sbi.2012.04.007 (2012).
23 Kratky, O. & Porod, G. Röntgenuntersuchung gelöster Fadenmoleküle. *Recl. Trav. Chim. Pays-Bas* **68**, 1106-1122, doi:10.1002/recl.19490681203 (1949).
24 Watson, J. D. & Crick, F. H. Molecular structure of nucleic acids. *Nature* **171**, 737-738 (1953).
25 Guharay, F. & Sachs, F. Stretch-activated single ion channel currents in tissue-cultured embryonic chick skeletal muscle. *The Journal of Physiology* **352**, 685-701 (1984).
26 Tamkun, J. W. *et al.* Structure of integrin, a glycoprotein involved in the transmembrane linkage between fibronectin and actin. *Cell* **46**, 271-282, doi:https://doi.org/10.1016/0092-8674(86)90744-0 (1986).
27 Mirkin, C. A., Letsinger, R. L., Mucic, R. C. & Storhoff, J. J. A DNA-based method for rationally assembling nanoparticles into macroscopic materials. *Nature* **382**, 607, doi:10.1038/382607a0 (1996).
28 Blakely, B. L. *et al.* A DNA-based molecular probe for optically reporting cellular traction forces. *Nat. Methods* **11**, 1229-1232, doi:10.1038/nmeth.3145 (2014).
29 Yehl, K. *et al.* High-speed DNA-based rolling motors powered by RNase H. *Nat. Nanotechnol.* **11**, 184, doi:10.1038/nnano.2015.259 (2015).
30 Shrestha, P. *et al.* Mechanical properties of DNA origami nanoassemblies are determined by Holliday junction mechanophores. *Nucleic Acids Res.* **44**, 6574-6582, doi:10.1093/nar/gkw610 (2016).
31 Wan, N. *et al.* A DNA Origami Mechanical Device for the Regulation of Microcosmic Structural Rigidity. *Small* **13**, doi:10.1002/smll.201700866 (2017).
32 Petrosyan, R. Improved approximations for some polymer extension models. *Rheol. Acta* **56**, 21-26, doi:10.1007/s00397-016-0977-9 (2017).
33 Marko, J. F. & Siggia, E. D. Stretching DNA. *Macromolecules* **28**, 8759-8770, doi:10.1021/ma00130a008 (1995).
34 Pfitzner, E. *et al.* Rigid DNA Beams for High-Resolution Single-Molecule Mechanics. *Angew. Chem. Int. Ed.* **52**, 7766-7771, doi:doi:10.1002/anie.201302727 (2013).
35 Kilchherr, F. *et al.* Single-molecule dissection of stacking forces in DNA. *Science* **353**, aaf5508, doi:10.1126/science.aaf5508 (2016).
36 Kostrz, D. *et al.* A modular DNA scaffold to study protein–protein interactions at single-molecule resolution. *Nat. Nanotechnol.* **14**, 988-993, doi:10.1038/s41565-019-0542-7 (2019).

37 Iwaki, M., Wickham, S. F., Ikezaki, K., Yanagida, T. & Shih, W. M. A programmable DNA origami nanospring that reveals force-induced adjacent binding of myosin VI heads. *Nat. Commun.* **7**, 13715, doi:10.1038/ncomms13715

38 Liedl, T., Högberg, B., Tytell, J., Ingber, D. E. & Shih, W. M. Self-assembly of three-dimensional prestressed tensegrity structures from DNA. *Nat. Nanotechnol.* **5**, 520, doi:10.1038/nnano.2010.107

39 Nickels, P. C. *et al.* Molecular force spectroscopy with a DNA origami-based nanoscopic force clamp. *Science* **354**, 305-307, doi:10.1126/science.aah5974 (2016).

40 Xiong, Q. *et al.* DNA Origami Post-Processing by CRISPR-Cas12a. *Angew. Chem. Int. Ed.* **59**, 3956-3960, doi:doi:10.1002/anie.201915555 (2020).

41 Kramm, K. *et al.* DNA origami-based single-molecule force spectroscopy unravels the molecular basis of RNA Polymerase III pre-initiation complex stability. *bioRxiv*, 775528, doi:10.1101/775528 (2019).

42 Albrecht, C. *et al.* DNA: a programmable force sensor. *Science* **301**, 367-370, doi:10.1126/science.1084713 (2003).

43 Wang, X. & Ha, T. Defining Single Molecular Forces Required to Activate Integrin and Notch Signaling. *Science* **340**, 991 (2013).

44 Zhang, Y. *et al.* Platelet integrins exhibit anisotropic mechanosensing and harness piconewton forces to mediate platelet aggregation. *Proc. Natl. Acad. Sci. U. S. A.*, doi:10.1073/pnas.1710828115 (2017).

45 Brockman, J. M. *et al.* Mapping the 3D orientation of piconewton integrin traction forces. *Nat. Methods* **15**, 115, doi:10.1038/nmeth.4536 (2017).

46 Liu, Y. *et al.* DNA-based nanoparticle tension sensors reveal that T-cell receptors transmit defined pN forces to their antigens for enhanced fidelity. *Proc. Natl. Acad. Sci. U. S. A.* **113**, 5610-5615, doi:10.1073/pnas.1600163113 (2016).

47 Wan, Z. *et al.* PI(4,5)P2 determines the threshold of mechanical force–induced B cell activation. *The Journal of Cell Biology* (2018).

48 Brockman, J. M. & Salaita, K. Mechanical Proofreading: A General Mechanism to Enhance the Fidelity of Information Transfer Between Cells. *Frontiers in Physics* **7**, doi:10.3389/fphy.2019.00014 (2019).

49 King, G. A., Biebricher, A. S., Heller, I., Peterman, E. J. G. & Wuite, G. J. L. Quantifying Local Molecular Tension Using Intercalated DNA Fluorescence. *Nano Lett.* **18**, 2274-2281, doi:10.1021/acs.nanolett.7b04842 (2018).

50 Song, J. *et al.* Reconfiguration of DNA molecular arrays driven by information relay. *Science* **357**, eaan3377, doi:10.1126/science.aan3377 (2017).

51 Thubagere, A. J. *et al.* A cargo-sorting DNA robot. *Science* **357** (2017).

52 Kopperger, E. *et al.* A self-assembled nanoscale robotic arm controlled by electric fields. *Science* **359**, 296 (2018).

53 Dutta, P. K. *et al.* Programmable Multivalent DNA-Origami Tension Probes for Reporting Cellular Traction Forces. *Nano Lett.* **18**, 4803-4811, doi:10.1021/acs.nanolett.8b01374 (2018).

54 Lahiri, H., Banerjee, S. & Mukhopadhyay, R. Free-Energy-Based Gene Mutation Detection Using LNA Probes. *ACS Sensors* **4**, 2688-2696, doi:10.1021/acssensors.9b01115 (2019).

55 Gerling, T., Kube, M., Kick, B. & Dietz, H. Sequence-programmable covalent bonding of designed DNA assemblies. *Sci. Adv.* **4**, eaau1157, doi:10.1126/sciadv.aau1157 (2018).
56 Feynman, R. P. in *Handbook of Nanoscience, Engineering, and Technology, Third Edition* 26-35 (CRC Press, 2012).
57 Sherman, W. B. & Seeman, N. C. A Precisely Controlled DNA Biped Walking Device. *Nano Lett.* **4**, 1203-1207, doi:10.1021/nl049527q (2004).
58 Yin, P., Yan, H., Daniell, X. G., Turberfield, A. J. & Reif, J. H. A Unidirectional DNA Walker That Moves Autonomously along a Track. *Angew. Chem. Int. Ed.* **43**, 4906-4911, doi:10.1002/anie.200460522 (2004).
59 Shin, J.-S. & Pierce, N. A. A Synthetic DNA Walker for Molecular Transport. *J. Am. Chem. Soc.* **126**, 10834-10835, doi:10.1021/ja047543j (2004).
60 Bath, J., Green, S. J. & Turberfield, A. J. A Free-Running DNA Motor Powered by a Nicking Enzyme. *Angew. Chem. Int. Ed.* **44**, 4358-4361, doi:10.1002/anie.200501262 (2005).
61 Omabegho, T., Sha, R. & Seeman, N. C. A Bipedal DNA Brownian Motor with Coordinated Legs. *Science* **324**, 67 (2009).
62 He, Y. & Liu, D. R. Autonomous multistep organic synthesis in a single isothermal solution mediated by a DNA walker. *Nat. Nanotechnol.* **5**, 778, doi:10.1038/nnano.2010.190 (2010).
63 Gu, H., Chao, J., Xiao, S.-J. & Seeman, N. C. A proximity-based programmable DNA nanoscale assembly line. *Nature* **465**, 202, doi:10.1038/nature09026 (2010).
64 Lund, K. *et al.* Molecular robots guided by prescriptive landscapes. *Nature* **465**, 206, doi:10.1038/nature09012 (2010).
65 Wang, Z.-G., Elbaz, J. & Willner, I. DNA Machines: Bipedal Walker and Stepper. *Nano Lett.* **11**, 304-309, doi:10.1021/nl104088s (2011).
66 Wickham, S. F. J. *et al.* A DNA-based molecular motor that can navigate a network of tracks. *Nat. Nanotechnol.* **7**, 169, doi:10.1038/nnano.2011.253 (2012).
67 You, M. *et al.* An Autonomous and Controllable Light-Driven DNA Walking Device. *Angew. Chem. Int. Ed.* **51**, 2457-2460, doi:doi:10.1002/anie.201107733 (2012).
68 Cha, T.-G. *et al.* A synthetic DNA motor that transports nanoparticles along carbon nanotubes. *Nat. Nanotechnol.* **9**, 39, doi:10.1038/nnano.2013.257 (2013).
69 Zhou, C., Duan, X. & Liu, N. A plasmonic nanorod that walks on DNA origami. *Nat. Commun.* **6**, 8102, doi:10.1038/ncomms9102 (2015).
70 Jung, C., Allen, P. B. & Ellington, A. D. A stochastic DNA walker that traverses a microparticle surface. *Nat. Nanotechnol.* **11**, 157, doi:10.1038/nnano.2015.246 (2015).
71 Wang, L., Deng, R. & Li, J. Target-fueled DNA walker for highly selective miRNA detection. *Chem. Sci.* **6**, 6777-6782, doi:10.1039/c5sc02784e (2015).
72 Dannenberg, F., Kwiatkowska, M., Thachuk, C. & Turberfield, A. J. DNA walker circuits: computational potential, design, and verification. *Nat. Comput.* **14**, 195-211, doi:10.1007/s11047-014-9426-9 (2015).
73 Yang, X., Tang, Y., Mason, S. D., Chen, J. & Li, F. Enzyme-Powered Three-Dimensional DNA Nanomachine for DNA Walking, Payload Release, and Biosensing. *ACS Nano* **10**, 2324-2330, doi:10.1021/acsnano.5b07102 (2016).

74 Qu, X. *et al.* An Exonuclease III-Powered, On-Particle Stochastic DNA Walker. *Angew. Chem. Int. Ed.* **56**, 1855-1858, doi:doi:10.1002/anie.201611777 (2017).
75 Urban, M. J. *et al.* Gold nanocrystal-mediated sliding of doublet DNA origami filaments. *Nat. Commun.* **9**, 1454, doi:10.1038/s41467-018-03882-w (2018).
76 Schliwa, M. & Woehlke, G. Molecular motors. *Nature* **422**, 759, doi:10.1038/nature01601 (2003).
77 Samii, L. *et al.* Time-dependent motor properties of multipedal molecular spiders. *Phys. Rev. E* **84**, 031111, doi:10.1103/PhysRevE.84.031111 (2011).
78 Olah, M. J. & Stefanovic, D. Superdiffusive transport by multivalent molecular walkers moving under load. *Phys. Rev. E* **87**, 062713, doi:10.1103/PhysRevE.87.062713 (2013).
79 Samii, L., Linke, H., Zuckermann, M. J. & Forde, N. R. Biased motion and molecular motor properties of bipedal spiders. *Phys. Rev. E* **81**, 021106, doi:10.1103/PhysRevE.81.021106 (2010).
80 Morozov, A. Y., Pronina, E., Kolomeisky, A. B. & Artyomov, M. N. Solutions of burnt-bridge models for molecular motor transport. *Phys. Rev. E* **75**, 031910, doi:10.1103/PhysRevE.75.031910 (2007).
81 Poon, W. C. K., Andelman D.,. *Soft Condensed Matter Physics in Molecular and Cell Biology*. (CRC Press, 2006).
82 Vecchiarelli, A. G., Neuman, K. C. & Mizuuchi, K. A propagating ATPase gradient drives transport of surface-confined cellular cargo. *Proc. Natl. Acad. Sci. U. S. A.* **111**, 4880 (2014).
83 Mosayebi, M., Louis, A. A., Doye, J. P. K. & Ouldridge, T. E. Force-Induced Rupture of a DNA Duplex: From Fundamentals to Force Sensors. *ACS Nano* **9**, 11993-12003, doi:10.1021/acsnano.5b04726 (2015).
84 Wan, Z. *et al.* The activation of IgM- or isotype-switched IgG- and IgE-BCR exhibits distinct mechanical force sensitivity and threshold. *eLife* **4**, e06925, doi:10.7554/eLife.06925 (2015).
85 Chowdhury, F. *et al.* Single molecular force across single integrins dictates cell spreading. *Integr. Biol.* **7**, 1265-1271, doi:10.1039/C5IB00080G (2015).
86 Wang, X. *et al.* Integrin Molecular Tension within Motile Focal Adhesions. *Biophys. J.* **109**, 2259-2267, doi:10.1016/j.bpj.2015.10.029 (2015).
87 Wang, X. *et al.* Constructing modular and universal single molecule tension sensor using protein G to study mechano-sensitive receptors. *Sci. Rep.* **6**, 21584, doi:10.1038/srep21584 (2016).
88 Roein-Peikar, M., Xu, Q., Wang, X. & Ha, T. Ultrasensitivity of Cell Adhesion to the Presence of Mechanically Strong Ligands. *Phys. Rev. X* **6**, 011001, doi:10.1103/PhysRevX.6.011001 (2016).
89 Ma, V. P.-Y. *et al.* The Mechanically-induced Catalytic Amplification Reaction for Readout of Receptor-Mediated Cellular Forces. *Angew. Chem. Int. Ed.* **55**, 5488-5492, doi:10.1002/anie.201600351 (2016).
90 Chowdhury, F. *et al.* Cdc42-dependent modulation of rigidity sensing and cell spreading in tumor repopulating cells. *Biochem. Biophys. Res. Commun.* **500**, 557-563, doi:10.1016/j.bbrc.2018.04.085 (2018).

91 Zhang, Y. *et al.* Platelet integrins exhibit anisotropic mechanosensing and harness piconewton forces to mediate platelet aggregation. *Proc. Natl. Acad. Sci. U. S. A.* **115**, 325, doi:10.1073/pnas.1710828115 (2018).
92 Wang, Y. *et al.* Force-activatable biosensor enables single platelet force mapping directly by fluorescence imaging. *Biosens. Bioelectron.* **100**, 192-200, doi:10.1016/j.bios.2017.09.007 (2018).
93 Su, H. *et al.* Light-Responsive Polymer Particles as Force Clamps for the Mechanical Unfolding of Target Molecules. *Nano Lett.* **18**, 2630-2636, doi:10.1021/acs.nanolett.8b00459 (2018).
94 Murad, Y. & Li, I. T. S. Quantifying Molecular Forces with Serially Connected Force Sensors. *Biophys. J.* **116**, 1282-1291, doi:10.1016/j.bpj.2019.02.027 (2019).
95 Guizar-Sicairos, M., Thurman, S. T. & Fienup, J. R. Efficient subpixel image registration algorithms. *Opt. Lett.* **33**, 156-158, doi:10.1364/OL.33.000156 (2008).
96 Maier, B., Potter, L., So, M., Seifert, H. S. & Sheetz, M. P. Single pilus motor forces exceed 100 pN. *Proc. Natl. Acad. Sci. U. S. A.* **99**, 16012 (2002).
97 Salaita, K., Wang, Y. & Mirkin, C. A. Applications of dip-pen nanolithography. *Nat. Nanotechnol.* **2**, 145, doi:10.1038/nnano.2007.39 (2007).
98 Kufer, S. K., Puchner, E. M., Gumpp, H., Liedl, T. & Gaub, H. E. Single-Molecule Cut-and-Paste Surface Assembly. *Science* **319**, 594 (2008).
99 Hu, L., Vecchiarelli, A. G., Mizuuchi, K., Neuman, K. C. & Liu, J. Directed and persistent movement arises from mechanochemistry of the ParA/ParB system. *Proc. Natl. Acad. Sci. U. S. A.* **112**, E7055 (2015).
100 Sugawara, T. & Kaneko, K. Chemophoresis as a driving force for intracellular organization: Theory and application to plasmid partitioning. *Biophysics (Oxf.)* **7**, 77-88, doi:10.2142/biophysics.7.77 (2011).
101 Wang, W., Duan, W., Ahmed, S., Mallouk, T. E. & Sen, A. Small power: Autonomous nano- and micromotors propelled by self-generated gradients. *Nano Today* **8**, 531-554, doi:10.1016/j.nantod.2013.08.009 (2013).
102 Ietswaart, R., Szardenings, F., Gerdes, K. & Howard, M. Competing ParA Structures Space Bacterial Plasmids Equally over the Nucleoid. *PLoS Comput. Biol.* **10**, e1004009, doi:10.1371/journal.pcbi.1004009 (2014).
103 Lim, H. C. *et al.* Evidence for a DNA-relay mechanism in ParABS-mediated chromosome segregation. *eLife* **3**, e02758, doi:10.7554/eLife.02758 (2014).
104 Jindal, L. & Emberly, E. Operational Principles for the Dynamics of the In Vitro ParA-ParB System. *PLoS Comput. Biol.* **11**, e1004651, doi:10.1371/journal.pcbi.1004651 (2015).
105 Surovtsev, I. V., Campos, M. & Jacobs-Wagner, C. DNA-relay mechanism is sufficient to explain ParA-dependent intracellular transport and patterning of single and multiple cargos. *Proc. Natl. Acad. Sci. U. S. A.* **113**, E7268-e7276, doi:10.1073/pnas.1616118113 (2016).
106 Le Gall, A. *et al.* Bacterial partition complexes segregate within the volume of the nucleoid. *Nat. Commun.* **7**, 12107, doi:10.1038/ncomms12107 (2016).
107 Walter, J. C. *et al.* Surfing on Protein Waves: Proteophoresis as a Mechanism for Bacterial Genome Partitioning. *Phys. Rev. Lett.* **119**, 028101, doi:10.1103/PhysRevLett.119.028101 (2017).

108 Hu, L., Vecchiarelli, A. G., Mizuuchi, K., Neuman, K. C. & Liu, J. Brownian Ratchet Mechanism for Faithful Segregation of Low-Copy-Number Plasmids. *Biophys. J.* **112**, 1489-1502, doi:10.1016/j.bpj.2017.02.039 (2017).
109 MacCready, J. S. *et al.* Protein gradients on the nucleoid position the carbon-fixing organelles of cyanobacteria. *eLife* **7**, e39723, doi:10.7554/eLife.39723 (2018).
110 Marras, A. E., Zhou, L., Su, H.-J. & Castro, C. E. Programmable motion of DNA origami mechanisms. *Proc. Natl. Acad. Sci. U. S. A.* **112**, 713, doi:10.1073/pnas.1408869112 (2015).
111 Funke, J. J., Ketterer, P., Lieleg, C., Korber, P. & Dietz, H. Exploring Nucleosome Unwrapping Using DNA Origami. *Nano Lett.* **16**, 7891-7898, doi:10.1021/acs.nanolett.6b04169 (2016).
112 Cangialosi, A. *et al.* DNA sequence–directed shape change of photopatterned hydrogels via high-degree swelling. *Science* **357**, 1126 (2017).
113 Kovacic, S. *et al.* Design and Construction of the Lawnmower, An Artificial Burnt-Bridges Motor. *IEEE Trans. NanoBiosci.* **14**, 305-312, doi:10.1109/TNB.2015.2393872 (2015).
114 Goel, A. & Vogel, V. Harnessing biological motors to engineer systems for nanoscale transport and assembly. *Nat. Nanotechnol.* **3**, 465, doi:10.1038/nnano.2008.190 (2008).
115 Bell, G. I. Models for the specific adhesion of cells to cells. *Science* **200**, 618-627 (1978).
116 Sedlak, S. M. *et al.* Monodisperse measurement of the biotin-streptavidin interaction strength in a well-defined pulling geometry. *PLoS One* **12**, e0188722, doi:10.1371/journal.pone.0188722 (2017).
117 Bizarro, C. V., Alemany, A. & Ritort, F. Non-specific binding of Na(+) and Mg(2+) to RNA determined by force spectroscopy methods. *Nucleic Acids Res.* **40**, 6922-6935, doi:10.1093/nar/gks289 (2012).
118 Whitley, K. D., Comstock, M. J. & Chemla, Y. R. Elasticity of the transition state for oligonucleotide hybridization. *Nucleic Acids Res.* **45**, 547-555, doi:10.1093/nar/gkw1173 (2017).
119 Hammer, D. A. Adhesive Dynamics. *J. Biomech. Eng.* **136**, 021006-021006-021010, doi:10.1115/1.4026402 (2014).
120 Paszek, M. J., Boettiger, D., Weaver, V. M. & Hammer, D. A. Integrin Clustering Is Driven by Mechanical Resistance from the Glycocalyx and the Substrate. *PLoS Comput. Biol.* **5**, e1000604, doi:10.1371/journal.pcbi.1000604 (2009).
121 Bidone, T. C., Skeeters, A. V., Oakes, P. W. & Voth, G. A. Multiscale model of integrin adhesion assembly. *PLoS Comput. Biol.* **15**, e1007077, doi:10.1371/journal.pcbi.1007077 (2019).
122 Anderson, N. R., Lee, D. & Hammer, D. A. Adhesive dynamics simulations quantitatively predict effects of kindlin-3 deficiency on T-cell homing. *Integr. Biol.* **11**, 293-300, doi:10.1093/intbio/zyz024 (2019).
123 Korosec, C. S., Zuckermann, M. J. & Forde, N. R. Dimensionality-dependent crossover in motility of polyvalent burnt-bridges ratchets. *Phys. Rev. E* **98**, 032114, doi:10.1103/PhysRevE.98.032114 (2018).

124 Arredondo, D. & Stefanovic, D. Effect of polyvalency on tethered molecular walkers on independent one-dimensional tracks. *Phys. Rev. E* **101**, 062101, doi:10.1103/PhysRevE.101.062101 (2020).
125 Semenov, O., Mohr, D. & Stefanovic, D. First-passage properties of molecular spiders. *Phys. Rev. E* **88**, 012724, doi:10.1103/PhysRevE.88.012724 (2013).
126 Semenov, O., Olah, M. J. & Stefanovic, D. Mechanism of diffusive transport in molecular spider models. *Phys. Rev. E* **83**, 021117, doi:10.1103/PhysRevE.83.021117 (2011).
127 Rank, M., Reese, L. & Frey, E. Cooperative effects enhance the transport properties of molecular spider teams. *Phys. Rev. E* **87**, 032706, doi:10.1103/PhysRevE.87.032706 (2013).
128 Becker, N. B., Rosa, A. & Everaers, R. The radial distribution function of worm-like chains. *The European Physical Journal E* **32**, 53-69, doi:10.1140/epje/i2010-10596-0 (2010).
129 Nitta, T. & Hess, H. Effect of Path Persistence Length of Molecular Shuttles on Two-stage Analyte Capture in Biosensors. *Cell. Mol. Bioeng.* **6**, 109-115, doi:10.1007/s12195-012-0262-7 (2013).
130 Stone, H. A., Stroock, A. D. & Ajdari, A. Engineering Flows in Small Devices: Microfluidics Toward a Lab-on-a-Chip. *Annual Review of Fluid Mechanics* **36**, 381-411, doi:10.1146/annurev.fluid.36.050802.122124 (2004).
131 Kim, S. T. *et al.* The alphabeta T cell receptor is an anisotropic mechanosensor. *J. Biol. Chem.* **284**, 31028 –31037, doi: 10.1074/jbc.M109.052712 (2009).
132 Huang, D. L., Bax, N. A., Buckley, C. D., Weis, W. I. & Dunn, A. R. Vinculin forms a directionally asymmetric catch bond with F-actin. *Science* **357**, 703 (2017).
133 Blanchard, A. T. & Salaita, K. Emerging uses of DNA mechanical devices. *Science* **365**, 1080-1081, doi:10.1126/science.aax3343 (2019).
134 Iqbal, A., Wang, L., Thompson, K. C., Lilley, D. M. J. & Norman, D. G. The Structure of Cyanine 5 Terminally Attached to Double-Stranded DNA: Implications for FRET Studies. *Biochemistry* **47**, 7857-7862, doi:10.1021/bi800773f (2008).
135 Zhang, Y., Ge, C., Zhu, C. & Salaita, K. DNA-based digital tension probes reveal integrin forces during early cell adhesion. *Nat Commun* **5**, 5167, doi:10.1038/ncomms6167 (2014).
136 Glazier, R. *et al.* DNA mechanotechnology reveals that integrin receptors apply pN forces in podosomes on fluid substrates. *Nat. Commun.* **10**, 4507, doi:10.1038/s41467-019-12304-4 (2019).
137 Zhanghao, K. *et al.* Super-resolution imaging of fluorescent dipoles via polarized structured illumination microscopy. *Nat. Commun.* **10**, 4694, doi:10.1038/s41467-019-12681-w (2019).
138 Haubner, R. *et al.* Structural and Functional Aspects of RGD-Containing Cyclic Pentapeptides as Highly Potent and Selective Integrin αVβ3 Antagonists. *J. Am. Chem. Soc.* **118**, 7461-7472, doi:10.1021/ja9603721 (1996).
139 Müller, M., Mönkemöller, V., Hennig, S., Hübner, W. & Huser, T. Open-source image reconstruction of super-resolution structured illumination microscopy data in ImageJ. *Nat. Commun.* **7**, 10980, doi:10.1038/ncomms10980 (2016).

140 Ma, R. *et al.* DNA probes that store mechanical information reveal transient piconewton forces applied by T cells. *Proc. Natl. Acad. Sci. U. S. A.* **116**, 16949, doi:10.1073/pnas.1904034116 (2019).
141 Brockman, J. M. *et al.* Live-cell super-resolved PAINT imaging of pN cellular traction forces. *Nat. Methods* **In Press** (2020).
142 Backer, A. S., Lee, M. Y. & Moerner, W. E. Enhanced DNA imaging using super-resolution microscopy and simultaneous single-molecule orientation measurements. *Optica* **3**, 659-666, doi:10.1364/OPTICA.3.000659 (2016).
143 Sandmeyer, A. *et al.* DMD-based super-resolution structured illumination microscopy visualizes live cell dynamics at high speed and low cost. *bioRxiv*, 797670, doi:10.1101/797670 (2019).
144 Mehta, S. B. *et al.* Dissection of molecular assembly dynamics by tracking orientation and position of single molecules in live cells. *Proc. Natl. Acad. Sci. U. S. A.* **113**, E6352-e6361, doi:10.1073/pnas.1607674113 (2016).
145 Cnossen, J. *et al.* Localization microscopy at doubled precision with patterned illumination. *Nat. Methods* **17**, 59-63, doi:10.1038/s41592-019-0657-7 (2020).
146 Blanchard, A. T., Brockman, J. M., Salaita, K. & Mattheyses, A. L. Variable incidence angle linear dichroism (VALiD): a technique for unique 3D orientation measurement of fluorescent ensembles. *Opt. Express* **28**, 10039-10061, doi:10.1364/OE.381676 (2020).
147 DeMay, Bradley S., Noda, N., Gladfelter, Amy S. & Oldenbourg, R. Rapid and Quantitative Imaging of Excitation Polarized Fluorescence Reveals Ordered Septin Dynamics in Live Yeast. *Biophys. J.* **101**, 985-994, doi:10.1016/j.bpj.2011.07.008 (2011).
148 Bartle, E. I., Urner, T. M., Raju, S. S. & Mattheyses, A. L. Desmoglein 3 Order and Dynamics in Desmosomes Determined by Fluorescence Polarization Microscopy. *Biophys. J.* **113**, 2519-2529, doi:10.1016/j.bpj.2017.09.028 (2017).
149 Duboisset, J. *et al.* Thioflavine-T and Congo Red Reveal the Polymorphism of Insulin Amyloid Fibrils When Probed by Polarization-Resolved Fluorescence Microscopy. *J. Phys. Chem. B* **117**, 784-788, doi:10.1021/jp309528f (2013).
150 Timr, Š. *et al.* Accurate Determination of the Orientational Distribution of a Fluorescent Molecule in a Phospholipid Membrane. *J. Phys. Chem. B* **118**, 855-863, doi:10.1021/jp4067026 (2014).
151 Kress, A. *et al.* Mapping the Local Organization of Cell Membranes Using Excitation-Polarization-Resolved Confocal Fluorescence Microscopy. *Biophys. J.* **105**, 127-136, doi:https://doi.org/10.1016/j.bpj.2013.05.043 (2013).
152 Abrahamsson, S. *et al.* MultiFocus Polarization Microscope (MF-PolScope) for 3D polarization imaging of up to 25 focal planes simultaneously. *Opt. Express* **23**, 7734-7754, doi:10.1364/OE.23.007734 (2015).
153 McQuilken, M. *et al.* Analysis of Septin Reorganization at Cytokinesis Using Polarized Fluorescence Microscopy. *Front. Cell Dev. Biol.* **5**, doi:10.3389/fcell.2017.00042 (2017).
154 Wang, X., Kress, A., Brasselet, S. & Ferrand, P. High frame-rate fluorescence confocal angle-resolved linear dichroism microscopy. *Rev. Sci. Instrum.* **84**, 053708, doi:10.1063/1.4807318 (2013).

155 Backer, A. S. *et al.* Single-molecule polarization microscopy of DNA intercalators sheds light on the structure of S-DNA. *Sci. Adv.* **5**, eaav1083, doi:10.1126/sciadv.aav1083 (2019).
156 Forkey, J. N., Quinlan, M. E., Alexander Shaw, M., Corrie, J. E. T. & Goldman, Y. E. Three-dimensional structural dynamics of myosin V by single-molecule fluorescence polarization. *Nature* **422**, 399, doi:10.1038/nature01529
157 Axelrod, D. Carbocyanine dye orientation in red cell membrane studied by microscopic fluorescence polarization. *Biophys. J.* **26**, 557-573 (1979).
158 Backlund, M. P., Lew, M. D., Backer, A. S., Sahl, S. J. & Moerner, W. E. The role of molecular dipole orientation in single-molecule fluorescence microscopy and implications for super-resolution imaging. *Chemphyschem* **15**, 587-599, doi:10.1002/cphc.201300880 (2014).
159 Chandler, T., Mehta, S., Shroff, H., Oldenbourg, R. & La Rivière, P. J. Single-fluorophore orientation determination with multiview polarized illumination: modeling and microscope design. *Opt. Express* **25**, 31309-31325, doi:10.1364/OE.25.031309 (2017).
160 Prummer, M., Sick, B., Hecht, B. & Wild, U. P. Three-dimensional optical polarization tomography of single molecules. *J. Chem. Phys.* **118**, 9824-9829, doi:10.1063/1.1569848 (2003).
161 Débarre, A. *et al.* Quantitative determination of the 3D dipole orientation of single molecules. *Eur. Phys. J D* **28**, 67-77, doi:10.1140/epjd/e2003-00295-1 (2004).
162 Ishitobi, H., Nakamura, I., Hayazawa, N., Sekkat, Z. & Kawata, S. Orientational Imaging of Single Molecules by Using Azimuthal and Radial Polarizations. *J. Phys. Chem. B* **114**, 2565-2571, doi:10.1021/jp905719b (2010).
163 Mortensen, K. I., Churchman, L. S., Spudich, J. A. & Flyvbjerg, H. Optimized localization analysis for single-molecule tracking and super-resolution microscopy. *Nat. Methods* **7**, 377-381, doi:10.1038/nmeth.1447 (2010).
164 Aguet, F., Geissbühler, S., Märki, I., Lasser, T. & Unser, M. Super-resolution orientation estimation and localization of fluorescent dipoles using 3-D steerable filters. *Opt. Express* **17**, 6829-6848, doi:10.1364/OE.17.006829 (2009).
165 Lieb, M. A., Zavislan, J. M. & Novotny, L. Single-molecule orientations determined by direct emission pattern imaging. *J. Opt. Soc. Am. B* **21**, 1210-1215, doi:10.1364/JOSAB.21.001210 (2004).
166 Backlund, M. P. *et al.* Simultaneous, accurate measurement of the 3D position and orientation of single molecules. *Proc. Natl. Acad. Sci. U. S. A.* **109**, 19087-19092, doi:10.1073/pnas.1216687109 (2012).
167 Backer, A. S. & Moerner, W. E. Determining the rotational mobility of a single molecule from a single image: a numerical study. *Opt. Express* **23**, 4255-4276, doi:10.1364/OE.23.004255 (2015).
168 Dale, R. E. *et al.* Model-Independent Analysis of the Orientation of Fluorescent Probes with Restricted Mobility in Muscle Fibers. *Biophys. J.* **76**, 1606-1618, doi:10.1016/S0006-3495(99)77320-0 (1999).
169 Gullapalli, R. R., Demirel, M. C. & Butler, P. J. Molecular dynamics simulations of DiI-C18(3) in a DPPC lipid bilayer. *Physical chemistry chemical physics : PCCP* **10**, 3548-3560, doi:10.1039/b716979e (2008).

170 Semechko, A. Suite of functions to perform uniform sampling of a sphere. *Suite of functions to perform uniform sampling of a sphere - MathWorks File Exchange* (2011).
171 Mattheyses, A. L., Shaw, K. & Axelrod, D. Effective elimination of laser interference fringing in fluorescence microscopy by spinning azimuthal incidence angle. *Microsc. Res. Tech.* **69**, 642-647, doi:10.1002/jemt.20334 (2006).
172 Zhang, O. & Lew, M. D. Fundamental Limits on Measuring the Rotational Constraint of Single Molecules Using Fluorescence Microscopy. *Phys. Rev. Lett.* **122**, 198301, doi:10.1103/PhysRevLett.122.198301 (2019).
173 Frehland, E., Kreikenbohm, R. & Pohl, W. G. Steady-state fluorescence polarization in planar lipid membranes: Experimental and theoretical analysis of the fluorophores 8-anilino-1-naphthalenesulfonate, 1,6-Diphenyl-1,3,5-hexatriene, dansyllysine-valinomycin and n-(9-anthroyloxy) fatty acids. *Biophys. Chem.* **15**, 73-86, doi:https://doi.org/10.1016/0301-4622(82)87018-X (1982).
174 Khaw, I. *et al.* Flat-field illumination for quantitative fluorescence imaging. *Opt. Express* **26**, 15276-15288, doi:10.1364/OE.26.015276 (2018).
175 Stock, K. *et al.* Variable-angle total internal reflection fluorescence microscopy (VA-TIRFM): realization and application of a compact illumination device. *J. Microsc.* **211**, 19-29, doi:doi:10.1046/j.1365-2818.2003.01200.x (2003).
176 Boulanger, J. *et al.* Fast high-resolution 3D total internal reflection fluorescence microscopy by incidence angle scanning and azimuthal averaging. *Proc. Natl. Acad. Sci. U. S. A.* **111**, 17164-17169, doi:10.1073/pnas.1414106111 (2014).
177 Zheng, C. *et al.* Three-dimensional super-resolved live cell imaging through polarized multi-angle TIRF. *Opt. Lett.* **43**, 1423-1426, doi:10.1364/OL.43.001423 (2018).
178 Paszek, M. J. *et al.* Scanning angle interference microscopy reveals cell dynamics at the nanoscale. *Nat. Methods* **9**, 825, doi:10.1038/nmeth.2077
179 Tokunaga, M., Imamoto, N. & Sakata-Sogawa, K. Highly inclined thin illumination enables clear single-molecule imaging in cells. *Nat. Methods* **5**, 159, doi:10.1038/nmeth1171
180 Bohannon, K. P., Holz, R. W. & Axelrod, D. Refractive Index Imaging of Cells with Variable-Angle Near-Total Internal Reflection (TIR) Microscopy. *Microsc. Microanal.* **23**, 978-988, doi:10.1017/S1431927617012570 (2017).
181 Irving, M. Steady-state polarization from cylindrically symmetric fluorophores undergoing rapid restricted motion. *Biophys. J.* **70**, 1830-1835, doi:https://doi.org/10.1016/S0006-3495(96)79748-5 (1996).
182 Stallinga, S. in *Proc.SPIE.*
183 Valades Cruz, C. A. *et al.* Quantitative nanoscale imaging of orientational order in biological filaments by polarized superresolution microscopy. *Proc. Natl. Acad. Sci. U. S. A.* **113**, E820-828, doi:10.1073/pnas.1516811113 (2016).
184 Ferrand, P. *et al.* Ultimate Use of Two-Photon Fluorescence Microscopy to Map Orientational Behavior of Fluorophores. *Biophys. J.* **106**, 2330-2339, doi:https://doi.org/10.1016/j.bpj.2014.04.011 (2014).

185 Kress, A. *et al.* Probing orientational behavior of MHC class I protein and lipid probes in cell membranes by fluorescence polarization-resolved imaging. *Biophys. J.* **101**, 468-476, doi:10.1016/j.bpj.2011.05.021 (2011).
186 Zhanghao, K. *et al.* Super-resolution dipole orientation mapping via polarization demodulation. *Light: Science & Applications* **5**, e16166, doi:10.1038/lsa.2016.166
187 Zhanghao, K. *et al.* Super-resolution Imaging of the Fluorescent Dipole Assembly with Polarized Structured Illumination Microscopy. *ArXiv*, 1712.05092 (2017).
188 Lew, M. D., Backlund, M. P. & Moerner, W. E. Rotational Mobility of Single Molecules Affects Localization Accuracy in Super-Resolution Fluorescence Microscopy. *Nano Lett.* **13**, 3967-3972, doi:10.1021/nl304359p (2013).
189 Chandler, T., Shroff, H., Oldenbourg, R. & La Rivière, P. Spatio-angular fluorescence microscopy I. Basic theory. *Journal of the Optical Society of America A* **36**, 1334-1345, doi:10.1364/JOSAA.36.001334 (2019).
190 Chandler, T., Shroff, H., Oldenbourg, R. & Rivière, P. L. Spatio-angular fluorescence microscopy II. Paraxial 4f imaging. *Journal of the Optical Society of America A* **36**, 1346-1360, doi:10.1364/JOSAA.36.001346 (2019).